

ÉCOLE DOCTORALE DES SCIENCES CHIMIQUES

**UMR 7006 - Institut de Science et d'Ingénierie Supramoléculaires
(I.S.I.S.)**

THÈSE

présentée par

Appan Merari MASILLAMANI

soutenue le : **04 Février 2013**

pour obtenir le grade de

Docteur de l'université de Strasbourg

Discipline / Spécialité : Chimie Physique

Propriétés électriques des nanostructures π -conjugués

THÈSE dirigée par :

M. SAMORI Paolo

Professeur, Université de Strasbourg

RAPPORTEURS :

Dr. VUILLAUME Dominique

**Research Director at CNRS, Institut
d'Electronique de Microélectronique et de
Nanotechnologie, Villeneuve**

Dr. SIMON Laurent

**Research Director at CNRS, Institut de Sciences
des Matériaux de Mulhouse, Mulhouse**

MEMBRES DU JURY :

Prof. DOUDIN Bernard

**Professeur, Université de Strasbourg –
Rapporteur interne**

Dr. VUILLAUME Dominique

Director at CNRS - Rapporteur externe

Dr. SIMON Laurent

Director at CNRS - Rapporteur externe

Prof. SAMORI Paolo

**Professeur, Université de Strasbourg – Directeur
de thèse**

Preface

I started research in the field organic based electronics rather by accident when I was completing my Master's degree courses in Sweden in the end of 2005. Prior to that I was trained as an electronics and communication engineer, mostly working with inorganic electronic devices, microprocessor circuits and communication systems during our laboratory assignments. As a part of the master's degree we had to complete a six month project in either an industrial organization or an academic institution. I chose to go to the University College London, UK in 2006 where I carried out research to understand the properties of charge transport in various organic transistors by electrical characterization. Furthermore, during the course of this project I developed the platform for testing these devices. I had been out of material science research for the next three years. One thing led to another and in the spring of 2010 I started my doctorate in the Nanochemistry laboratory, based at the *Institut de Science et d'Ingénierie Supramoléculaires* of Université de Strasbourg, France. During the course of my PhD I worked in completely diverse aspects to address physical and chemical such as structural and electronic properties of organic semiconductors and small molecule based devices. I would honestly say that many a times it seemed impossible to reach a goal like making an experiment work or finding a solution to assemble and improve the setup of an instrument, but I always had a strong inherent belief within myself that it could be done. So I persevered, tried harder, thought innovatively out the box, repeated experiments, even failed sometimes, but every time I was learning and gradually improving my knowledge how to make a system work better than the previous trial. Eventually as I pen down these last few sentences as my thesis is coming to an end, I can look back and boldly state that I gave it my best shot and I really cherished the challenge.

Appan Merari Masillamani

Strasbourg, 11/01/2013

Statement of work

I Appan Merari Masillamani do solemnly state that the works carried out during my thesis are of my undertaking, unless otherwise explicitly mentioned.

The cyclic voltammogram for the biphenyl thiol SAMs and many initial experiments with the mercury drop junctions were jointly performed with Dr. Núria Crivillers. Dr. Emanuele Orgiu prepared the P3HT:PTTP and P3HT/DAE blend transistors and performed the ionization energy characterization of P3HT:PTTP films. Dr. Jörn-Oliver Vogel performed the morphological characterization with atomic force microscopy of P3HT:PTTP blend films.

Dr. Florian Dötz synthesized the PTTP small molecules. Dr. Jürgen Rotzler and Mr. David Bossert from the University of Basel synthesized the biphenyl thiol derivatives. Dr. Federica Reinders synthesized the fluorinated azobenzene derivatives. Prof. Jean-Charles Ribierre provided the quinoidal oligomer semiconductor.

Dr. Ramakrishnappa Thippeswamy and Prof. Michael Zharnikov carried out the X-ray absorption characteristics of the biphenyl thiol SAMs on gold. Mr. Adam Kiersnowski and Dr. Wojtek Pisula performed the microstructure characterization of the P3HT:PTTP blend films.

I carried out theoretical simulations jointly with Mr. Silvio Osella to study the work function change induced by fluorinated azobenzene self-assembled monolayers on gold and started the initial transmission studies through single azobenzene molecule linked to gold electrodes. Later on Mr. Osella extended the work to different azobenzene derivatives.

To

Ashok, Geetha and Linda

The essence of the beautiful is unity in variety.

-Felix Mendelssohn (1809-1847), Composer

Appan Merari MASILLAMANI

Propriétés électriques des nanostructures π -conjuguées

Résumé

Mots-clés: molécules π -conjugués, transistors organiques, monocouche auto assemblée, transport de charge

Cette thèse traite de l'étude du transport de charge à travers les semi-conducteurs organiques au sein de transistors à effet de champ organiques (OFET). Une grande attention a été accordée aux interfaces dans les OFET dont les propriétés ont été accordées pour moduler la réponse transistor. La stabilité de l'appareil en état de commutation et le mécanisme régissant l'injection de charges ont été étudiés systématiquement. Le transport de charge au niveau fondamental à travers les monocouches auto-assemblées comprenant une grande variété des molécules π -conjuguées a été étudié.

Dans cette thèse, le processus de transport de charge et différents paramètres affectant ce phénomène sont examinées en détail par la fabrication et la caractérisation de trois terminaux basés sur des architectures OFET et deux dispositifs de jonctions terminales constituées d'une couche mono-moléculaire sur la surface de l'électrode métallique.

Parmi les différents aspects relatifs à l'injection de charge dans des transistors organiques macroscopiques à couches minces, un accent particulier a été mis sur l'interface¹ de l'engineering¹ en réglant (i) le diélectrique / l'interface semi-conducteur, et (ii) l'électrode en métal / le semi-conducteur. Pour explorer les aspects régissant le transport de charge dans le canal de l'appareil, nous avons étudié la propriété de (iii) la mobilité intrinsèque dans la semi-conductivité des matériaux et (iv) l'utilisation de mélanges dans la couche active du dispositif.

A l'échelle nanométrique, le transport de charge, grâce à une mono-couche moléculaire chimisorbé sur des électrodes métalliques, a été étudié. L'auto-assemblage avec des groupes terminaux thiol sur des électrodes d'or² a été exploité pour former une monocouche.² Pour effectuer la caractérisation électrique sur la mono couche auto-assemblée (SAM), nous avons construit un système de configuration comprenant des alliages eutectiques de gallium et d'indium liquide métallique (Gain^E) comme électrode.

¹ Le terme « interface » se réfère à la limite entre le semi-conducteur organique avec couche isolante ou avec des électrodes d'injection de charge ou inter-moléculaires frontières.

² Thiol à base de petites molécules en raison de son affinité chimique s'adsorbe sur la surface d'or par auto-assemblage processus et la structure qui est formée est nommé comme monocouche auto-assemblée (SAM).

Avant l'utilisation du Gain^E comme électrode supérieure, Hg(goutte) a été utilisé comme électrode de test pour effectuer la caractérisation électrique sur les SAMs. La raison du choix d'utilisation du Gain^E est explicitée dans ma thèse.

Nous avons entrepris les méthodes suivantes pour moduler les propriétés qui affectent le transport de charge dans les OFET:

1) **L'interface semi-conducteur / diélectrique:** Dans ce travail nous avons étudié l'influence que le changement dans la masse moléculaire de polymères diélectriques pourrait avoir sur les transistors. Le transport de charge dans les transistors organiques se produit à l'interface.³ Pour régler les propriétés de surface du diélectrique en contact avec le semiconducteur⁴ on utilise deux diélectriques polymériques avec des constantes diélectriques différentes. Les effets de commutation de stabilité et de l'hystérésis ont été observés.

2) **L'interface métal / semi-conducteurs:** Pour mieux comprendre les propriétés d'injection de charge de SAM biphényle thiols chimisorbées sur l'électrode source drain du transistor, nous avons fabriqué et caractérisé une famille de biphényles dérivés thiols avec un degré variable de torsion dans son squelette moléculaire. Des paramètres tels que la modification de la fonction de travail,⁵ les électrodes de mouillage et son effet correspondant à la mobilité de charge et tension dans le transistor à base de poly (3 hexylthiophène) ont été étudiés.

Nous avons étudié le transport de charge grâce à des thiols fluorés azobenzène avec des substitutions mono et biphényle auto-assemblés sur électrode d'or. Ces molécules ont été synthétisées par le groupe du professeur Marcel Mayor. Le transport de charge à travers les deux formes isomères trans et cis, a été étudié. Pour le biphényle substitué azobenzène fluoré, le mouillage de surface et les variations de la fonction de travail de l'électrode modifiée avec le SAM ont été évalués par différentes techniques.

3) **Transport de charge en vrac semi-conducteur intrinsèque:** pour rechercher la mobilité des porteurs intrinsèques pour OFET basé sur thiophène quinoidal possédant une nature amorphe dans la masse du film, nous avons effectué une caractérisation dans un cryostat. De précieux renseignements sur le mécanisme de piégeage possible et l'énergie d'activation correspondant à la fois à des systèmes de types p et n ont été acquis. Une autre étude a également été réalisée pour enregistrer l'énergie d'activation d'un transistor avec un mélange à deux composants de la couche de transport de charge dans l'appareil.

4) **Mélanges dans la couche active:** Pour moduler la mobilité des trous porteurs de charge des transistors, nous avons employé la technique de mélanger une petite molécule avec un polymère conjugué. Les effets de la séparation de phase et de l'orientation moléculaire sur le mélange et son influence sur le transport de charge sont détaillés dans cette étude.

L'interface semi-conducteur / diélectrique

Les chercheurs ont essayé de remplacer le dioxyde de silicium avec des diélectriques polymères par des OFET au courant du siècle.⁶ Les principaux avantages de l'utilisation de diélectriques polymères sont leur processabilité dans la solution, la flexibilité, la facilité de dépôt sur des substrats et programmabilité des propriétés de surface. Jusqu'à présent, pour notre projet nous avons utilisé deux diélectriques avec des constantes diélectriques différentes allant de la plus petite à la plus grande masse moléculaire, en combinaison avec un polymère fluoré conjugué dont les caractéristiques de transport de charge ambipolaire ont été démontrées. Tous les diélectriques polymériques et semi-conducteurs utilisés ont été acquis auprès de sources commerciales. Le rôle de l'énergie de surface diélectrique et la modification de polarité de surface lors d'un changement du poids moléculaire et son influence sur les performances du dispositif ont été étudiés. La question de la stabilité de commutation l'Etat OFF à ON et vice versa a été examinée pour toutes les configurations diélectriques / semi-conducteur, car cela donne des informations cruciales quant à la fiabilité de l'appareil sur un fonctionnement prolongé.

L'interface métal / semi-conducteurs

Dans le cas de la modulation d'injection de charges avec les électrodes des transistors à couches minces au moyen de la famille des SAM biphényles nous avons collaboré avec le groupe du prof. Marcel Mayor de l'Université de Bâle (Suisse) qui nous a fourni ces molécules. Pour avoir un aperçu de la densité structurale de l'empilement moléculaire et de l'angle d'inclinaison des molécules sur la surface de l'électrode en or, nous avons collaboré avec le groupe du prof. Michael Zharnikov de l'Universität Heidelberg (Allemagne) qui a effectué les travaux de spectroscopie d'absorption des rayons X (NEXAFS) et de spectroscopie de photoélectrons (XPS). Une série de mesures ont été faites sur des OFET pour mieux comprendre l'injection de charge électrique et le transport à travers les SAM, qui dépendent de l'ordre structurel, de l'épaisseur effective et de l'angle d'inclinaison à la surface des électrodes. La modulation de la mobilités de trous d'électrons a été atteinte sur l'intégration des SAM thiolés biphényle dans les électrodes OFET en raison de la modification de la fonction de travail des électrodes source-drain.^{7,8}

Nous avons également effectué la caractérisation électrique sur des thiols fluorés azobenzène substitués mono ou biphényle auto-assemblés sur électrode d'or. La caractérisation électrique des SAM a été réalisée avec une configuration développée spécialement en interne dans ce but. Nous avons peaufiné et amélioré la configuration progressivement au cours du temps de du travail de doctorat afin d'améliorer la fiabilité et la qualité des mesures. Nous avons testé notre configuration avec les systèmes déjà étudiés pour vérifier la sensibilité de nos mesures avec les résultats publiés dans la littérature.

Pour mieux comprendre comment la transmission à travers une seule molécule d'azobenzène est liée aux changements des électrodes d'or nous avons réalisé une étude théorique avec nos collaborateurs à l'Université de Mons (Belgique) projet de réseau SUPERIOR, avec notamment Silvio Osella et le Dr. Jérôme Cornil.

Transport de charge en vrac du semi-conducteur intrinsèque

Pour étudier la mobilité de la charge intrinsèque de transistors à base d'oligothiophène quinoidal sur la couche active dans les OFET nous avons collaboré avec le groupe du prof. Jean-Charles Ribierre, Ewha Womans University (Corée du Sud) qui nous a fourni ce composé. La caractérisation à des températures allant de 80 K à 300 K a été effectuée au moyen d'un cryostat configuré spécifiquement pour effectuer la caractérisation électrique sur des OFET. Un porte-échantillon personnalisé avec les connexions électriques pour la même caractérisation des OFET dans le cryostat a été construit. Le oligothiophène quinoidal, lors du dépôt, présente la propriété de se comporter comme un matériau de transport de trous et d'électrons après réchauffement.^{9,10}

Les énergies d'activation pour le cas particulier des modes de fonctionnement de type *p* et *n* ont été estimées.

Pour comprendre le rôle de la température dans le mécanisme de transport de charge par le biais d'un polymère semi-conducteur avec un photochrome comme couche active du transistor, la caractérisation électrique de cet OFET a été réalisée dans un cryostat. Les énergies d'activation ont été estimées pour les deux configurations d'état (ouvert et fermé) de la molécule diaryléthène, photochromique mélangé à un semi-conducteur. Le déséquilibre énergétique entre les niveaux d'énergie d'ionisation de poly (3 hexylthiophène) et diaryléthène ouvert est beaucoup plus grand comparé au diaryléthène fermé. Par conséquent, les énergies d'activation requises pour thermiquement activer le saut de charge devraient être différentes dans les deux cas.

Mélanges dans la couche active

Le projet sur les mélanges comme couche active d'OFET était un travail de collaboration avec les membres de la ISOF-Consiglio Nazionale delle Ricerche (Italie) et BASF (Suisse) à partir desquels les phénylène-thiophène-thiophène-phénylène (la petite molécule) ont été acquises. L'alliage de différents matériaux est l'une des méthodes utilisées pour modifier les niveaux d'ionisation énergétiques de la plus grande partie de la couche mince dans un transistor et donc la mobilité du porteur de charge.¹¹ L'étude de la diffraction des rayons X et la caractérisation grand angle de la diffusion des rayons X ont été effectuées à l'institut Max Planck de recherche sur les polymères (Mainz). A partir de ces résultats le rôle de la petite molécule de polymère d'emballage a été établi. On a effectué la qualification électrique complète de l'OFET qui a une couche active différente selon la quantité de petite molécule mélangée au polymère semi-conducteur. La caractérisation morphologique a été faite à l'aide d'un microscope à force atomique (AFM).

Résumé

Une étude approfondie a été réalisée au cours de mon travail de thèse sur les différents facteurs régissant le transport de charge dans les molécules organiques. Nous nous sommes concentrés sur l'optimisation des propriétés des interfaces dans le transistor à couche mince. L'influence de l'énergie de surface, de la polarité et du mouillage des polymères diélectriques ou semi-conducteurs sur la stabilité et la fiabilité des OFET « top gate » a été étudié en détail. Le rôle de l'injection de charges variable en raison de différentes molécules de thiol chimisorbées sur le transistor entraînant la modification des niveaux énergétiques des électrodes de « source » et « drain » a été étudié. Sur un plan fondamental le transport de charge intrinsèque à travers le semi-conducteur chauffé après déposition a été étudié. L'effet du mélange entre une petite molécule photochrome dans ses deux états bistables avec un semi-conducteur polymère sur le transport de charge a été étudié au moyen de caractérisation électrique thermo-dépendante. Nous avons étudié en détail comment les propriétés structurelles affectent la fonction du transport de charge pour des molécules telles que l'azobenzène fluoré et les biphenyle thiolates chimisorbés sur des électrodes en or.

Ces résultats fournissent des indices essentiels pour la conception de transistors avec un bon contrôle de l'injection de charge à partir d'électrodes. Ils mettent également en évidence le fait que ces approches de fabrication entraînent une baisse de coût et que le post-traitement des dispositifs peut être amélioré de manière significative sans l'utilisation de techniques onéreuses.

Références

- 1 Don Park, Y., Lim, J. A., Lee, H. S. & Cho, K. Interface engineering in organic transistors. *Mater. Today* 10, 46-54, (2007).
- 2 Poirier, G. & Pylant, E. The self-assembly mechanism of alkanethiols on Au (111). *Science* 272, 1145-1148 (1996).
- 3 Dodabalapur, A., Torsi, L. & Katz, H. E. Organic Transistors: Two-Dimensional Transport and Improved Electrical Characteristics. *Science* 268, 270-271, (1995).
- 4 Veres, J., Ogier, S., Lloyd, G. & De Leeuw, D. Gate insulators in organic field-effect transistors. *Chem. Mater.* 16, 4543-4555 (2004).
- 5 Heimel, G., Romaner, L., Zojer, E. & Bredas, J. L. The interface energetics of self-assembled monolayers on metals. *Acc. Chem. Res.* 41, 721-729 (2008).
- 6 Facchetti, A., Yoon, M. H. & Marks, T. J. Gate dielectrics for organic field-effect transistors: new opportunities for organic electronics. *Adv. Mater.* 17, 1705-1725 (2005).
- 7 Stoliar, P. et al. Charge injection across self-assembly monolayers in organic field-effect transistors: Odd-even effects. *J. Am. Chem. Soc.* 129, 6477-6484 (2007).
- 8 Boudinet, D. et al. Modification of gold source and drain electrodes by self-assembled monolayer in staggered n-and p-channel organic thin film transistors. *Org. Electron.* 11, 227-237 (2010).
- 9 Ribierre, J. C. et al. Direct Laser Writing of Complementary Logic Gates and Lateral p-n Diodes in a Solution-Processible Monolithic Organic Semiconductor. *Adv. Mater.* 22, 1722-1726, (2010).
- 10 Ribierre, J.-C. et al. Reversible Conversion of the Majority Carrier Type in Solution-Processed Ambipolar Quinoidal Oligothiophene Thin Films. *Adv. Mater.* 22, 4044-4048, (2010).
- 11 Meijer, E. et al. Solution-processed ambipolar organic field-effect transistors and inverters. *Nat. Mater.* 2, 678-682 (2003).

Résumé en anglais (Abstract in English)

Keywords: π -conjugated molecules, organic transistors, self-assembled monolayers, charge transport

This thesis deals with the study of charge transport through organic semiconductors incorporated in Organic Field-Effect Transistors (OFETs). Great attention is given to the interfaces in the OFETs and the properties of which were tuned to modulate transistor response. The stability of the device under switching states and the mechanism governing charge injection were studied systematically. In a fundamental level the charge transport through self-assembled monolayers comprising of variety of π -conjugated molecules were investigated.

In this thesis the charge transport process and different parameters affecting this phenomenon are investigated in detail by fabrication and characterization of three terminal devices based on OFET architectures and two terminal devices consisting junctions incorporating mono-molecular layer on surface of metal electrode.

Among the different aspects governing the charge injection in macroscopic organic thin film transistors particular emphasis was given to the interface³ engineering¹ by tuning the (i) Dielectric/semiconductor interface, and (ii) Metal electrode/semiconductor. To explore aspects governing charge transport within the channel of the device we investigated the property of (iii) semiconductor intrinsic mobility and (iv) usage of blends in the active layer of the transistor.

On the nanoscale the charge transport through a mono molecular layer chemisorbed onto metal electrodes was investigated. The self-assembly of thiol molecules on gold electrodes⁴ was exploited to form monolayer.² To perform electrical characterization on self-assembled monolayer (SAM) a custom in-house setup comprising of eutectic alloy of liquid metallic gallium indium (GaIn^E) probe electrode was built. Prior to the using GaIn^E as the top electrode Hg-drop was employed as the probe electrode for performing electrical characterization on SAMs. The reasoning for preference of the GaIn^E is detailed in the methods section.

We undertook the following routes to modulate the properties affecting the charge transport in the OFETs:

1) **Semiconductor/dielectric interface:** In this work we investigated the influence which the change in the molecular weight of polymeric dielectrics might have in top-gate bottom-contact transistors. The charge transport in organic transistors occurs at the semiconductor/dielectric interface.³

³ The term interface refers to the boundary between organic semiconductor with insulator layer or with charge injection electrodes or inter-molecular borders.

⁴ Thiol based small molecules due to its chemical affinity get adsorbed onto the surface of gold by self-assembly process and the structure which is formed is termed as self-assembled monolayer (SAM).

To tune the surface properties of the dielectric in contact with the semiconductor⁴ we used two dielectrics with different dielectric constants. The switching stability and hysteresis effects were examined.

2) **Metal/Semiconductor interface:** To gain insight into the charge injection properties of biphenyl thiol SAMs chemisorbed on source-drain electrodes of the transistor we fabricated and characterized a family of biphenyl thiol derivatives with a varying degree of torsion in its molecular backbone. Parameters such as work function modification,⁵ wettability of the electrodes and their corresponding effect in charge mobility and threshold voltage of bottom-gate bottom-contact transistors based on poly(3 hexylthiophene) were studied. We studied the charge transport through fluorinated azobenzene thiols with mono and biphenyl substitutions self-assembled on gold electrodes. These molecules were synthesized by the group of Prof. Marcel Mayor. Charge transport through the two forms *trans* and *cis* isomers were studied. For fluorinated azobenzene substituted biphenyl, the surface wettability and changes in the work function of the electrode modified with the SAM were evaluated by different techniques.

3) **Semiconductor bulk intrinsic transport:** For investigating the intrinsic carrier mobility for OFETs based on quinoidal thiophene which has an amorphous nature in the bulk of the film we performed electrical characterization in a cryostat. Valuable insight into the possible trapping mechanism and the respective activation energy for both p and n-type systems was acquired. A separate study was also carried out to record the activation energy of a transistor with a bicomponent mixture as the charge transport layer in the device.

4) **Blends in the active layer:** To modulate the charge carrier hole mobility of transistors we followed the approach to blend a small molecule with conjugated polymer. The effects of phase separation and molecular orientation upon blending and its influence on the charge transport are detailed in this study.

Semiconductor/dielectric interface

Researchers have been trying to replace silicon dioxide with polymeric dielectrics over in OFETs at the turn of the century.⁶ The major advantages of using polymeric dielectrics are their solution processability, flexibility and ease of deposition onto substrates. Hitherto for our project we employed two dielectrics with different dielectric constants spanning from a lower to high molecular weights in combination with a conjugated fluorinated polymer which had been shown to exhibit ambipolar charge transport characteristics. All the polymeric dielectrics and semiconductor used were acquired from commercial sources. This was an intra-team project and a better part of this undertaking was particularly challenging, especially to attain the necessary parameters to successfully fabricate and characterize the devices without impediments resulting in failed devices was quite a thought provoking and exploratory task. The role of dielectric surface energy and surface polarity modification upon changing the molecular weight and its influence on the device performance were investigated.

The issue of switching stability from off to on state and vice versa was examined for all dielectric/semiconductor configurations, since this gives crucial information regarding the reliability of the device on prolonged operation.

Metal/Semiconductor interface

In the case of the charge injection modulation with electrodes of the thin-film transistors by means of biphenyl family of SAMs we collaborated with the group of prof. Marcel Mayor from University of Basel (Switzerland) who provided us with these molecules. To gain insight into the structural order, molecular packing density and tilt angle of the molecules on the surface of the gold electrode we collaborated with the group of prof. Michael Zharnikov from Universität Heidelberg (Germany) who conducted the near-edge X-ray absorption spectroscopy (NEXAFS) and X-ray photoelectron spectroscopy (XPS) measurements. A series of OFET measurements were undertaken to shed light upon the charge injection and the transport across the SAMs, which was found to be depend on the structural order, effective thickness and tilt angle on the surface of the electrodes. The corresponding modulation of hole mobilities were achieved upon integration of the thiolated biphenyl SAMs in OFET electrodes due to the work function modification of the source-drain electrodes.^{7,8}

We also performed the electrical characterization for SAMs of fluorinated azobenzene thiols with mono and substitutions biphenyl on gold electrodes. Electrical characterization of SAM was performed with a specially developed setup. We have refined and improved gradually during the course of time during my doctoral work to improve the reliability and integrity measures. We tested our setup with the systems already studied to test the sensitivity of our measurements with the results published in the literature.

To further understand how the transmission through a single azobenzene molecule linked to gold electrodes changes we performed a theoretical study with our collaborators at the University of Mons (Belgium) network project SUPERIOR in particular Silvio Osella and Dr. Jérôme Cornil.

Semiconductor bulk intrinsic transport

To study the intrinsic charge carrier mobility of transistors based on quinoidal oligothiophene as the active layer in the OFETs we collaborated with the group of prof. Jean Charles Ribierre, Ewha Womans University (South Korea) who provided us with this compound. The characterization at temperatures ranging from 80 K – 300 K was performed by means of a cryostat configured specifically to perform electrical characterization on the OFETs. A customized sample holder along with the electrical connections for the same in the cryostat was built for characterization of OFETs. The quinoidal oligothiophene exhibits the property to behave like a hole and electron transporting material upon deposition and then post annealing respectively.^{9,10} The activating energies for the individual case of p and n-type operational mode were estimated.

To understand the temperature dependent charge transport mechanism through a polymeric semiconductor-photochromic small molecule blend as the active layer of the transistor, electrical characterization of this OFET was performed in a cryostat. The activation energies were estimated for both the ring opened and closed state of the photochromic diarylethene molecule blended with semiconductor respectively. The energetic mismatch between the ionization energy levels of P3HT and diarylethene open is much greater compared to diarylethene closed. Hence the activation energies required for thermally activated charge hopping is expected to be different in the two cases.

Blends in the active layer

The project with blends as the active layer of OFETs was a collaborative work with members at the ISOF–Consiglio Nazionale delle Ricerche (Italy) and BASF (Switzerland) from whom the compounds were acquired. Blending different materials is one of methods used to modify the ionization energetic levels of the thin-film bulk in a transistor and thereby the mobility of charge carriers.¹¹ The X-ray diffraction and the wide angle X-ray scattering characterization were carried out at the Max Planck institute for polymer research, Mainz from which the role of small molecule-polymer packing was gathered. We performed the complete electrical characterization of the blend OFETs which had different ratio of small molecule-polymer mix by volume as the active layer of the transistor. The morphological characterization on the semiconductor film was performed by means of atomic force microscope (AFM).

Summary

A comprehensive study was carried out on various factors governing the charge transport in π -conjugated organic molecules during this thesis work. We focused on tuning the properties of the interfaces in the thin-film transistor. The influence of surface energy, polarity, wettability of the polymeric dielectrics/semiconductor on the stability and reliability for top gate OFETs interface were studied in detail. The role of variable charge injection due to different thiol molecules chemisorbed on the transistor resulting in modification of the energetic levels source and drain electrodes were investigated. On a fundamental level the intrinsic charge transport through the semiconductor upon post annealing and as deposited was investigated. The effect of blending photochromic small molecule in its two bistable states with a polymeric semiconductor on the charge transport was studied by means of temperature dependent electrical characterization. We investigated in detail, how the structural properties affect the function of the charge transport for molecules such as fluorinated azobenzene and biphenyl thiolates chemisorbed onto gold electrodes.

These results provide vital clues for designing transistors with good control over charge injection from electrodes and more crucially also highlights the fact that following lost-cost fabrication approaches without expensive post-processing techniques the efficiency of the devices can be improved significantly.

References

- 1 Don Park, Y., Lim, J. A., Lee, H. S. & Cho, K. Interface engineering in organic transistors. *Mater. Today* **10**, 46-54, (2007).
- 2 Poirier, G. & Pylant, E. The self-assembly mechanism of alkanethiols on Au (111). *Science* **272**, 1145-1148 (1996).
- 3 Dodabalapur, A., Torsi, L. & Katz, H. E. Organic Transistors: Two-Dimensional Transport and Improved Electrical Characteristics. *Science* **268**, 270-271, (1995).
- 4 Veres, J., Ogier, S., Lloyd, G. & De Leeuw, D. Gate insulators in organic field-effect transistors. *Chem. Mater.* **16**, 4543-4555 (2004).
- 5 Heimel, G., Romaner, L., Zojer, E. & Bredas, J. L. The interface energetics of self-assembled monolayers on metals. *Acc. Chem. Res.* **41**, 721-729 (2008).
- 6 Facchetti, A., Yoon, M. H. & Marks, T. J. Gate dielectrics for organic field-effect transistors: new opportunities for organic electronics. *Adv. Mater.* **17**, 1705-1725 (2005).
- 7 Stoliar, P. et al. Charge injection across self-assembly monolayers in organic field-effect transistors: Odd-even effects. *J. Am. Chem. Soc.* **129**, 6477-6484 (2007).
- 8 Boudinet, D. et al. Modification of gold source and drain electrodes by self-assembled monolayer in staggered n-and p-channel organic thin film transistors. *Org. Electron.* **11**, 227-237 (2010).
- 9 Ribierre, J. C. et al. Direct Laser Writing of Complementary Logic Gates and Lateral p-n Diodes in a Solution-Processible Monolithic Organic Semiconductor. *Adv. Mater.* **22**, 1722-1726, (2010).
- 10 Ribierre, J.-C. et al. Reversible Conversion of the Majority Carrier Type in Solution-Processed Ambipolar Quinoidal Oligothiophene Thin Films. *Adv. Mater.* **22**, 4044-4048, (2010).
- 11 Meijer, E. et al. Solution-processed ambipolar organic field-effect transistors and inverters. *Nat. Mater.* **2**, 678-682 (2003).

Contents

Résumé.....	VII
Abstract in English.....	XIII
1 Introduction	1
1.1 Organic electronics	1
1.1.1 Scope.....	2
1.2 Molecular electronics.....	3
1.2.1 Prospects	4
1.3 References.....	5
2 Charge Transport in organic semiconductors	7
2.1 Introduction.....	7
2.2 Energetic profile of organic semiconductors	9
2.3 CHARGE TRANSPORT: Mechanisms and models.....	12
2.3.1 Multiple trapping and release	13
2.3.2 Gaussian disorder model.....	15
2.3.3 Polaron hopping model.....	17
2.3.4 Bipolaron model	19
2.4 Organic Field-effect transistor	20
2.4.1 OFET-working principles	20
2.4.2 Transistor performance indicators	23
2.5 References and notes	27

3	Charge Transport in molecular junctions.....	29
3.1	Introduction.....	29
3.1.1	Molecular junctions - building blocks	29
3.1.2	Metal-molecule-metal junctions	30
3.1.3	Quantum tunneling	32
3.1.4	References and notes	35
4	Methods and procedures	37
4.1	OFET PREPARATION.....	37
4.1.1	F8BT based OTFTs	37
4.1.2	P3HT based OTFTs	39
4.1.3	QQT(CN) ₄ based OFETs	39
4.1.4	P3HT, diarylethene blend OFETs.....	39
4.1.5	P3HT, PTPP blend OFETs	40
4.2	OFET CHARACTERIZATION TECHNIQUES.....	40
4.2.1	Electrical characterization inside glovebox.....	40
4.2.2	Electrical characterization in cryostat.....	40
4.2.3	Work function of electrodes	43
4.2.4	Ionization energy of semiconductor film.....	43
4.2.5	Morphological characterization	44
4.2.6	Microstructural characterization of P3HT:PTPP blend films	44
4.2.7	Surface wettability tests.....	44
4.2.8	UV/Vis spectroscopy on films.....	44
4.3	SAM PREPARATION	45
4.4	SAM CHARACTERIZATION TECHNIQUES	46
4.4.1	Electrical characterization of SAMs.....	47
4.4.2	Structural characterization of SAMs	50
4.5	References.....	51

5	Organic field-effect transistors	53
5.1	Dielectric molecular weight influence in ambipolar F8BT OFETs.....	53
5.1.1	Scope.....	53
5.1.2	Dielectric surface properties	55
5.1.3	Morphological characterization	58
5.1.4	Electrode-Semiconductor interfacial energetics	60
5.1.5	Standard OFET electrical characterization	62
5.1.6	Effect of gate bias dependent hysteresis in TFTs	67
5.1.7	TFT switching capacity and instability under dynamic bias stress influence	72
5.1.8	Conclusions.....	79
5.1.9	References.....	80
5.2	Intrinsic charge transport in polymeric semiconductor/photochromic molecular blend OFETs	83
5.2.1	Motivation.....	83
5.2.2	Results and discussions.....	86
5.2.3	Conclusions.....	94
5.2.4	References and notes	95
5.3	Activation energy of OFETs based on Quinoidal Oligothiophene derivative.....	97
5.3.1	Scope.....	97
5.3.2	Results and discussions.....	98
5.3.3	Conclusions.....	107
5.3.4	References.....	108
5.4	Improved field-effect mobility in a polymeric semiconductor/small molecular blend transistors	109
5.4.1	Prospects	109
5.4.2	Results and discussions.....	110
5.4.3	Conclusions.....	116
5.4.4	References.....	117

6	Charge transport through SAMs.....	119
6.1	Charge Injection and Transport through Biphenylthiol SAMs	119
6.1.1	Introduction.....	119
6.1.2	SAM Packing Density and Orientation.....	122
6.1.3	Charge Transport through Biphenylthiol SAMs.....	127
6.1.4	Biphenylthiol SAMs in OTFT electrodes	133
6.1.5	Discussions	140
6.1.6	Conclusions.....	144
6.1.7	References.....	145
6.2	Comparative study of work function modification of Au electrodes by fluorinated azobenzene	149
6.2.1	Motivation.....	149
6.2.2	Results and discussions.....	150
6.2.3	Conclusions.....	157
6.2.4	References.....	160
6.3	Charge transport through self-assembled monolayers of fluorinated azobenzene on Au electrodes.....	161
6.3.1	Motivation.....	161
6.3.2	Results and discussions.....	162
6.3.3	References.....	173
6.4	Transmission studies through single molecule azobenzene derivatives linking gold electrodes.....	175
6.4.1	Motivation.....	175
6.4.2	Provisional results.....	175

7	Epilogue.....	181
	7.1 Conclusions and outlooks.....	181
	7.2 General long-term perspectives and directives.....	183
	Appendix.....	185
	List of publications.....	189
	Acknowledgements.....	191

No problem is too small or too trivial if we can really do something about it

– Richard Feynman (1918-1988), Physicist

1 Introduction

Electronics deals with the physics of movement of electrons in devices such as transistors, diodes to perform functions such as transport and amplification of current, rectification, signal filtering and processing etc. In modern times electronic components are ubiquitous in our daily lives encompassing from small and simple pocket calculators, display panels to complex supercomputers. In the infancy of the electronics industry inorganic systems, such as those based on single crystals of silicon, were incorporated as active materials in the devices for transporting the charge carriers. Traditionally doped silicon was used as the semiconducting material. In the late 1970's after the discovery of increase in electrical conductivity of carbon based polyacetylene upon electrochemical doping,¹ the possibility of using organic materials as active layers was proposed. This eventually led to the incorporation of π -conjugated carbon based compounds in electronic components, thus paving the way for a new branch called '*organic electronics*'.

1.1 ORGANIC ELECTRONICS

In organic semiconductors the interaction between the molecules are of loosely bound nature, typically of van der Waals forces which is different from their inorganic counterpart which has strong covalent bond in their crystal lattice. Due to the variations in intramolecular bond strength of organic compounds, the net charge is not uniformly localized (i.e., not delocalized) in the molecule and mobility is lower compared to crystalline silicon. The charge transport rates in the organic materials are greatly influenced by their structural ordering in the bulk of the thin film in the device. The organic materials can be divided into two main categories (i) small molecules/ monomeric units, and (ii) polymers. besides the molecular weight and polydispersity the major difference between the small molecules and polymers is the methods employed for deposition. In the case of small molecules the deposition is predominantly performed via thermal evaporation, while in polymers techniques such as drop casting, spin coating or ink-jet printing have been employed owing to its solution processability.

1.1.1 Scope

π -conjugated carbon based materials comprise of a broad class of materials and primarily provide some unique advantages² such as:

Processability: Most of the polymeric semiconductors are soluble in solvents, thereby facilitating the process of deposition over large-area substrates by means of simple techniques like spin coating, printing etc. The deposition can be carried out at low, i.e., room temperatures; this also reduces the fabrication cost.

Flexibility: The organic compounds can be deposited on flexible light weight plastic substrates, greatly reducing the bulkiness of the device.

Cost effective fabrication: Since the deposition can be done in standard condition (ambient pressure and temperature) without the need of working in ultra-high vacuum the fabrication cost is much less.

Versatile: With the aid of synthesis, the electronic properties of these organic compounds can be modified by adding suitable substitutions in the molecular structure.

Though there are many *pros* for carbon based organic materials to be integrated into electronic components, still the switching speed are lower than that of state of the art inorganic electronics technology. One of the challenges is to optimize conditions for deposition of the semiconductor film to minimize disorders like grain boundaries and pin holes that are known to hamper the rate of charge transport in the thin film. Some of the potential applications are organic thin film transistors (OTFTs),³ organic photovoltaics (OPVs), bio-sensors and organic light-emitting diodes (OLEDs).^{4,5} Recent research is focused on improving the mobility, stability, efficiency, lowering power consumption and reliability of operation over extended period of time in organic electronic devices, with the eventual goal to nearly match the performance of their inorganic counterpart. Each of the aforementioned issues were addressed during my thesis and it is organized as the following:

Chapter 2 and 3 introduces the reader to fundamental concepts of charge transport in organic field-effect transistors and in metal-molecule-metal based junctions, respectively.

Chapter 4 contains the complete set experimental methods and procedures followed for each of the projects.

Chapter 5 deals with the charge transport problem in OTFTs focusing in particular on issues such as influence of varying molecular weight of polymeric gate dielectrics, optical tuning of intrinsic semiconductor properties by blending with photochromic small molecules and temperature dependence of a quinoidal oligomeric compound.

Chapter 6 describes the charge transport and injection properties of biphenyl self-assembled monolayers (SAMs) with varying torsion angles, the rates of transport was studied in photochromic fluorinated azobenzene compounds SAMs. Furthermore the work function shift induced by the two isomeric forms of a fluorinated azobenzene was studied. Theoretical simulations were performed to understand the transmission through single molecular junction comprising of azobenzene linking gold electrodes.

Chapter 7 provides short and long term perspectives from this research.

1.2 MOLECULAR ELECTRONICS

'*Molecular electronics*' as a branch of science began to flourish after the proposition of Aviram and Ratner about the rectification by an organic molecule in donor-bridge-acceptor systems.⁶ Since then the research in molecular electronics increased considerably, motivated by the fact of possible miniaturization of electronic components. The fundamental distinction between organic electronics to molecular electronics is the scale in which the charge transport occurs. To this end one may consider molecular electronics as the offspring of organic electronics, just the charge transport happens in much smaller dimensions (typically spanning from nanometers to few angstroms) and by different physical principles. The molecular junctions are comprised of two junctions sandwiched between metallic electrodes. The functionality could be varied depending upon the structure of the molecular layer composed in the metal-molecule-metal junction. The number of molecules contacted depends on the technique employed for characterization.

1.2.1 Prospects

The feature size of state of the art silicon based technology is 50 nm,⁷ if the trend to further down scaling is sustained this would require the imminent fabrication of devices in molecular dimensions. This opens up avenues for molecules to be incorporated in electronic devices.⁸ The dimensionality of charge transport for molecular electronics is typically <10 nm, whereas for organic electronics it can be from few nanometers to micrometers. Due to advancements in chemical synthesis a wide range of functional molecules have been synthesized and the molecular structures have been modified by precise placement of atoms/ substitutions. By means of self-assembly of the molecules covalently tethering interaction with metallic/ glass substrates, well-defined monolayer films can be formed with a good degree of hierarchical order.⁹ The self-assembly primarily adopted are by means of two routes namely, (i) thiols on films of Au or Ag and (ii) Organosilanes or siloxanes on glass surface. Hitherto certain basic functions such as photo-sensing,^{10,11} current switching¹² and rectification^{13,14} have been demonstrated. The functionality achieved from a self-assembled molecular structure in the junction directly depends on the properties of the molecules adsorbed on the metal electrode. Current research is focused on the fundamental interplay between the structure and function, aiming at the integration of different individual functional components for achieving more complex functionalities. The synergy between physics and chemistry opens up countless possibilities for modulating and tuning the function of electronic transport on the nanoscale.

1.3 REFERENCES

- 1 Shirakawa, H., Louis, E. J., MacDiarmid, A. G., Chiang, C. K. & Heeger, A. J. Synthesis of electrically conducting organic polymers: halogen derivatives of polyacetylene, (CH)_x. *J. Chem. Soc., Chem. Commun.*, 578-580 (1977).
- 2 Gundlach, D. J. Organic electronics: Low power, high impact. *Nat. Mater.* **6**, 173-174 (2007).
- 3 Dimitrakopoulos, C. D. & Malenfant, P. R. L. Organic thin film transistors for large area electronics. *Adv. Mater.* **14**, 99 (2002).
- 4 Kelley, T. W. *et al.* Recent progress in organic electronics: Materials, devices, and processes. *Chem. Mater.* **16**, 4413-4422 (2004).
- 5 Facchetti, A. π -conjugated polymers for organic electronics and photovoltaic cell applications. *Chem. Mater.* **23**, 0897-4756 (2011).
- 6 Aviram, A. & Ratner, M. A. Molecular rectifiers. *Chem. Phys. Lett.* **29**, 277-283 (1974).
- 7 Thompson, S. *et al.* 61-64 (IEEE).
- 8 Aviram, A. Molecules for memory, logic, and amplification. *J. Am. Chem. Soc.* **110**, 5687-5692 (1988).
- 9 Fendler, J. H. Chemical self-assembly for electronic applications. *Chem. Mater.* **13**, 3196-3210 (2001).
- 10 Mativetsky, J. M. *et al.* Azobenzenes as Light-Controlled Molecular Electronic Switches in Nanoscale Metal–Molecule–Metal Junctions. *J. Am. Chem. Soc.* **130**, 9192-9193 (2008).
- 11 Lilly, G. D. *et al.* Switchable photoconductivity of quantum dot films using cross-linking ligands with light-sensitive structures. *J. Mater. Chem.* **21**, 11492-11497 (2011).
- 12 Lau, C. N., Stewart, D. R., Williams, R. S. & Bockrath, M. Direct observation of nanoscale switching centers in metal/molecule/metal structures. *Nano Lett.* **4**, 569-572 (2004).
- 13 McCreery, R. *et al.* Molecular rectification and conductance switching in carbon-based molecular junctions by structural rearrangement accompanying electron injection. *J. Am. Chem. Soc.* **125**, 10748-10758 (2003).
- 14 Nijhuis, C. A., Reus, W. F., Siegel, A. C. & Whitesides, G. M. A Molecular Half-Wave Rectifier. *J. Am. Chem. Soc.* **133**, 15397-15411 (2011).

Research is to see what everybody else has seen, and to think what nobody else has thought.

Albert Szent-Györgi (1893-1986), Biochemist

2 Charge Transport in Organic Semiconductors

2.1 INTRODUCTION

Carbon is one of the chief constituent in organic semiconductors. In its elemental form carbon has 6 electrons, of which in ground state 2 electrons are in the inner most s shell ($1s^2$), 2 in the second s shell ($2s^2$) and 2 more in the p shell (one each for $2p_x$ and $2p_y$). Among them 4 electrons occupying the valence shell can participate in forming a bond, while the remaining 2 in the inner core shell do not take part in the chemical bonding process. When a methane molecule is formed one electron from the $2s$ shell gets hybridized with the electrons in the p shell resulting in sp^3 hybridized state, due to this covalent bonds of equal energy are formed with the $1s$ electron of 4 hydrogen atoms. Carbon can also be sp^2 hybridized this occurs in alkenes. In an ethene molecule the two carbons share one electron from their $2s$ shell resulting in a σ bond, p_x and p_y electrons form a bond with the $1s$ of hydrogen thus leaving a free p_z electron which is perpendicular to the plane of the C and H atoms to form a π bond (Figure 2.1.1). Thus there is a double bond between the carbons of which one is a strong σ bond and another weaker π bond. The electron conduction can occur due to the change in weak π orbital overlap.

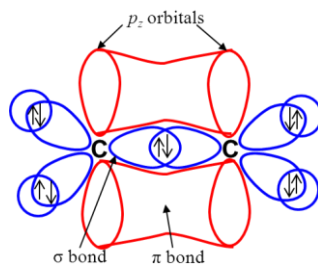


Figure 2.1.1 Illustration of the carbon-carbon double bonding in ethene indicating the σ and π bonds, arrows denote the spin state of the electrons

Building up from simple small molecules, due to the versatile hybridization of carbon more complex molecular structures and networks can be realized to deliver varied functions.

Polymers or small molecules are said to have π -conjugation if they possess alternative single and double bonds. The π -conjugated structures can have the form of aliphatic chain structure (i.e., without any aromatic benzene rings), aromatic structures or a combination of both. Depicted in Figure 2.1.2 a and b are the chemical structures of linear backbone polyacetylene and poly aromatic pentacene respectively, the p_z orbital overlap is also shown.

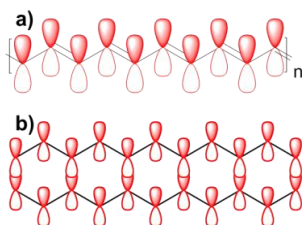


Figure 2.1.2 Chemical structure of (a) polyacetylene and (b) pentacene, the π -orbital perpendicular to the plane of the carbon is shown.

Due to the π -orbital overlap in conjugated systems, the electron energy states are delocalized within the molecule. In the case of 1,3,5-hexatriene the arrangement of the π molecular orbitals are according to Figure 2.1.3(a). In the bonding situation lobes of same sign interact whereas in the anti-bonding case the lobes of opposite sign interact thus forming a node in the wavefunction Figure 2.1.3(b).

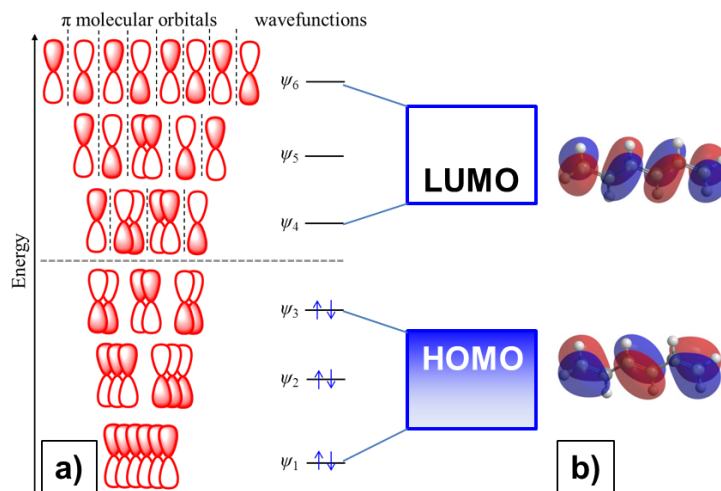


Figure 2.1.3 Energy diagram of hexatriene molecule showing (a) the bonding and the anti-bonding states along with the respective wave functions (b) Illustration of HOMO and LUMO in gas phase

2.2 ENERGETIC PROFILE OF ORGANIC SEMICONDUCTORS

In inorganic semiconductors the electrons present in the outer most shell are considered to be in the bound to the atoms in the valence band. When an electron is freed from its valence band into the conduction band which has higher energy, these unbound electrons can freely participate in charge conduction. In the case of organic semiconductors the highest occupied molecular orbital (HOMO) and the lowest unoccupied molecular orbital (LUMO) are analogous to the valence and conduction bands in inorganic counterpart respectively. The HOMO level represents the energetic molecular orbital where the electron charge cloud is occupied (i.e., filled), while the LUMO level denotes the energy orbital where the charge unoccupied. In other words the HOMO level is electron rich while in contrast the LUMO level is completely electron deficient. Similar to inorganic semiconductors, the energy of the HOMO level is lower and more stable since the electrons are bound in this molecular orbital. However if the bound electrons are excited to a higher energetic state, it will reside unbounded in the unoccupied molecular orbital and these electrons are free to participate in charge conduction.

In a π -conjugated oligomer the alternation of the single and double bond signifies delocalization of the charge along the molecule. Note that due to the sp^2 hybridization of carbon (Figure 2.1.1), one bond which is due to the sharing of the electrons in the s shell results in a strong sigma (σ) bond and the other due to the weaker pi (π) orbital overlap. Coincidentally the π orbital is higher in energy than the sigma bonded electrons, hence can be excited to its anti-bonding π^* state with lesser energy. On the other hand for the electrons in the σ orbital to be excited into σ^* state which is higher in energy than the π^* state will necessitate greater energy.

In crystalline inorganic semiconductors the interaction between the atoms are strong due to covalent bonds between atoms in the periodic crystal lattice. When many atoms are bonded together due the overlap of the orbitals the energy bands widens resulting in the broadening of the valence and the conduction bands. In π -conjugated organic semiconductors however, due to weaker van der Waals interaction between adjacent molecules the π orbital overlap is not well defined. Since the overlap of π molecular orbitals and the electron wavefunctions are anisotropic this results in broadening of occupied and unoccupied molecular orbitals into continuous bands similar to the valence and conduction bands from the energy band theory of inorganic materials.

Metallic behavior might be hypothetically expected while the delocalized orbitals are half-filled due to finite density of states (DOS) at the Fermi level, but in reality due to Peierls instability within the molecule a band gap arises between the filled bonding (π bands) and empty anti-bonding states (π^* bands), which results in lowering the energy of the filled states.¹ According to Peierls theorem in a one dimensional molecular system where the bands are not fully filled, this causes the band to distort and open up an energetic band gap near the Fermi level. The emergence of a band gap in π -conjugated polymers thus favors a semiconducting than a conductive metallic state. The more electron rich the molecule the greater the overlap and the corresponding energy bands are broader. The energy band gap between the HOMO and LUMO levels of conjugated polymers varies from ca. 0.8 to 4 eV, thus encompassing wavelengths ranging from the infrared (IR) to the ultraviolet (UV) in the electromagnetic (EM) spectrum.² The band gap in semiconducting polymers also depends on the extent of delocalization of π -electrons. The wide range of band gap in conjugated polymers offers a possibility to tune charge transport properties in organic electronic devices.

Due to the existence of the band gap between the HOMO and LUMO level of an organic semiconductor the energy band diagram profile fairly resembles that of an amorphous inorganic semiconductor. The crucial difference however among the two arises due the difference in the strength of the intramolecular bonds resulting in the appearance of localized states in the band gap near the valence and conduction band edges. Localized states tend to occur at the bottom of the conduction band or top of the valence band in disordered organic semiconductors. An illustration of the partial density of states for a hypothetical organic semiconductor is shown in Figure 2.2.1. The DOS denoted by $N(E)$ (or $D(E)$) gives the number of states in unit volume which is available for an electron (or hole) with given spin direction with energies ranging between E and dE and this states can either be occupied or unoccupied. The width of the density of states reflects the extent of energetic disorder in the semiconductor bulk and any extrinsic impurities. Theoretical calculations have shown that the density of localized states decrease exponentially towards the center of the band gap. The slope of the tail states close the band edges depends of the molecular order. In the case of the well-ordered semiconductor the slope of the tail state is steep indicating a narrow band tail, while in contrast for more disordered materials the slope is lesser which correspondingly indicates a broader band tail. The carrier mobility in

lower in the case when majority of the charges move between localized states. When the carriers move between states near the valence (E_V) or conduction (E_C) band edges the hole and electron mobility increases respectively. Dopants and impurities in the organic semiconductor conductor can give rise to trap states which are referred to as deep trap states, the carriers trapped in this state therefore require much greater energy to move to more mobile states. However, in the case of inorganic semiconductors, the deep states arise from dangling bonds between atoms.

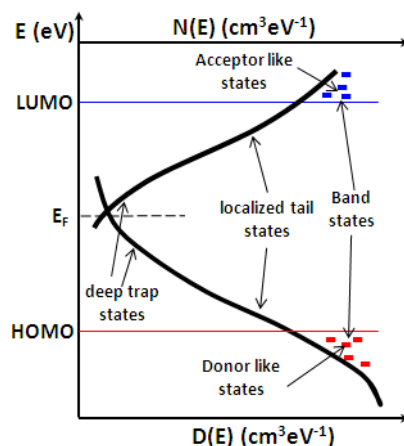


Figure 2.2.1. Scheme of the partial density of states as a function of energy indicated for both valence and conduction bands of an organic semiconductor.

Owing to the poor periodicity and amorphous nature of organic semiconductors the band states where the charge is delocalized is narrow thus the mobility edge is not explicit. From the DOS plots the energy at which the partial density of states tail has the most and least energy an estimate of mobility edge could be obtained for electrons and holes in a semiquantitative manner. Majority of organic semiconductors exhibit particularly p-type (hole carrier transport) nature, this is due to the asymmetry which exists for the band tails of the electrons and holes, with a much broader localized states close to the valence band edge. The existence of such asymmetry in the width of localized band tail states favors the conduction of one particular carrier over the other (electron or hole); this is the reason why most of the organic semiconductors show more predominant conduction of one carrier type. Organic semiconductors can also exhibit the property of ambipolar charge carrier conduction, in this case the width of the band tail states are matched more evenly in energy. This provides an added flexibility to tune the type of carrier

conduction by designing organic semiconductors with suitable molecular structure and chemical substituents necessary to engineer the band gap, warranted for a specific type of application.

2.3 CHARGE TRANSPORT: MECHANISMS AND MODELS

In addition to charge delocalization another aspect which plays a major role in governing the charge transport in π -conjugated polymers are inter-chain interactions. For small molecules such as pentacene (Figure 2.1.2) which forms more crystalline films due to the π - π stacking between molecules, the charge transport have been demonstrated to follow band-like properties in low temperatures similar to inorganic semiconductors.³ Charge transport depends heavily on the packing order of the chains in the film, structural defects and grain boundaries.⁴ Regioregularity affects the π - π stacking in alky-thiophene polymers. Highly regioregular (RR) alkyl-thiophene structures have been demonstrated to possess greater carrier mobility due to the better planar arrangement of the neighboring thiophene units. It has been shown that there is huge anisotropy in the field-effect mobility of a RR polymer, which is greatly influenced by the orientational order of π - π stacking between adjacent molecules on the substrate in particular the in plane arrangement had much greater carrier mobility over across the plane case. The enhanced mobility for the in plane oriented molecular arrangement was attributed to more efficient inter-chain transport due to the two-dimensional delocalization of carriers⁵ in the self-ordered stacking lamellae.

The mobile charge carriers in organic semiconductors can be broadly classified into hole and electrons. Depending on the type of charge carrier which the semiconductor can transport they are categorized into three types, (i) p-type, (ii) n-type and (iii) bipolar (or ambipolar). In p-type and n-type materials, holes and electrons are the majority carriers respectively, while in ambipolar semiconductors both hole and electrons participate in charge transport. Shown in Figure 2.3.1 are the molecular structures of some of the common p, n and ambipolar organic semiconductors incorporated as functional components to serve as active layer in devices. The charge transfer can happen via,

- (i) intra-chain hopping or tunneling along the conjugated molecular backbone,
- (ii) inter-chain hopping between adjacent molecules and

(iii) Tunneling between localized energetic states.

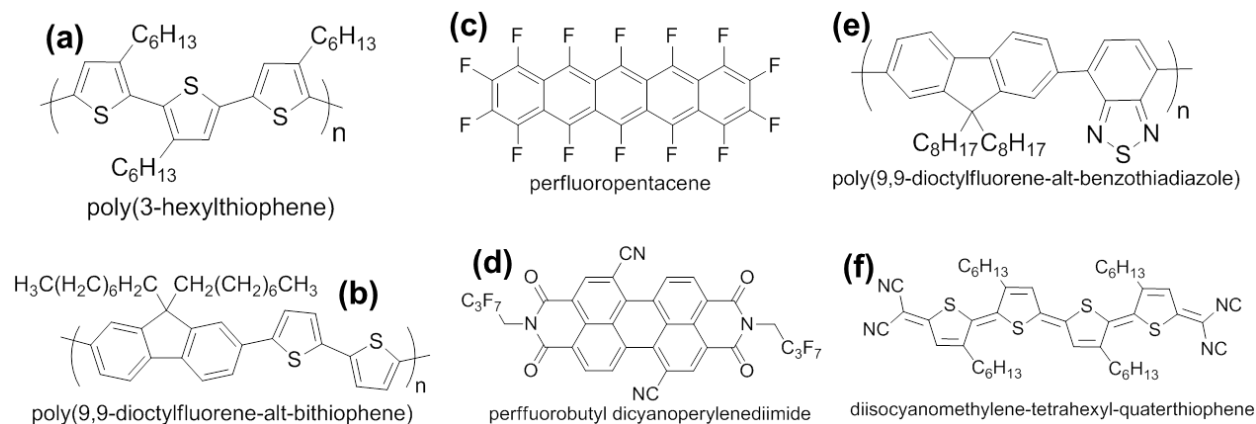


Figure 2.3.1. Chemical structures of predominantly (a) and (b) hole transporting (p-type), (c) and (d) electron transporting (n-type), (e) and (f) ambipolar (p/n type) organic semiconductors.

The side group substitutions along the main π -conjugated molecular backbone which are generally introduced to improve solution processability influences the chain alignment, inter-chain interaction, the extent of charge delocalization and also can cause additional change in the molecular geometry such as torsional angle between the rings all of these factors affect the electronic properties.

Hitherto several models have been proposed to describe the charge transport phenomenon in organic semiconductors such as multiple trapping and release, variable range hopping, Gaussian disorder and mobility edge which will be described in the following sections.

2.3.1 Multiple trapping and release

In organic semiconductors due to the greater disorder in the film localized states occur near the conduction and valence band edges, the carriers which occupy these localized states are trapped and immobile. The trapped charges can be released by thermal activation energy near the localized tail states successively until it reaches the mobility edge. The thermally activated release of trapped charges was explained as the possible model for transport in amorphous inorganic semiconductors⁶ termed as multiple trapping and release (MTR). This was later extended and applied for the treatment of charge transport in organic semiconductors by Horowitz et al.^{7,8} Shown in figure 6 is the mechanism of the multiple trapping and release model.

The duration in which the charge resides trapped energetic levels is called as the relaxation time, which is greater for the deep traps than the shallow traps in the tail states.

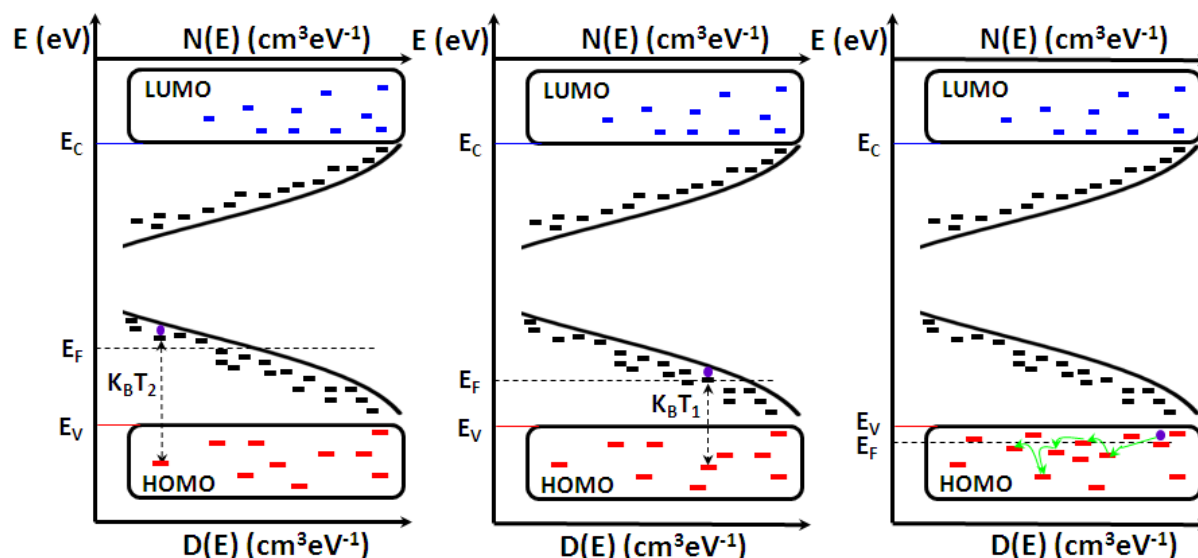


Figure 2.3.2. Illustration of the multiple trapping and release mechanism, the charge carrier is trapped at deep tail states (left panel) when there is large energetic offset between the Fermi level and the hole transport state, carrier is localized near the tail states (middle panel) and carrier hops in the extended transport states (right panel) after the Fermi level crosses the valence band edge.

In amorphous organic semiconductors the localized density of states is quite broad with respect to the total carrier density due to greater disorder, while in crystalline semiconductors it is narrower. The transport and mobility of the charge carrier according to the MTR model is described according to the hindered/trapped carrier by the successive capture in the localized states until the Fermi level moves closer to the mobility edge of the semiconductor material, at which point the concentration of mobile carriers increase significantly which leads to corresponding increase in carrier mobility.

The temperature dependence of carrier mobility follows Arrhenius relation which is described by the following relationship,^{9,10}

$$\mu = \mu_0 \alpha \exp\left(\frac{-\Delta E}{K_B T}\right) \quad (2.1)$$

Where μ_0 is the prefactor mobility which occurs when there is no energetic disorder (i.e., when $T \rightarrow \infty$), ΔE is the activation energy, α is the ratio of density of states at the energy band to trap densities and K_B is the Boltzmann constant.

2.3.2 Gaussian disorder model

In disordered organic semiconductors the charge transport was described due to hopping in localized electronic sites distributed according to a Gaussian shaped profile. The idea behind this model was put forth by Bässler et al based on Monte Carlo simulations from which they proposed a Gaussian DOS.¹¹ The DOS in inorganic semiconductors can be determined by means from the optical spectra of the transition from the valence band to conduction band, while a similar treatment cannot be directly applied to organic semiconductors due to the existence of excitonic transitions. The energetic disorder arises due to the fluctuations in the lattice polarization energies and the random spread of the π and σ bond units along the polymeric chains.¹² Accordingly the transport along the intra molecular segments and/or inter molecular ensemble of organic molecules had been described by hopping between sites for both hole and electron transporting levels residing in energies with a Gaussian distribution.

The charge transport between adjacent sites follows Miller-Abrahams (M-A) jump-rates,¹³ which describes a single phonon supplies adequate energy to complete hopping over an energetic barrier (Figure 2.3.3). The charge transfer from site $i \rightarrow j$ separated by a distance Δr_{ij} follows the relation in equation 2.2,

$$v_{ij} = v_0 \exp(-2\alpha\Delta r_{ij}) \begin{cases} \exp\left(\frac{-\Delta\varepsilon_{ij}}{K_B T}\right); & \varepsilon_j > \varepsilon_i \\ 1; & \varepsilon_i > \varepsilon_j \end{cases} \quad (2.2)$$

Where v_0 is the wavefunction overlap parameter of the molecular orbitals and α^{-1} is the charge localization distance. ε_i and ε_j represent the energy of sites i and j respectively.

According to expression 2.2, the hopping to higher energetic state is favored when there is the presence of a temperature dependent energy barrier. This process occurs by phonon absorption, which is released once the higher energy hop is completed. If the final state is of the same energy

the charge transfer happens by tunneling without phonon absorption. The distance Δr_{ij} is the wavefunction overlap between the sites i and j .

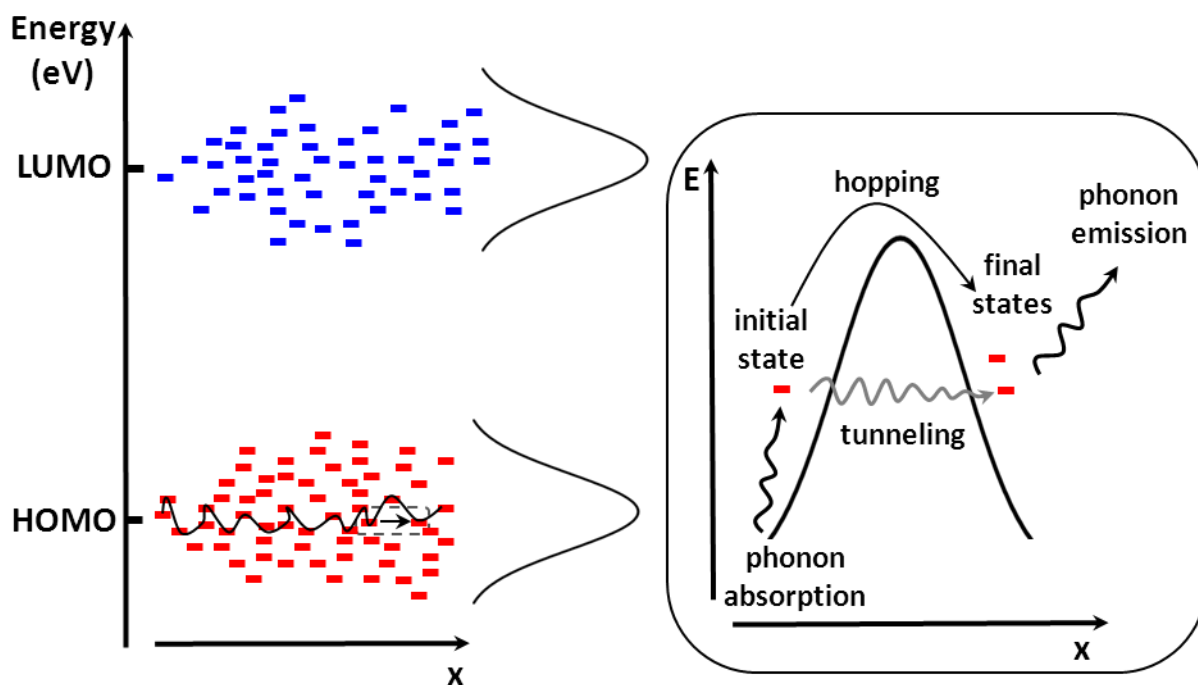


Figure 2.3.3 Illustration of hopping between sites in a Gaussian distributed DOS hole transport sites. The hole and electron transport sites are denoted by red and blue lines respectively. The right panel represents the zoom of the dotted region of the plot in the left side, which describes the hopping event to a site with higher energy upon phonon absorption.

The activation energy and carrier mobility according to the Gaussian disorder model (GDM) follows a non-Arrhenius temperature dependence and is described according to the following relation,¹⁰

$$\mu(T) = \mu_0 \exp\left(-\frac{2}{3} \frac{\sigma}{k_B T}\right)^2 \quad (2.3)$$

Where σ is the standard deviation of the Gaussian DOS and μ_0 represents the hypothetical mobility at zero field and infinite temperature (T).

2.3.3 Polaron hopping model

When the charge travels in a one dimensional molecular crystal deformation along its lattice structure gives rise to what is known as polarons. The polaron hopping mechanism was put forth by Holstein^{14,15} and they occur by electron-phonon coupling due to the interaction of the electrons in the crystal lattice. The framework of transition rate for polarons is described according to the Marcus theory,¹⁶ in which its hopping rate either to higher or lower energetic sites of equal distance is similar if the intramolecular reorganization energy is uniform. Conwell et al reported polaron hopping normal to the polyacetylene chains, while at extremely low temperatures a transition from hopping to band transport was attributed.^{17,18} A comparative study between small Holstein (SHP) and Fröhlich (SFP) polarons in an adiabatic regime was described by Alexandrov.¹⁹ According to the Alexandrov model the interaction between a two-site single electron system with vibrating ions (phonon modes) in an infinite lattice can be described by the sum of the Hamiltonian due to the electron, phonon and electron-phonon and is mathematically expressed as,¹⁹

$$H = H_{ph} + H_{e-ph} + H_e \quad (2.4)$$

Where H_{ph} , H_{e-ph} and H_e are the energy due to phonons (vibrating ions), electron-phonon interaction and electrons respectively and each of these Hamiltonians are expressed by,

$$H_{ph} = \sum_m \left(-\frac{\partial^2}{2M\partial u_m^2} + \frac{M\omega^2 u_m^2}{2} \right) \quad (2.5)$$

The interaction between the electrons and ions is given by,

$$H_{e-ph} = \sum_{i=1,2} \sum_m c_i^\dagger c_i f_m(i) u_m \quad (2.6)$$

and the electron hopping energy is expressed as,

$$H_e = -t(c_1^\dagger c_2 + H.c) \quad (2.7)$$

Where ω is the characteristic phonon frequency, t is the bare hopping integral, u_m is the displacement integral, $f_m(i)$ is the interaction force between the site i and the m^{th} ion in the

lattice. A graphical representation of the electron in two sites interacting with ions in a long lattice is shown in Figure 2.3.4. For the complete treatment of long-range Fröhlich interaction in the adiabatic case and its hopping integral can be found in referred to¹⁹ and references therein.

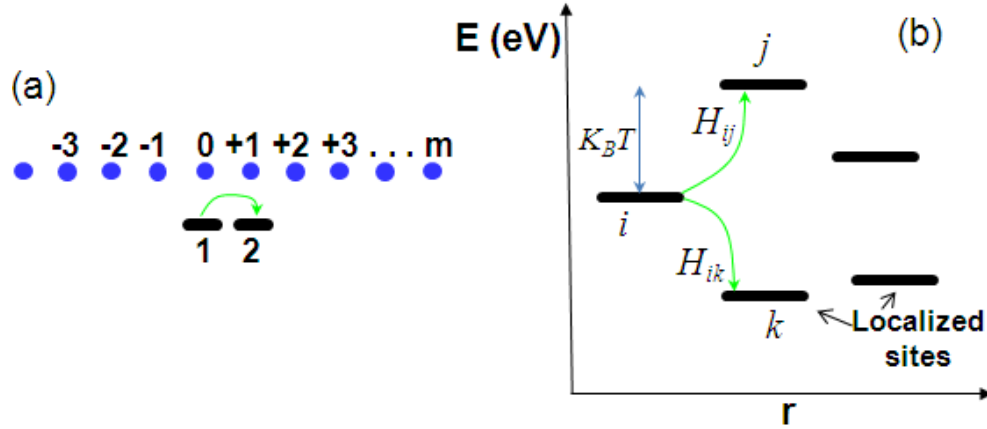


Figure 2.3.4 (a) Schematic of electron hop from one site to another upon interaction with ions in an infinite lattice, (b) Polaron hopping rates between two sites with equal Hamiltonians $H_{ij}; H_{ik} = 1$ on the condition that the reorganization energy is same.

For a polaron to overcome the energetic barrier and complete the charge hop a minimum electrical field is required which corresponds to the inter-chain coupling t_{\perp} , this happens when there is two localized sites in the band gap and a reversal of the alternation of the bond along the molecule. When the energy gained due to lattice vibrations is greater than the Coulombic repulsion between charges of same polarity two distinct polarons can form in the polymer chain.²⁰ While in the contrary if the Coulombic repulsion force is less persistent between like-charges bipolarons can be formed. The thermally activated hopping of charges depending on the electrical field and temperature is expressed as,²¹

$$\mu = \mu_0 \exp\left(\frac{-E_a}{K_B T} - A_1 \left[\frac{\sigma}{K_B T}\right]^2\right) \exp\left(A_2 \left[\left(\frac{\sigma}{K_B T}\right)^{\frac{3}{2}} - \Gamma\right] \sqrt{\frac{eaE}{\sigma}}\right) \quad (2.8)$$

Where σ is the width of the Gaussian DOS, E_a is the activation energy, a denotes the average intersite hopping distance and A_1 , A_2 and Γ are constants.

2.3.4 Bipolaron model

The formation of tightly bound charge trapping states due to bipolarons has been observed and suggested as the possible cause for the gradual reduction in the channel current in OFETs based on polyfluorene compounds such as poly(9-9'-dioctyl-fluorene-cobithiophene) (FET2).²² The evidence for the possible bipolaron states within the semiconductor was based on experimental observations of the slow decay in the drain current (I_D) in F8T2 based OFETs under continual gate bias stress conditions. When the bipolaron states are formed within the semiconductor layer the hole carrier removal rate was found to be proportional to square of the carrier concentration present in the device channel. The following mathematical equations relate the carrier rate constants, concentration and change in carrier concentration with time.



Equation 2.9 represents the reaction between two electrons or holes to form a corresponding bipolaron ee_{bpol} or hh_{bpol} . Now the rate equation for each of the carrier can be written as,

$$\begin{aligned} dN_e / dt &= -r_e N_e^2 + b_e N_{e,bpol} \\ dN_h / dt &= -r_h N_h^2 + b_h N_{h,bpol} \end{aligned} \quad (\text{or}) \quad (2.10)$$

Where N_e and N_h are the electron and hole carrier concentrations and r_e (r_h), b_e (b_h) and $N_{e,bpol}$ ($N_{h,bpol}$) are the rates constants and number of bipolaron states for electrons (and holes) respectively.

If the square of the electron or hole concentration (N_e^2 or N_h^2) follows a linear relationship with the change in carrier concentration with time (dN_e / dt or dN_h / dt) according to equation 2.10 for a fixed gate bias (V_{GS}) the validity of bipolaron states can be considered as the trap centers in the transistor channel, since the rate of bipolaron formation is extremely slow owing to the Coulombic repulsion between the like-charge carriers.

2.4 ORGANIC FIELD-EFFECT TRANSISTOR

The basic device geometry of an organic field-effect transistor (OFET) is comprised of two electrodes source and drain which is isolated from the third electrode namely the gate by means of an insulator layer. Thus in principle the transistor operates as a parallel plate capacitor when charges are collected at the proximity of the insulator interface upon the application of an electric field between the gate and the source electrode. Since the amount of charges collected is proportional to the potential applied to the gate electrode, thus by varying the magnitude of the field applied the quantity of charges can be modulated thus giving rise to the literal meaning of the transistor for its namesake as a “Field-effect transistor”.

2.4.1 OFET-working principles

The principle of operation of a transistor was reported by Lilienfeld as early as 1930.²³ After which many decades of great technological strides were made by using inorganic materials as the active layers in the devices. Research advances in the conductivity of a new class of materials entirely based on organic compounds in the 1970’s subsequently led to the integration of organic materials into devices such as transistors, diodes and solar cells. The basic principle in which the transistor operates on is that of a metal-insulator-semiconductor-metal (MISM) capacitor, shown in Figure 2.4.1 are the various biasing conditions of the MISM configuration.

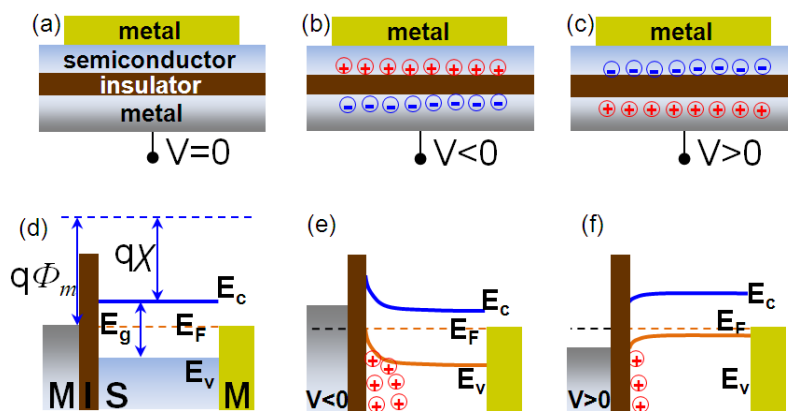


Figure 2.4.1 Schematic of metal-insulator-semiconductor-metal junctions at (a) no bias (b) bottom electrode negatively biased with respect to the top electrode, (c) positively biased, (d) ideal band diagram of the MISM junction, (e) at accumulation and (f) depletion respectively. The + and – symbols in the red and blue circles represent hole and electron carrier respectively.

The ideal energy band diagram of a MISM diode is depicted in Figure 2.4.1d, since the bands are flat at zero bias and Φ_m , E_g , E_F , E_c , E_v , X and q indicate the metal electrode work function, band gap, Fermi level, conduction band, valence band, the electron affinity and the elementary electron charge respectively. There is small bending of the bands in the real case due to a small built-in potential called as flat band voltage V_{fb} (this is the offset potential which needs to be applied to obtain flat band levels). The case of a p-type semiconductor sandwiched between two metallic electrodes is illustrated in the Figure 2.4.1a-c, when a negative potential is applied to the bottom electrode there is the accumulation of negative (electron carrier) and positive (hole carrier) charges at the proximity of the bottom electrode/insulator and insulator/semiconductor interfaces respectively. If one views the energetic band profile for this biasing condition (Figure 2.4.1e), there is a upward band bending of the valence band which results in the accumulation of hole carriers near the insulator interface. There is depletion of hole carriers which arises due to the downward band bending when the electrode is positively biased (Figure 2.4.1f) which results in the reduction (depletion) of the hole carrier, and this eventually causes increase in electron carrier concentration at the conduction band of the semiconductor. Now if we consider a three terminal electrode configuration of a transistor (Figure 2.4.2) depending on the polarity of the bias applied to the gate electrode the charges are accumulated in the HOMO or LUMO level of the semiconductor.

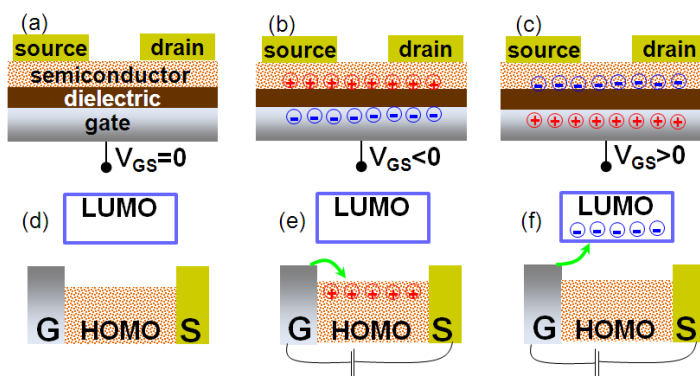


Figure 2.4.2 Schematic of the charge accumulation in the semiconductor upon biasing of the gate electrode, the source is held at electrical ground (a) Zero gate bias, (b) negative gate bias causes accumulation of hole carriers in the HOMO level of the semiconductor and (c) When $V_{GS} > 0$ V electron carriers are accumulated at the LUMO level of the semiconductor. The dotted points in the semiconductor have neutral charge.

According to the field applied from the gate electrode the charge density in the semiconductor can be varied. The total amount of charges accumulated is proportional to the gate bias and the capacitance of the dielectric (C_i).

When a bias is applied between the drain and the source (V_{DS}), this potential difference gives rise to a linear gradient across the channel. That is to say that at the source electrode where $x=0$ the potential $V(x) = 0$ and when $x = L$ (the channel length) $V(x) = V_{DS}$. For a n-type channel when $V_{GS} > V_{DS} > 0$, the current due to the flow of electrons as majority carriers in the channel increases linearly, this regime is termed as the linear regime. When the value of the V_{DS} is increased to a value which is greater than the difference between V_{GS} and threshold voltage (V_T) the drain current pinches-off and reaches saturation (appropriately named as saturation regime). The working scheme of a transistor operating in both P and N channel modes is illustrated in Figure 2.4.3.

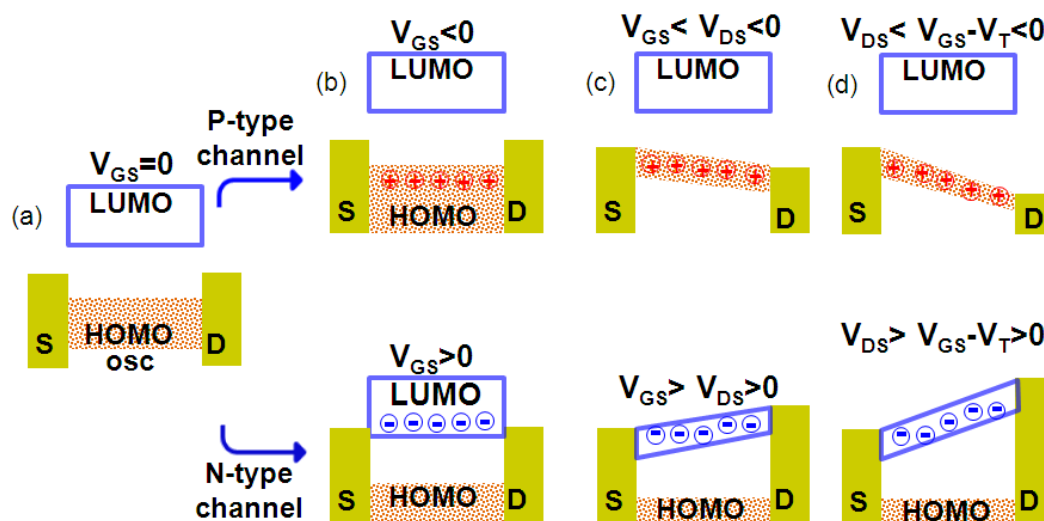


Figure 2.4.3 Schematic of a transistor operation in P-Channel (b-d, top) and N-channel (b-d, bottom). For P-channel when $V_{GS} < V_{DS}$ holes start to flow towards the drain from the source and when the V_{DS} exceeds the threshold voltage (in magnitude) maximum number of charges are collected near the drain and a depletion region is formed in its vicinity. For N-channel when $V_{GS} > V_{DS}$ electrons start to flow towards the drain from the source and when the V_{DS} exceeds the threshold voltage maximum number of charges are collected near the drain and a depletion region is formed in its vicinity.

2.4.2 Transistor performance indicators

The performance of the transistor is estimated by some key parameters such as charge carrier mobility, threshold voltage, I_{on}/I_{off} ratio, turn on voltage and subthreshold slope. These parameters can be extracted from the current vs. voltage (I - V) characteristics of the device. Specifically two types of characteristics can be recorded namely,

- (1) Output characteristics, and
- (2) Transfer characteristics

The I - V characteristics for a field-effect transistor can be reasonably described according to the gradual channel approximation. This condition is satisfied when the electric field perpendicular through the channel is larger than that of the lateral field between the drain and the source (i.e., $\partial E_x / \partial x < \partial E_y / \partial y$) and this happens when the device channel length (L) is larger than the dielectric thickness (d_i).

The output characteristics is the plot (Figure 2.4.4) which gives the variation in the drain current (I_D) with respect to the drain-source bias (V_{DS} , this is referred as drain voltage frequently) at fixed gate-source potential (V_{GS}) values. The transfer characteristics (Figure 2.4.5) is the plot which gives the variation in the I_D with respect to the V_{GS} , this is referred as drain voltage frequently) at fixed values of V_{DS} .

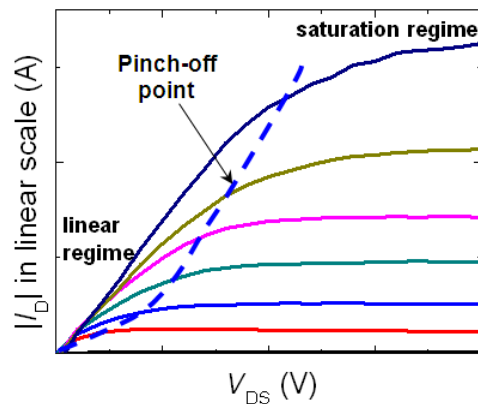


Figure 2.4.4 Typical output (I_D vs. V_{DS}) characteristics of a field-effect transistor. The curved dashed line intersects the pinch-off points after which there is saturation of the I_D .

When the gate potential is greater than the threshold voltage the number of induced mobile charges (Q_{mob}) collected at the proximity of the source electrode is given by,

$$Q_{mob} = C_i(V_{GS} - V_T) \quad (2.11)$$

When taking into the account the position along the channel in the lateral direction (at a position x) the induced charge density is expressed as,

$$Q_{mob} = C_i(V_{GS} - V_T - V(x)) \quad (2.12)$$

The magnitude of the drain current in the channel can be approximated as in absence of influence to the charge carrier diffusion,

$$I_D = W\mu_{eff}Q_{mob}E_x \quad (2.13)$$

Where W is the channel width, and μ_{eff} is the effective mobility taking into account of the mobile carriers only.

The **carrier mobility** of electrons or holes is the average drift velocity per unit applied electric field, in other words it provides an estimate of the maximum frequency of conductivity limit for a material and it is related to the conductivity (σ) as,

$$\sigma = nq\mu = \frac{nq^2\tau}{m} \quad \text{where} \quad \mu = \frac{q\tau}{m} \quad (2.14)$$

Where q the elementary charge, m is the mass of the charge carrier, and τ is the frequency.

By substituting for the lateral electric field E_x , with dV/dx results in,

$$I_D dx = W\mu_{eff}C_i(V_{GS} - V_T - V(x))dV \quad (2.15)$$

Using the gradual channel approximation the expression for the drain current can be obtained by numerical integration from $x=0$ to L (i.e., the lateral distance of separation between the source and drain electrodes) and is expressed as shown in equation 2.16 in the linear regime,

$$I_D = \frac{W}{L} \mu_{\text{eff}} C_i \left[(V_{GS} - V_T) V_{DS} - \frac{1}{2} V_{DS}^2 \right] \quad (2.16)$$

This can be simplified since at the linear regime $V_{DS} \ll V_{GS}$,

$$I_D = \frac{W}{L} \mu_{\text{lin}} C_i (V_{GS} - V_T) V_{DS} \quad (2.17)$$

Since the drain current is directly proportional to the linear carrier mobility, it can be estimated from the **transconductance** (g_{m1}) which is defined as the change in the drain current (∂I_D) with the gate source potential (∂V_{GS}) at a constant V_{DS} .²⁴

$$\mu_{\text{lin}} = \frac{\partial I_D}{\partial V_{GS}} \cdot \frac{L}{WC_i V_{DS}} \quad (2.18)$$

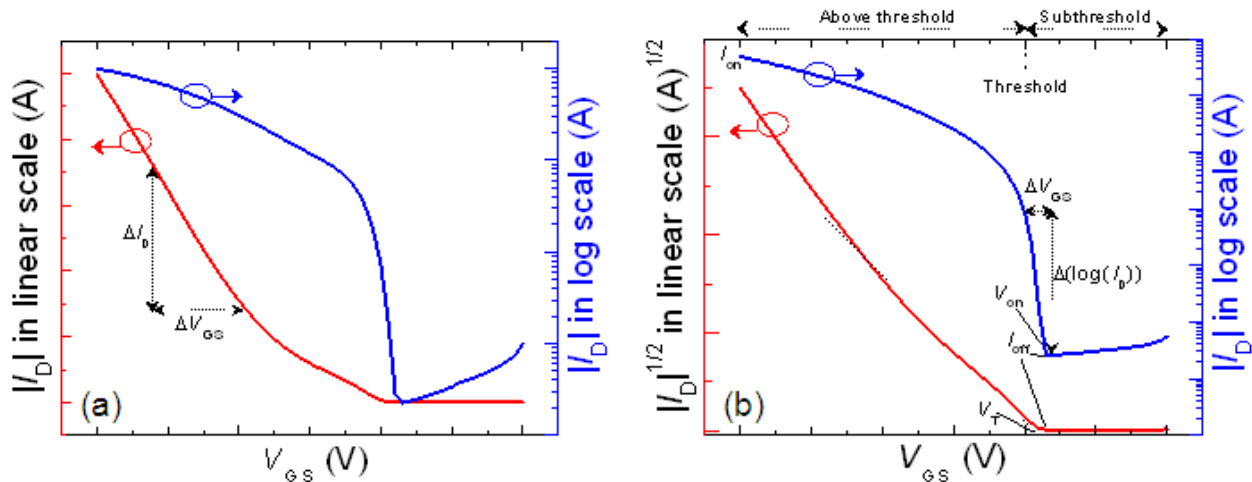


Figure 2.4.5 Transfer characteristics of a field-effect transistor in (a) I_D vs. V_{GS} linear regime and (b) $I_D^{1/2}$ vs. V_{GS} saturation regime at a fixed V_{DS} . The left and right axis illustrates the drain current in the linear and logarithmic scales respectively. The drain current is expressed in absolute value, for a p-type (hole conducting) semiconductor the sign of the drain current is negative and it's the contrary for n-type semiconductor.

In the linear regime the x -axis inflection point from the plot of I_D vs. V_{GS} the threshold voltage of the device can be extrapolated. After the **threshold voltage** (V_T) there is saturation of the drain current and the device goes into the on state, in other words it is the minimum potential required to turn the transistor on. In the saturation regime it is gate voltage which is extracted from the x -axis intercept from the $I_D^{1/2}$ vs. V_{GS} plot (Figure 2.4.5b).

The minimum potential which is required to rise the drain current due to the majority carriers²⁵ in the device channel is termed as the **turn-on voltage** (V_{on}) (see Figure 2.4.5b).

As seen earlier in Figure 2.4.4 once the drain current reaches the pinch-off point there is minimal change or saturation of the drain current, hence equation 2.16 cannot be applied for the device operating at the saturation regime. This occurs when the $V_{DS} > (V_{GS} - V_T)$ and by ignoring the short channel effects the relation between the drain current in the saturation regime with mobility can be written as,²⁴

$$I_{D,sat} = \frac{W}{2L} \mu_{sat} C_i (V_{GS} - V_T)^2 \quad (2.19)$$

From the above expression we find that the drain current is directly proportional to the square of the gate potential. Now the expression for the gate voltage dependent mobility in the saturation regime can be expressed as,²⁴

$$\mu_{sat}(V_{GS}) = \frac{\partial I_{D,sat}}{\partial V_{GS}} \cdot \frac{L}{WC_i (V_{GS} - V_T)} \quad (2.20)$$

The ability of the transistor switching capability can be estimated from the **subthreshold** swing (S), which is defined as the ratio of the change in the (∂V_{GS}) with respect to the log of drain current ($\partial(\log I_D)$). For instance the subthreshold slope gives the gate potential required to raise the drain current per decade in magnitude and it is expressed in units of V/dec or mV/dec (i.e., volts/decade).

$$S = \frac{\partial V_{GS}}{\partial(\log I_D)} \quad (2.21)$$

The transistor which has a steep S indicates a better the switching capacity to on state from the off state.

The **I_{on}/I_{off} ratio** is another parameter which gives the ratio of the drain current in the on-state to that in its off-state (Figure 2.4.5b). The larger this value the better is the switching behavior in the transistor.

2.5 REFERENCES AND NOTES

- 1 Heeger, A. J. Nobel Lecture: Semiconducting and metallic polymers: The fourth generation of polymeric materials. *Rev. Mod. Phys.* **73**, 681-700 (2001).
- 2 Jaiswal, M. & Menon, R. Polymer electronic materials: a review of charge transport. *Polym. Int.* **55**, 1371-1384 (2006).
- 3 Ostroverkhova, O. *et al.* Bandlike transport in pentacene and functionalized pentacene thin films revealed by subpicosecond transient photoconductivity measurements. *Phys. Rev. B* **71**, 035204, (2005).
- 4 Coropceanu, V. *et al.* Charge transport in organic semiconductors. *Chem. Rev.* **107**, 926-952, (2007).
- 5 Siringhaus, H. *et al.* Two-dimensional charge transport in self-organized, high-mobility conjugated polymers. *Nature* **401**, 685-688 (1999).
- 6 Le Comber, P. G. & Spear, W. E. Electronic Transport in Amorphous Silicon Films. *Phys. Rev. Lett.* **25**, 509-511 (1970).
- 7 Horowitz, G., Hajlaoui, M. E. & Hajlaoui, R. Temperature and gate voltage dependence of hole mobility in polycrystalline oligothiophene thin film transistors. *J. Appl. Phys.* **87**, 4456-4463 (2000).
- 8 Horowitz, G. & Hajlaoui, M. Grain size dependent mobility in polycrystalline organic field-effect transistors. *Synth. Met.* **122**, 185-189 (2001).
- 9 Chesterfield, R. J. *et al.* Variable temperature film and contact resistance measurements on operating n-channel organic thin film transistors. *J. Appl. Phys.* **95**, 6396-6405 (2004).
- 10 Majewski, L. A., Schroeder, R., Grell, M., Glarvey, P. A. & Turner, M. L. High capacitance organic field-effect transistors with modified gate insulator surface. *J. Appl. Phys.* **96**, 5781-5787 (2004).
- 11 Borsenberger, P. M. & Bassler, H. Concerning the role of dipolar disorder on charge transport in molecularly doped polymers. *J. Chem. Phys.* **95**, 5327-5331 (1991).
- 12 Bässler, H. Charge transport in disordered organic photoconductors a Monte Carlo simulation study. *phys. stat. sol. (b)* **175**, 15-56 (1993).
- 13 Miller, A. & Abrahams, E. Impurity Conduction at Low Concentrations. *Phys. Rev.* **120**, 745-755 (1960).
- 14 Holstein, T. Studies of polaron motion: Part II. The “small” polaron. *Ann. Phys.* **8**, 343-389 (1959).
- 15 Holstein, T. Studies of polaron motion: Part I. The molecular-crystal model. *Ann. Phys.* **8**, 325-342, (1959).
- 16 Marcus, R. A. Electron transfer reactions in chemistry. Theory and experiment. *Rev. Mod. Phys.* **65**, 599-610 (1993).
- 17 Conwell, E. M. & Jeyadev, S. Free soliton transport and photoconductivity in trans-polyacetylene. *Synth. Met.* **28**, D439-D446, (1989).
- 18 Conwell, E. M., Choi, H. Y. & Jeyadev, S. Interchain polaron transport in trans-polyacetylene. *Synth. Met.* **49**, 359-365, (1992).
- 19 Alexandrov, A. S. & Yavidov, B. Y. Small adiabatic polaron with a long-range electron-phonon interaction. *Phys. Rev. B* **69**, 073101 (2004).
- 20 Bredas, J. L. & Street, G. B. Polarons, bipolarons, and solitons in conducting polymers. *Acc. Chem. Res.* **18**, 309-315, (1985).
- 21 Kreouzis, T. *et al.* Temperature and field dependence of hole mobility in poly(9,9-dioctylfluorene). *Phys. Rev. B* **73**, 235201 (2006).
- 22 Street, R., Salleo, A. & Chabiny, M. Bipolaron mechanism for bias-stress effects in polymer transistors. *Phys. Rev. B* **68**, 085316 (2003).

- 23 Lilienfeld, J. S. E. Method and apparatus for controlling electric currents. US patent 1745175 (1930).
- 24 Horowitz, G. Organic field-effect transistors. *Adv. Mater.* **10**, 365-377 (1998).
- 25 *Majority carriers are the carriers which are predominant in the semiconductor. For instance in a n-type semiconductor the majority carriers are electrons, while in a p-type semiconductor they are holes. In ambipolar or bipolar semiconductor both electrons and holes can contribute to the device current.*

Nature may reach the same result in many ways.

-Nikola Tesla (1856-1943), Inventor/ Electrical engineering pioneer/ Wizard

3

3.1 CHARGE TRANSPORT IN MOLECULAR JUNCTIONS

In this chapter the fundamentals of the charge transport through molecular junctions is outlined. The basic components of a molecular junction and its respective functions are elaborated. The physics behind the charge transport phenomenon in particular tunneling process is explained. The role of quantum tunneling and its use in molecular junctions particularly for electronics is briefed.

3.1.1 Molecular junctions - building blocks

The field of molecular electronics as such was present in the mid of 21st century, but it was due to a landmark proposition by Aviram and Ratner that an organic molecule could behave like a rectifier¹ brought in great interest from the research community. Their premise was molecule/s with certain intrinsic functionality could be integrated into building more complex molecular electronic circuits.² A basic molecular junction is comprised of a single molecule or a set of molecules attached to a metallic electrode. To understand the electron transport and the rates of charge transfer vast number of molecular systems has been studied. A molecular junction based on an azobenzene derivative is shown in Figure 3.1.1. The building units of molecular junction in broad terms are comprised of molecules and electrodes. The electrodes can be either highly conducting metal or carbon based structures such as nanotubes. The molecules bridging the electrodes are in general much more resistive and in essence behave like an insulator, their conductance increased if a high degree of conjugation along the molecular backbone is present. Upon application of an electric field across the molecular junction charges start to flow from one electrode to the other. Thus depending on the structure, type and length of π -conjugated bridge of the molecule the electron transfer rates vary. For the purpose of electrical current rectification a donor-bridge-acceptor (DBA) type of molecule was theoretically found to be a suitable candidate.

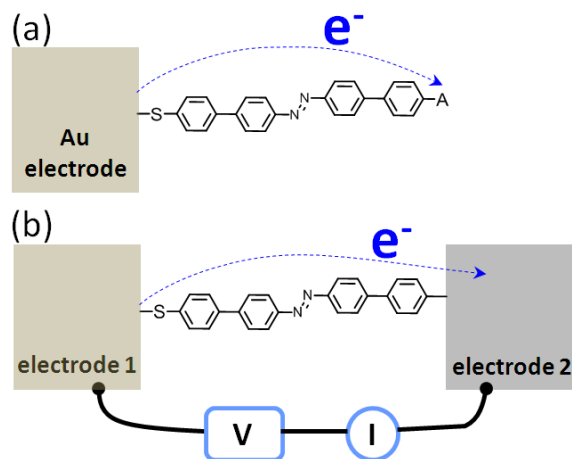


Figure 3.1.1 Schematic of molecular junction (a) Molecule chemisorbed on Au electrode linking an acceptor unit (b) Azobenzene molecule linking two conducting electrodes.

3.1.2 Metal-molecule-metal junctions

The link between the metal electrode and the molecule could range from strong covalently bounded to weak van der Waals type of interaction. To understand how the charge transport occurs in a molecular junction it is necessary to consider the molecular junction in terms of individual components with respective energetic barriers among each of them.^{3,4} For instance, metallic electrodes have uniform distribution of electronic states (DOS), while the molecules have distinct conduction (LUMO) and valence (HOMO) levels separated by a band gap. The offset between the respective electronic transport levels and the Fermi level of the metal contact gives rise to a potential barrier.

Figure 3.1.2 shows the metal-molecule-metal junction at zero bias and with potential applied to the electrodes. At zero bias the Fermi levels of the electrodes line up and there is a uniform distribution of electronic charge across the metal contacts. Upon application of a positive bias to the right electrode (RE) the Fermi level is lowered and there is a greater population of electronic charge near the left electrode (LE). When the RE is negatively biased the Fermi level is raised with respect to that of the LE resulting in a greater population of electronic charge near the RE. The height of the tunneling barrier is denoted by $\Phi_{T,bh}$ which changes corresponding to the change in the electrical potential applied to the electrodes.

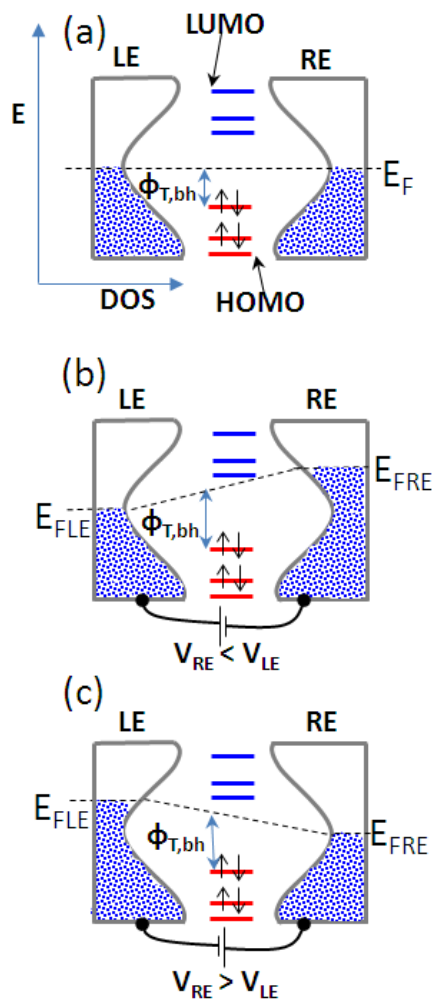


Figure 3.1.2 Illustration of the energy levels of a metal-molecule-metal junction at (a) Zero bias, (b) right electrode negatively biased with respect to left electrode and (c) left electrode negatively biased with respect right electrode.

The current flowing in the molecular junctions is predominantly due to coherent tunneling and is dependent on some factors such as,

- (i) The composition of the molecular bridge and the electrodes
- (ii) The strength of the metal-molecule or electrode-molecule interaction
- (iii) The linking entity between the molecule and electrode
- (iv) The Fermi energy of adjoining electrodes
- (v) The electrostatic spatial charge distribution through the molecule

- (vi) The orientation of the molecule
- (vii) The roughness of the electrodes
- (viii) The length and extent of conjugation along the molecular unit.

3.1.3 Quantum tunneling

When charge transport through a molecular layer of thickness < 5 nm is involved the predominant mode by which the transport occurs is by a process what is termed by physicists as quantum tunneling. In the view point of classical physics any electron with energy less than that of the interfacial potential barrier at the metal/insulator interface always is reflected at the interface. Depicted in Figure 3.1.3 is the quantum tunneling phenomenon of a particles in a wave packet with mass m through a potential barrier V_0 and distance l . The energetic state of the particles are Gaussian distributed with momentum centered around the kinetic energy, $E = \hbar^2 k_0^2 / 2m$ according to classical physics the particles do not possess enough energy to surmount the barrier $0 < x < l$. However in terms of quantum mechanics which takes into account the wave nature of the electrons provides the small possibility to traverse the forbidden region of the barrier.

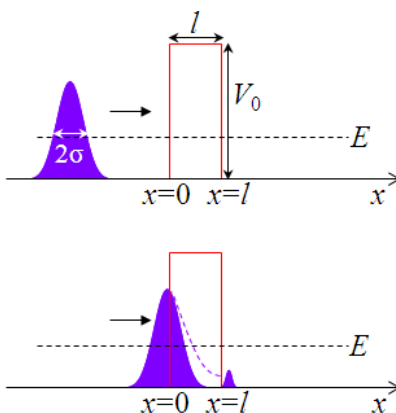


Figure 3.1.3 Quantum tunneling through one dimensional potential well with a barrier of height V_0 and distance l . The dotted purple line represents the tunneling decay which the wave packet undergoes upon encountering the barrier.

The wavefunction associated with the electron decays exponentially with the depth of penetration from its initial starting point at the metal/insulator interface. For macroscopic

thickness the decay is such that there is virtually zero probability to find an electron in the other side of the interface. In the case that the barrier is very thin of the dimensions of less than 5 nm, the wavefunction has a non-zero value at the opposite interface, thus there is finite probability that the electron can pass from one electrode to the other by penetrating through the barrier. A graphical illustration of the tunneling process in a metal-molecule-metal junction is shown in Figure 3.1.4.

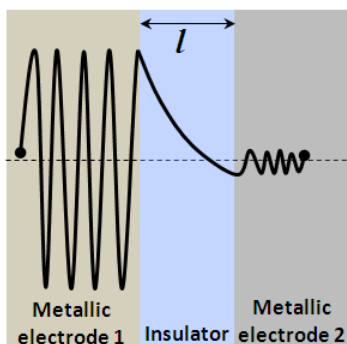


Figure 3.1.4 Quantum tunneling at a metal/insulator interface, illustrating the decay of the electron wavefunction with distance l .

The electron wavefunction from metal electrode 1 rapidly decays as it passes through the potential barrier induced by the presence of the molecule which behaves as an insulator. Note that while there is an attenuation of the wavefunction the phase is maintained uniform throughout. The rate of this coherent tunneling is given expressed in terms of the barrier width and height in its simplest form according to Simmons model^{5,6}

$$J = \frac{q^2 V}{h^2 l} (\sqrt{2m\Phi}) \exp\left[-\frac{4\pi l}{h} (\sqrt{2m\Phi})\right] \quad (1)$$

Where J is the current density (in A/cm²), q is the elementary charge, V is the applied potential, h is Planck's constant, m is the electron mass, Φ is the barrier height and l is the thickness of the barrier. According to equation 1 the tunneling barrier is assumed to be rectangular.

For molecular junctions such as the case illustrated in Figure 3.1.2 the tunneling barrier height $\Phi_{T,bh}$ is noted in units of Joules or electron volts.

To minimize the inherent complexity of the tunneling barrier profile the equation 1 is expressed in its simplified approximation,

$$J = Ae^{-\beta l} \quad (2)$$

Where A is a constant which refers to the current density in the case of a hypothetical barrier with thickness $l=0$ and β (in \AA^{-1} or nm^{-1}) is the rate of tunneling decay.

The charge tunneling through the molecule can be described by “through-bond” and “through-space”.^{7,8} In through-bond tunneling the electron interaction with the molecular orbitals enhances the rate of tunneling and is generally faster than through-space tunneling, thus through-bond tunneling is frequently referred to as “superexchange”.^{8,9} However coherent tunneling process is effective only for short distances of less than 3 nm since its decay rate is small $\sim 0.5\text{\AA}^{-1}$.¹⁰⁻¹²

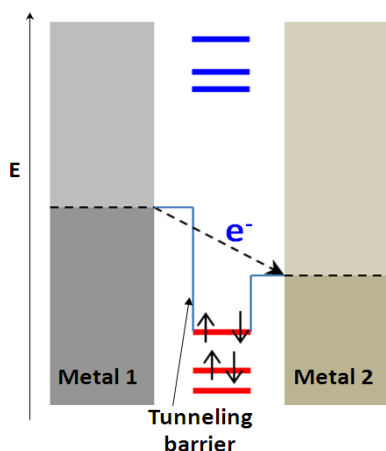


Figure 3.1.5 Illustration of coherent tunneling through a potential barrier induced by the molecule sandwiched between two metal electrodes. The occupied electronic states in the electrodes are in dark gray/golden yellow shades. The blue and red lines represent the LUMO and HOMO levels of the molecule. The Fermi level of the electrodes lies between the molecular HOMO-LUMO gap.

For a distances greater than 3 nm the hopping is prevalent mode of transport.^{10,11}

3.1.4 References and notes

- 1 Aviram, A. & Ratner, M. A. Molecular rectifiers. *Chem. Phys. Lett.* **29**, 277-283 (1974).
- 2 Aviram, A. Molecules for memory, logic, and amplification. *J. Am. Chem. Soc.* **110**, 5687-5692 (1988).
- 3 Nitzan, A. & Ratner, M. A. Electron transport in molecular wire junctions. *Science* **300**, 1384-1389 (2003).
- 4 McCreery, R. L. Molecular electronic junctions. *Chem. Mater.* **16**, 4477-4496 (2004).
- 5 Simmons, J. G. Generalized formula for the electric tunnel effect between similar electrodes separated by a thin insulating film. *J. Appl. Phys.* **34**, 1793-1803 (1963).
- 6 Wang, W., Lee, T. & Reed, M. A. Mechanism of electron conduction in self-assembled alkanethiol monolayer devices. *Phys. Rev. B* **68**, 035416 (2003).
- 7 Slowinski, K., Chamberlain, R. V., Miller, C. J. & Majda, M. Through-bond and chain-to-chain coupling. Two pathways in electron tunneling through liquid alkanethiol monolayers on mercury electrodes. *J. Am. Chem. Soc.* **119**, 11910-11919 (1997).
- 8 Segal, D., Nitzan, A., Davis, W. B., Wasielewski, M. R. & Ratner, M. A. Electron transfer rates in bridged molecular systems 2. A steady-state analysis of coherent tunneling and thermal transitions. *J. Phys. Chem. B* **104**, 3817-3829 (2000).
- 9 Petrov, E. G., Shevchenko, Y. V., Teslenko, V. I. & May, V. Nonadiabatic donor--acceptor electron transfer mediated by a molecular bridge: A unified theoretical description of the superexchange and hopping mechanism. *J. Chem. Phys.* **115**, 7107-7122 (2001).
- 10 Choi, S. H., Kim, B. S. & Frisbie, C. D. Electrical resistance of long conjugated molecular wires. *Science* **320**, 1482-1486 (2008).
- 11 Lu, Q. *et al.* From Tunneling to Hopping: A Comprehensive Investigation of Charge Transport Mechanism in Molecular Junctions Based on Oligo (p-phenylene ethynylene) s. *ACS nano* **3**, 3861-3868 (2009).
- 12 Kronemeijer, A. J. *et al.* Universal Scaling of the Charge Transport in Large-Area Molecular Junctions. *small* **7**, 1593-1598 (2011).

Design is not just what it looks like and feels like. Design is how it works.

-Steve Jobs (1955-2011), Visionary entrepreneur

4 Methods and Procedures

4.1 OFET PREPARATION

OFETs with two different device geometries were fabricated during the course of this thesis namely,

- (i) Bottom-gate bottom-contact and
- (ii) Top-gate bottom-contact.

The deposition of the active semiconducting layer was carried out by means of either spin casting or drop casting from respective solutions.

4.1.1 F8BT based OTFTs

Poly[(9,9-di-*n*-octylfluorenyl)-2,7-diyl]-*alt*-(benzo[2,1,3]thiadiazol-4,8-diyl] (Aldrich) abbreviated as F8BT was the organic semiconductor in all the devices. Poly(methyl methacrylate) (PMMA, $M_w = 4, 50, 500 \text{ kgmol}^{-1}$, Aldrich) and Polystyrene of three different molecular weights (PS, $M_w = 4, 48.1, 500 \text{ kgmol}^{-1}$, Aldrich) served as the polymer gate dielectric. All materials were used as received without further purification. The organic thin film transistors were fabricated on n^{++} - Si/SiO₂ wafer (IPMS Fraunhofer, Germany), which served as support substrates. The substrates were cleaned by thoroughly rinsing in acetone followed by sonication at room temperature with acetone ($\geq 99.5\%$ purity) and 2-propanol for 15 minutes respectively and dried under a steady stream of nitrogen. Interdigitated gold source-drain electrodes (30 nm) were then evaporated with a shadow mask using Plassys MEB 300 thermal evaporator at $0.04\text{-}0.06 \text{ nms}^{-1}$. The evaporation of the electrodes prior to the deposition of semiconductor ensured no gold atoms penetrate into the semiconductor layer thereby hindering carrier injection. Undecanethiol (Aldrich) self-assembled monolayer was coated on the Au electrodes by incubation of the substrates in 1 mM thiol solution (in ethanol) overnight. After removal of the substrates from the thiol solution they were rinsed with copious amount of the ethanol solvent to

remove any physisorbed molecules on the electrodes. The next step was the surface passivation of the SiO₂ by hexamethyldisilazane (HMDS) vapor treatment of the substrates overnight prior to deposition of the semiconducting layer. F8BT in chloroform (6 mg mL⁻¹) was spin coated at 1800 rpm and subsequently annealed at 80°C for 10 minutes. After allowing the substrates to cool down, PMMA and PS of appropriate concentration in anhydrous n-butyl acetate were spin coated at different speeds which gave a thickness of (~ 620 nm), the substrates were then annealed immediately at 80°C for 1 hour to allow evaporation of any solvent which might be trapped in the film. After annealing the substrates were allowed to cool for 1 hour before evaporation of the top gate gold electrode (30 nm) with a shadow mask, manually aligned under an optical microscope this completed the fabrication of the device with top-gate bottom-contact device geometry. The complete fabrication cycle of the OTFT is depicted in Figure 4.1.1. The spin coating and annealing of the organic semiconductor and polymer dielectric was carried out entirely under inert atmosphere in a nitrogen filled glove box.

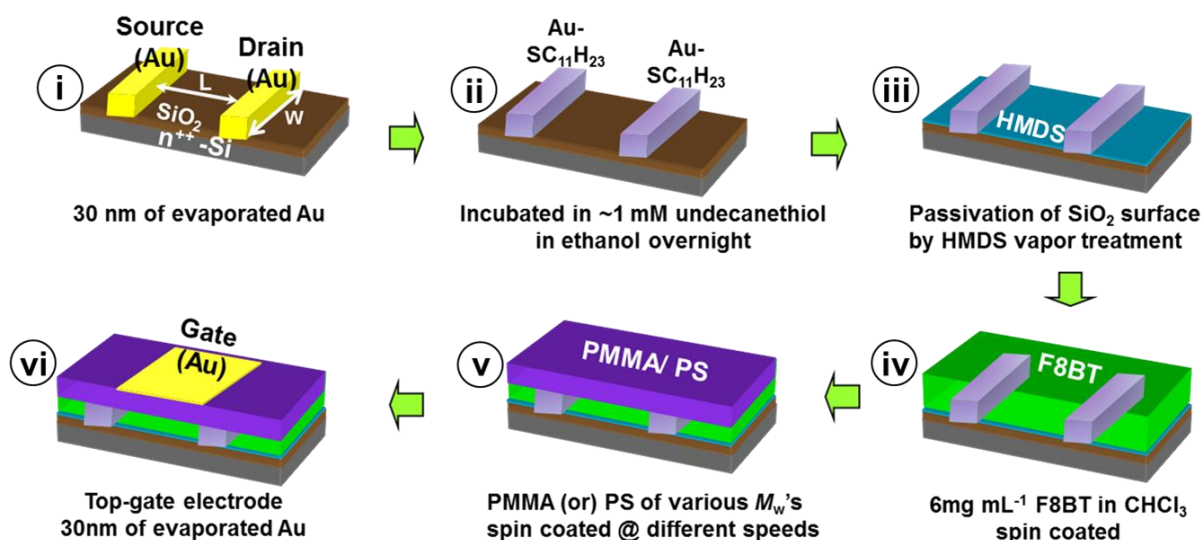


Figure 4.1.1 Fabrication cycle of top-gate bottom-contact F8BT based OTFT comprising of the following steps, (i) evaporation of gold source-drain electrodes on bare Si/SiO₂ substrate, (ii) treatment of Au electrodes with undecanethiol, (iii) Passivation of the SiO₂ surface by with HMDS vapor overnight, (iv) Spin coating F8BT to form the active layer, (v) Spin casting of the dielectrics PMMA or PS from n-butyl acetate, and (vi) evaporation of 30 nm Au to form the top-gate electrode.

4.1.2 P3HT based OTFTs

1.5×1.5 cm² Si/SiO₂ substrates (IPMS Fraunhofer) comprising of thermally grown SiO₂ layer on a n⁺⁺ Si, which served as the gate, and pre-patterned Au electrodes deposited on the SiO₂ layer, which served as source-drain electrodes, were used to fabricate the thin-film transistor. The substrates were cleaned by rinsing with acetone to remove the photoresist film followed by sonication in an ultrasonic bath (Fisher) with acetone and isopropanol for 15 minutes each. The channel length (*L*) and width (*W*) for the TFTs which were characterized amounted to 10 and 10000 μm, respectively. To complete the OTFT device a poly(3-hexylthiophene) (P3HT) solution (120 μl of 2 mg ml⁻¹ in toluene) was spin-coated on the substrates. After spin-coating of P3HT the solvent was allowed to evaporate for ~ 48 h prior to electrical characterization.

4.1.3 QQT(CN)₄ based OFETs

For p and n-type operation: Devices were fabricated by spin casting 50 μL QQT(CN)₄ from CHCl₃ onto substrates with pre-patterned electrodes (IPMS Fraunhofer, Germany).

n-type operation: Devices were fabricated by spin casting QQT(CN)₄ onto pre-patterned substrates followed by an annealing step at 180 °C for 10 s in ambient conditions.

4.1.4 P3HT, diarylethene blend OFETs

P3HT+DAE_{open} blend OFET: DAE of 20% by weight was blended with P3HT at a concentration of 1 mg mL⁻¹ in chloroform. The blend solution was then spin coated onto a Si/SiO₂ substrate comprising of pre-patterned interdigitated electrodes (IPMS Fraunhofer, Germany). Heavily n doped Si layer served as the gate electrode, thermally grown SiO₂ layer was the gate dielectric (*C_i* = 15 nF cm⁻²). In the case of the P3HT with DAE_{open} form, the solution was plainly spin casted and allowed to cure inside a N₂ filled Jacomex glovebox (O₂ < 5 ppm, H₂O < 0.6 ppm) for 15 minutes.

P3HT+DAE_{closed} blend OFET: The starting substrate was similar to the OFETs based on DAE_{open} and P3HT but after spin coating of the blend solution, the substrate was irradiated with UV light at a λ of 366 nm for 10 minutes to convert the DAE_{open} molecules embedded in the bulk of the blend film to its ring closed state. For this end the substrate was held in the chuck of the spin coater and the UV light was irradiated on the large face ensuring maximum amount of exposure to the light on the semiconducting thin film.

Encapsulation of OFETs: To improve the stability of the OFET in ambient conditions the OFETs were encapsulated with a film of PMMA. The concentration of 50 mg ml⁻¹ PMMA in methyl ethyl ketone was spin casted directly on top of the semiconducting film for devices with DAE in both states.

4.1.5 P3HT, PTTP blend OFETs

The base substrates for transistors with a blend of poly(3-hexylthiophene) (P3HT) and PTTP as the active layer in the film was pre-patterned Fraunhofer ones. The amount of the ratio of the PTTP by weight in blend with P3HT varied from 0, 5, 25, 75, 95 and 100 %. The concentration of the solution used for all the blend cases were 5 mg mL⁻¹ in *para*-xylene. To fabricate the transistors 100 µL of blend solution was drop casted onto the substrates and allowed to cure in an inert N₂ filled atmosphere of glovebox.

4.2 OFET CHARACTERIZATION TECHNIQUES

For performing the charge transport measurements in the OFETs characterization was performed in a standard probe station setup inside a glovebox for air-sensitive devices while characterization was performed in ambient conditions for air stable devices. For probing the temperature dependent behavior in OFETs a setup interfaced with a static cryostat was employed.

4.2.1 Electrical characterization inside glovebox

This characterization was performed by means of a dual channel source meter (Keithley 2636A SMU) in the dark. Triaxial cables were employed to minimize signal losses. The OFET under test was placed in a sample stage of Cascade Mikrotek probe station and probed by means of süss probes. For all the cases when the devices were air-sensitive the complete electrical characterization were performed inside a N₂ filled glovebox (Jacomex) with O₂ levels < 10 ppm. The levels of O₂ and H₂O in the glovebox were periodically monitored.

4.2.2 Electrical characterization in cryostat

A static cryostat OptistatDN (Oxford instruments, UK) was employed to house the OFET. The electrical contact with the OFET were realized by means of a custom built sample pad (Figure 4.2.1c) which could be mounted or dismounted from the protruding electrical connector pins. The connections to the OFET electrodes were then established between first by affixing the gate

electrode and a copper pad by means of conductive silver adhesive (Figure 4.2.1d) and the source-drain electrode pads were connected to their respective terminals with copper wires (0.1mm diameter). Teflon tapes were wrapped around the soldered joints of the cable with the connector pins, to provide shielding over the contacts. The cryostat was interfaced with an external dual channel electrometer Keithley 2636A (Keithley Instruments Inc, USA) with coaxial cables from the SMB sockets for each of the individual electrodes (Figure 4.2.1).

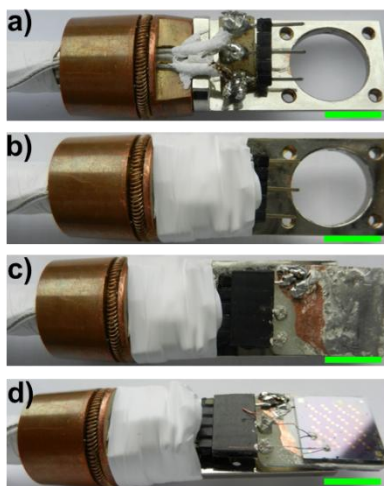


Figure 4.2.1 Photographs illustrating the connection sequence of an OFET with the cryostat sample rod (a and b) electrical connector pins, (c) OFET holder pad plugged into the connector pins and (d) OFET affixed to the sample holder pad with electrical connections established at source, drain and gate electrodes. Green bar represents the scale of 1 cm.

Figure 4.2.2 shows the entire setup schematic of the cryostat along with the external temperature control unit and the electrometer. Temperature control was maintained and monitored by an intelligent temperature controller (ITC) unit attached to a heating sensor of the cryostat. Once the OFET was attached to the sample rod and placed in the cryo sample space, it was pumped to high vacuum. The sample space was cooled by thermal conduction due to heat exchanged by the flow of nitrogen gas in contact with liquid nitrogen reservoir. Prior to loading the sample rod the outer vacuum chamber was pumped to high vacuum to ensure good thermal isolation. The temperature was regulated by the manual flow of nitrogen gas and the heating of the sensor controlled by the electrical power dispensed from the ITC.

The electrical connections to the OFETs was established by suitable SMB port feed through which could be connected a coaxial cable, which was then further connected to the electrometer by means of the coaxial to triaxial adapter. The complete electrical characterization of the OFETs inside the cryostat was performed in dark.

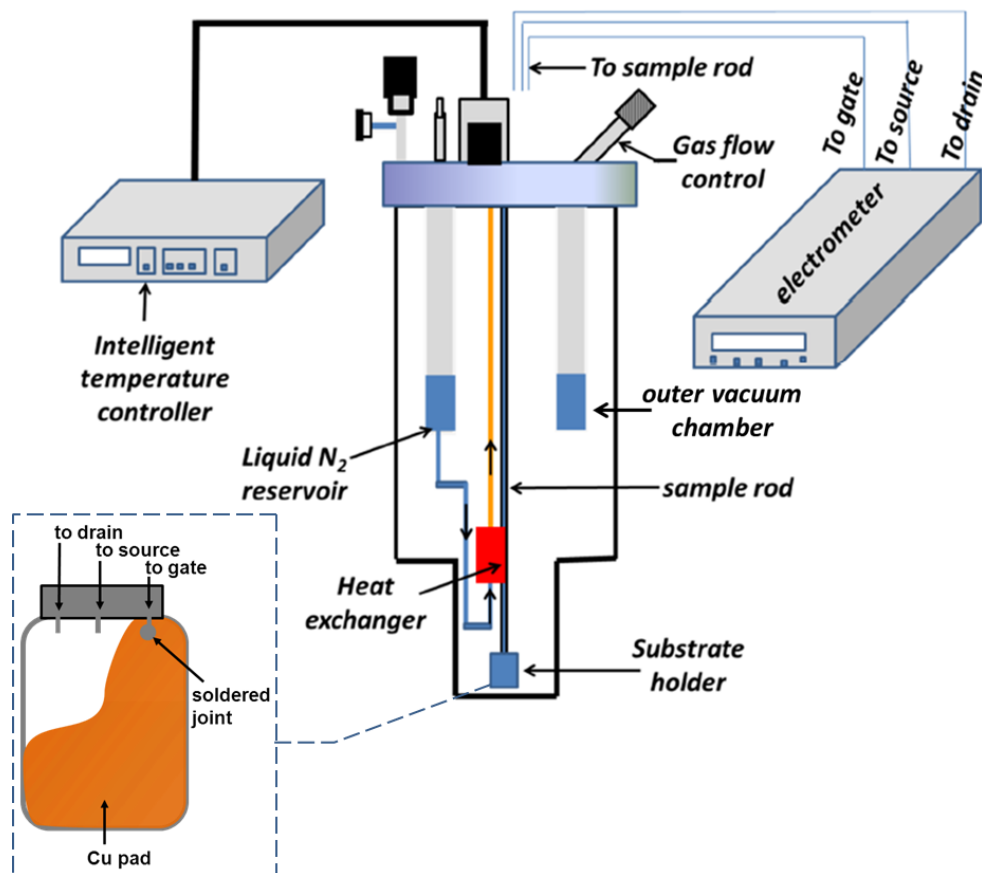


Figure 4.2.2 Layout of the complete cryostat setup equipped with an external temperature control unit and an electrometer to source electric potential and measure current of a three terminal device such as OFET. The OFET sample holder is shown in inset along with the respective electrode connection terminals.

Prior to lowering the temperature inside the sample chamber the integrity of the electrical contact with the OFET was checked after placing the sample rod along with the OFET attached to the custom sample pad shown in the inset of Figure 4.2.2. The temperature inside the cryostat sample space could be varied from 80 K to 300 K.

4.2.3 Work function of electrodes

The work functions of the metal and gold-SAM electrodes were measured by means of macroscopic Kelvin probe (Kelvin Probe Technology Ltd, UK) or ambient ultraviolet photoelectron spectroscopy (UPS) (Riken AC2 spectrophotometer, Japan).

The contact potential difference method, using a commercial Au reference tip was employed to record the work function of the Au and Au-SAM surface.

Using the UPS (Figure 4.2.3) the work function of Au which was estimated by the minimum threshold energy required for commencement of photoelectrons from the ground state.

4.2.4 Ionization energy of semiconductor film

The ionization energy levels of our semiconductor films were recorded by means of ambient UPS from Riken Keiki Co Ltd model AC-2. The ionization energy (IE) gives the lowest energy required to create a hole in the highest occupied molecular orbital upon the photoemission of an electron.

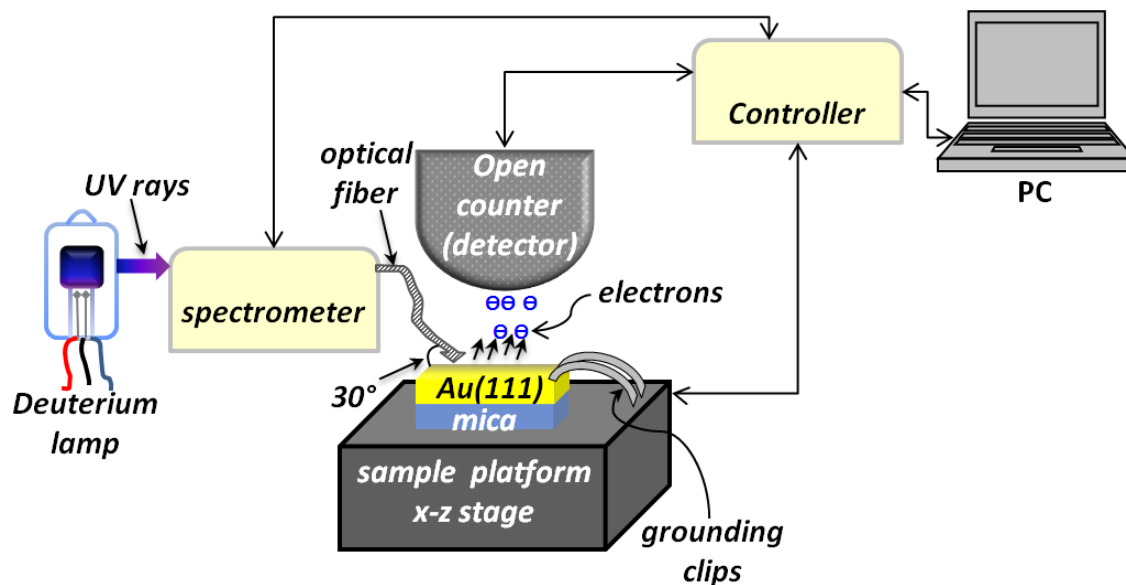


Figure 4.2.3 Schematic layout of the UPS with illustration of the basic working principle of the setup. The incident UV beam arrives at the surface of the sample under test through an optical fiber at an angle of 30° .

For F8BT film, firstly $\sim 120 \mu\text{L}$ of 6 mg mL^{-1} F8BT solution in CHCl_3 was drop casted onto a custom solution holder inside N_2 filled glovebox and the solvent was allowed to dry.

For QQT(CN)₄ films, 50 μL of varying concentration of 1, 2, 3, 5, 8 mg mL^{-1} QQT(CN)₄ solution in CHCl_3 was casted from solution onto cleaned ITO substrates in ambient conditions after which the IE levels were recorded.

For P3HT film, the IE was recorded after drop casting and curing of 2 mg mL^{-1} P3HT in toluene onto a metallic solution holder inside the glovebox.

4.2.5 Morphological characterization

The morphology of the semiconductor films, dielectric films and the Au electrodes of the OFETs was mapped by atomic force microscopy (AFM) from Digital Instruments Dimension 3100 (Bruker Instruments Inc, USA) operating in the intermittent-mode.

4.2.6 Microstructural characterization of P3HT:PTTP blend films

GIWAXS measurements were performed using a custom setup consisting of rotating anode X-ray source (Rigaku Micromax, operated at 42kV and 20mA), Osmic confocal MaxFlux optics and a three pin-hole collimation system (JJ X-ray). Samples on the top of approx. 1.5×1.5 cm silicon platelets were irradiated at the incident angle (α_i) of $0,20^\circ$. Diffraction patterns were recorded for 3h on a MAR345 image plate detector. Finally, the data was processed and imaged using Datasqueeze 2.2.5 program. For one-dimensional XRD, a θ - θ Siemens D500 Kristalloflex with a graphite-monochromatized $\text{CuK}\alpha$ X-ray beam was used.

4.2.7 Surface wettability tests

The aqueous contact angle at the SAM-ambient interface was measured by means of a Krüss DSA 100 goniometer (Krüss GmbH, Germany). The contact angle and the derived work of adhesion provided qualitative information on the surface wettability of electrodes incorporated in OTFTs.

The contact angle characterization was also performed on PMMA, PS and F8BT films to elucidate the surface wettability and thereby the corresponding surface free energy.

4.2.8 UV/Vis spectroscopy on films

Absorbance spectrum of the spin cast blend film of P3HT and 20% weight DAE_{open} (2 mg mL^{-1}) on quartz slides were acquired by means of a Jasco V-670 spectrophotometer (Jasco analytical instruments Inc, USA).

The absorption spectrum of spin coated QQT(CN)₄ films pre and post annealing was recorded with by UV/Vis spectrophotometer. To this end 50 μL of QQT(CN)₄ in CHCl_3 was spin coated onto quartz substrates after which the absorption spectrum on this film was collected.

4.3 SAM PREPARATION

Depending on the air stability of the molecules used to form the self-assembled monolayer (SAM), it was either formed inside an inert glovebox or in ambient laboratory conditions.

The preparation of the SAM on gold substrate follows the steps as depicted in Figure 4.3.1. Firstly the Au substrate is cleaned by gently blowing with a N_2 followed by UV/Ozone treatment. Once the cleaning procedure of the Au surface is done the substrate is immediately immersed in the respective thiol solution for a predetermined amount of time to allow the formation of the SAM on the surface of the gold. After the removal of the Au substrate from the thiol solution the substrate is rinsed with the solvent in which the thiol molecules are dissolved in for at least 20 times by splashing the solvent from the pipette and always holding the substrate at the bottom edge with a pair of tweezers as illustrated in Figure 4.3.1. Once the solvent drips off the surface of the Au substrate it is gently blow dried with a stream of the N_2 to remove any residual solvent which might be entrapped between the molecules.

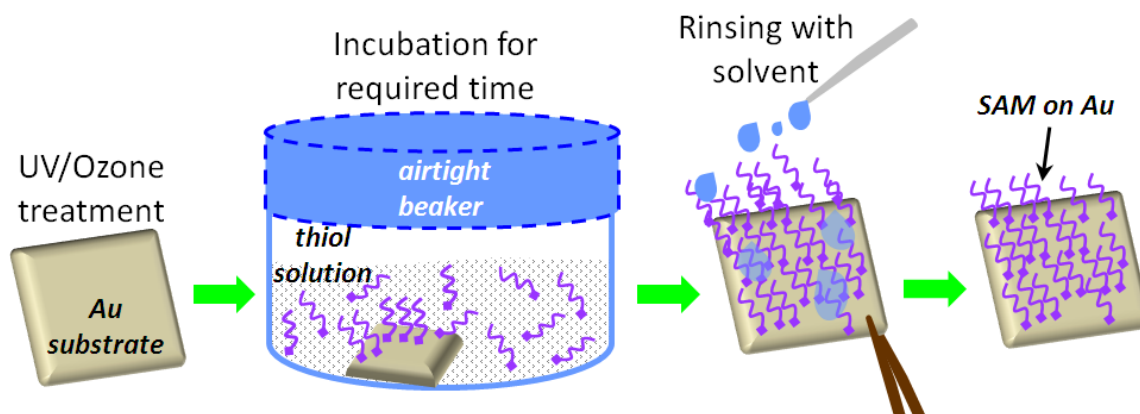


Figure 4.3.1 Illustration of the preparation steps of SAM on a gold substrate. The purple symbols represent the molecules which chemisorb onto the gold surface.

For biphenylthiol family of SAMs: Firstly the 1mM biphenylthiol solutions in CHCl_3 were prepared and stored in an inert N_2 filled atmosphere of a glove box (Jacomex). Next for X-ray spectroscopy and charge transport measurements with GaIn^{E} setup the SAMs were prepared on

commercial gold (111) evaporated on mica substrates (Georg Albert PVD, Germany) with Au thickness of 300 nm. The substrates were immersed and incubated in the corresponding 1mM biphenyl thiol solution under N₂ atmosphere for 24 h to obtain the desired monolayers. For work function and contact angle experiments, 50 nm Au were evaporated on glass slides with an adhesion Cr layer of 10 nm at a base pressure of $\sim 10^{-6}$ mbar in a Plassys MEB 300 thermal evaporator and then immediately immersed in the respective biphenylthiol solution for 24 h under inert conditions inside the glovebox. For all the experiments, once removed from the thiol solution the substrates were rinsed with generous amount of CHCl₃ in ambient conditions. All the substrates were treated with UV/Ozone prior to immersion in the respective thiol solutions for SAM formation.

For fluorinated azobenzene SAMs with mono and biphenyl substitutions: Solution concentration of fluorinated azobenzene (Fazo) of 10 μ M in chloroform was prepared and stored in a cool dark environment (inside refrigerator).

To form Fazo SAM in *trans* form in the Fazo solution for a period of 24 h in a beaker under standard laboratory conditions (SLC).

To form Fazo SAM in *cis* conformational form, firstly the Fazo solution was irradiated with UV light at the wavelength of 366 nm (8 W intensity) for duration of 120 s, during which due to process of photo-isomerization the Fazo molecules changes the confirmation from *trans* \rightarrow *cis* confirmation (as confirmed by the change in intensity of absorption of the UV/vis spectrum). Then the Au(111) substrate on mica was immediately immersed in the Fazo *cis* solution and stored inside a refrigerator at 4 °C for a period of 24 h to allow the formation of the Fazo SAM in its *cis* isomeric state.

After 24 h once the *trans* and *cis* SAM were formed, were rinsed with the solvent in which the Fazo molecules were dissolved in. Since CHCl₃ was used as the solvent for the Fazo, the Au-Fazo SAM substrates were rinsed with abundant quantity of the same solvent.

4.4 SAM CHARACTERIZATION TECHNIQUES

The electrical characterization of the SAMs were performed by means of a custom built two terminal setup and the structural characterization of the SAMs were performed by means of high

resolution X-ray photoelectron spectroscopy (HRXPS) and angle-resolved near-edge X-ray absorption fine structure spectroscopy (NEXAFS).

4.4.1 Electrical characterization of SAMs

To estimation of the rate of charge transport through the SAMs on Au electrodes was experimentally performed by means of a two terminal setup which comprised of a eutectic liquid metallic gallium-indium alloy (GaIn^E) which was employed as a top-probe electrode. An airtight digital syringe (Hamilton N cemented needle pst3, 25 μl , with a 90° bevel nozzle edge fitted to a digital dispenser 22S gauge) held an adequate reservoir of GaIn^E which could be manipulated to dispense the alloy in a controlled manner, which was then molded to a conical shaped tip (see Figure 4.4.1). The junction comprising the SAM sandwiched between Au and GaIn^E could be realized very accurately by means of a servo controlled xyz stage (MT3-Z8, THORLABS) via careful approach of the GaIn^E tip. This was accomplished by raising the stage supporting the Au-SAM substrate by means of a DC servo motor controller (T-Cube, THORLABS) interfaced to the supporting platform with an actuator (Z8 actuator, THORLABS) to gently establish contact with the apex of the hanging GaIn^E tip (monitored in real-time using a CCD camera).

To ensure a greater control during approach in the z-axis direction (vertical) and higher versatility of movement in the x-y axes direction (lateral) we kept the position of the syringe holding the GaIn^E tip fixed, thereby only moving the stage supporting the sample. The complete setup of the setup is shown in Figure 4.4.1.

The entire setup was placed on a bulky concrete stage free from minute vibrations and housed in a custom made Faraday cage to provide electrostatic shielding and triaxial cables were used to minimize signal losses. The necessary potentials across the junctions were provided by an external supply unit Keithley 2635 source measure unit interfaced through a 2600-ALG-2 (Keithley instruments Inc) cable to minimize signal losses.

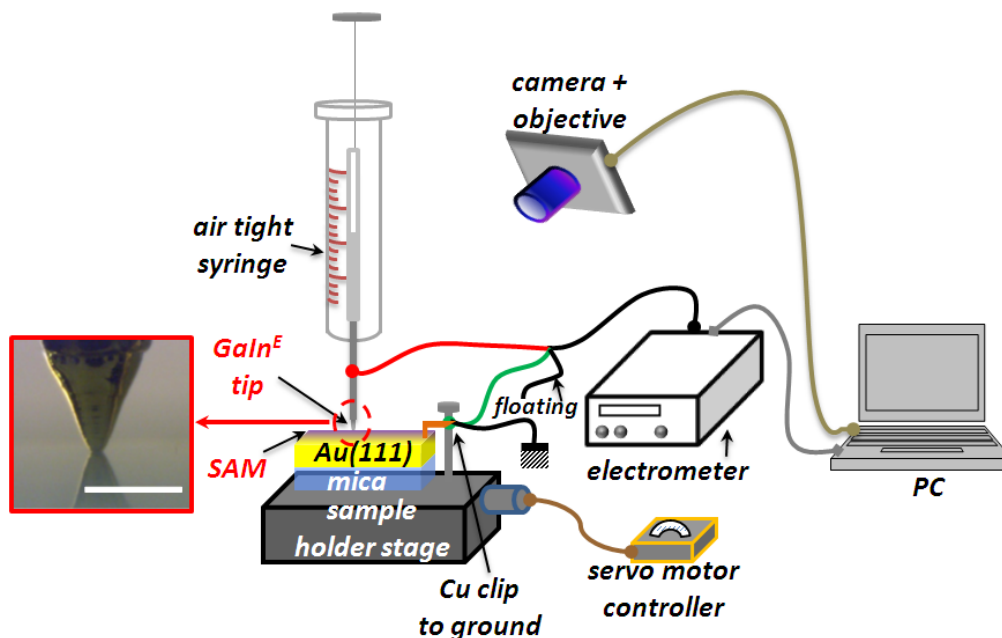


Figure 4.4.1 Two terminal setup with GaIn^E as the top probe electrode along with the biasing configuration. The inset shows the image of the conical shaped GaIn^E tip employed to contact the tail of the SAM, white bar is lateral scale of 100 μm .

In particular, a DC bias was applied to the GaIn^E tip while holding the Au electrode in electrical ground. Current vs. potential (I - V) traces were recorded by applying potential sweep across the junction from $-0.5\text{ V} \rightarrow +0.5\text{ V}$ (unidirectional trace) or starting from -0.5 V proceeding to $+0.5\text{ V}$ ending at -0.5 V for the case of a bidirectional trace (see Appendix) in 20 mV steps. The measured I values were translated into a corresponding current density (J) by normalizing to the junction contact area.

The area in contact with the GaIn^E tip was estimated from the image captured using a USB camera and calibrating that to a sample of known thickness. The procedure for contact area estimation followed these steps, a cross sectional side view image of a substrate with standard thickness (IPMS Fraunhofer) or the external diameter of the syringe was captured and the corresponding number in pixels was estimated for this thickness. From this the distance value for an individual pixel was extracted, as a way to calibrate our optical system. Images were captured for each junction formed and then the total number of pixels estimated in the region of tip contact using ImageJ 1.42q (an open source software). The number of pixels was then retranslated into distance in μm , corresponding to the diameter for the junctions when GaIn^E tip

established contact with the SAM. This diameter was then used to estimate the contact area using a standard formula for the area of a circle. It has previously been shown that the actual area of the GaIn^{E} tip in contact with an ITO surface is roughly 25% of the actual area,¹ this is probably due to the formation of micromenisci² at the sides of the liquid metallic GaIn^{E} tip apex, hence to arrive at an accurate consensus of the current density for the a given applied bias in the sweep voltage range we measured a large number of J - V traces, in ‘ n ’ junctions.

GaIn^{E} tip formation: An appropriated quantity of liquid metallic gallium-indium was administered by adjusting the plunger to form a hanging droplet in the edge of the air tight digital syringe (Hamilton N cemented needle pst3, volume 25 μl , Gauge 22S).

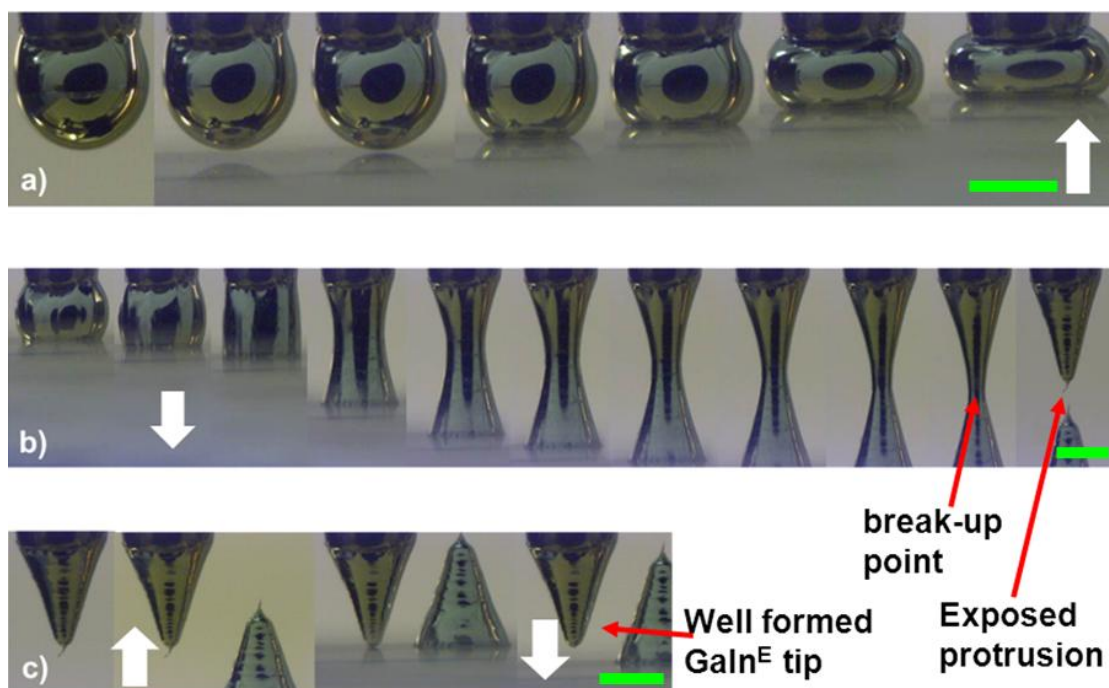


Figure 4.4.2 The complete sequence of GaIn^{E} tip formation illustrating the stages of (a) approach and compression. (b) Retreat and drag. (c) Cropping of extended protrusion. White arrows indicate the direction of movement of the sample holder stage and green bar represents scale of 500 μm .

For forming the conical shaped tip we followed the following three basic steps Figure 4.4.2 (a-c)),

(i) Approach and compress: A sample comprising of a pristine Au on mica was used as a substrate to adhere and stick to the liquid GaIn^{E} was raised carefully on a motorized platform

until it reached the hanging GaIn^E droplet. Once the Au surface established contact with the GaIn^E the sample platform was further raised until it compressed the GaIn^E droplet roughly until the hemisphere shape was reached (Figure 4.4.2a).

(ii) Retreat and drag: After the stage of attainment hemisphere GaIn^E shape the motorized support stage was retreated during which the quantity of GaIn^E which got adhered to the surface got dragged until it reached the break-up point. Upon further downward movement of the stage results in a distinct top and bottom conically shaped tip with a small protrusion.

(iii) Crop and trim: The protrusion extending from the conical tip then needed to be removed, this was done by approach until adequate contact just to extent until the protrusion distance is compressed and then the stage is pull down which leaves a freshly formed conical shaped tip.

The entire tip formation sequence takes ~30 – 40 s. It necessitates that the shape of the conical tip are well-defined which makes the estimate of area for the junctions formed more precise.

4.4.2 Structural characterization of SAMs

For the biphenylthiol family of SAMs HRXPS and NEXAFS characterization methods were employed to shed light into quality of the SAMs on Au(111) according to the following conditions,

X-ray spectroscopy measurements: The structural characterization of the SAMs was performed by means of synchrotron-based HRXPS and NEXAFS spectroscopy. The HRXPS and NEXAFS spectroscopy experiments were performed at the bending magnet HE-SGM beamline at the synchrotron storage ring BESSY II in Berlin, Germany. The measurements were carried out under room temperature and ultra-high vacuum (UHV) conditions with a base pressure of at least 1.5×10^{-9} mbar or higher. High precaution was exercised by selecting the time for spectral acquisition such that no noticeable sample damage by the primary X-rays was observed during the measurements.³⁻⁵ The spectra were recorded in normal emission geometry. C 1s, S 2p, and Au 4f HRXPS spectra were acquired at photon energies (PEs) of 350 and 580 eV. The O 1s spectral range was monitored and the binding energy (BE) scale was referenced to the position of the Au 4f_{7/2} emission line of Au substrate comprising a SAM of dodecanethiol at 83.95 eV energy value

which is given by the latest ISO standard.⁶ The energy resolution was ~ 0.3 eV at a PE of 350 eV. The resulting HRXPS spectra was fitted by symmetric Voigt functions of either a Shirley-type or linear background, the fits were performed self-consistently (i.e., the same peak parameters were used in identical regions of the spectrum) which resulted in the spectrum accuracy for the BE at FWHM values in the range of 0.05 eV. In the case of the S $2p_{3/2,1/2}$ doublets we used a pair of peaks with the same FWHM, a branching ratio of 2 ($2p_{3/2}/2p_{1/2}$), and a spin-orbit splitting verified by the fit of ~ 1.18 eV.⁷

The NEXAFS spectra were acquired at C K-edge in partial electron yield mode with a retarding voltage of -150 V and linearly polarized light with a polarization factor of $\sim 91\%$. To gather details of the orientational order of the SAMs the angle of the incident light was varied from 90° to 20° in steps of 10° - 20° which corresponds to progression of the E vector from the surface normal to the plane close to the sample surface.⁸ The energy resolution of the spectra was ~ 0.3 eV. The raw NEXAFS spectrum of each sample was normalized by dividing by the incident photon flux for a clean gold reference sample⁹ and the energy scale was gauged to the most pronounced π^* resonance of highly oriented pyrolytic graphite at 285.38 eV.¹⁰

4.5 REFERENCES

- 1 Nijhuis, C. A., Reus, W. F. & Whitesides, G. M. Molecular Rectification in Metal–SAM–Metal Oxide–Metal Junctions. *J Am Chem Soc* **131**, 17814-17827, (2009).
- 2 Timsit, R. S. The True Area of Contact at a Liquid Metal-Solid Interface. *Appl Phys Lett* **40**, 379-381 (1982).
- 3 Jäger, B. *et al.* X-ray and Low Energy Electron Induced Damage in Alkanethiolate Monolayers on Au-substrates. *Z. Phys. Chem.* **202**, 263-272, (1997).
- 4 Wirde, M., Gelius, U., Dunbar, T. & Allara, D. L. Modification of self-assembled monolayers of alkanethiols on gold by ionizing radiation. *Nucl. Instrum. Methods Phys. Res., Sect. B* **131**, 245-251, (1997).
- 5 Zharnikov, M. & Grunze, M. Modification of thiol-derived self-assembling monolayers by electron and x-ray irradiation: Scientific and lithographic aspects. *J Vac Sci Technol B* **20**, 1793-1807 (2002).
- 6 X-ray photoelectron spectrometers-Calibration of the energy scales. *ISO 15472 Surface chemical analysis* (2001).
- 7 Azzam, W., Wehner, B. I., Fischer, R. A., Terfort, A. & Wöll, C. Bonding and orientation in self-assembled monolayers of oligophenyldithiols on Au substrates. *Langmuir* **18**, 7766-7769 (2002).
- 8 Stöhr, J. *NEXAFS spectroscopy*. (Springer-Verlag, 1992).
- 9 Frey, S. *et al.* Structure of Thioaromatic Self-Assembled Monolayers on Gold and Silver. *Langmuir* **17**, 2408-2415, (2001).
- 10 Batson, P. E. Carbon 1s near-edge-absorption fine structure in graphite. *Phys Rev B* **48**, 2608-2610 (1993).

No problem can withstand the assault of sustained thinking.

-François-Marie Arouet Voltaire (1694-1778), Philosopher

5 Organic Field- Effect Transistors

5.1 DIELECTRIC MOLECULAR WEIGHT INFLUENCE IN AMBIPOLAR F8BT OFETS

Gate dielectrics in organic field-effect transistors play a vital role in governing the overall performance of the device since the charge transport channel is formed in the active layer of the device at the interface with the dielectric. To effectively modulate the transistor function dielectric surface modification offers a viable and highly feasible strategy. In this part we discuss the influence of varying the dielectric molecular weight on the device stability and reliability. The change in the molecular weights induces subtle changes to the surface free energy and polarity, the interplay between these influences charge carrier mobility, trapping and hysteresis. The mechanism of rates of channel current decay upon continuous operation for both hole and electron carriers are discussed according the bipolaron trapping model.

5.1.1 Scope

Research in the development of Organic thin-film transistors (OTFTs) has attracted considerable interest in the past two decades owing to distinctive advantages such as reduced fabrication complexity, significantly lower manufacturing costs and thus paving a way towards potential applications in flexible large area electronics,^{1,2} radio-frequency identification (RFID) tags³ and e-paper.⁴ Traditionally SiO₂ had been used as the dielectric of choice in the OTFTs since it has high dielectric breakdown strength and is less prone to gate leakage currents i.e., current flowing from the gate electrode upon polarization of the dielectric layer under the influence of an electrical field between the gate and source electrodes. However for the realization of transistors on light-weight flexible substrates, polymeric dielectrics are a better alternative which can nearly match the SiO₂ in terms of leakage losses.⁵ Polymeric dielectrics offer further benefits of easy deposition, solution processability, variable surface adhesion/wetting properties, higher range of dielectric constants and surface free energies. The surface roughness of the dielectric has been shown to affect the overall device performance,⁶ the surface chemistry has been shown to

influence the densities of traps in OTFTs,⁷ the polymer tacticity has been shown to influence the gate leakage,⁸ the surface glass transition temperature which affects the polymer chain motion⁹ and surface free energy of the polymeric dielectrics has been shown to influence charge carrier mobilities in vapor deposited organic semiconductors.^{7,10-12}

Since the conductance, mobility, and switching capability of the transistor is governed by the carrier channel formed in the semiconductor layer at the interface with the dielectric,¹³⁻¹⁵ the surface properties of the dielectric play a vital role in the outcome of the device function.^{14,16,17} Until now there is no systematic study in the literature on the stability and reliability of top gate TFTs based on solution deposited semiconductor-dielectric films to the best of our knowledge. To understand the influence of transistor performance by varying molecular weights of the polymeric dielectric layer in OTFT, in this article we consider two different polymeric dielectrics poly(methyl methacrylate) (PMMA) and polystyrene (PS) of low, medium and higher molecular weights (M_w) casted from solution on an organic semiconductor in a top-gate bottom-contact (TGBC) device layout (Figure 5.1.1). PMMA and PS were chosen as dielectrics since the chemical structural variation between the aromatic styrene and aliphatic methyl methacrylate units induces different degree of surface polarity, and more particularly the dielectric constants (k) of 3.6 and 2.6 respectively for these two dielectrics was not too different, hence we could characterize and compare quantitatively the parameters affecting the transistor performance, stability and reliability.

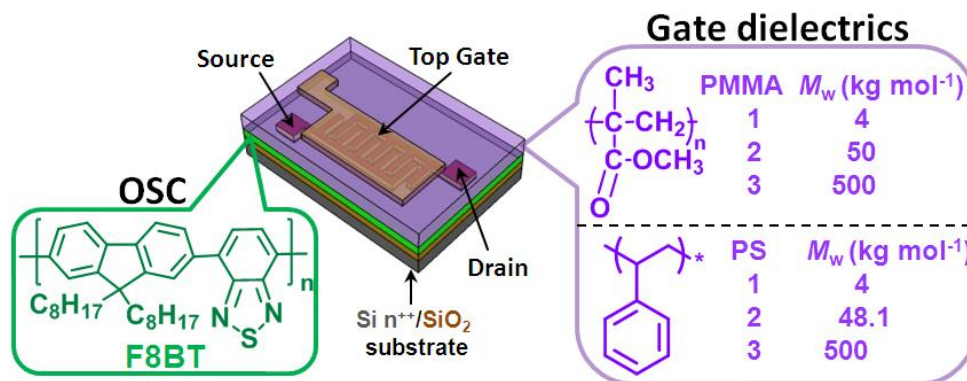


Figure 5.1.1 OFET layout and the chemical structures of the semiconductor and different M_w of the dielectric incorporated in the device.

For this report we will denote PMMA1, PS1 for low, PMMA2 and PS2 for medium and PMMA3, PS3 for higher M_w respectively. Charge carrier mobility improvement for a P3HT based device was observed while changing the molecular weight of the organic semiconductor,¹⁸ which was attributed to the better packing of the regioregular semiconductor, hence changing the M_w of the active layer in the device offers a pathway to tune device performance. We aimed to study if by changing the M_w of the dielectric layer in the device the overall device efficiency could be improved. The use of two polymeric dielectrics of different dielectric constants spanning a wider range of molecular weights allowed us to probe the dependence of charge carrier transport with variable surface free energy caused by the change in molecular weight. Moreover employing polymeric dielectrics minimizes permanent irreversible deep trapping of either electron or hole carriers on application of an gate electric field, in particular electron-traps caused by hydroxyl radical terminated (-OH) groups in silicon oxide layer.^{19,20} The TGBC architecture offers reduced contact resistance (vide infra) due to staggered as opposed to coplanar configuration,²¹ better encapsulation of the underlying organic semiconducting layer which is more sensitive to doping on exposure to environmental conditions and the electrodes, evades footprint i.e., interpenetration of metal atoms caused by thermal deposition of source-drain metallic contacts on top of the insulating/semiconducting layer, enables deposition of semiconductor/dielectric layer by means of orthogonal solvents without swelling/intermixing and increases device channel length scalability.²² We demonstrate that changing the surface energy of the gate dielectric by means of varying the intrinsic molecular weight of the polymeric dielectric induces changes in the electrical properties of an ambipolar TFT (electron and hole

conducting) comprised of a solution deposited semiconductor and has a profound effect on the device stability operating under continual dynamic bias stress.

5.1.2 Dielectric surface properties

The surface free energy of the polymeric dielectrics and organic semiconductor was estimated from the Owens and Wendt method.²³

The contact angle for Millipore water, ethylene glycol and dimethyl sulfoxide (DMSO) was first measured on the thin films of polymer dielectrics or organic semiconductor spin casted from solution on Si/SiO₂ substrates by means of a Krüss DSA100 (Drop shape analysis system) goniometer. The resulting contact angle values were utilized in the equation 1 to estimate the dispersive and polar components, from which the resulting sum of the dispersive and polar components gave the total surface free energy of the organic semiconductor (F8BT) and the polymeric dielectric (PMMA and PS) films.

$$\frac{\sigma_L(1 + \cos\theta)}{2\sqrt{\sigma_L^D}} = \sqrt{\sigma_S^P} \frac{\sqrt{\sigma_L^P}}{\sqrt{\sigma_L^D}} + \sqrt{\sigma_S^D} \quad (1)$$

Note that the equation 1 is of the form $y = mx + c$ (the equation of a straight line) hence from the Figure 5.1.2 the polar component of the solid surface energy i.e., the component due to dipolar can be estimated the slope of the line and dispersive component can be extracted from the intercept with the y-axis. The total surface free energy of the thin films can be estimated by taking the sum of dispersive and polar components (Table 5.1-1).

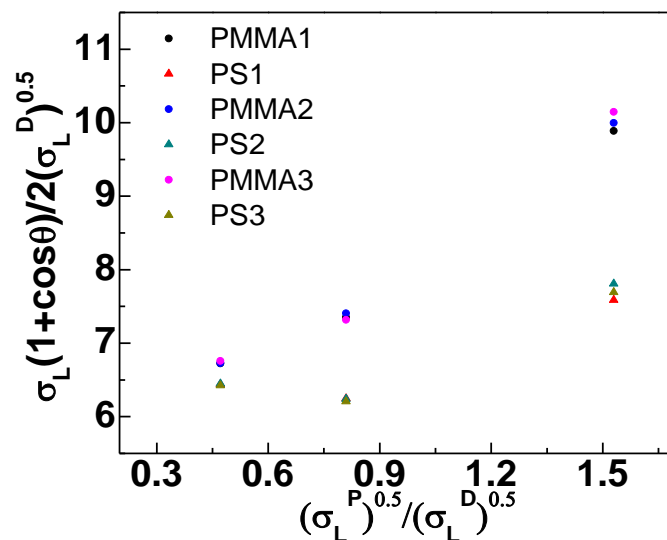


Figure 5.1.2 Plot of contact angle of the three different solvents with the surface of the polymeric dielectrics and the ratio the square root of the polar and dispersive components.

Table 5.1-1 Film surface wettability properties of polymeric dielectrics and organic semiconductor employed in this study

Film surface	$\theta_{a,water} \pm sd$ (°)	$\theta_{a,MEG} \pm sd$ (°)	$\theta_{a,DMSO} \pm sd$ (°)	σ_s^D (mJ/m ²)	σ_s^P (mJ/m ²)	γ_e (mJ/m ²)	χ_p
PMMA1	74.4 ± 0.4	49.5 ± 0.1	33.6 ± 1.1	26.1	9.5	35.53	0.27
PMMA2	73.6 ± 1.1	48.6 ± 0.4	33.4 ± 0.1	25.8	10.0	35.80	0.28
PMMA3	72.5 ± 0.6	50.1 ± 0.1	32.5 ± 0.1	24.7	11.0	35.67	0.31
PS1	91.5 ± 0.7	66.3 ± 0.1	40.8 ± 3.6	31.7	1.4	33.17	0.04
PS2	89.9 ± 1.1	66.4 ± 0.4	40.7 ± 0.1	30.2	2.0	32.24	0.06
PS3	90.8 ± 0.6	66.9 ± 0.5	41.3 ± 0.8	30.5	1.8	32.28	0.06
F8BT	97.4 ± 4.9	73.8 ± 0.6	65.7 ± 1.5	19.8	2.3	22.18	0.11

The surface wettability nature with water, ethylene glycol and DMSO as solvents were recorded from which the surface energy and corresponding surface polarity were estimated using the mean θ_a values by employing Owens and Wendt method.

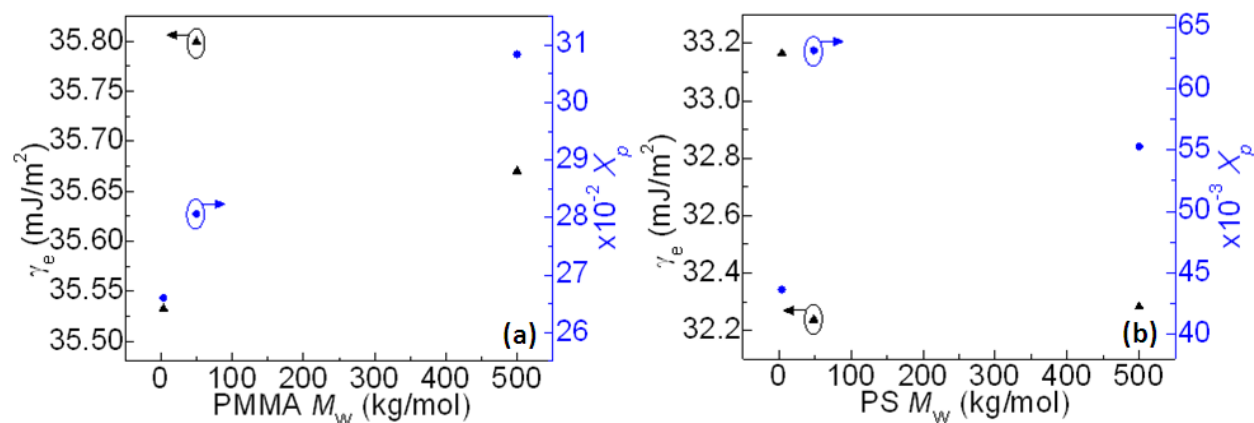


Figure 5.1.3 Estimated surface energy and surface polarity for (a) PMMA and (b) PS films at different M_w

The insets of Figure 5.1.4 portrays the images of the static aqueous contact angle ($\theta_{a,water}$) on the surface of the dielectrics of various M_w . Note that the surface polarity of PS is much lower than the PMMA.

5.1.3 Morphological characterization

The morphology of the PMMA and PS for all the different molecular weights exhibited amorphous nature (Figure 5.1.4 a-f). Table 5.1-2 collects the root mean square roughness of the spin coated thin polymeric dielectric and the F8BT films.

Table 5.1-2 Root mean square roughness values of dielectric and semiconductor film surface.

Film surface	R_{RMS} (nm)
PMMA1	0.37
PMMA2	0.36
PMMA3	0.41
PS1	0.34
PS2	0.35
PS3	0.31
F8BT	0.41

For the PMMA and PS dielectrics the RMS roughness was estimated from an area of $2 \times 2 \mu\text{m}^2$ while it was $1 \times 1 \mu\text{m}^2$ F8BT film.

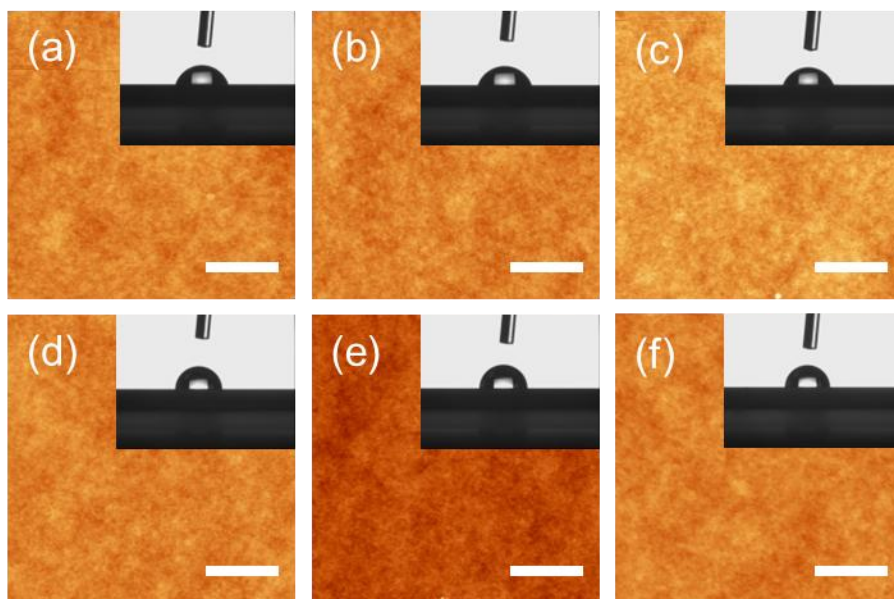


Figure 5.1.4 $2 \times 2 \mu\text{m}^2$ TM-AFM height images of polymer dielectric films (a) PMMA1, (b) PMMA2, (c) PMMA3, (d) PS1, (e) PS2, and (f) PS3. White scale bar represents 500 nm and Z height scale is 8.93 nm. The inset shows the optical images of the static aqueous contact angle on the dielectric surface.

The morphology of the F8BT film as shown in Figure 5.1.5 exhibits small grain like nanocrystalline domains surrounded by amorphous parts.

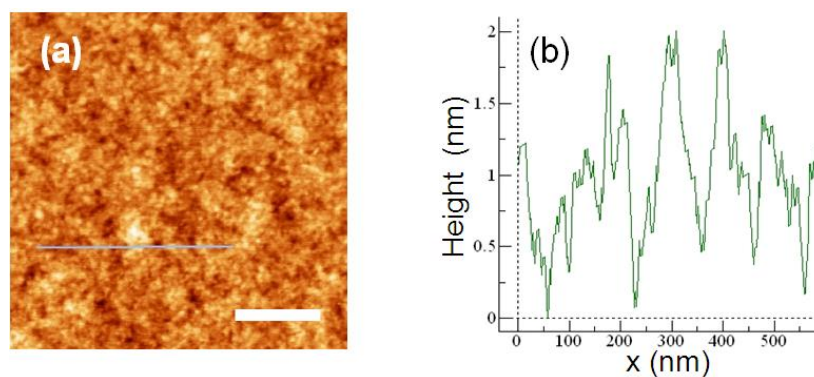


Figure 5.1.5 (a) $1 \times 1 \mu\text{m}^2$ area, height image of spin casted F8BT film on Si/SiO₂ substrate, Z scale is 3.5 nm and white bar denotes a scale of 250 nm. (b) Height profile image of the selected gray line.

5.1.4 Electrode-Semiconductor interfacial energetics

The work function of the gold electrode modified by undecanethiol SAM and the ionization energy level of F8BT as recorded by means of UPS is shown in Figure 5.1.6.

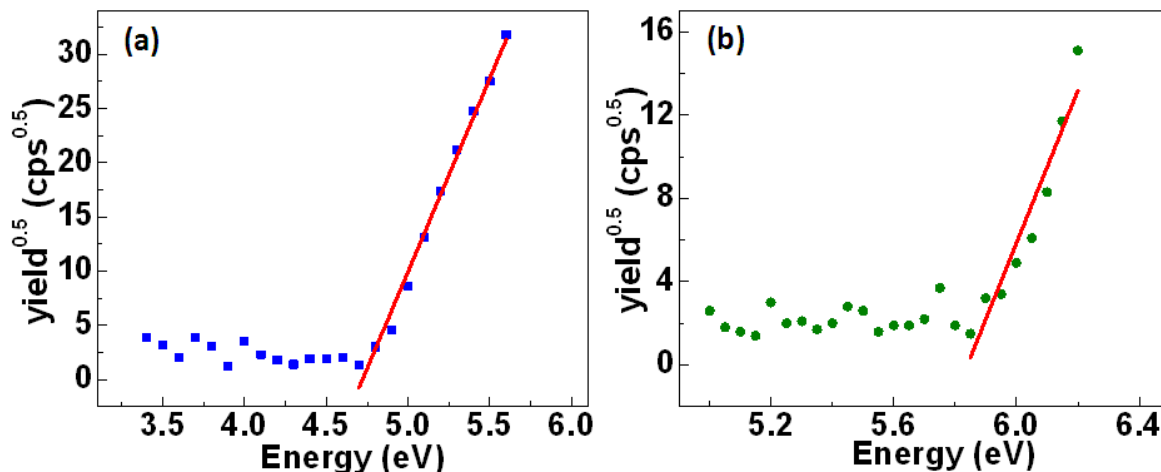


Figure 5.1.6 (a) Work function of evaporated Au film estimated from the threshold energy after which the photoelectron yield starts to increase from the ground energy state. (b) Ionization energy of drop casted F8BT film estimated from the ratio of square root of photoelectron yield as a function of energy.

As the active layer of the device we employed conjugated block copolymer Poly((9,9-di-*n*-octylfluorenyl-2,7-diyl)-*alt*-(benzo[2,1,3]thiadiazole-4,8-diyl)) (F8BT), which has a relatively high electron affinity (EA) level of 3.3 eV and has previously been used in organic field effect transistors,^{24,25} organic light emitting transistors (OLETs)²⁶ and in organic blend photovoltaics (OPVs) for enhancing electron transport.²⁷⁻²⁹

The ionization energy of F8BT is 5.9 eV is high, hence by collectively incorporating Au contacts to serve as electrodes, functionalized with a thiol to form a self-assembled monolayer (SAM) we were able to align the energetic levels of the electrodes favorably close to the middle of the HOMO-LUMO band gap of this semiconductor³⁰ (Figure 5.1.7). The work function of the Au ($\Phi_{\text{Au}} \sim 4.8$ eV) source-drain electrodes were lowered by treating with 1-undecanethiol (C_{11}), this resulted in shifting the Φ_{Au} to 4.4 eV ($\Delta\Phi \sim 0.4$ eV) due to the molecular dipole induced by the SAM at the Au- $\text{SC}_{11}\text{H}_{23}$ interface.³¹

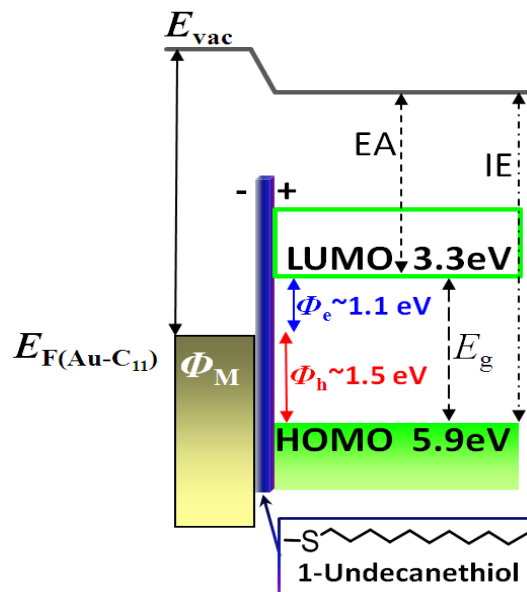


Figure 5.1.7 Schematic of the interface of the electrode and the 1-undecanethiol SAM showing Φ_h the hole injection barrier i.e., the energy gap between the HOMO level of the organic semiconductor and the Fermi level (E_F) of the electrode modified by the SAM and Φ_e denoting the electron injection barrier which is the energy gap between the LUMO level of the organic semiconductor and the Fermi level of the metal electrode.

The lower $\Phi_{Au/C_{11}}$ promotes better electron carrier injection due to the reduction of the electron injection barrier ($\Phi_e \sim 1.1$ eV) but simultaneously this increases the hole injection barrier ($\Phi_h \sim 1.5$ eV) which may reduce hole carrier injection, nevertheless the $\Delta\Phi_{Au}$ ensures attainment of more balanced mobilities for both charge carriers. The coating of the gold source-drain electrodes with the undecanethiol introduces a contact resistivity of ~ 942.7 M Ω cm. Top gate transistors were fabricated on Si/SiO₂ substrates (Figure 5.1.1) after cleaning the substrates firstly gold source-drain electrodes were evaporated followed by functionalization of the electrodes with 1-undecane thiol and coating a hexamethyldisilazane (HMDS) primer to improve surface wettability by the formation of a more hydrophobic ($\theta_a \sim 89.9^\circ$) capping layer and to minimize electron charge trapping groups.²⁰ The subsequent deposition of semiconducting layer and respective dielectrics casted from solution in the same order was finally completed by evaporating Au top contact which served as the gate electrode.

The deposition of the organic semiconductor (F8BT) first on the substrate was crucial since it addresses some key issues such as i) elimination of intermixing in the semiconductor/dielectric

interface, ii) having a common bottom layer of uniform surface morphology and geometric roughness (root mean square roughness, R_{RMS}) allowed us to tune the properties in the interface only by varying the top lying dielectric film, iii) the surface free energy of the active layer is the same for all the semiconductor/dielectric combinations, iv) a film with constant surface polarity and v) identical surface wetting nature, with a aqueous contact angle of $\sim 97.4 \pm 4.9^\circ$.

Essentially for the F8BT film the $R_{\text{RMS}} \sim 0.4$ nm and surface energy ($\gamma_e \sim 22.2$ mJ/m²) remained the same for all semiconductor/dielectric combinations, since the semiconductor was deposited first followed by the dielectric layer on top. Table 5.1-1 collects the contact angle for different probe liquids, surface energies, polar and dispersive components along with the surface polarity of the semiconductor and dielectric films deposited on Si/SiO₂ substrates. The surface polarity (χ_p) defined as the ratio of polar component to total surface free energy,³² gives an estimate of the polar nature of the surface of the bulk due to surface dipoles and hydrogen bonding.

5.1.5 Standard OFET electrical characterization

The transfer characteristics (I_D vs. V_{GS}) for devices under n and p-channel operation is shown (Figure 5.1.8) for devices based on PMMA and PS dielectrics of all molecular weights investigated in this study. The threshold voltage (V_T) was estimated from the slope and x-axis intercept (V_{GS}) of the $\sqrt{I_D}$ vs. V_{GS} plot and carrier mobility (μ_{sat}) in the saturation regime was calculated using the standard equations for TFTs (see equation 2.18).³³

Table 5.1-3 shows the figures of merit which was estimated from the electrical characterization of the TFTs. The electron and hole mobility (μ_{e^-} and μ_{h^+}) F8BT TFTs showed a marked dependence on k of the polymeric gate dielectric.

Table 5.1-3 Figures of merit indicating overall performance of devices

Polymer dielectric	M_w (kg mol ⁻¹)	$\mu_{e^-} \pm \sigma \times 10^{-5}$ (cm ² /Vs)	$V_{T,e^-} \pm \sigma$ (V)	$V_{on,e^-} \pm \sigma$ (V)	$\mu_{h^+} \pm \sigma \times 10^{-5}$ (cm ² /Vs)	$V_{T,h^+} \pm \sigma$ (V)	$V_{on,h^+} \pm \sigma$ (V)
PMMA1	4	2.5 ± 0.8	24.2 ± 5.6	27.5 ± 9.8	3.0 ± 0.9	-38.9 ± 6.4	-41.5 ± 8.1
PMMA2	50	3.5 ± 1.7	28.6 ± 1.0	36 ± 5.2	4.3 ± 2.9	-31.7 ± 5.3	-36 ± 4.9
PMMA3	500	3.5 ± 0.6	33.5 ± 4.0	38.7 ± 4.6	4.8 ± 2.4	-35.1 ± 9.4	-38 ± 7.2
PS1	4	10.1 ± 9.5	34.7 ± 16.2	52 ± 2.8	89.4 ± 37.4	-42.7 ± 3.9	-37 ± 9.9
PS2	48.1	14.5 ± 14.3	41.9 ± 3.4	39 ± 2.6	38.8 ± 32.8	-42.2 ± 6.0	-28 ± 4
PS3	500	6.9 ± 2.8	39.8 ± 4.3	40 ± 9.1	37.2 ± 22.5	-33.4 ± 6.9	-28.5 ± 10.1

Parameters extracted from the saturation regime in the transfer characteristics, I_D vs. V_{GS} for devices with channel length, $L = 80\mu\text{m}$ and channel width, W of 10 mm.

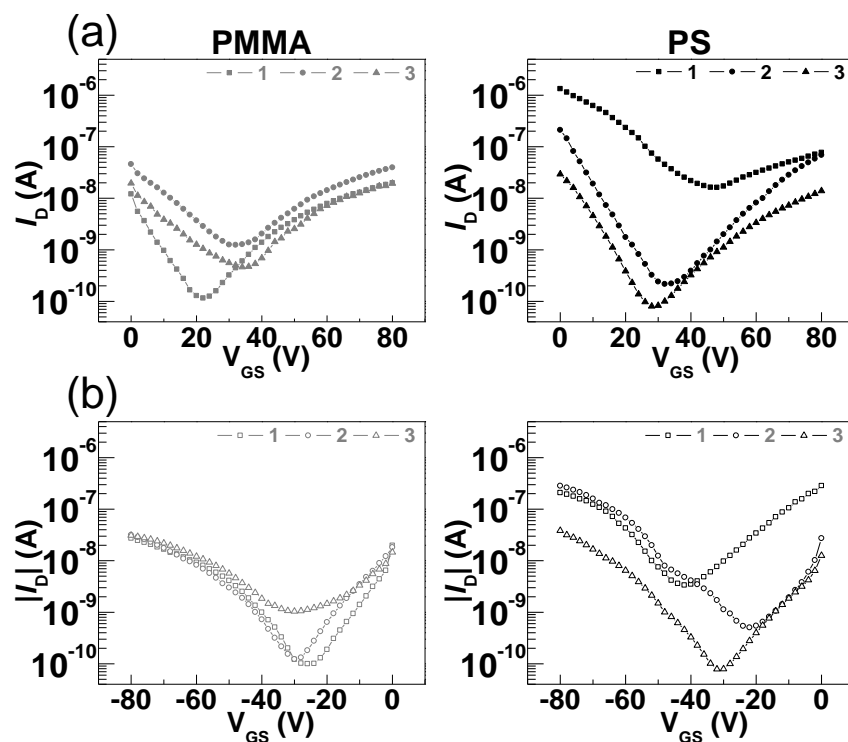


Figure 5.1.8 Measured transfer characteristics plotted in semi-log I_D vs. V_{GS} plots for devices based on PMMA and PS dielectrics having (a) electrons as the majority carrier ($V_{GS} \leq 0V$), and (b) holes as the majority carrier ($V_{GS} \geq 0V$) in OTFT operation. A constant V_{DS} of ± 60 V was applied pertaining to the respective carrier type while recording the drain current.

The output characteristics (I_D vs. V_{DS}) for a transistor comprising of PMMA1 dielectric is portrayed in Figure 5.1.9.

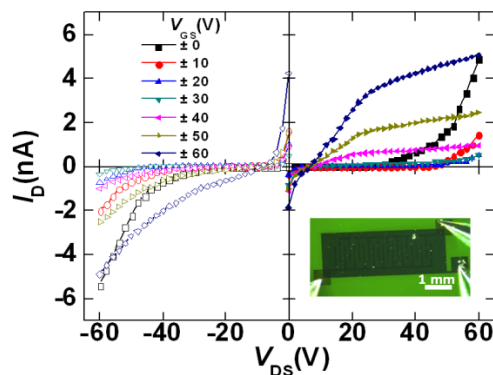


Figure 5.1.9 Measured output characteristics for a transistor of channel length 80 μm , comprising PMMA1 as the dielectric. The first and third quadrants show the n-channel (filled symbols) and p-channel (empty symbols) characteristics respectively. Inset shows the image of a transistor with the probes in contact with the electrodes.

The charge transport in the OTFT occurs in few nanometers in the organic semiconductor-dielectric interface.^{13,15} Hence the surface properties of the dielectric layer at the interface with the active layer would certainly affect the field-effect carrier mobility. We observed an increase in μ_{e-} and μ_{h+} by a factor of ~ 1.5 for devices based on PMMA dielectrics going from low to the highest M_w , this observed increase in carrier mobility is likely to the corresponding increase in the surface energy of PMMA. For devices based on PS dielectrics the μ_{e-} increased by a factor of ~ 1.4 and decreased by a factor of ~ 1.5 when the M_w changed from low to medium and low to highest respectively while the μ_{h+} was ca. 2.3 greater for the lowest M_w compared to the medium and the high. The surface energy variation also likely affects the devices with PS dielectrics more particularly for the lower M_w . The μ_{e-} increased by a factor of ~ 4 , ~ 6 and ~ 2 when k of the gate dielectric decreased from 3.6 to 2.6 for the M_w of 4, ~ 50 and 500 kg mol^{-1} respectively. The μ_{h+} was more sensitive to the decreasing k from PMMA (3.6) to PS (2.6), exhibiting a ~ 30 , ~ 9 and ~ 8 fold increase with for the devices with the low, medium and higher M_w of the corresponding dielectrics respectively. It was shown that for an amorphous p-type polymer, PTAA the μ_{h+} decreased nearly by a factor of 20 with the increase in k from 2.0 to 3.6, this was attributed to the broadening of the density of states (DOS) of the semiconductor³⁴ at the interface with the dielectric due to the static dipolar disorder. For an electron transporting P(NDI2OD-T2) based TFT it was shown that the charge mobility was showed a weak dependence on the k of the dielectric,³⁵ this was reasoned by the effective decoupling of the conjugated NDI-T2 core from the surface of the dielectric due to the branched 2-octyldodecyl chains linked to the core by a

separation distance upwards of 1 nm from the surface of the dielectric. A recent study showed using scanning transmission X-ray microscopy (STXM) a comprehensive account of the molecular order and orientation of polycrystalline F8BT films.³⁶

The predominantly amorphous F8BT films in our devices most likely would have the π -conjugated core stacked closer to the dielectric of the surface ~ 0.8 to <1 nm (see Figure 5.1.10). A theoretical model developed by Richards *et al.* explains the implications of static dipolar disorder of the polymer dielectric on the DOS of the semiconductor, it was concluded from that study the energetic disorder in the semiconductor was strongly influenced by the distance from the semiconductor/dielectric interface,³⁷ this was in good agreement with experimental results for PTAA based TFTs.

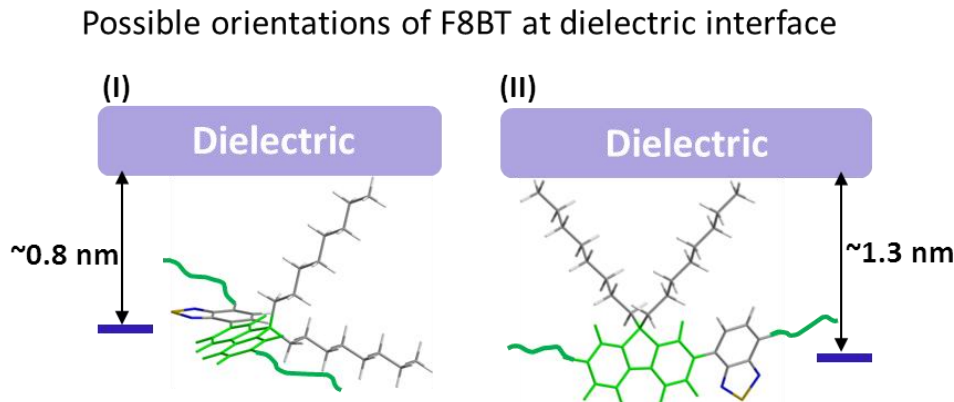


Figure 5.1.10 Possible orientations of the semiconductor π -conjugated core lying on the interface with the polymeric dielectric layer.

The charge transport in OTFT is highly localized and particularly confined in semiconductor layer at the region of close proximity to the boundary with the dielectric (usually ~ 1 nm).³⁸ In F8BT based devices the profound influence of k on μ is probably due the lower distance of separation (<1 nm) of the conjugated core in the surface of the dielectric. The difference between hole and electron carrier mobility due to the variation in the M_w of the dielectrics is likely due to the different regions in which the charge is localized in the semiconductor molecule. For instance, the electron withdrawing benzodiazole unit in the π -conjugated core of F8BT promotes high electron accretion and localization in the HOMO whereas the electron can occupy the entire core in the unoccupied state and thus the interaction of the molecules at the interface of the

dielectric is apparently different for both electron carriers and holes, since difference in the surface polarity of the dielectrics causes variation of localized states for both electrons and hole.

Shown in Figure 5.1.11 a, b are the V_T and turn-on voltage (V_{ON}) for several devices comprised of PMMA and PS dielectrics with varying M_w under n-type and p-type operation respectively. It was observed that the V_{on} and V_T for the TFTs in general lowered by a small magnitude for hole (p-type) and exhibited the opposite trend for electron (n-type) carrier transport with increasing molecular weights of both the polymeric dielectrics.

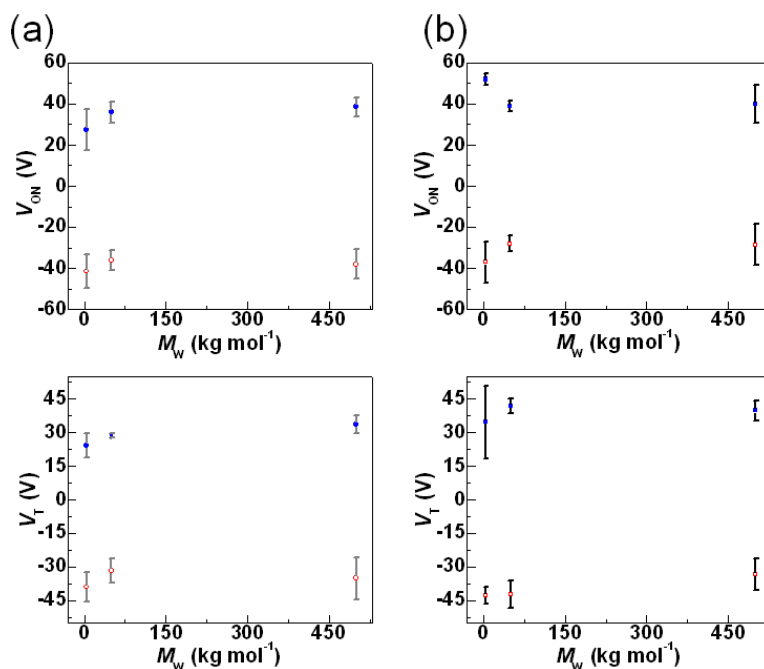


Figure 5.1.11 Comparison of (a) V_{ON} and V_T for PMMA based (circular symbols) devices with (b) V_{ON} and V_T for PS (square symbols) based OTFTs at different corresponding M_w range. Blue and red symbol colors indicate corresponding values for devices operating in n and p-channel modes respectively.

We believe this subtle variation in the both V_T and V_{on} is due to the surface polarity variations of the polymeric dielectrics when going from low to higher molecular weights. The surface polarity is strongly influenced polar component of the surface free energy (see section 5.1.2) of the dielectric film surface which in turn can be tuned by changing the molecular weights of the polymer dielectric films. It is interesting to note that the V_T increased by a factor of ~ 1.4 for devices comprising of PS dielectrics compared to PMMA based ones, this factor of increase in

the V_T is due to the ratio of the permittivity of the higher k PMMA dielectric with PS, under the assumption that the charge accumulated in the channel is equal for both dielectrics.

5.1.6 Effect of gate bias dependent hysteresis in TFTs

One of the key parameters which governs the reliability of transistor operation is the influence of hysteresis and trapping of charges thereof which might occur at the semiconductor/dielectric interface.^{39,40} Although controlled hysteresis effect has been exploited for potential applications in nonvolatile memory components,⁴¹ this effect hinders device operational efficiency particularly inducing significant shifts in the threshold voltage.

The hysteresis arises due to the filling up of deep trapped states⁶ or due to the rearrangement of mobile ions accumulations (H^+ and OH^-) due to moisture trapped at the semiconductor-dielectric interface. To elucidate the effect of hysteresis in our ambipolar transistors we swept the gate electrode starting from 0 V \rightarrow +80 V in the forward I_D - V_{GS} trace (Figure 5.1.12a) immediately followed by +80 V \rightarrow 0 V in the reverse trace for the device operating in n-type mode and from 0 V \rightarrow -80 V in the forward I_D - V_{GS} trace (Figure 5.1.12b) immediately followed by -80 V \rightarrow 0 V in the reverse trace for probing p-type channel operation.

Table 5.1-4 summarizes the hysteresis parameters obtained for the OTFTs. All the tested devices regardless of the dielectric employed operating in the n-channel mode exhibited clockwise hysteresis, where the reverse gate potential sweep causes a more positive offset in the gate bias for recording the similar magnitude of I_D . Whereas in the case of p-channel mode anticlockwise hysteresis was observed, this is due to a more negative shift during the backward trace of the gate potential required to measure an equivalent I_D value in the forward sweep.

The shift in the gate bias (ΔV_{GS}) between the forward and reverse I_D - V_{GS} trace at a particular I_D of 1 nA for devices based on PMMA dielectrics was by a factor of ~ 2 greater for hole conduction compared to electron. Similarly the ΔV_{GS} for devices incorporating PS dielectrics at an I_D of 10 nA was nearly twice for the hole than the electron carriers.

Table 5.1-4 Hysteresis parameters for the devices extracted from the transfer characteristic I_D vs. V_{GS} plots, for devices with channel length, $L = 80 \mu\text{m}$ and channel width, W of 10 mm .

Polymer dielectric	M_w (kg mol ⁻¹)	$\Delta V_{G,e-} \pm \sigma$ (V)	$V_{\text{off-on},e-} \pm \sigma$ (V)	S_{e-} (V/dec)	$N_{\text{traps},e-}^{\text{max}}$ $\times 10^{-13}$ (cm ⁻²)	$\Delta V_{G,h+} \pm \sigma$ (V)	$V_{\text{off-on},h+} \pm \sigma$ (V)	S_{h+} (V/dec)	$N_{\text{traps},h+}^{\text{max}}$ $\times 10^{-13}$ (cm ⁻²)
PMMA1	4	5.7 ± 0.6	4.7 ± 3.1	10.3	2.92	8.7 ± 1.1	-6.0 ± 2.0	10.2	2.88
PMMA2	50	5.0 ± 1.1	4.0 ± 2.3	11.6	3.44	9.3 ± 3.2	-5.3 ± 2.3	11.2	3.33
PMMA3	500	4.3 ± 2.5	4.0 ± 6.9	11.1	3.10	8.3 ± 4.1	-4.7 ± 9.9	11.1	3.09
PS1	4	8.0 ± 4.8	0.0 ± 3.0	9.4	1.83	13.0 ± 3.0	-4.0 ± 3.0	9.7	1.84
PS2	48.1	2.3 ± 1.5	-2.0 ± 6.3	10.0	2.25	5.3 ± 1.0	-8.0 ± 7.4	9.9	2.32
PS3	500	3.3 ± 2.6	2.0 ± 3.6	10.2	2.19	4.5 ± 0.6	2.0 ± 3.7	10.4	2.08

ΔV_{GS} is collected at 1 nA and 10 nA for devices based on PMMA and PS polymeric dielectrics.

The difference in the ΔV_{GS} for the electrons and holes can be attributed to the interplay of the differences in the localization of the electronic charge in the conjugated core of F8BT molecule and its interaction at the dielectric interface along with the energetic mismatch between the charge injecting/extracting electrodes with the HOMO/LUMO levels of the semiconductor.

The offset between the V_{ON} and the V_{OFF} (this is referred to the gate potential at which the majority carriers in the channel gets completely depleted and the current due to transport of minority carriers commence) give vital clues about the hysteresis behavior in the transistor, wherein the larger the offset the greater the hysteresis effect and vice versa. The mean V_{OFF-ON} exhibits a lesser offset which implies that the temporarily trapped majority charges in the channel at the interface with the dielectric is released with a relatively lower potential lag for the higher M_w dielectric compared to the lowest one. The smaller V_{OFF-ON} observed for the devices with higher M_w dielectrics are likely due to the increase of the surface polarity of the dielectric layer going from low via medium to higher M_w at the semiconductor interface, wherein the more polar surface leads to greater disorder and traps.

The origin of the hysteresis effect in our devices are believed to be due to a combination of factors such as slow polarization of the dielectric, trapping of charges in exponential tail states, slower release of the trapped charges at the semiconductor/dielectric interface, and intrinsic defects in the active layer.

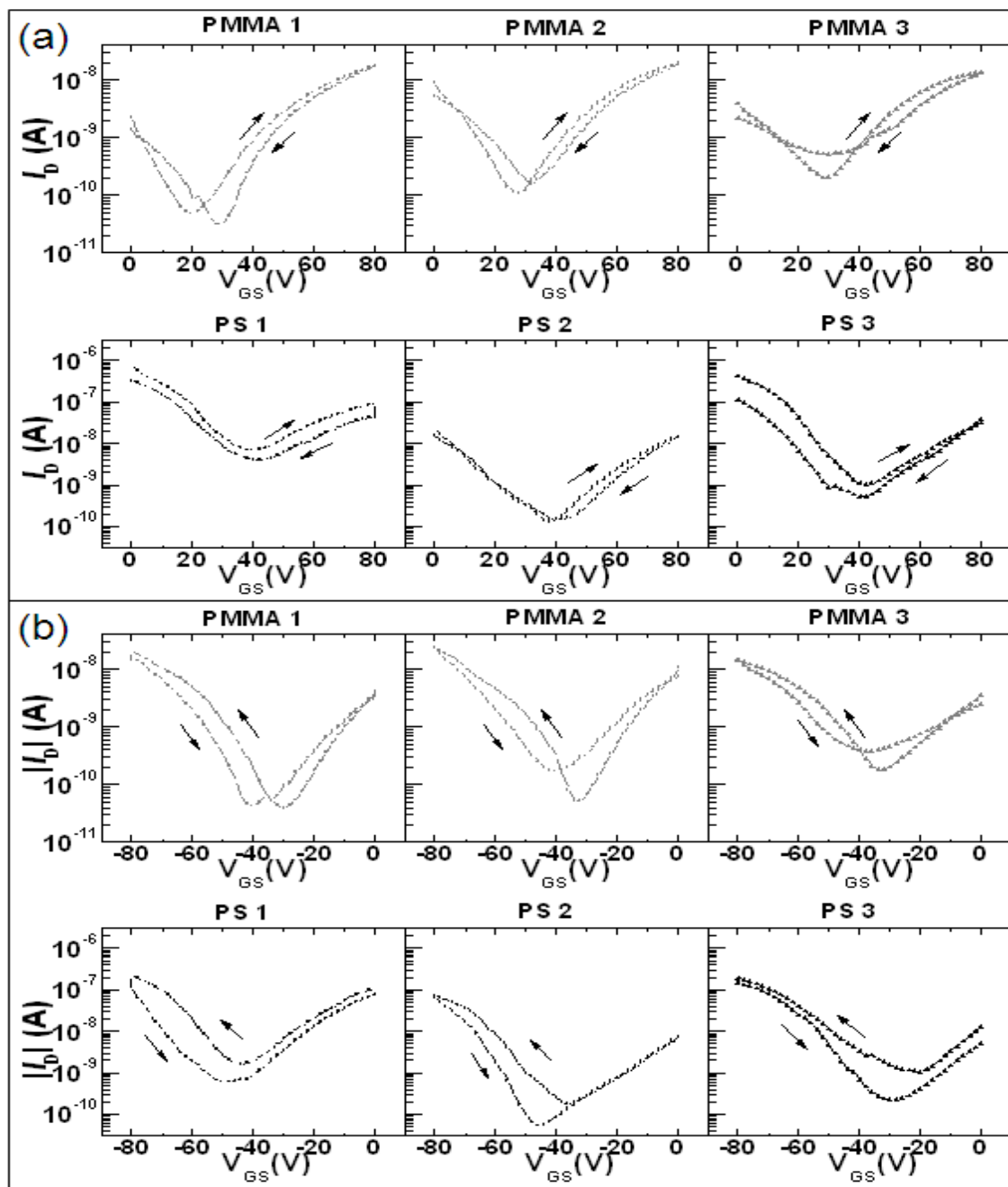


Figure 5.1.12 Measured transfer characteristic curves indicating forward and reverse I_D vs. V_{GS} traces for (a) n-type channel (top panel) and (b) p-type channel (bottom panel) for transistors based on each of the respective dielectrics. The drain voltage was held at +60 V and -60 V for electron and hole carrier channels respectively. PMMA and PS based device characteristics are explicitly represented by gray and black lines and symbols respectively. The arrows represent the direction of the V_{GS} sweep.

There is some evidence in literature that suggests TGBC transistors based on F8BT show hysteresis behavior.^{26,42} Since the devices with both set of dielectrics regardless of M_w or carrier type exhibited hysteresis, we believe defects in the F8BT film such as grain boundaries and heterogeneous distribution of nanocrystalline/amorphous domains in the channel (see morphology of the film as imaged with AFM in Figure 5.1.5) contributes significantly to this effect by acting as trap states.

The trapping of charges independent of energy is supposed to originate at the bulk typically due to the grain boundaries and are termed as deep traps (N_{bulk}) and interfacial traps (N_{its}) i.e., traps formed in semiconductor/dielectric interface. The amount of the trapped charges can be calculated using subthreshold slope (S) which is extracted from the semi-log plots of I_D vs. V_{GS} (Figure 5.1.8). The subthreshold slope (eq 5.1.2) with units of Volts/decade, gives the measure of transistor switching capacity from off to on state when I_D rises linearly until it reaches threshold.⁴³

$$S = \left[\frac{d(\log I_D)}{dV_{\text{GS}}} \right]^{-1} \quad (5.1.2)$$

It is interesting to note that the subthreshold slope for the devices with PMMA dielectrics was ~ 1 V/dec greater than that of PS based dielectrics, which supports the fact that it necessitates lesser gate potential for the device comprised of the lower k PS dielectric to cause a raise in drain current magnitude by a decade. The higher subthreshold slope observed for the PMMA based devices is likely due to the greater dipolar disorder and the surface polarity modifications which is nearly 5 fold higher for the PMMA films than PS at all M_w which in turn introduces additional trap states at channel/dielectric interface.³⁴

The relationship between N_{bulk} and N_{its} with subthreshold swing can be written in the form as shown in eq 5.1.3 and in its simplified form (eq 5.1.4).^{44,45}

$$S = \frac{K_B T (\log_{10} e)^{-1}}{q} \left[1 + \frac{q}{C_i} \left(\sqrt{\varepsilon_s N_{\text{bulk}}} + q N_{\text{its}} \right) \right] \quad (5.1.3)$$

$$S = \frac{K_B T (\log_{10} e^1)^{-1}}{q} \left[1 + \frac{q^2}{C_i} N_{traps} \right] \quad (5.1.4)$$

From which N_{traps} , the maximum number of traps is derived as shown in eq 5.1.5

$$N_{traps} = \frac{C_i}{q} \left[\frac{qS \log e}{K_B T} - 1 \right] \quad (5.1.5)$$

Where q is the elementary charge, K_B is Boltzmann's constant, T is temperature with unit of Kelvin, C_i is the capacitance of the dielectric and e is the base of natural logarithm (\ln) and ϵ_s is the permittivity of the semiconductor. Using eq 5.1.4 we estimated the total trap densities for all our transistors (Figure 5.1.13). The maximum number of traps for devices comprising of PS based dielectrics tended to trap charges by a factor of $\sim <1.5$ than devices based on PMMA dielectrics. We believe this is due to the lesser dipolar disorder for the lower k PS dielectric at interface with the semiconductor compared with the higher k PMMA dielectric based devices,³⁴ this is further confirmed by the higher χ_p for the devices comprising of PMMA dielectrics by a factor of ~ 5 greater than the PS based devices (see Table 5.1-1).

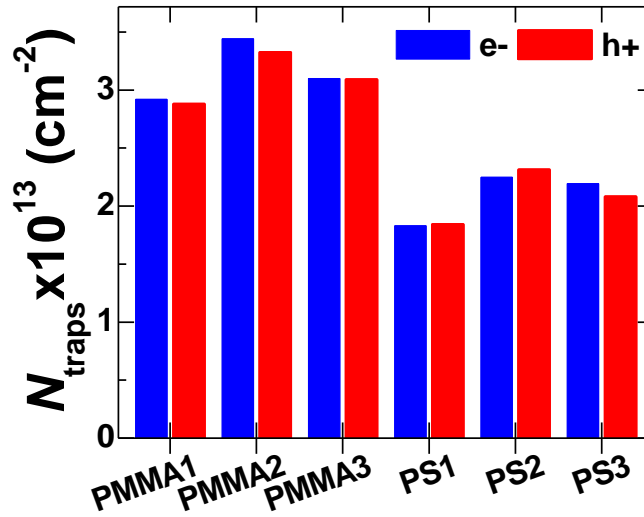


Figure 5.1.13 Bar chart showing the maximum number of traps for devices based on PMMA and PS dielectrics of various M_w . Electron traps are represented by blue bars while hole traps are indicated by red bars.

On close inspection of Figure 5.1.12 the hysteresis for devices with electron carriers are universally smaller than the hole carriers for devices with both PMMA and PS dielectrics, this can be attributed to the smaller injection/extraction barrier for electrons than holes.

5.1.7 TFT switching capacity and instability under dynamic bias stress influence

To unravel the consequences of dynamic bias stress, which is the electrical field dependent stress induced by the repeated polarization effects of gate dielectric on the device channel during continuous operation while the transistor was cycled from “OFF” to “ON” and back to “OFF” states,⁴⁶ a suitable reversible cyclic gate potential trace was dispensed. This was accomplished by the application of a gate voltage sweep from below subthreshold to above threshold regime immediately followed in the reverse polarity potential sweep direction which was repeated for ‘*n*’ number of cycles.⁴⁷ For all the F8BT/polymer dielectric combination of TFTs we applied a sweep potential to the gate electrode for 20 consecutive cycles each in the sequence of 0 V → +80 V → 0 V while transport of electrons was probed followed by 0 V → -80 V → 0 V while transport of hole was the majority charge carrier respectively and the I_D was recorded at intervals of ± 2 V with keeping a constant bias of ± 60 V at the drain depending on the corresponding carrier type. To avoid any photo doping of the device these measurements were performed in the dark.

The maximum drain current ($I_{D,max}$) taken at $V_{GS} = \pm 80$ V for device comprising of PS2 dielectric is shown in Figure 5.1.14a. The $I_{D,max}$ current from the first cycle 17.7 nA ($V_{ON} \sim 20$ V) reduced to 14.6 nA (-18%, $V_{ON} \sim 30$ V) in the 20th cycle while electron conduction and 13 nA ($V_{ON} \sim -36$ V) reduced to 2.4 nA (-81%, $V_{ON} \sim -52$ V) during hole conduction for the device with PMMA1 dielectric. Similarly the $I_{D,max}$ current from the first cycle 25.6 nA ($V_{on} \sim 26$ V) reduced to 22.4 nA (-12%, $V_{ON} \sim 24$ V) in the 20th cycle while electron conduction and 21.9 nA ($V_{ON} \sim -32$ V) reduced to 4.1 nA (-82%, $V_{ON} \sim -42$ V) during hole conduction and the $I_{D,max}$ current from the first cycle 22.6 nA ($V_{ON} \sim 28$ V) reduced to 19.5 nA (-14%, $V_{ON} \sim 36$ V) in the 20th cycle while electron conduction and 5 nA ($V_{ON} \sim -34$ V) reduced to 0.3 nA (-95%, $V_{ON} \sim -50$ V) during hole conduction for the devices with PMMA2 and PMMA3 dielectrics respectively.

Table 5.1-5 TFT performance indicators under dynamic bias stress effects.

Polymer gate dielectric	$V_{on}^{1^{st}}$ (V) ^a	$V_{on}^{20^{th}}$ (V) ^b	S 1 st (V/dec) ^c	S 20 th (V/dec) ^d	ΔS (V/dec) ^e	$I_{D,max}^{1^{st}}$ x10 ⁻⁸ (A) ^f	$I_{D,max}^{20^{th}}$ x10 ⁻⁸ (A) ^g	$\Delta I_{D,max}^{1^{st}}$ / $I_{D,max}^{1^{st}}$ % ^h	$I_{on}/I_{off}^{1^{st}}$ ⁱ	$I_{on}/I_{off}^{20^{th}}$ ^j	$\Delta I_{on}/I_{off}$ % ^k
<i>Electrons as majority carriers (n-channel transistor operation)</i>											
PMMA1	20	30	10.6	11.7	1.1	1.8	1.5	-17.84	2	5	150.0
PMMA2	26	24	10.3	12.2	1.9	2.6	2.2	-12.46	2	4	100.0
PMMA3	28	36	10.4	11.6	1.1	2.3	1.9	-13.91	3	4	33.3
PS1	24	16	9.2	9.6	0.4	17.5	14.5	-17.17	2	3	50.0
PS2	40	48	10.1	10.2	0.1	1.4	1.2	-18.62	2	2	0.0
PS3	50	56	9.7	9.9	0.1	1.5	1.1	-27.47	2	2	0.0
<i>Holes as majority carriers (p-channel transistor operation)</i>											
PMMA1	-36	-52	10.5	11.6	1.1	-1.30	-0.24	-81.4	2	5	150
PMMA2	-32	-42	10.0	12.0	2.0	-2.19	-0.40	-81.5	2	4	100
PMMA3	-34	-50	11.0	12.3	1.3	-0.50	-0.03	-94.7	2	2	0
PS1	-30	-24	8.6	9.7	1.1	-62.40	-19.98	-68.0	2	3	50
PS2	-42	-56	10.2	10.5	0.3	-5.18	-0.97	-81.3	2	2	0
PS3	-54	-60	10.2	10.9	0.7	-0.85	-0.05	-94.4	2	2	0

Ambipolar switching operation parameters extracted from forward and reverse I_D - V_{GS} traces with V_{DS} held at ± 60 V, ^a V_{on} at 1st cycle. ^b V_{on} at 20th cycle. ^c Subthreshold slope in 1st cycle. ^d S in 20th cycle. ^e Change in S. ^f $I_{D,max}$ 1st cycle collected when $V_{GS} = 80$ V for electron ($V_{GS} = -80$ V for hole). ^g $I_{D,max}$ 20th cycle collected when $V_{GS} = 80$ V for electron ($V_{GS} = -80$ V for hole). ^h Change in $I_{D,max}$ from 1st to 20th switching cycle collected when $V_{GS} = 80$ V for electron ($V_{GS} = -80$ V for hole). ⁱ I_{on}/I_{off} at 1st cycle. ^j I_{on}/I_{off} at 20th cycle. ^k Change in I_{on}/I_{off} from 1st to 20th switching cycle.

It was observed also for the devices based on PS dielectrics, the $I_{D,max}$ current from the first cycle 0.18 μ A ($V_{ON} \sim 24$ V) reduced to 0.15 μ A (-17%, $V_{ON} \sim 16$ V) in the 20th cycle while electron conduction and 0.62 μ A ($V_{ON} \sim -30$ V) reduced to 0.2 μ A (-68%, $V_{ON} \sim -24$ V) during hole conduction, the $I_{D,max}$ current from the first cycle 14.5 nA ($V_{ON} \sim 40$ V) reduced to 11.8 nA (-19%, $V_{ON} \sim 48$ V) in the 20th cycle while electron conduction and 51.8 nA ($V_{ON} \sim -42$ V) reduced to 9.7 nA (-81%, $V_{ON} \sim -56$ V) during hole conduction and the $I_{D,max}$ current from the first cycle 14.9 nA ($V_{ON} \sim 50$ V) reduced to 10.8 nA (-27%, $V_{ON} \sim 56$ V) in the 20th cycle while electron conduction and 8.5 nA ($V_{ON} \sim -54$ V) reduced to 0.48 nA (-94%, $V_{ON} \sim -60$ V) during hole conduction for the devices with from the lower to the higher molecular weights of polymer dielectric respectively.

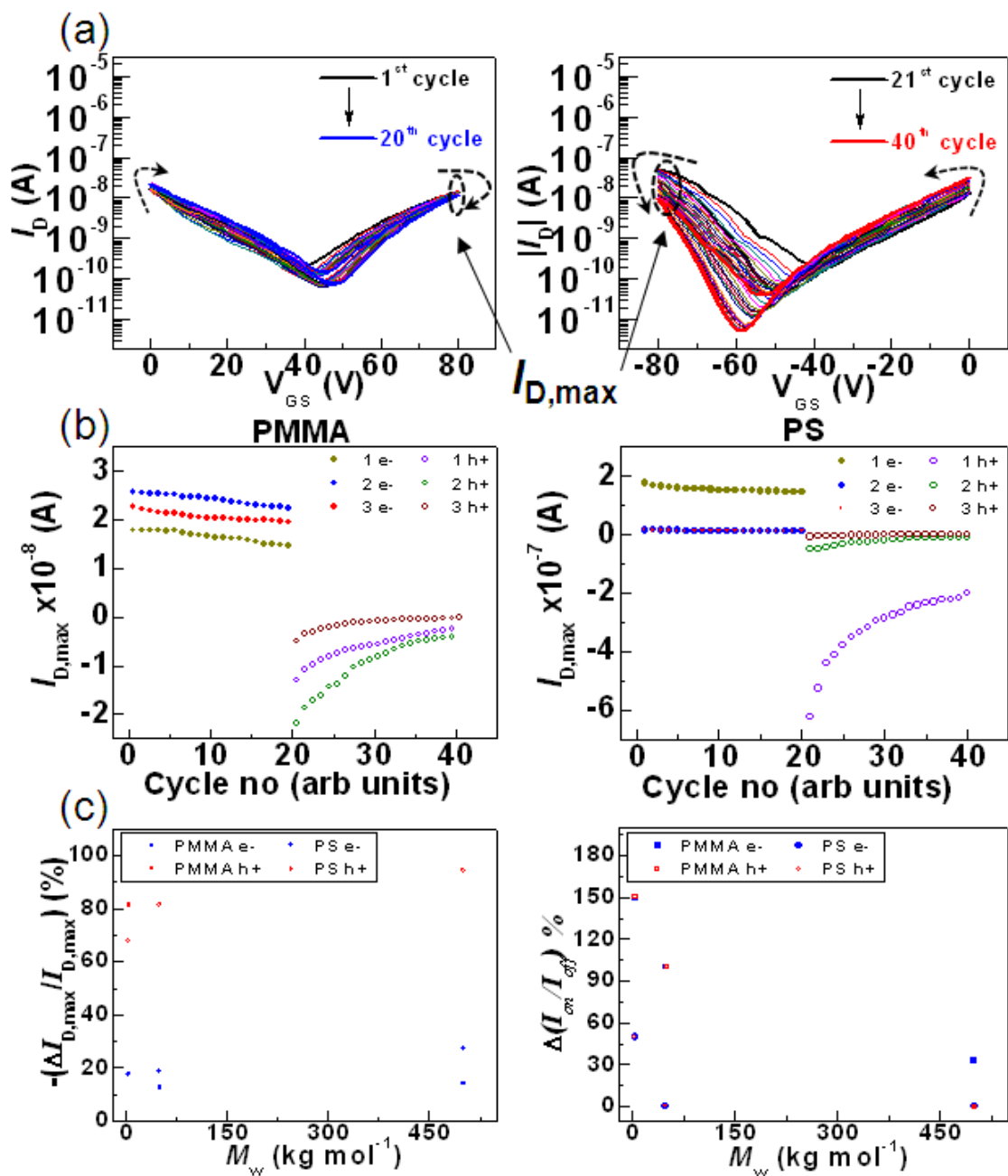


Figure 5.14 (a) Transfer characteristics (semi-log I_D vs. V_{GS} plots) of device based on PS2 dielectric indicating 20 cycles for both n-type (left panel) and p-type (right panel) operation, the V_{DS} was fixed at ± 60 V depending of the majority carrier. (b) $I_{D,max}$ progression over the complete switching cycles for TFTs based on PMMA and PS dielectrics represented with filled circles for electron and empty circles for hole carriers respectively. (c) Variation of $I_{D,max}$ in the left panel and I_{on}/I_{off} in the right panel from the 1st to 20th cycle for tested devices represented with filled blue symbols for electron and empty red symbols for hole carriers.

Note that majority of the devices with varying M_w of dielectrics exhibited a more positive or negative ΔV_{ON} shift operating in n-channel or p-channel mode respectively with the exception of PS1. The ΔV_{ON} instability over extended cycles of operation is attributed to the slow trapping at the dielectric/semiconductor interface and dielectric surface charging effects.^{6,48} Some carriers become immobile by the initial filling up of shallow trap levels when the gate bias is below the threshold regime and after the critical threshold potential more number of the carriers become mobile as seen by the rise in the I_D (Figure 5.1.14a), when this process is repeated many number of times the evolution of the dielectric polarization effect on the device characteristics becomes apparent. Figure 5.1.14b shows the progression of the maximum current for each cycle of operation for devices based on PMMA and PS dielectrics at all M_w . On close inspection of the change in $I_{D,max}$ with successive cycles there is a clear steady decay of the current, this is likely due to the slow formation of bipolaron electronic states in the F8BT layer.⁴⁹ The major twofold effect of bias stress in polyfluorenes⁵⁰ which causes shifts in V_{ON} and diminution of the current has been proposed to be caused by hole paired bipolarons which self-traps charges.

We believe the primary cause of the decay of the I_D in our devices is due to the formation of bipolaron electron or hole paired states within the F8BT film, since (1) the gradual decay of the current strongly suggests the capture of free carriers in a tightly bound electronic state of poor mobility and (2) irrespective of the dielectric in the device this behavior was persistent. To validate the bias stress effect due to charge trapping according to the bipolaron model,⁵⁰ we plotted the square of the electron concentration (N_e^2) against its corresponding rate of decrease with time (dN_e/dt). The near linear decrement of the carrier concentration with respect to N_e^2 within experimental uncertainties is shown in Figure 5.1.15a for device based PS2 dielectric, gives a good indication that one of the major cause of the bias stress in these devices are due to bipolarons. A similar graph was plotted for the case when the transistor was operating in p-channel mode from which the rate constant for hole carriers was estimated from the slope of the linear least squares fitting of N_h^2 vs. dN_h/dt (Figure 5.1.15b). The respective rate constants for electrons (r_e) and holes (r_h) for a device based on PS2 dielectric was found to be $\sim 1.6 \times 10^{-19}$ cm^2/s and $\sim 2.1 \times 10^{-20}$ cm^2/s .

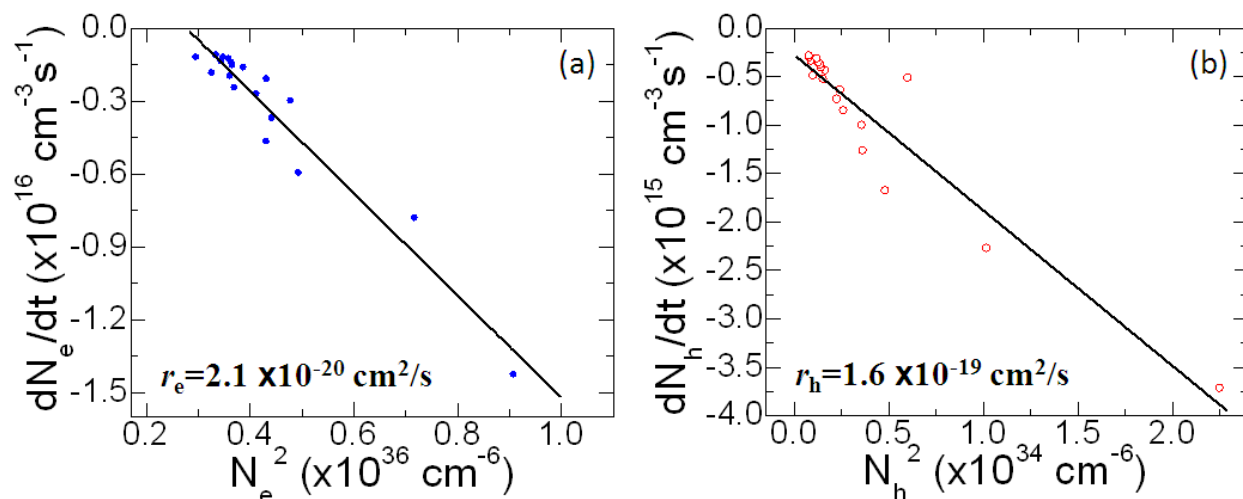


Figure 5.1.15 The rate of decrease of carrier concentration vs. square of the respective carrier concentration measured at varying time illustrated for (a) electrons at a V_{GS} of 60 V and (b) holes at a V_{GS} of -60 V.

On closer observation of the channel current it is apparent that there is a much larger decay of hole current than the electron current for devices comprising of both dielectrics in all M_w scales, this is attributed to the larger rate constant for holes than electrons as estimated for the transistor with PS2 dielectric to be ~ 8 . Note that the current decay in p-channel devices where much greater than n-channel ones, this is believed to be due to (1) larger hole injection barrier to the HOMO than electron injection barrier with the LUMO, and (2) More trapping of holes by bipolaron hole pairs than that of electrons and consequently larger rate constants. It is also likely that upon successive forward-reverse gate potential traces the carrier concentration injected into the channel increases and this can lead to overcharging within the polymer semiconductor⁵¹ resulting in reduction of conductivity.

The variation in I_{on} to I_{off} over several cycles of operation exhibited the opposite trend to $\Delta I_{D,max}$ while increasing the molecular weights of polymer dielectric. In general the $\Delta I_{on}/I_{off}$ lowered or remained constant from the first cycle of operation to the 20th cycle of operation, Figure 6c shows the variation of I_{on}/I_{off} over several cycles of operation for all the molecular weights of both the dielectrics employed in this study. We believe that the improved stability of the I_{on}/I_{off} over continuous switching OTFT operation for devices with comprising of higher molecular weight dielectric is due to the lower densities of the polymeric dielectric chain ends at the surface of the bulk (Figure 5.1.16). Consequently the devices with higher molecular weight dielectrics

are more prone to cause $I_{D,max}$ diminution over successive switching operation we believe this is due to the increase of charge trapping at the semiconductor/dielectric interface on the application of pulse sweep at the gate (see Figure 5.1.13) probably due to the increased dipolar disorder at the interface due to greater surface polarity of the higher M_w dielectrics.

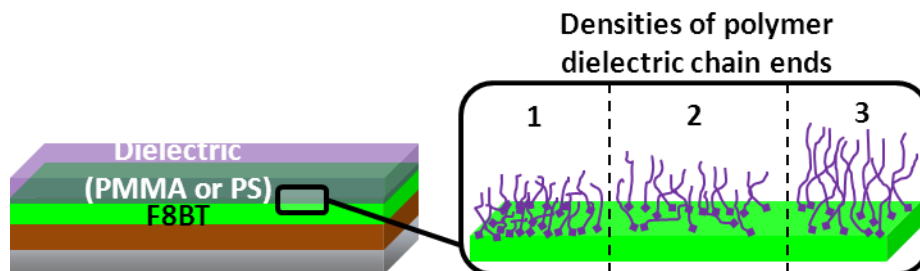


Figure 5.1.16 Schematic of device layout without electrodes illustrating the densities of chain ends of the polymeric dielectric surface at the interface with the semiconductor film.

Table 5.1-5 collects the figures of merit while the devices underwent dynamic bias stress tests. The change in the subthreshold slope (ΔS) from the 1st to the 20th cycle with devices based on PMMA based dielectrics was greater than that of PS based devices by ~ 0.6 V/dec, this is attributed to the greater dipolar disorder of the higher k dielectric³⁴ which causes the broadening of the tail states and hence it necessitates higher gate potential to increase the drain current by one order of magnitude.

The ΔS showed a tendency to reduce toward higher M_w dielectric for PMMA and PS, this is due to the respective variations in the densities of polymer chain ends and surface polarity. Noteworthy feature of incorporating polymeric dielectrics in TFTs is that the effects of dynamic bias stress is not severe compared to the inorganic dielectric particularly SiO_2 , which manifests in much greater shifts in V_{ON} and V_T .⁵²

We probed the dielectric strength under the application of high electric field (see Figure 5.1.17), all dielectrics used in our transistors exhibited fairly good dielectric strength typically exceeding 1MV/cm.

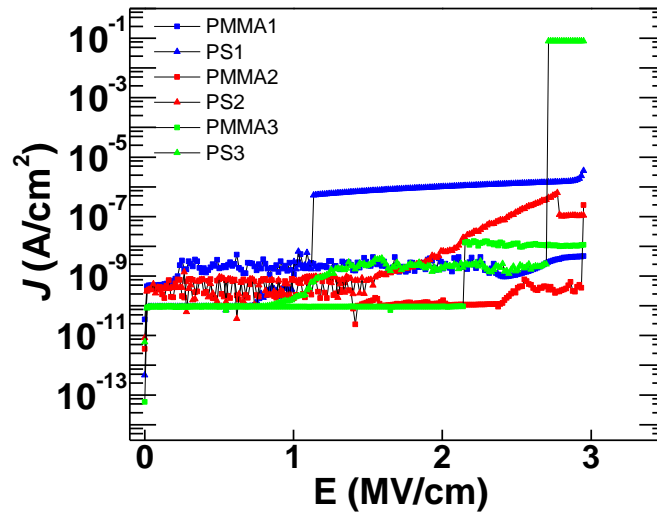


Figure 5.1.17 Plot showing the magnitude of electric field which the polymeric dielectrics could withstand before occurrence of break down.

5.1.8 Conclusions

We have shown that the effect of varying intrinsic molecular weight of the polymer dielectric on the OTFT device performance in a single cycle of operation itself exists due to the subtle variations in the surface energy and polarity. The tuning and modification of the dielectric surface energy and polarity by change of the M_w comes into play by the improvement of device power consumption efficiency manifested by lower threshold voltage required for devices with higher M_w dielectrics. The hysteresis behavior observed in all the TFTs suggests trapping of mobile carriers in shallow tail states. Smaller offsets between the V_{ON} and V_{OFF} was observed for the devices with higher M_w dielectrics which is due to the increase in the surface polarity of PMMA and PS dielectrics going from low to higher M_w and a corresponding increase in trap levels due to the energetic disorder at the semiconductor/dielectric interface. The influence on the device stability particularly under dynamic bias stress was prominent and suggests a bipolaron mechanism as its primary cause. The channel current for device operating in p-channel condition reduced more severely compared to n-channel mode, this observed difference is expected to be due to the greater trapping of hole than electrons as revealed by the estimated respective rate constants. On general in most dielectric M_w the decay of the maximum drain current was larger for devices with higher M_w dielectrics this is attributed to the greater trapping of mobile carriers during continuous operation. However devices with higher molecular weight dielectrics exhibited more stable ratio of I_{on} to I_{off} which is essential for prolonged reliable device operation. In conclusion for prolonged continuous reliable transistor operation it is preferable to incorporate dielectrics of higher M_w .

5.1.9 References

- 1 Forrest, S. R. The path to ubiquitous and low-cost organic electronic appliances on plastic. *Nature* **428**, (2004).
- 2 Huitema, E. *et al.* Plastic transistors in active-matrix displays. *Isscc Dig Tech Pap I* **46**, 380-381 (2003).
- 3 Baude, P. F. *et al.* Pentacene-based radio-frequency identification circuitry. *Appl Phys Lett* **82**, 3964-3966, (2003).
- 4 Rogers, J. A. *et al.* Paper-like electronic displays: Large-area rubber-stamped plastic sheets of electronics and microencapsulated electrophoretic inks. *P Natl Acad Sci USA* **98**, 4835-4840 (2001).
- 5 Roberts, M. E. *et al.* Water-stable organic transistors and their application in chemical and biological sensors. *P Natl Acad Sci USA* **105**, 12134-12139, (2008).
- 6 Knipp, D., Street, R. A., Volkel, A. & Ho, J. Pentacene thin film transistors on inorganic dielectrics: Morphology, structural properties, and electronic transport. *J Appl Phys* **93**, 347-355, (2003).
- 7 Yoon, M. H., Kim, C., Facchetti, A. & Marks, T. J. Gate dielectric chemical structure-organic field-effect transistor performance correlations for electron, hole, and ambipolar organic semiconductors. *J Am Chem Soc* **128**, 12851-12869, (2006).
- 8 Park, J. H., Hwang, D. K., Lee, J., Im, S. & Kim, E. Studies on poly(methyl methacrylate) dielectric layer for field effect transistor: Influence of polymer tacticity. *Thin Solid Films* **515**, 4041-4044, (2007).
- 9 Kim, C., Facchetti, A. & Marks, T. J. Polymer gate dielectric surface viscoelasticity modulates pentacene transistor performance. *Science* **318**, 76-80, (2007).
- 10 Sun, X. *et al.* Interfacial Heterogeneity of Surface Energy in Organic Field-Effect Transistors. *Adv. Mater.* **23**, 1009-1014, (2011).
- 11 Singh, T. B. *et al.* High-Performance Ambipolar Pentacene Organic Field-Effect Transistors on Poly(vinyl alcohol) Organic Gate Dielectric. *Adv. Mater.* **17**, 2315-2320, (2005).
- 12 Yang, S. Y., Shin, K. & Park, C. E. The Effect of Gate-Dielectric Surface Energy on Pentacene Morphology and Organic Field-Effect Transistor Characteristics. *Adv. Funct. Mater.* **15**, 1806-1814, (2005).
- 13 Peng, X. Z., Horowitz, G., Fichou, D. & Garnier, F. All-Organic Thin-Film Transistors Made of Alpha-Sexithienyl Semiconducting and Various Polymeric Insulating Layers. *Appl Phys Lett* **57**, 2013-2015 (1990).
- 14 Horowitz, G., Peng, X. Z., Fichou, D. & Garnier, F. Role of the semiconductor/insulator interface in the characteristics of π -conjugated-oligomer-based thin-film transistors. *Synthetic Metals* **51**, 419-424 (1992).
- 15 Parashkov, R. *et al.* All-organic thin-film transistors made of poly(3-butylthiophene) semiconducting and various polymeric insulating layers. *J Appl Phys* **95**, 1594-1596, (2004).
- 16 Facchetti, A., Yoon, M. H. & Marks, T. J. Gate dielectrics for organic field-effect transistors: new opportunities for organic electronics. *Adv. Mater.* **17**, 1705-1725 (2005).
- 17 Effertz, C. *et al.* Design of Novel Dielectric Surface Modifications for Perylene Thin-Film Transistors. *Adv. Funct. Mater.* (2012).
- 18 Kline, R. J., McGehee, M. D., Kadnikova, E. N., Liu, J. S. & Frechet, J. M. J. Controlling the field-effect mobility of regioregular polythiophene by changing the molecular weight. *Adv. Mater.* **15**, 1519-1522, (2003).
- 19 Nicollian, E. H., Berglund, C. N., Schmidt, P. F. & Andrews, J. M. Electrochemical Charging of Thermal SiO₂ Films by Injected Electron Currents. *J Appl Phys* **42**, 5654-5664, (1971).
- 20 Chua, L. L. *et al.* General observation of n-type field-effect behaviour in organic semiconductors. *Nature* **434**, 194-199, (2005).

- 21 Richards, T. & Sirringhaus, H. Bias-stress induced contact and channel degradation in staggered and coplanar organic field-effect transistors. *Appl Phys Lett* **92**, 023512-023513, (2008).
- 22 Gelinck, G. H. *et al.* Flexible active-matrix displays and shift registers based on solution-processed organic transistors. *Nat Mater* **3**, 106-110, (2004).
- 23 Owens, D. K. & Wendt, R. C. Estimation of the surface free energy of polymers. *J. Appl. Polym. Sci.* **13**, 1741-1747, (1969).
- 24 Zheng, Z. J. *et al.* Uniaxial alignment of liquid-crystalline conjugated polymers by nanoconfinement. *Nano Lett* **7**, 987-992, (2007).
- 25 Kajii, H., Koiwai, K., Hirose, Y. & Ohmori, Y. Top-gate-type ambipolar organic field-effect transistors with indium-tin oxide drain/source electrodes using polyfluorene derivatives. *Org Electron* **11**, 509-513, (2010).
- 26 Zaumseil, J., Donley, C. L., Kim, J. S., Friend, R. H. & Sirringhaus, H. Efficient Top-Gate, Ambipolar, Light-Emitting Field-Effect Transistors Based on a Green-Light-Emitting Polyfluorene. *Adv. Mater.* **18**, 2708-2712, (2006).
- 27 Snaith, H. J., Arias, A. C., Morteani, A. C., Silva, C. & Friend, R. H. Charge Generation Kinetics and Transport Mechanisms in Blended Polyfluorene Photovoltaic Devices. *Nano Lett* **2**, 1353-1357, (2002).
- 28 Kim, Y. *et al.* Effect of electron-transport polymer addition to polymer/fullerene blend solar cells. *Synthetic Metals* **152**, 105-108, (2005).
- 29 Westenhoff, S. *et al.* Charge Recombination in Organic Photovoltaic Devices with High Open-Circuit Voltages. *J Am Chem Soc* **130**, 13653-13658, (2008).
- 30 Cheng, X. *et al.* Controlling Electron and Hole Charge Injection in Ambipolar Organic Field-Effect Transistors by Self-Assembled Monolayers. *Adv. Funct. Mater.* **19**, 2407-2415 (2009).
- 31 de Boer, B., Hadipour, A., Mandoc, M. M., van Woudenberg, T. & Blom, P. W. M. Tuning of Metal Work Functions with Self-Assembled Monolayers. *Adv. Mater.* **17**, 621-625, (2005).
- 32 Kim, J. S., Friend, R. H. & Cacialli, F. Surface energy and polarity of treated indium-tin-oxide anodes for polymer light-emitting diodes studied by contact-angle measurements. *J Appl Phys* **86**, 2774-2778 (1999).
- 33 Horowitz, G. Organic field-effect transistors. *Adv. Mater.* **10**, 365-377 (1998).
- 34 Veres, J., Ogier, S. D., Leeming, S. W., Cupertino, D. C. & Khaffaf, S. M. Low-k insulators as the choice of dielectrics in organic field-effect transistors. *Adv. Funct. Mater.* **13**, 199-204 (2003).
- 35 Yan, H. *et al.* A high-mobility electron-transporting polymer for printed transistors. *Nature* **457**, 679-U671, (2009).
- 36 Watts, B., Schuettfort, T. & McNeill, C. R. Mapping of Domain Orientation and Molecular Order in Polycrystalline Semiconducting Polymer Films with Soft X-Ray Microscopy. *Adv. Funct. Mater.* **21**, 1122-1131, (2011).
- 37 Richards, T., Bird, M. & Sirringhaus, H. A quantitative analytical model for static dipolar disorder broadening of the density of states at organic heterointerfaces. *J Chem Phys* **128**, 234905, (2008).
- 38 Klauk, H. *Organic electronics : materials, manufacturing and applications.* (Wiley-VCH, 2006).
- 39 Singh, T. B. *et al.* Nonvolatile organic field-effect transistor memory element with a polymeric gate electret. *Appl Phys Lett* **85**, 5409-5411 (2004).
- 40 Gu, G., Kane, M. G., Doty, J. E. & Firester, A. H. Electron traps and hysteresis in pentacene-based organic thin-film transistors. *Appl Phys Lett* **87**, (2005).
- 41 Baeg, K.-J., Noh, Y.-Y., Sirringhaus, H. & Kim, D.-Y. Controllable Shifts in Threshold Voltage of Top-Gate Polymer Field-Effect Transistors for Applications in Organic Nano Floating Gate Memory. *Adv. Funct. Mater.* **20**, 224-230, (2010).

- 42 Naber, R., Bird, M. & Sirringhaus, H. A gate dielectric that enables high ambipolar mobilities in polymer light-emitting field-effect transistors. *Appl Phys Lett* **93**, 023301-023303 (2008).
- 43 Sze, S. M. *Physics of semiconductor devices*. 2nd edn, (Wiley, 1981).
- 44 Rolland, A., Richard, J., Kleider, J. P. & Mencaraglia, D. Electrical-Properties of Amorphous-Silicon Transistors and Mis-Devices - Comparative-Study of Top Nitride and Bottom Nitride Configurations. *J Electrochem Soc* **140**, 3679-3683 (1993).
- 45 Kalb, W. L. & Batlogg, B. Calculating the trap density of states in organic field-effect transistors from experiment: A comparison of different methods. *Phys. Rev. B* **81**, 035327 (2010).
- 46 *The OFF and ON states are referred to the conditions when the drain current (I_D) due to the majority carries are minimum and maximum respectively.*
- 47 *The number of I_D vs. V_{GS} forward and reverse traces in this experiment was terminated at 20 cycles each first for the device with n-channel followed by the p-channel. The number of cycles recorded was manipulated by a custom developed software code.*
- 48 Gundlach, D. *et al.* High mobility n-channel organic thin-film transistors and complementary inverters. *J Appl Phys* **98**, 064502-064508 (2005).
- 49 Fung, M. *et al.* Distinct interfaces of poly (9, 9-dioctylfluorene-co-benzothiadiazole) with cesium and calcium as observed by photoemission spectroscopy. *J Appl Phys* **94**, 5763-5770 (2003).
- 50 Street, R., Salleo, A. & Chabinyc, M. Bipolaron mechanism for bias-stress effects in polymer transistors. *Phys. Rev. B* **68**, 085316 (2003).
- 51 Paulsen, B. D. & Frisbie, C. D. Dependence of Conductivity on Charge Density and Electrochemical Potential in Polymer Semiconductors Gated with Ionic Liquids. *J. Phys. Chem. C* **116**, 3132-3141 (2012).
- 52 Salleo, A. & Street, R. A. Light-induced bias stress reversal in polyfluorene thin-film transistors. *J Appl Phys* **94**, 471-479, (2003).

5.2 INTRINSIC CHARGE TRANSPORT IN POLYMERIC SEMICONDUCTOR/PHOTOCHROMIC MOLECULAR BLEND OFETS

In this section the charge transport properties in a bicomponent system comprising of the polymeric semiconductor blended with a photochromic molecule in the active layer of an organic field effect transistor is reported. The focus of this work was to estimate the activation energy, intrinsic mobility and the temperature dependence of field effect transistors based on a photochromic diarylethene (DAE) small molecule embedded in a poly(3-hexylthiophene) (P3HT). The property of diarylethene to undergo transition from a ring opened to closed conformational state upon ultraviolet light irradiation was exploited to probe the properties of the transistor in both these distinct operating bistable modes.

5.2.1 Motivation

While dealing with a system of a blended materials incorporated as the active layer of the device the intrinsic carrier mobility can be significantly affected by parameters such as,

- (i) Morphological orientation of the molecules on the channel,
- (ii) Energetic mismatch in the charge transport levels and the disorder caused thereof in the blend,
- (iii) Substrate wettability, affinity and phase separation effects,
- (iv) Charge localization in the bulk and
- (v) Grain boundaries in the film.

All of the aforementioned properties affect the carrier mobility in some form or another either by selectively enhancing or diminishing the performance of an OFET. To understand what would be intrinsic mobility of the blend in the active layer of the device dependent and independent of the gate field and the temperature it is essential to record the electrical performance of the OFET in a cryostat. Since with the cryostat the control over a wide range of temperatures can be maintained

and the electric field applied to the OFET can be controlled simultaneously by means of an external electrometer interfaced with the cryostat.

Shown in Figure 5.2.1 is the schematic structure of the OFET characterized along with the corresponding biasing conditions at the individual electrodes. The bistable states of DAE molecule are represented as DAE_open and DAE_closed in accordance to the ring open and closed structural form at the bridge of diarylethene molecule.

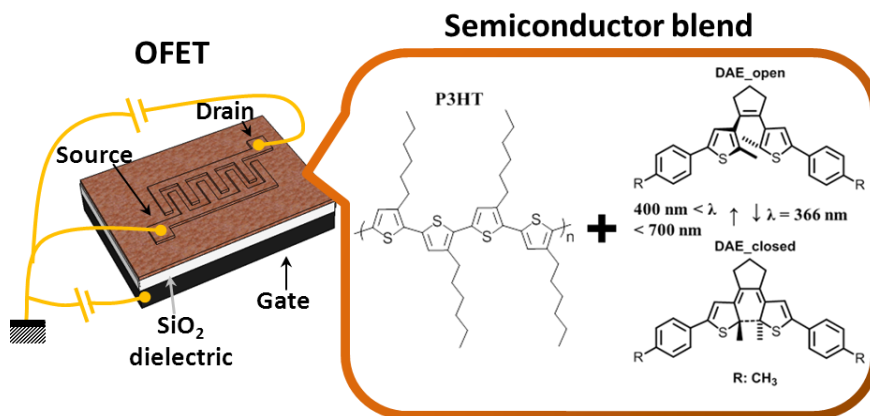


Figure 5.2.1 Schematic of the OFET with biasing configurations along with the chemical structure of the active layer in the device

In the case of P3HT/DAE_{open} based OFET devices were characterized without any electromagnetic wave irradiation while in the case of P3HT/DAE_{closed} based OFET UV irradiation for 10 min was undertaken to transform the DAE molecules in the polymer matrix to ring closed state.

5.2.1.1 Photochromic switching mechanism

The photochromic molecules embedded in a polymeric matrix allows the possibility to tune charge transfer energetic states between these two separate entities by means of optical stimulation. The diarylethene molecules undergoes electrocyclization when exposed to ultraviolet light at wavelength of 366 nm, this process closes the ring of the DAE molecule.¹ Upon absorption of UV rays the excitation of an electron from the HOMO to the LUMO level occurs (Figure 5.2.2). The initial ring open form can be recovered by subsequent irradiation with a white light source with λ is the range of 400 to 700 nm.

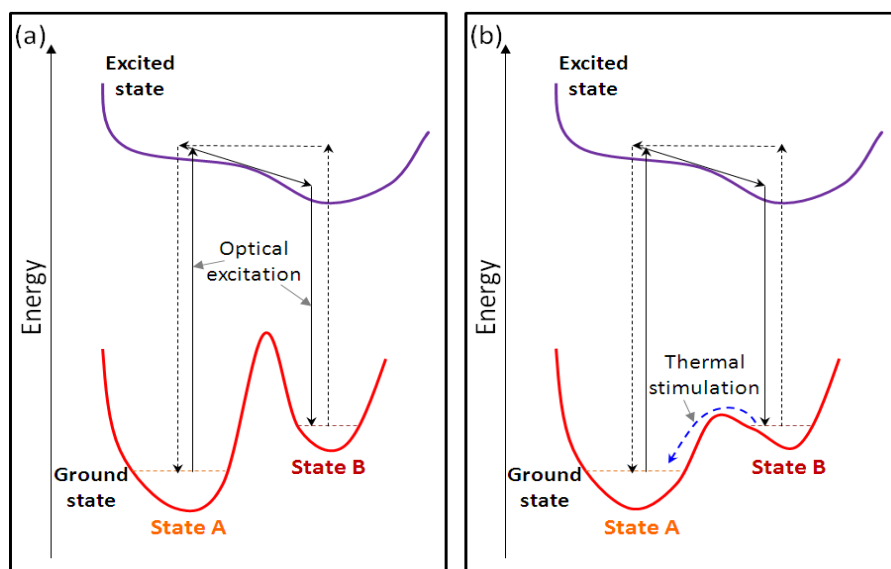


Figure 5.2.2 Schematic energy diagram illustrating the switching between the bistable states of the photochromic molecule. The change in states from A to B is triggered by external optical stimulus via the excited electronic state. (a) When the energetic barrier is large in the ground state optical excitation is the preferred mechanism. (b) For low energy barrier between the ground states of A and B, the reverse reaction can be triggered optically and by thermal stimulus.

The switching process in a photochromic molecule such as diarylethene is proposed² to follow the steps as shown in Figure 5.2.2. The reversible opening of the ring in the bridge of the diarylethene is likely due to multiple photon absorption involving across different intermediate energetic states.³ This effective optical tuning of the energetic states of the diarylethene molecule has been exploited to control current in an organic electronic device such as a field-effect transistor.⁴ The light driven reversible switching behavior is realized by the change in the electronic energetic levels and the charge distribution in the molecule.

5.2.2 Results and discussions

5.2.2.1 Absorbance of spin coated blend film

To estimate the time duration necessary for irradiation with the UV light to enable the complete transformation of the DAE_{open} to the DAE_{closed} state we performed UV/Vis absorption characterization. The absorption spectrum was recorded after irradiation with UV light with λ of 366 nm (8 W) for time intervals of 30, 30, 60, 120 and 300 seconds respectively. Figure 5.2.3 shows the absorption spectrum of when the P3HT/DAE_{open} film undergoes transition to P3HT/DAE_{closed} state. Prominent change in absorbance occurs at λ of 256 nm, 518 nm, 552 nm and 597 nm.

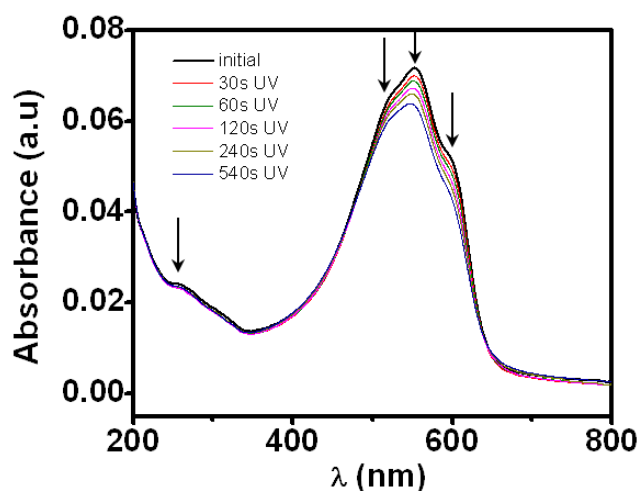


Figure 5.2.3 Absorption spectrum of spin coated blend film of P3HT and DAE_{open} on quartz slide. The arrows indicate the change in the magnitude of absorbance upon successive irradiation times. The time (seconds) in the legend indicates the interval with reference to the initial measurement.

The absorption of the film reduces and exhibits a small blue shift at λ of 552 nm and 597 nm while at λ of 518 nm there is small red shift. On careful inspection of the absorbance spectrum, it can be noted that after UV irradiation for \sim 540 s the majority of the photochromic DAE molecules in the blend film adopt closed state configuration. Hence we decided to irradiate the spin casted blend film for 10 min to allow the DAE molecules to metamorphose from the open to closed state.

5.2.2.2 Temperature dependence of transport in OFETs based on P3HT/DAE blend

The electrical characterization was performed on a device with channel length (L) of 20 μm and a channel width (W) of 10000 μm . The employed device geometry was of bottom-gate bottom-contact configuration. The surface of the SiO_2 dielectric layer was kept in its pristine state prior to deposition of the semiconducting thin film; this allowed us to examine the intrinsic charge transport properties of the blend film. In the case of P3HT/DAE_{open} based OFET devices were characterized without any electromagnetic wave irradiation while in the case of P3HT/DAE_{closed} based OFET UV irradiation for 10 min was undertaken to transform the DAE molecules in the polymer matrix to its closed form.

The transfer characteristics (drain current, I_D versus gate bias, V_{GS}) of transistors based on predominantly hole carrier transporting (p-type) P3HT/DAE blend films were acquired from 80 K to 300 K in intervals on 20 K. Once the OFET was housed inside the cryostat, prior to starting measurements at different temperatures a single $I_D - V_{GS}$ measurement was recorded to ensure the integrity and the stability of the electrical contact.

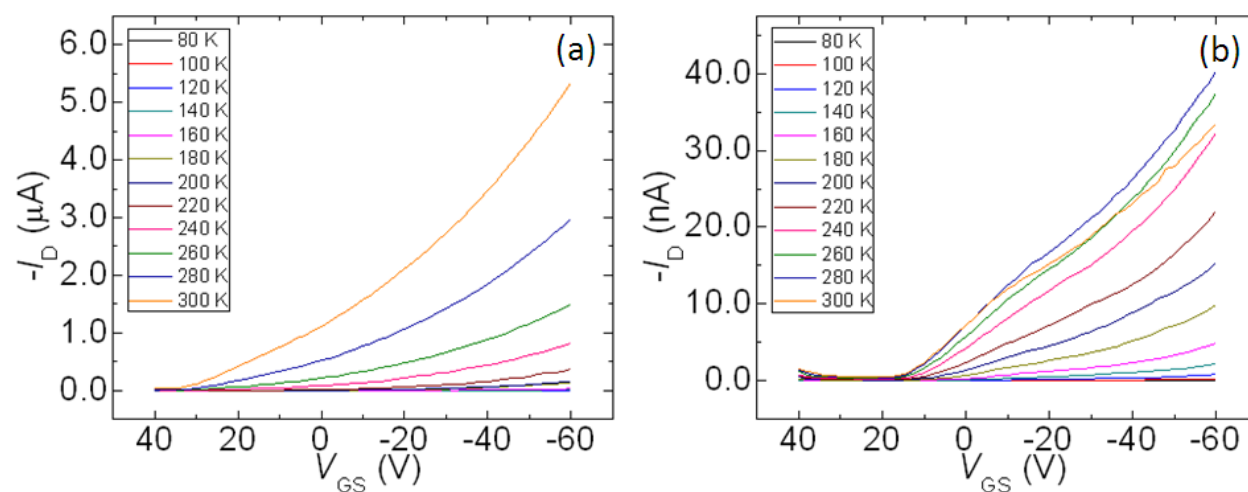


Figure 5.2.4 Transfer characteristics for the P3HT/DAE blend based OFET when the DAE molecule was in the (a) open state and (b) ring closed state. The V_{DS} was held at -10 V while the gate bias was swept.

Shown in Figure 5.2.4 a and b are the $I_D - V_{GS}$ response of the OFET in the linear regime for different temperatures. For acquiring the transfer characteristic the gate bias was sourced starting from +40 V \rightarrow -60 V and the drain current was measured at 2 V intervals, while the drain bias was held fixed at a low bias (-10 V) and higher bias (-60 V) for each complete gate bias sweep.

The semi-log plots of $I_D - V_{GS}$ for the OFET based on P3HT with DAE in open or closed forms is shown in Figure 5.2.5. From the Figure 5.2.5 the temperature dependence of the blend can be clearly visualized. The temperature dependent variation in drain current gives rise to corresponding dependence of hole mobility.

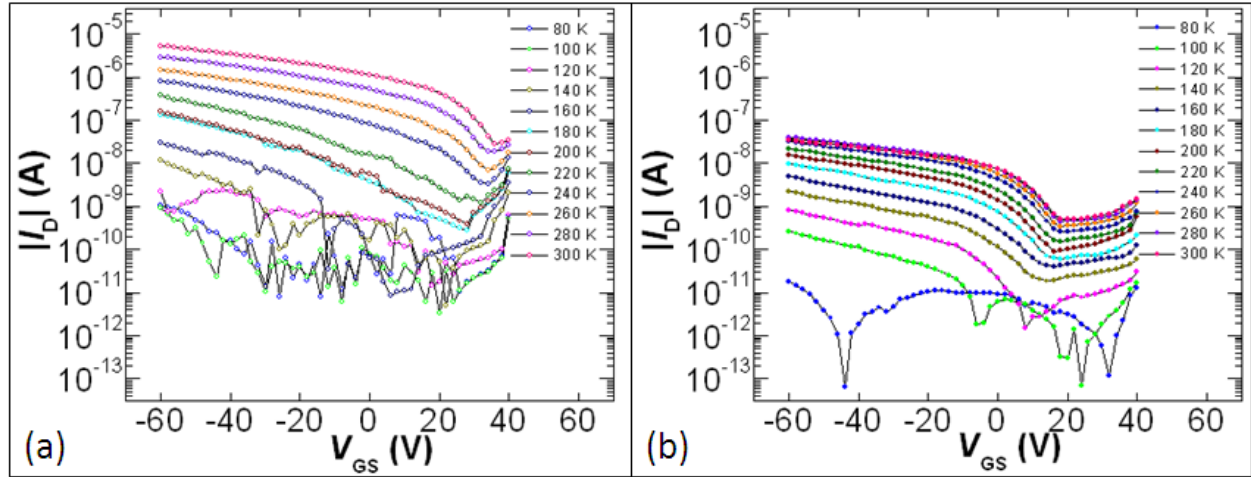


Figure 5.2.5 Semi-log plots of $I_D - V_{GS}$ clearly illustrating the variation of linear regime drain current ($V_{DS} = -10$ V) with temperature for OFET with (a) P3HT/DAE_{open} and (b) P3HT/DAE_{closed} molecules in the active layer.

The hole carrier mobility can be estimated in the linear regime from the drain current dependence on the gate bias by equation 5.2.1,⁵

$$\mu_{lin}(T, V_{GS}) = \frac{I_D}{C_i V_{DS} (V_{GS} - V_T^{amb})} \cdot \frac{L}{W} \quad (5.2.1)$$

Where C_i is the gate dielectric capacitance and V_T^{amb} is the gate voltage at which the device strongly turns on (i.e., where the I_D starts to rise) extracted at ambient temperature. In our experiment the V_T^{amb} remained fairly constant and not shift over different temperatures. The V_T^{amb} values were thus estimated when the I_D started to increase from its minimal value for the P3HT/DAE_{open} and closed to be +10.25 V and +17.72 V respectively. Then using equation 5.2.1 the linear mobility was estimated as a function of both temperature and gate bias. Shown in Figure 5.2.6 are the linear regime hole mobility across different temperature and the gate bias range. Note the increase at most temperatures mobility with the gate field suggests the shift in the Fermi level of the semiconductor blend closer the mobility edge. When the Fermi level

moves near the mobility edge more number of carriers is localized near the valence band edge and thus there are more mobile carriers which contribute to the charge transport. At lower gate bias the Fermi level is likely further away from the valence band edge where some charges can be trapped in deep immobile states which consequently lower the hole mobility.

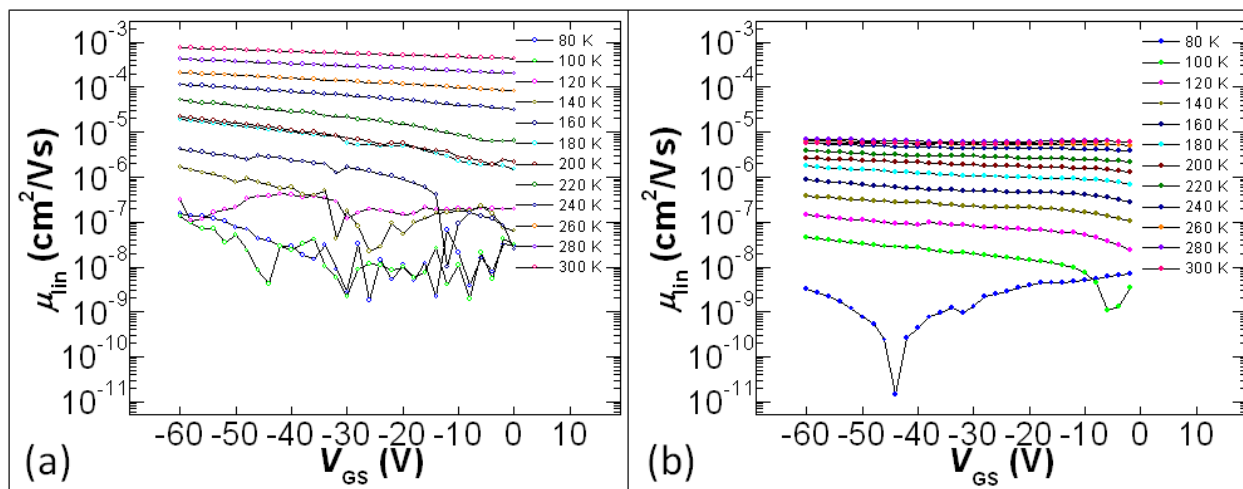


Figure 5.2.6 Semi-log plots of hole carrier mobility in the linear regime as a function of temperature and gate field for OFET with (a) P3HT/DAE_open and (b) P3HT/DAE_closed molecules in the active layer.

The variation in hole carrier mobility depending on temperature also suggest that there exists a thermally activated behavior. Upon inspection of the variation of hole mobility with temperature for we can observe that the variation of hole mobility with temperature is much higher for devices comprising of P3HT/DAE_open molecules as the semiconducting film suggested that the thermal activation is slightly higher in this case. The increase in hole mobility with temperature can be attributed to the activation energy, which is the energy required to the move the charges localized in immobile states to hop mobile states. The activation energy can be estimated from the Arrhenius relationship of mobility with temperature as shown in equation 5.2.2.^{6,7}

$$\mu_{in} = \mu_0 \exp\left(\frac{-E_a}{k_B T}\right) \quad (5.2.2)$$

Where E_a is the activation energy,⁸ K_B is Boltzmann constant ($8.617 \times 10^{-5} \text{ eV K}^{-1}$), T is absolute temperature and μ_0 is the prefactor mobility which is a mobility at infinite temperature. Figure

5.2.7 and Figure 5.2.8 show the variation of mobility with temperature at different fixed gate bias values for devices based on P3HT with DAE_open or closed films.

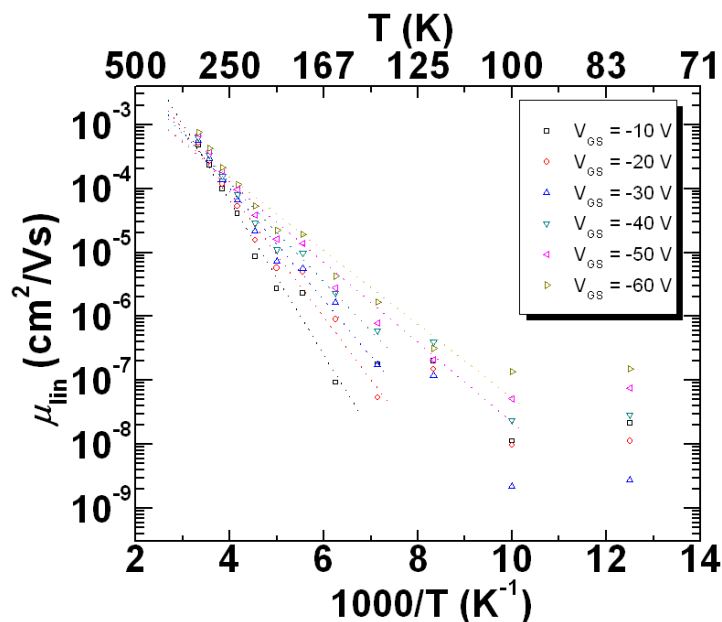


Figure 5.2.7 Arrhenius plot showing the linear mobility as function of temperature at different fixed gate bias values for OFET with P3HT/DAE_open blend in active layer.

For the P3HT/DAE_open device there is thermally activated hopping behavior from 300 K to 100 K below which there is weak dependence of charge transport which suggests tunneling between localized states. In the case of transistor based on P3HT/DAE_closed semiconductor film there is strong dependence of charge transport with temperature from 280 K to 80 K. On close observation from the Arrhenius plots of carrier mobility as a function of inverse temperature besides the onset temperature of thermal activation, there is major differences in the profile of the change in hole mobility with temperature and gate bias. For instance, the slope of the linear fits to the μ_{lin} vs. $1/T$ plot for P3HT/DAE_open is much steeper in comparison to that of P3HT/DAE_closed based device which manifests as greater levels of activation energy required to promote carrier hopping.

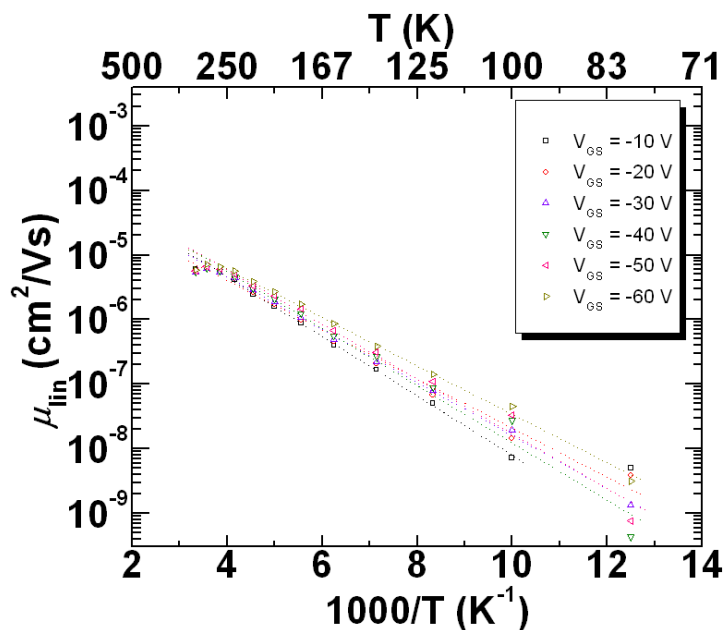


Figure 5.2.8 Arrhenius plot showing the linear mobility as function of temperature at different fixed gate bias values for OFET with P3HT/DAE_closed blend in active layer.

The activation energy as a function of gate bias is shown in Figure 5.2.9. As expected the activation energy shows an exponential decrease with increase in the gate bias, this again supports the fact that the Fermi level shifting closer the valence band edge of the blend film.^{5,9}

The greater activation energy of the device with P3HT/DAE_open with respect to the P3HT/DAE_closed based device can be attributed to the higher energetic mismatch between the P3HT and the DAE molecule in its open form. The E_a ranges from ~280 to 120 K as the gate bias approaches -60 V for the P3HT/DAE_open FET while for P3HT/DAE_closed it varies from ~110 to 75 eV. The much larger activation energy computed for the device with DAE_open molecule in the P3HT blend is attributed to the significant energetic barrier imposed between the respective ionization energy (IE) levels these compounds in its pristine form.⁴

The IE values determined by means of ultraviolet photoelectron spectroscopy for P3HT, DAE_open and closed molecules were reported to be ~4.4 to 4.9, 5.1 and 5.7 eV respectively (Figure 5.2.10).^{4,10} For P3HT the reported IE values in the literature measured by means of cyclic voltammetry was 4.8 eV.⁴

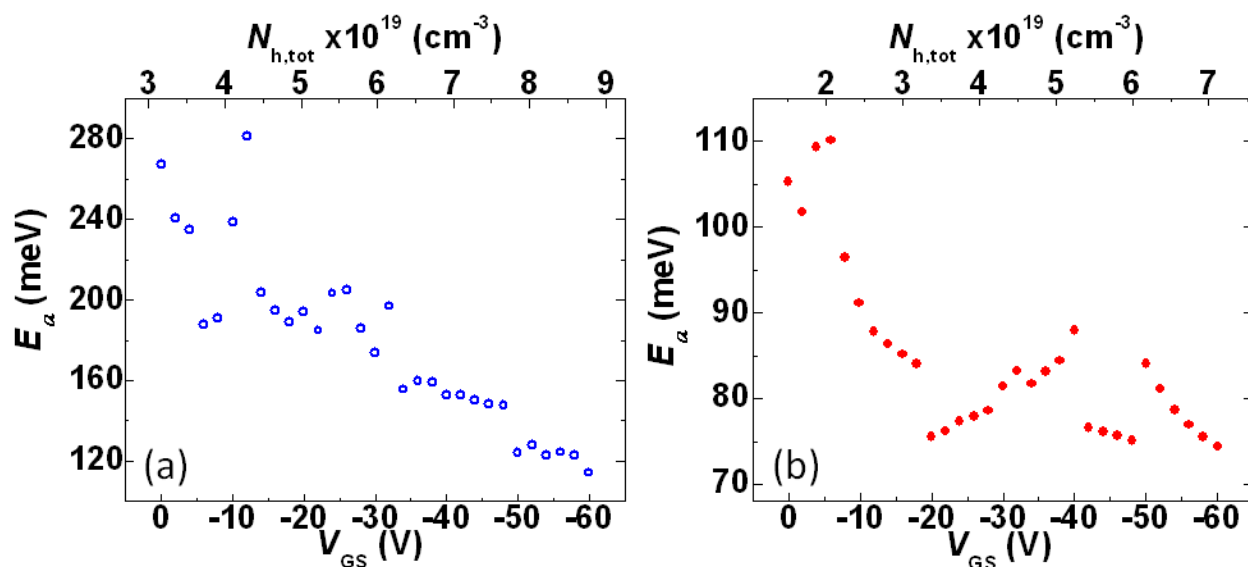


Figure 5.2.9 Activation energy as a function of gate bias for OFET based on (a) P3HT/DAE_{open} and (b) P3HT/DAE_{closed} semi-conductive film in the active layer.

The energetic barrier becomes apparent if we represent the IE values of the individual compounds of the bicomponent semiconductor film on a common energetic scale.

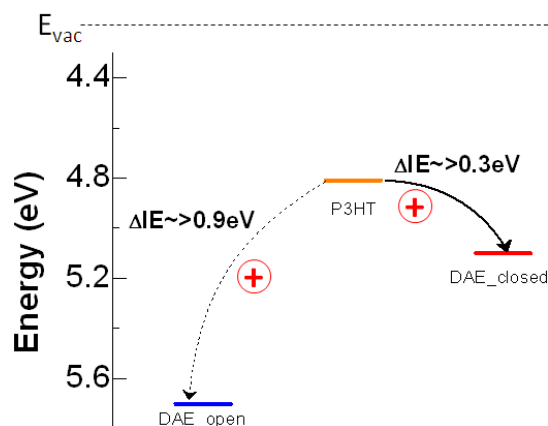


Figure 5.2.10 Illustration of the ionization energy levels of DAE small molecules in both open and closed forms along with P3HT. The IE offset between the P3HT and DAE isomers is depicted. The + symbol inside a circle represents the hole carrier barrier between the P3HT and DAE in open and closed forms respectively.

If we consider variable range hopping of hole carriers within a Gaussian density of states (DOS), the mobility shows a dependence with the $1/T^2$ from which the width of the DOS (σ_{DOS}) can be estimated,^{7,11,12}

$$\mu = \mu_0 \exp\left[-\left(\frac{2 \sigma_{DOS}}{3 K_B T}\right)^2\right] \exp\left[CE^{0.5}\left(\left(\frac{\sigma_{DOS}}{K_B T}\right)^2 - \Sigma^2\right)\right] \quad (5.2.3)$$

Where K_B is Boltzmann constant, μ_0 is the prefactor mobility which occurs in the case if there is no energetic disorder when $T \rightarrow \infty$, E is the applied gate electrical field and Σ describes the extent of spatial disorder.

Due to the very low lateral field applied to our devices $E \leq 5$ kV/cm, the Poole-Frenkel like second exponential term in equation 5.2.3 can be neglected. Thus the description of the carrier mobility in terms of Gaussian disorder model can be written as,

$$\mu = \mu_0 \exp\left[-\left(\frac{2 \sigma_{DOS}}{3 K_B T}\right)^2\right] \quad (5.2.4)$$

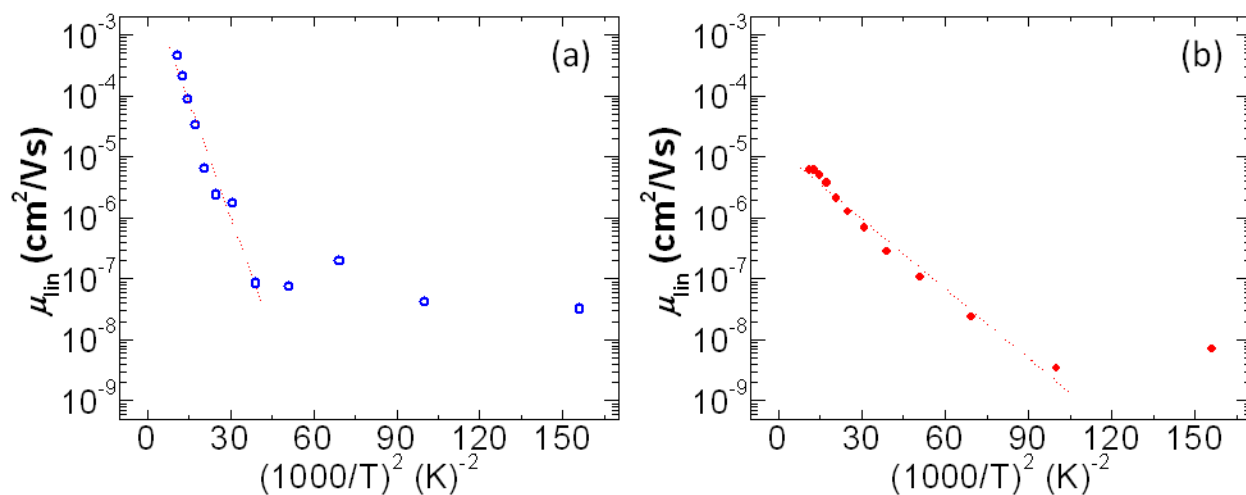


Figure 5.2.11 Non Arrhenius plot with linear hole Mobility vs. inverse square of temperature for transistor with semiconductor film comprising of P3HT blended with (a) DAE_{open} and (b) DAE_{closed} molecules.

The change in mobility with respect to the inverse of the square of temperature for devices with DAE in both its isomeric forms blended with P3HT is shown in Figure 5.2.11. The σ_{DOS} estimated amounts to ~ 70 and 38 meV for transistors with P3HT mixed with DAE_{open} and closed forms respectively.

The larger standard deviation of the Gaussian DOS for the FET based on P3HT/DAE_open by a factor >1.8 affirms the greater amount of ionization energetic disorder in the blend when P3HT is blended with DAE_open as opposed to DAE_closed molecule, if we consider the separate IE values as a reference. Another way to view this aspect is, the charge requires much more energy to perform hops from one energetic site to another as it travels along the channel composed of P3HT/DAE_open molecules. In essence the large offset existing between the IE levels of the DAE_open with respect to the P3HT makes it much more difficult for hole carrier hopping than the lower offset which is required to perform charge hopping along the P3HT/DAE_closed film.

More crucially the σ_{DOS} of 38 meV for the P3HT/DAE_closed is lower than the pristine P3HT FET of 45 meV reported in literature,⁷ this suggests that the addition of DAE_closed molecule to the P3HT film does not significantly cause diagonal energetic offset disorder in the bulk. This is probably due to the arrangement of the small DAE molecules in the amorphous regions of the P3HT matrix.⁴

5.2.3 Conclusions

The activation energy required for charge hopping in transistors based on P3HT and DAE_open molecules is at least a factor of two greater than for P3HT/DAE_closed active layer. The higher energy required to perform inter molecular hole carrier hopping in the FET channel comprising of P3HT/DAE_open film can be directly attributed to the greater energetic offset between the ionization energy levels of P3HT and DAE_open molecules and the contrary is true for DAE_closed molecules in the polymeric blend. The smaller IE difference between P3HT and DAE_closed molecules directly correlates to the narrower width of the Gaussian density of states, of 38 meV if we consider variable range hopping as the prevalent charge transport mechanism. Interestingly the σ_{DOS} of P3HT/DAE_closed was less than that of the pristine P3HT, which suggests that the addition of more resistive DAE_closed molecule to the P3HT does not significantly affect the energetic disorder in the bulk of the film since it is packed into the amorphous regions of the polymeric semiconductor.

5.2.4 References and notes

- 1 Li, J., Speyer, G. & Sankey, O. F. Conduction switching of photochromic molecules. *Phys. Rev. Lett.* **93**, 248302 (2004).
- 2 Sworakowski, J. & Lutsyk, P. Bistable organic materials in optoelectrical switches: Two-electrode devices vs. organic field effect transistors. *Ukr. J. Phys.* **56**, 1021-1029 (2011).
- 3 Goldberg, A. *et al.* Rotational isomerization of dithienylethenes: A study on the mechanism determining quantum yield of cyclization reaction. *J. Phys. Chem. A* **107**, 4982-4988 (2003).
- 4 Orgiu, E. *et al.* Optically switchable transistor via energy-level phototuning in a bicomponent organic semiconductor. *Nat Chem* **4**, 675-679 (2012).
- 5 Salleo, A. *et al.* Intrinsic hole mobility and trapping in a regioregular poly (thiophene). *Physical Review B* **70**, 115311 (2004).
- 6 Chesterfield, R. J. *et al.* Variable temperature film and contact resistance measurements on operating n-channel organic thin film transistors. *J. Appl. Phys.* **95**, 6396-6405 (2004).
- 7 Majewski, L., Schroeder, R., Grell, M., Glarvey, P. & Turner, M. High capacitance organic field-effect transistors with modified gate insulator surface. *J. Appl. Phys.* **96**, 5781-5787 (2004).
- 8 *This is defined as the minimum amount of energy required to complete the charge transport which is frequently described to occur by hopping between sites and it is expressed in units of eV or meV.*
- 9 Chang, J. F., Sirringhaus, H., Giles, M., Heeney, M. & McCulloch, I. Relative importance of polaron activation and disorder on charge transport in high-mobility conjugated polymer field-effect transistors. *Physical Review B* **76**, 205204 (2007).
- 10 Masillamani, A. M. *et al.* Multiscale Charge Injection and Transport Properties in Self-Assembled Monolayers of Biphenyl Thiols with Varying Torsion Angles. *Chem. Eur. J.* **18**, 10335-10347, (2012).
- 11 Bäessler, H. Charge Transport in Disordered Organic Photoconductors a Monte Carlo Simulation Study. *physica status solidi (b)* **175**, 15-56, (1993).
- 12 Veres, J., Ogier, S. D., Leeming, S. W., Cupertino, D. C. & Mohialdin Khaffaf, S. Low-k Insulators as the Choice of Dielectrics in Organic Field-Effect Transistors. *Adv. Funct. Mater.* **13**, 199-204 (2003).

5.3 ACTIVATION ENERGY OF OFETs BASED ON QUINOIDAL OLIGOTHIOPHENE DERIVATIVE

In this part of the chapter the investigation of the intrinsic charge transport properties of ambipolar field-effect transistors based on quinoidal oligothiophene oligomer incorporated as the semiconducting layer in the device is investigated in detail. The quinoidal oligothiophene derivative employed in this study undergoes changes in its morphological arrangement and energetic profile of charge transport levels upon certain post-processing conditions such as annealing and solvent vapor treatment. The focus of this study was to estimate the intrinsic mobility and activation energy by means of electrical characterization of these OFETs in a static cryostat. The activation energy for electron charge carriers (n-channel transistor operation) was investigated for pristine spin coated and post-annealed QQT(CN)₄ films.

5.3.1 Scope

The intrinsic charge transport properties in organic semiconductor films can be tuned by means of post-processing of the deposited films.¹⁻³ The most commonly employed method for the deposition of the semiconductor film is by means of spin casting. This technique for deposition has some crucial advantages such as reduced processing complexity, possibility to obtain homogenous thickness and morphology over a wide region of the substrate and minimal duration required to achieve good quality thin films with homogenous spread of thickness over large areas.

One of the prominent advantages of organic materials is that once the material is deposited on the substrate surface the morphological properties and its respective opto-electronic properties can be tuned by means of simple post-deposition methods. Among the post-deposition processing methods the widely employed route is by means of,

- (i) Thermal annealing³ and
- (ii) Solvent vapor treatment

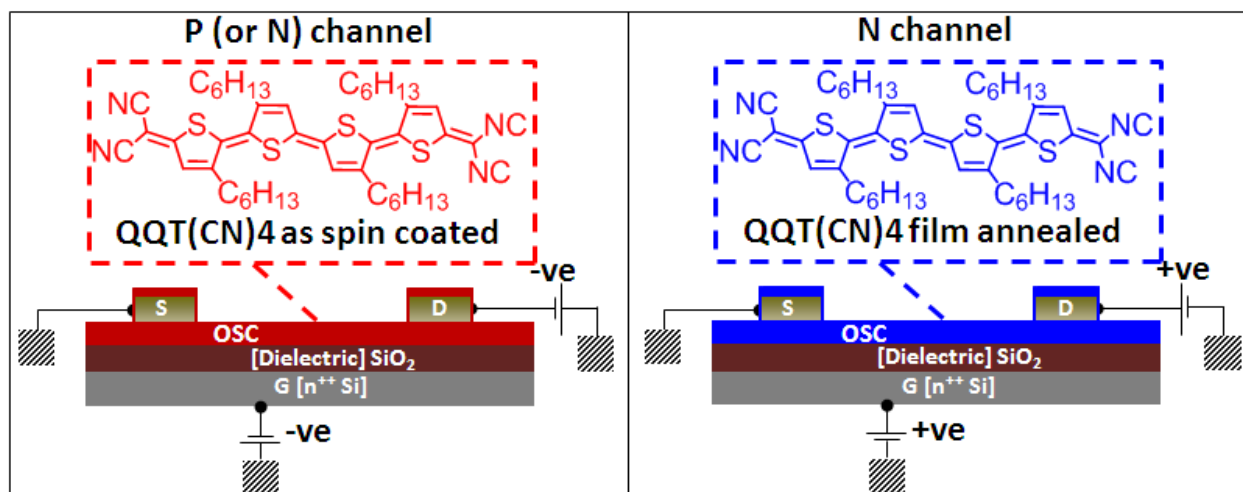


Figure 5.3.1 Structure of bottom-gate bottom-contact OFETs based on quinoidal oligothiophene derivative, shown in the left and right panels are the hole and electron transporting transistors along with the respective biasing configurations. Note that the as spin casted QQT(CN)4 film exhibits ambipolar behavior.

In this study we make use of thermal annealing to alter the electronic transport levels and thereby the charge transport properties in the quinoidal oligothiophene (see Figure 5.3.1 inset) based field-effect transistors.

5.3.2 Results and discussions

5.3.2.1 Absorption spectra of QQT(CN)4 film

The as-spun QQT(CN)4 film on quartz substrate has a broad absorption band, λ from ~ 790 nm to 1495 nm at full width at half maximum (fwhm). Upon annealing of the film for 180 °C for 10 s the absorption band width becomes narrower (λ from 780 nm to 1130 nm) and more blue shifted. Figure 5.3.2 shows the absorption profiles of the QQT(CN)4 film pre and post annealing.

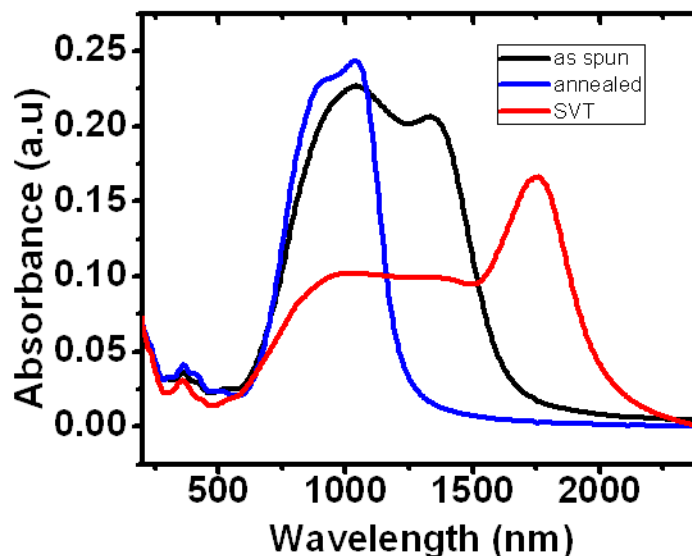


Figure 5.3.2 UV/Vis absorption spectrum profiles of the QQT(CN)4 film, as spun (black), annealed (blue) and solvent vapor treated in CHCl_3 after annealing (red)

The consequence of the shift in the absorption profile of the film of the QQT(CN)4 is that the energetic band gap (HOMO-LUMO) levels change correspondingly. The HOMO level of the drop casted QQT(CN)4 film as estimated from the ionization energy level from UPS measurements were ~ 5.3 eV. After annealing the QQT(CN)4 film undergoes blue shift in absorption resulting in increase in optical band gap and down shifting of the LUMO level to ~ 4.7 eV from ~ 4.5 eV. The LUMO levels were estimated from the recorded optical band gap from the long absorption tail of the absorption spectrum (Figure 5.3.2). The shift in the energetic orbital levels had been attributed to the changes in molecular packing and crystallinity for the annealed film with respect to the spin coated one. The pertinent feature of this molecule is that, just by thermal annealing of the film the property of the molecule in the bulk can be modified to transport electrons converse to the initial state of majority hole carrier conduction.^{1,2} These salient features enable the usage of the air stable Au electrodes for injecting both holes and electrons, thus enabling the possibility of realizing bipolar devices based on complementary metal-oxide semiconductor (CMOS) logic circuits.

5.3.2.2 Energetic profile of electronic charge transport levels

Shown in Figure 5.3.3 is the energy band diagram of the drop casted QQT(CN)4 film as deposited by drop casting and annealed, the work function of the injecting Au electrodes is indicated for visualizing the energetic barrier with the corresponding molecular orbitals.

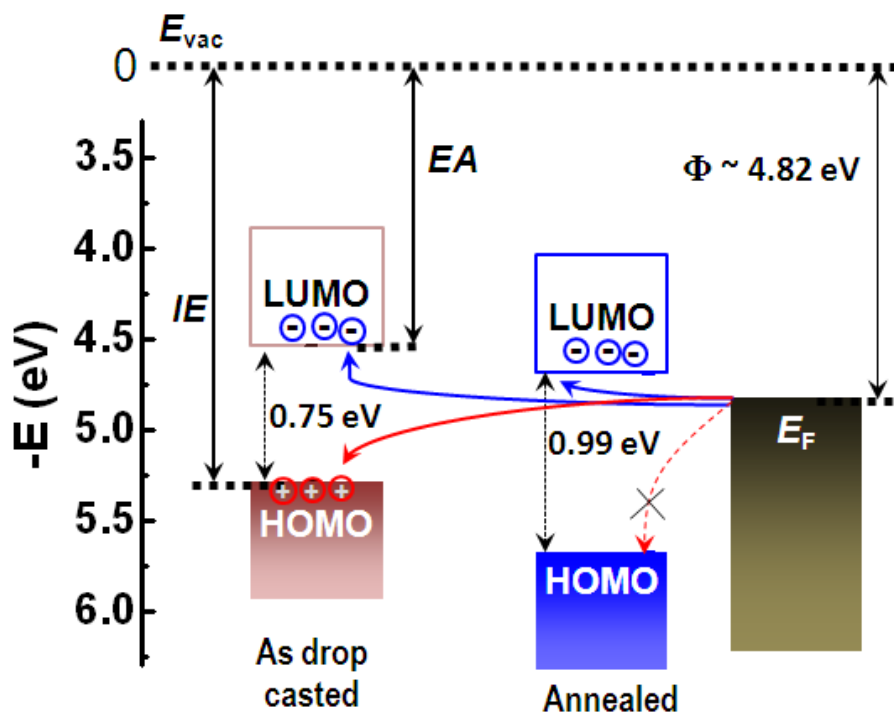


Figure 5.3.3 Energy band diagram of QQT(CN)4 film, as drop casted (maroon), annealed (blue) along with the work function of the gold electrode as recorded by UPS.

Since the work function (Φ) of the Au electrodes (measured with UPS) was ~ 4.82 eV, the injection barrier to the HOMO level is favorable towards p and n-type behavior while the same film upon annealing results in the LUMO level shift closer to the Fermi level of the Au electrode which favors electron transport (n-type). With the flexibility and versatility to the change the intrinsic charge transport properties of the semiconducting material we aimed to investigate the activation energy which might be required for the transistors operating in both p and n-type operational mode. For this end we fabricated TFTs in bottom-gate bottom-contact device geometry on a highly doped Si substrate which served as the gate electrode with a dielectric layer of SiO_2 sandwiched between the bottom gate and the top interdigitated source-drain gold

electrodes. The fabrication of the device was completed upon the spin coating of 75 μl of QQT(CN)4 solution (2 mg ml^{-1} in CHCl_3) onto the cleaned substrates.

5.3.2.3 Electrical characterization of QQT(CN)4 OFETs in a cryostat

Device with channel length (L) of 20 μm and width (W) of 10000 μm was characterized for both p and n-type QQT(CN)4 OFETs.

QQT(CN)4 ambipolar OFET: Device was characterized after spin casting QQT(CN)4 from CHCl_3 onto substrates with pre-patterned electrodes. The transfer characteristics for QQT(CN)4 OFET in n-type operational mode in linear regime is shown in Figure 5.3.4a.

QQT(CN)4 n-type OFET: Device was characterized after spin casting QQT(CN)4 and then a subsequent annealing step at 150 $^\circ\text{C}$ for 5 s in ambient conditions.

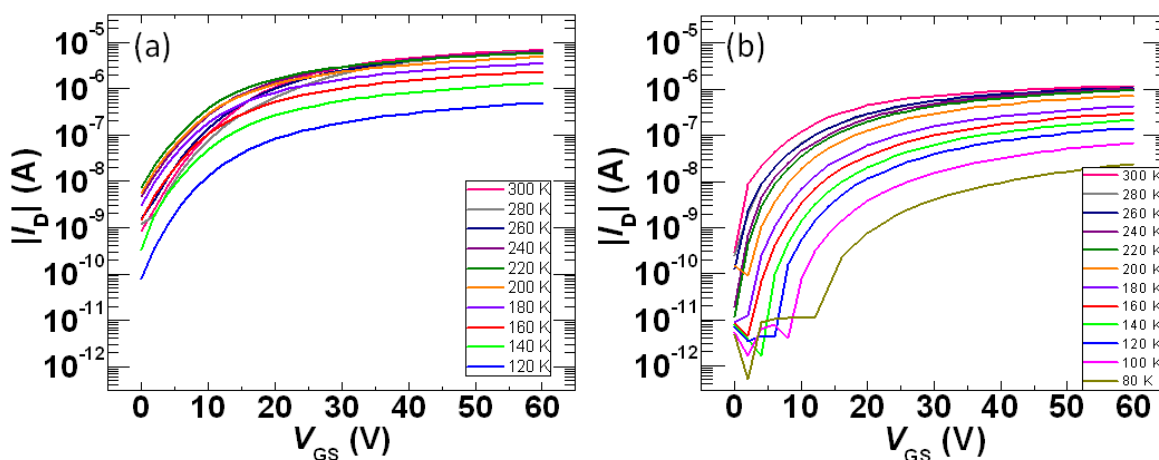


Figure 5.3.4 Semi-log plots of I_D vs. V_{GS} for n-channel spin coated (left panel) and annealed (right panel) QQT(CN)4 OFETs at different temperatures, the corresponding drain potential was held constant at +10V.

Depicted in Figure 5.3.4b are the transfer characteristics for QQT(CN)4 OFET in n-type operational mode in linear regime at various temperatures.

Transfer characteristics of the OFETs were recorded from temperature range of 300 K to 80 K for n-type and from 300 K to 120 K for ambipolar OFETs in steps of 20 K.

It is interesting to note that thermal annealing of the QQT(CN)4 film causes the lowering of the magnitude of the *off* drain current with respect to that recorded for device with pristine spin coated film at similar temperature scales. While the I_{on}/I_{off} is greater and the saturation of the drain current is maintained which suggests clean switching behavior and no significant doping due to moisture as in other polythiophene FETs.⁴ It is also likely that since the electron injection barrier between the source electrode and the LUMO level of the annealed QQT(CN)4 film is lower it leads to observation of increase in I_D at a lower applied gate potentials, this clearly confirms the fact of full conversion of the intrinsic charge transporting properties of the ambipolar (electron and hole conducting) pristine spin casted QQT(CN)4 film to a pure electron conducting n-type semiconductor. Moreover the subthreshold slope of the FET based on annealed QQT(CN)4 film is lower than that of the bare spin coated semiconductor.

For majority of the temperature the drain current (I_D) increases with rise in temperature. The effective mobility (μ_{eff}) which describes the mobility considering the mobile and immobile charge carriers was calculated from the linear regime.

The μ_{lin} was estimated using assuming that (i) The onset voltage (V_{on}) is close to 0 and (ii) V_{on} is independent of temperature.⁵ The increase in I_D causes a corresponding increase in mobility which suggests an activated behavior of charge transport depending on temperature.

$$\mu_{eff}(V_{GS}, T) = \frac{I_D}{C_i V_{DS} (V_{GS} - V_{on})} \cdot \frac{L}{W} \quad (5.3.1)$$

$$\mu_{lin}(V_{GS}, T) = \frac{I_D}{C_i V_{DS} V_{GS}} \cdot \frac{L}{W} \quad (5.3.2)$$

The point by point electron mobility varying with the gate potential was determined in the linear regime from equation 5.3.2 and is depicted in Figure 5.3.5. Similar to the variation of the I_D modulation with V_{GS} the mobility also reflects the change with respect to gate potential and temperature.

On close observation of the influence of temperature on the mobility it is apparent that there is a much larger amount of thermally activation of charge transport for transistor based on annealed QQT(CN)4 film.

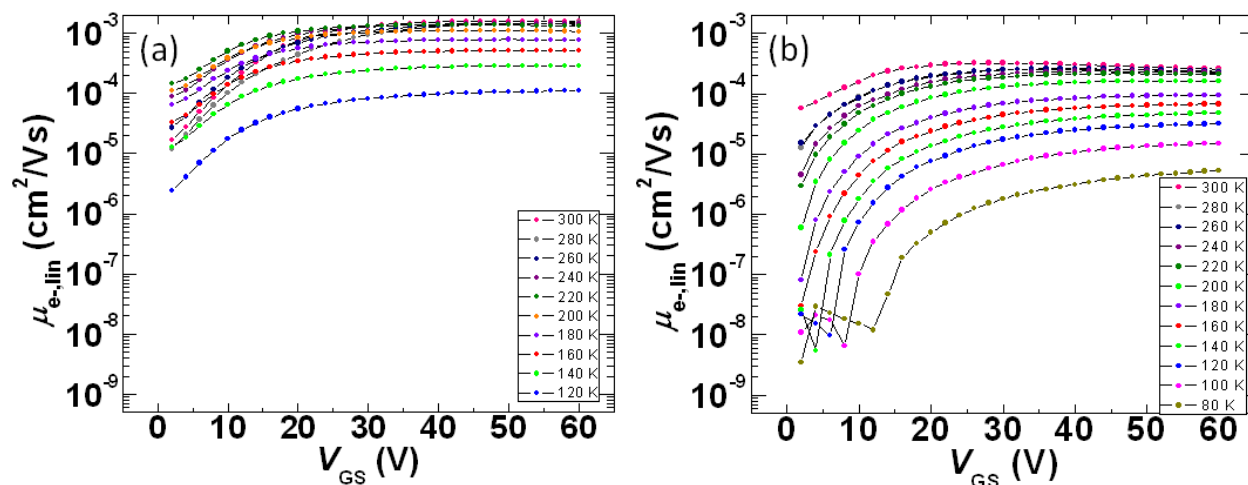


Figure 5.3.5 Effective mobility as a function gate bias and temperature for the QQT(CN)4 TFTs under n-channel operation for (a) spin coated film (b) annealed film after spin casting.

The variability of effective mobility with respect to gate field and temperature suggests that the relation between exponential of activation energy and field-effect mobility by the following equation,⁶

$$\mu_{eff} = \mu_0 \exp\left(\frac{-E_a}{k_B T}\right) \quad (5.3.3)$$

Where E_a is the activation energy, k_B is the Boltzmann constant, T is the absolute temperature and μ_0 is the prefactor.

For n-type semiconductor the activation energy is the offset in energy between the conduction band edge (E_c) and the discrete trap state (E_T) when the E_a is greater than the width of the trap distribution⁷ and this can be expressed according to the Arrhenius relation and represented graphically as in Figure 5.3.6,

$$\mu_{eff} \approx \mu_0 \exp\left(\frac{-(E_c - E_T)}{k_B T}\right) \quad (5.3.4)$$

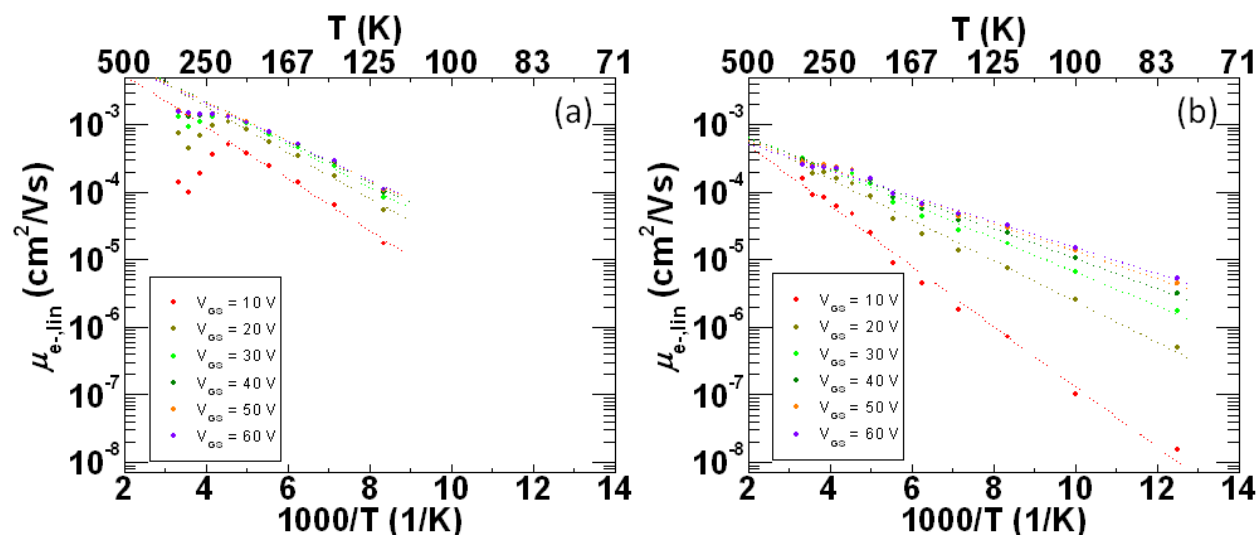


Figure 5.3.6 Arrhenius plot showing linear regime mobility variation with temperature for n-channel QQT(CN)4 based OFET for gate bias from +10 V to +60 V, at a constant V_{DS} of +10 V (a) spin coated film and (b) Post annealed film after spin coating.

On close observation of the variation of mobility with temperature for the devices without or with annealed QQT(CN)4 film as the active layer in the semiconductor we can observe clear difference in temperature dependent activation in charge transport among these two. The first major difference is that the change in mobility with temperature is much lower for the device with QQT(CN)4 spin cast film than the post-annealed film device, in other words the slope of the device with annealed film is much larger in magnitude than the device comprising of the spin coated film. This is likely due to the greater amount of trap densities at the dielectric/semiconductor interface, since the untreated surface of the SiO_2 dielectric in these devices which comprises of hydroxyl groups can act as effective electron trap sites⁸ and as a consequence which the E_a of the n-channel only QQT(CN)4 based FET is greater. Secondly, there are two distinct regime of temperature activation for the device comprising of the spin casted film. Thirdly the onset of thermal activation is much higher for the device with the annealed film, starting from ~ 300 K whereas for the device pristine spin coated semiconductor

film it starts ~ 200 K. All of these factors suggest that the post processing plays a major role of modifying the intrinsic charge transport properties of the semiconductor layer.

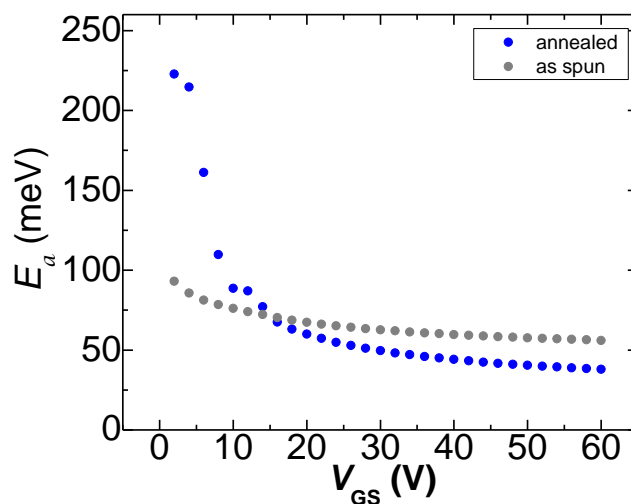


Figure 5.3.7 The point by point activation energy as a function of the gate bias for transistors based on film of pristine spin casted and annealed QQT(CN)4 semiconductor film at n-channel operation condition.

To probe these fact we extrapolated the activation energy for QQT(CN)4 based device operating in n-channel mode with or without annealing. The activation energy calculated for each of the gate potential for the QQT(CN)4 transistor operation in n-channel mode is shown in Figure 5.3.7.

The lower activation energy at higher gate fields suggest that the accumulated charges in the channel will occupy higher energy sites closer to the conduction band mobility edge,^{3,7} wherein lesser energy would be required to activated hopping to neighboring sites. Coincidentally the E_a ranges from ~ 220 to 38 meV and ~ 93 to 56 meV with increasing gate voltages for the transistor with annealed and spin coated films respectively.

If we assume that the density of electronic states (DOS) of the carriers is distributed randomly, it can be described according to a Gaussian profile proposed by Bäessler.⁹ Alternatively the density of states in the band gap is considered to be exponentially distributed. A unified description of these two models was suggested by Tanase and co-workers where they show that in FETs with conjugated semiconductor structures when the magnitude of the areal charge density is large the

exponential DOS is a reasonable approximation of Gaussian DOS.¹⁰ The width of the Gaussian density of states, σ_{DOS} extrapolated at T_0 of ~ 191 K for amounts to 67 meV which lies within the energy range of annealed QQT(CN)4 FET.

Similarly the σ_{DOS} of spin coated QQT(CN)4 transistor was estimated to be 37 meV at a T_0 of ~ 109 K which lies within its E_a range from 93 to 56 meV. The dependence of mobility with inverse square of temperature as described by the Gaussian disorder model^{6,9} is plotted in Figure 5.3.8.

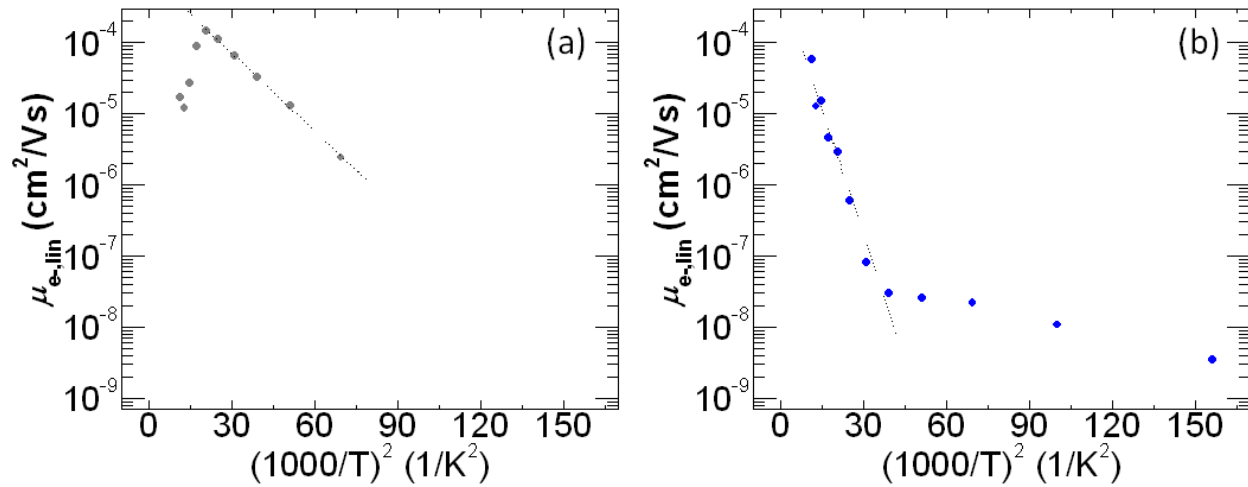


Figure 5.3.8 Mobility as a function of inverse T^2 according to the Gaussian disorder model for QQT(CN)4 FET with (a) spin coated and (b) annealed films.

The prefactor is furthermore related to the E_a by the following empirical relation,¹¹

$$\mu_0 = \mu_{00} \exp\left(\frac{E_a}{k_B T_{iso}}\right) \quad (5.3.5)$$

Substituting equation 5.3.5 in 5.3.3 yields the following relationship,¹²

$$\mu_{eff} = \mu_{00} \exp\left(-E_a \left(\frac{1}{k_B T} - \frac{1}{k_B T_{iso}}\right)\right) \quad (5.3.6)$$

Where μ_{00} is the compensation factor which increases exponentially with rise in E_a according to Meyer-Neldel rule (MNR) and the isokinetic temperature T_{iso} is related to the Meyer-Neldel

energy, $E_{MN} = k_B T_{iso}$. In other words the E_{MN} is the energy estimated at a single crossing point of different E_a at the isokinetic temperature, which is obtained by plotting the prefactor μ_0 against the activation energy. We did not observe an intersection of prefactor mobility for the n-channel spin coated QQT(CN)4 FET when the mobility was extrapolated to $1/T=0$, however for the transistor comprising of the annealed film a common intersection point was observed. The variation of the μ_0 spanned several orders of magnitude with respect to E_a as shown in Figure 5.3.9. The Meyer-Neldel energy at the isokinetic temperature of 807 K was estimated to be ~ 70 meV.

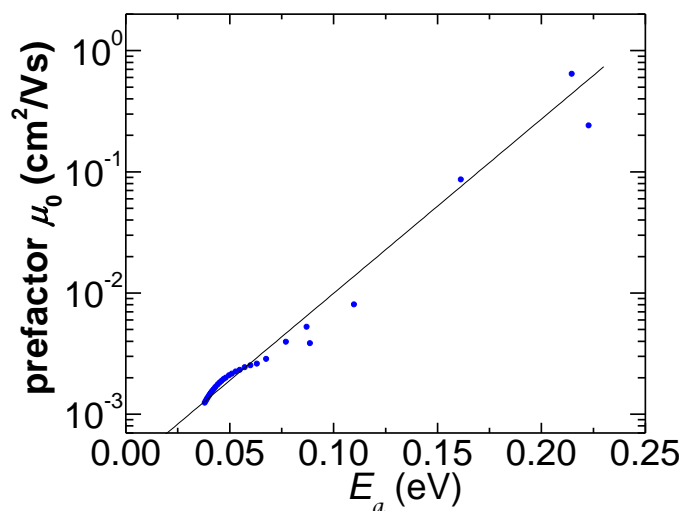


Figure 5.3.9 Prefactor μ_0 as a function of E_a for n-channel annealed QQT(CN)4 FET

The origin of the MNR is consistent with a charge hopping as the mechanism of transport.¹³ It is likely that the annealed film has more defect sites at the grain boundaries of microcrystalline domains as opposed to the neat spin coated film² hence the compensation of prefactor satisfies the MNR well.

5.3.3 Conclusions

The temperature dependence of charge transport in QQT(CN)4 transistors operating in n-channel mode for two different preparation conditions investigated. The transistor with the annealed QQT(CN)4 film exhibited a much higher activation energy than the spin casted one, which could be attributed to the presence of greater number of energetic defects sites and grain boundary

disorders in the film. For the annealed device there was a strong thermally activated behavior below 300 K and for the as spun device strong variation in mobility commenced from 200K. The charge transport seems to follow a hopping behavior between localized trap states. The width of the Gaussian DOS lied within the activation energy range for both transistors with or without annealing highlighting the strong dependence of mobility with the density of charge carriers. The Meyer-Neldel rule was obeyed by annealed film QQT(CN)₄ field-effect transistor.

5.3.4 References

- 1 Ribierre, J. C. *et al.* Direct Laser Writing of Complementary Logic Gates and Lateral p–n Diodes in a Solution-Processible Monolithic Organic Semiconductor. *Adv. Mater.* **22**, 1722-1726 (2010).
- 2 Ribierre, J. C. *et al.* Reversible Conversion of the Majority Carrier Type in Solution-Processed Ambipolar Quinoidal Oligothiophene Thin Films. *Adv. Mater.* **22**, 4044-4048 (2010).
- 3 Salleo, A. *et al.* Intrinsic hole mobility and trapping in a regioregular poly (thiophene). *Phys. Rev. B* **70**, 115311 (2004).
- 4 Hoshino, S. *et al.* Influence of moisture on device characteristics of polythiophene-based field-effect transistors. *J. Appl. Phys.* **95**, 5088-5093 (2004).
- 5 Chang, J. F., Sirringhaus, H., Giles, M., Heeney, M. & McCulloch, I. Relative importance of polaron activation and disorder on charge transport in high-mobility conjugated polymer field-effect transistors. *Phys. Rev. B* **76**, 205204 (2007).
- 6 Majewski, L., Schroeder, R., Grell, M., Glarvey, P. & Turner, M. High capacitance organic field-effect transistors with modified gate insulator surface. *J. Appl. Phys.* **96**, 5781-5787 (2004).
- 7 Chesterfield, R. J. *et al.* Variable temperature film and contact resistance measurements on operating n-channel organic thin film transistors. *J. Appl. Phys.* **95**, 6396-6405 (2004).
- 8 Chua, L. L. *et al.* General observation of n-type field-effect behaviour in organic semiconductors. *Nature* **434**, 194-199 (2005).
- 9 Bässler, H. Charge Transport in Disordered Organic Photoconductors a Monte Carlo Simulation Study. *Phys. Status Solidi B* **175**, 15-56, (1993).
- 10 Tanase, C., Meijer, E., Blom, P. & De Leeuw, D. Unification of the hole transport in polymeric field-effect transistors and light-emitting diodes. *Phys. Rev. Lett.* **91**, 216601 (2003).
- 11 Meyer, W. & Neldel, H. Relation between the energy constant and the quantity constant in the conductivity–temperature formula of oxide semiconductors. *Z. tech. Phys* **18**, 588-593 (1937).
- 12 Meijer, E. J., Matters, M., Herwig, P. T., de Leeuw, D. M. & Klapwijk, T. M. The Meyer–Neldel rule in organic thin-film transistors. *Appl. Phys. Lett.* **76**, 3433-3435 (2000).
- 13 Horowitz, G., Hajlaoui, M. E. & Hajlaoui, R. Temperature and gate voltage dependence of hole mobility in polycrystalline oligothiophene thin film transistors. *J. Appl. Phys.* **87**, 4456-4463 (2000).

5.4 IMPROVED FIELD-EFFECT MOBILITY IN A POLYMERIC SEMICONDUCTOR/SMALL MOLECULAR BLEND TRANSISTORS

In this part the influence of blending a thiophene based small molecule with a polymeric semiconductor and incorporated as the charge transport layer in field-effect transistor is reported. The focus of this project was to determine the effect of varying ratios of 5,5'-bis(4-n-hexylphenyl)-2,2'-bithiophene (dH-PTTP) by weight in a poly(3-hexylthiophene) (P3HT) mixture deposited as the active layer of FETs on the hole carrier mobility. The relation between the electronic and morphological ordering of the molecules was systematically investigated. Possible correlations between the enhancements of mobility at certain blend films and phase segregation effects are discussed.

5.4.1 Prospects

Organic thin-film transistors (OTFTs) are attracting a great attention as promising candidates for cheap, flexible and large-area electronics.¹⁻⁸ In particular, the use of solution-deposited polymers featuring semiconducting properties represents a valid alternative to amorphous silicon, with the advantage of a versatile processability using ink-jet printing/roll-to-roll techniques which are suitable for the mass production of low-cost electronics. In this regard, poly(3-hexylthiophene) (P3HT) is a prototypical p-type polymer that combines a good solubility in numerous organic solvents with large field-effect mobilities in thin films.⁹ However the semi crystalline nature of the polymer based assemblies limits their electrical characteristics. On the other hand, small molecules, which typically exhibit greater mobilities,^{10,11} suffer from problems related to their tendency to aggregate forming microscopic crystals. These crystals cannot be easily interfaced to metallic electrodes, limiting charge injection at metal-semiconductor interfaces, and are characterized by grain boundaries, which negatively affect the charge transport within the film. For this reason, blends of polymer/small molecule are used in all those applications where multiple requirements are necessary and cannot be fulfilled by employing a single component. Mobilities measured upon blending two p-type components exhibited improved charge transport characteristics over the starting mobilities of the single components.¹²⁻¹⁶

5.4.2 Results and discussions

Here we show that the mobility within a P3HT based OTFT film can be increased by co-deposition with 5,5'-bis(4-n-hexylphenyl)-2,2'-bithiophene (dH-PTTP) (Figure 5.4.1), a small molecule that displayed in the past interesting charge transport properties in organic transistors and volatile memories.¹⁷⁻¹⁹ Significantly, we have found that a field-effect mobility of $\sim 0.1 \text{ cm}^2\text{V}^{-1}\text{s}^{-1}$ can be achieved upon modulating the ratio of the two components in the blend, with the highest value measured in 1:1 blends of P3HT:dH-PTTP in weight ratio. Such a mobility is about 10-fold higher than the mobility measured in bare P3HT films, and about 50-fold greater than those measured in bare dH-PTTP films. Furthermore, ultraviolet ambient photoelectron spectroscopy technique is employed to monitor the work-function variation of the blend upon changing the two components ratio, providing a reliable means to evaluate the vertical phase-segregation process that has been found to characterize polymer/small molecule systems.²⁰

5.4.2.1 Electrical characterization of P3HT:PTTP OFETs

Transistors in bottom-contact bottom-gate configuration were fabricated on n^{++} -Si substrates with 230 nm of thermally grown SiO_2 as the gate dielectric and pre-patterned pairs of gold electrodes with interdigitated geometry as the source and drain. The semiconductor layer was deposited by drop-casting from a 5 mg/ml solution in p-xylene.

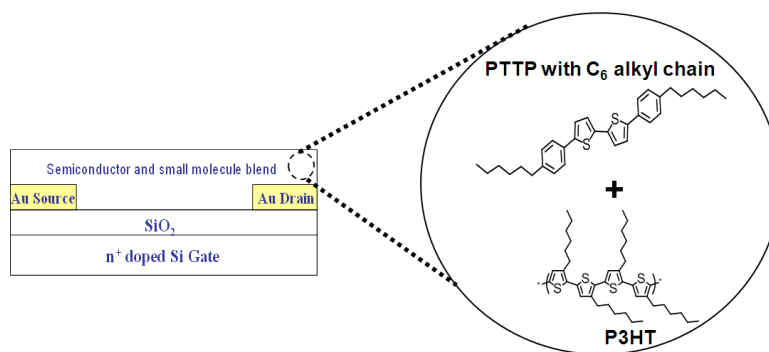


Figure 5.4.1 Schematic illustration of OTFT structure (bottom contact) and the chemical structures of PTTP (5,5'-bis(4-n-hexylphenyl)-2,2'-bithiophene, P3HT (poly(3-hexylthiophene))

Samples having different ratio in weight were prepared, comprising ratios spanning from 0% of dH-PTTP, i.e. pure P3HT, to 100% of dH-PTTP. The range included 5%, 25%, 50%, 75% and 95%. After drop-casting, films were dried up at room temperature overnight.

All samples were prepared and measured in a N₂ filled glovebox to avoid oxidative doping of the materials and ensure reproducibility of the experiments. It is worth noting that differently from other works^{12,20} i) drop-casting was chosen as the deposition technique since it is more similar, if compared to spin-coating, to the ink-jet printing process used in real device fabrication; ii) no electrode treatment with self-assembled monolayers was required since both the polymer and the small molecule were chosen also based on their ionization energy with respect to that of the gold electrodes. In fact, the latter would represent a further and delicate technological step. iii) The solvent employed is p-xylene which is non-chlorinated; iv) no annealing was utilized at any preparation step. These experimental conditions have been carefully chosen in order to simplify the data analysis and most importantly to provide a model system more suitable for future industrial applications.

All the devices showed good electrical performance and field-effect response (Figure 5.4.2). The reported field-effect mobility, μ was extracted from the transfer curves in the saturation regime, i.e., at $V_{DS} = -80$ V (Figure 5.4.2b). In all the characterized sets, the voltage range was kept constant for both I_D - V_{DS} and I_D - V_{GS} to ensure full comparison among different samples.

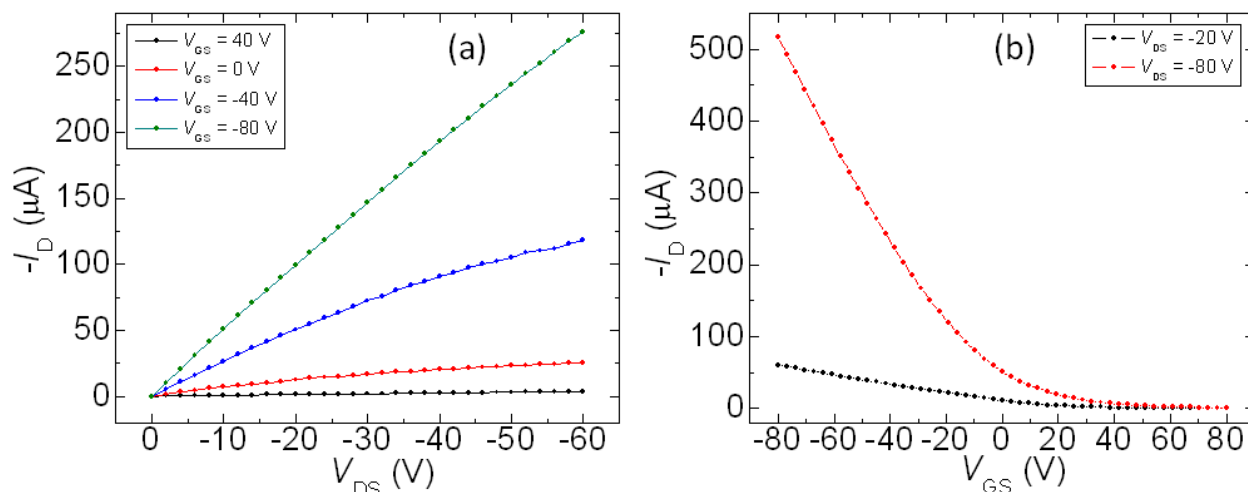


Figure 5.4.2 Electrical characteristics of a transistor with channel width and length of 10mm and 20 μm based on 1:1 P3HT and PTPP blend, (a) Output characteristics (I_D vs. V_{DS}) and (b) Transfer characteristics (I_D vs. V_{GS})

The estimated values for saturation hole carrier mobility, μ_{sat} , of the single components amounts to 0.002 and 0.01 $\text{cm}^2\text{V}^{-1}\text{s}^{-1}$ for dH-PTTP and P3HT, respectively (Figure 5.4.3).

P3HT mobility does not vary considerably upon addition of a small quantity of dH-PTTP (5%), showing a very mild decrease that is representative for a polymer film in which charge percolation is altered by the presence of a few and unconnected domains of dH-PTTP featuring lower mobility. However, the concentration percolation factor, C_0 ,¹² occurs between 5% and 25% as testified by an increase in mobility of a factor of 3. The mobility peak at 50% concentration is due to the presence of dH-PTTP islands $\sim 1\mu\text{m}$ in diameter, surrounded by a P3HT matrix.

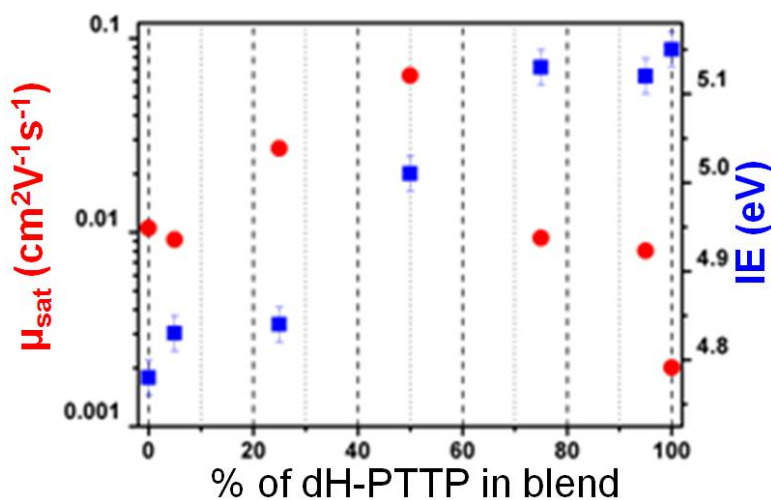


Figure 5.4.3 Variation of the TFT mobility (saturation regime) for different percentage of dH-PTTP in the dH-PTTP/P3HT blend (W/L=500) on the left y-axis and the corresponding ionization energy on the right y-axis.

At 1:1 ratio the vertical phase separation which may arise between the two components is minimized as found through ultraviolet ambient photoelectron spectroscopy (see below). This optimal intermixing is undoubtedly essential factor influencing the charge transport. A remarkable decrease in μ takes place at concentrations exceeding 50%, i.e. at 75% and 95%: at such ratios the percolation path begins to be dominated by larger and larger crystalline domains of dH-PTTP which are less and less interconnected by the surrounding polymer network. Noteworthy, if one considers the mobility of the pristine dH-PTTP it is evident that upon addition of 5% of P3HT, which corresponds to the 95% case shown in Figure 5.4.3, an abrupt increase in device mobility up to 4-fold is observed. This result can be ascribed to the capacity of highly conductive P3HT chains to bridge and connect the large crystalline domains having lower mobility formed by dH-PTTP, thereby enhancing percolation pathways for charge transport.

5.4.2.2 Morphological characterization

Atomic Force Microscopy characterization (Figure 5.4.4) of the film morphology for all the blends provided evidence for the variation of percolation paths for all the different film composition, confirming the charge transport scenario described above. Specifically, for the 75% blend, smooth dH-PTTP islands with a thickness of 2.5 nm are alternated to P3HT domains featuring a height of 3-7 nm height and a lateral size 8.0-20.0 μm . For the 50% blend, P3HT islands with a thickness of 5.8-6.2 nm are at the edge of smooth domains with a diameter of 7.5-27.0 μm and a height of 2.5 nm. For the 25% blend, the features have a height difference of $\sim 2.85 - 4.48$ nm with a “comb mesh” appearance.

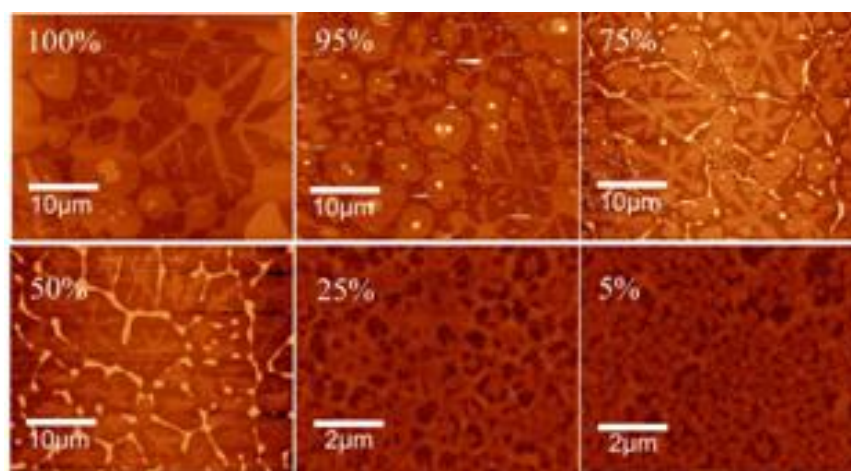


Figure 5.4.4 Topographical Atomic Force Microscopy images of spin-coated dH-PTTP/P3HT blend film (conc. 0.5 mg/mL) in different ratio from 100% down to 5% of dH-PTTP content in the blend. For consistency with the device architecture, the imaged films are realized on a SiO_2 substrate. Z-scale is 20 nm.

It has been already demonstrated that blends of polymer/small molecule give rise to a vertical phase separation: the solvent evaporation leads to a concentration gradient with the more soluble component (dH-PTTP) moving to the top surface.

5.4.2.3 Hole transport levels of the blend

In order to monitor this phenomenon ultraviolet ambient photoelectron spectroscopy measurement were performed to quantify the ionization energy (IE) of the film over a large area of about 4 mm^2 (beam size) with sampling depth of 10-15 nm hence providing an optimal indication of the material under test. The film thickness exceeded 100nm.

The IE levels (Figure 5.4.3) of the single components provided 5.15 eV and 4.78 eV for the dH-PTTP and the P3HT, respectively. Ratio between 75% and 95% featured 5.13 eV and 5.12 eV, respectively, indicating the existence of dH-PTTP at the top surface of the film. Analogously, the measured IE in the 5% and 25% case amounted to 4.84 eV and 4.83 eV which is indicative of a small increase in ionization energy with respect to the bare P3HT case owing to the presence of dH-PTTP in the film. Remarkably, the IE of the 50% blend ratio resulted in 5.01 eV. This indicates that in that specific case the vertical phase-separation is minimized since the work-function, measured over a large area, falls within the average of the values measured in single components. This efficient intermixing between the two species also along the vertical direction can be directly related to the electrical performances which peaked exactly at 50%.

5.4.2.4 Microstructure characterization by GIWAXS and XRD

To gain detailed insight into the molecular organization of P3HT and PTTP in the blended films two-dimensional grazing incidence wide-angle X-ray scattering (GIWAXS) was performed. Surprisingly, after drop-casting pure P3HT is well ordered on the surface and arranges into a typical edge-on lamellar organization towards the surface (Figure 5.4.5a). An out-of-plane oriented chain-to-chain distance of 1.68 nm and an in-plane aligned π -stacking correlation of 0.39 nm are determined which are characteristic values for this polymer.

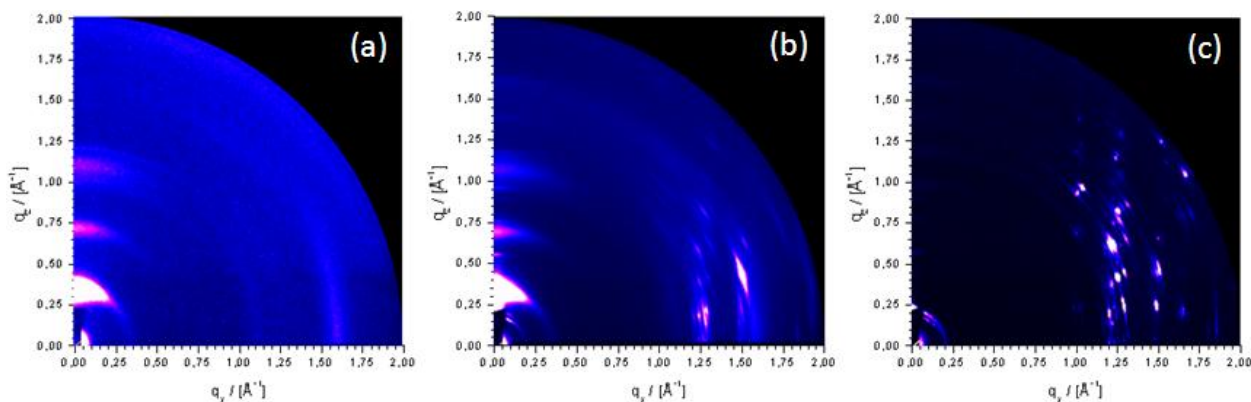


Figure 5.4.5 GIWAXS patterns of drop-cast films of (a) P3HT, (b) dH-PTTP/P3HT blend (50%) and (c) dH-PTTP.

As expected, small molecular PTTP is highly crystalline giving rise to a higher number of reflections (Figure 5.4.5c). The organization is in agreement to the previously reported solution deposited film with two distinct out-of-plane interlamellae spacings of 3.12 nm and 2.78 nm of

edge-on arranged PTTP.²¹ Additional one-dimensional X-ray diffraction (XRD), which corresponds the $q_y = 0 \text{ \AA}^{-1}$ line in the GIWAXS patterns, confirms the presence of two distinct growth orientations or polymorphs of PTTP by the appearance of two main peaks in the small-angle region (Figure 5.4.6).

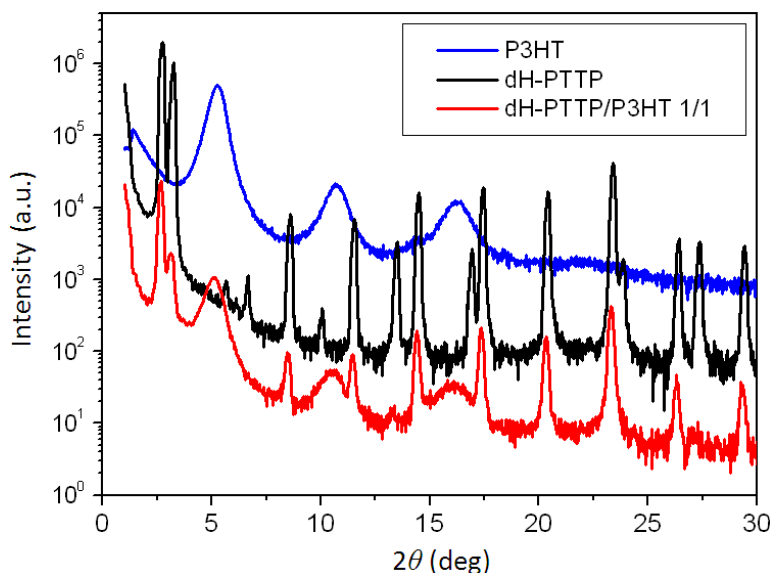


Figure 5.4.6 X-ray diffraction profile of drop-cast dH-PTTP, P3HT and dH-PTTP/P3HT blend film (50%).

Numerous reflections in the wide-angle q_y, z region of the pattern suggest that the molecules are tilted towards the substrate surface.²² For the blended films (see example for 50% dH-PTTP/P3HT blend in Figure 5.4.5b and the XRD pattern in Figure 5.4.6), only reflections for the pure compounds appear confirming a phase separation between P3HT and PTTP and no significant mutual influence on the self-assembly during solution deposition.

The same observation was made for the other blend ratios (Figure 5.4.7). Interestingly, the intensity ratio of the peaks in the XRD for the two crystal orientations of PTTP changes in the blended films towards only one preferred (spacing of 3.1nm), more defined molecular arrangement (Figure 5.4.6).

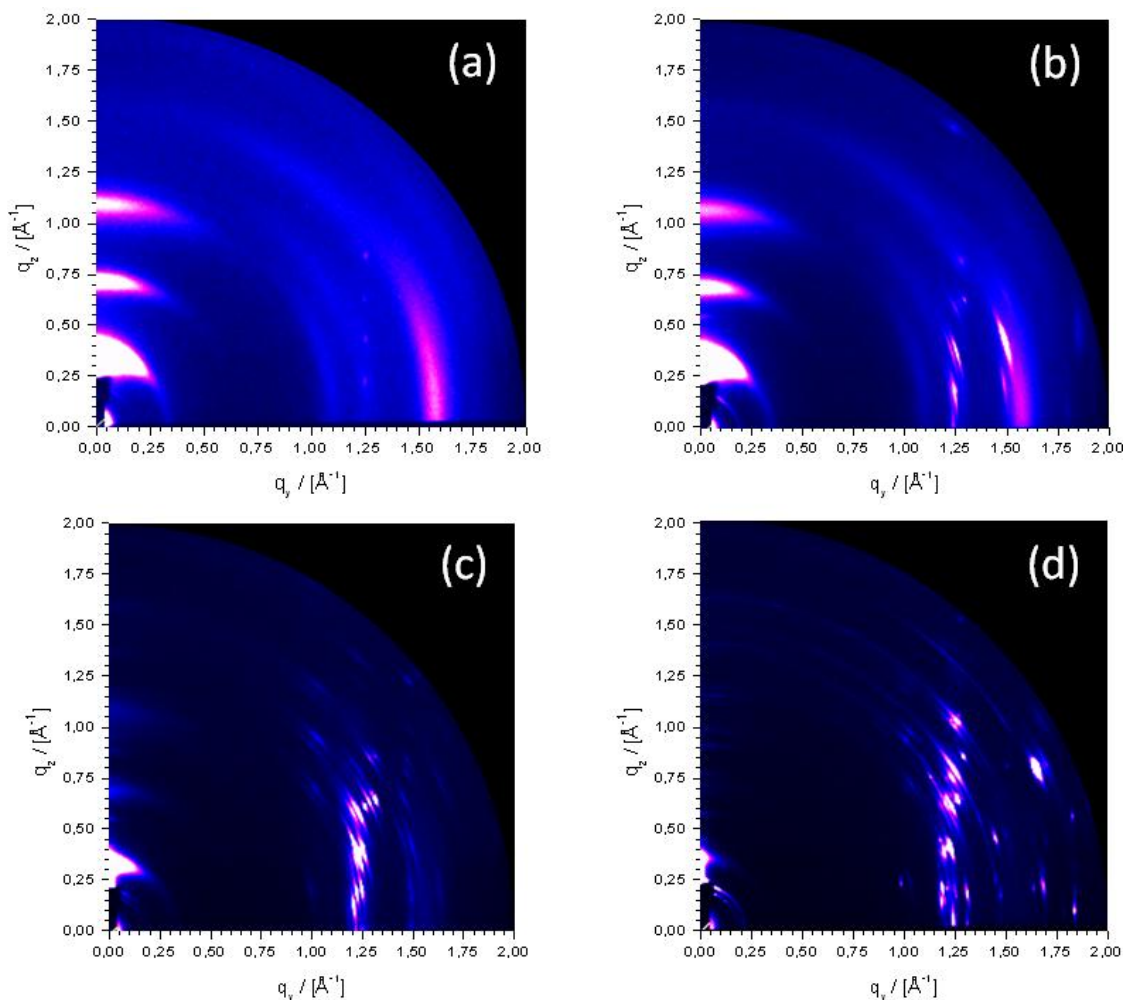


Figure 5.4.7 GIWAXS patterns of drop-cast dH-PTTP/P3HT blend films with a P3HT fraction of (a) 95%, (b) 75%, (c) 25% and (d) 5%.

5.4.3 Conclusions

In summary, the blending of P3HT with a small molecule (dH-PTTP) featuring itself a lower mobility led to an improvement in the conductivity of the electroactive polymer layer. The final hole mobility is as high as $0.1 \text{ cm}^2\text{V}^{-1}\text{s}^{-1}$ in 1:1 blends OTFT, thus a 10-fold enhancement with respect to the mobility of the pristine P3HT was observed. The charge transport of the polymer is improved by the presence of oligomeric crystalline assemblies bridging conducting polymer domains. This remarkable improvement was achieved without introduction of any further surface functionalization or annealing step. Hence, it is highly suitable for real device fabrication processes.

5.4.4 References

- 1 Dimitrakopoulos, C. D. & Malenfant, P. R. L. Organic thin film transistors for large area electronics. *Adv. Mater.* **14**, 99 (2002).
- 2 Gelinck, G. H. *et al.* Flexible active-matrix displays and shift registers based on solution-processed organic transistors. *Nat. Mater.* **3**, 106, (2004).
- 3 Dodabalapur, A. Organic and polymer transistors for electronics. *Mater. Today* **9**, 24 (2006).
- 4 Noh, Y. Y., Zhao, N., Caironi, M. & Sirringhaus, H. Downscaling of self-aligned, all-printed polymer thin-film transistors. *Nat. Nanotech.* **2**, 784, (2007).
- 5 Smits, E. C. P. *et al.* Bottom-up organic integrated circuits. *Nature* **455**, 956, (2008).
- 6 Yan, H. *et al.* A high-mobility electron-transporting polymer for printed transistors. *Nature* **457**, 679, (2009).
- 7 Arias, A. C., MacKenzie, J. D., McCulloch, I., Rivnay, J. & Salleo, A. Materials and Applications for Large Area Electronics: Solution-Based Approaches. *Chem Rev* **110**, 3, (2010).
- 8 Mas-Torrent, M. & Rovira, C. Novel small molecules for organic field-effect transistors: towards processability and high performance. *Chem Rev* **37**, 827, (2008).
- 9 Sirringhaus, H. *et al.* Two-dimensional charge transport in self-organized, high-mobility conjugated polymers. *Nature* **401**, 685 (1999).
- 10 Park, S. K., Jackson, T. N., Anthony, J. E. & Mourey, D. A. High mobility solution processed 6,13-bis(triisopropyl-silylethynyl) pentacene organic thin film transistors. *Appl. Phys. Lett.* **91**, 063514, (2007).
- 11 Anthony, J. E. *et al.* Chromophore fluorination enhances crystallization and stability of soluble anthradithiophene semiconductors. *J. Am. Chem. Soc.* **130**, 2706, (2008).
- 12 Russell, D. M. *et al.* Blends of semiconductor polymer and small molecular crystals for improved-performance thin-film transistors. *Appl. Phys. Lett.* **87**, 222109, (2005).
- 13 Anthopoulos, T. D. *et al.* Solution-processed organic transistors based on semiconducting blends. *J. Mater. Chem.* **20**, 2562, (2010).
- 14 Hamilton, R. *et al.* High-Performance Polymer-Small Molecule Blend Organic Transistors. *Adv. Mater.* **21**, 1166, (2009).
- 15 Dabirian, R. *et al.* The Relationship between Nanoscale Architecture and Charge Transport in Conjugated Nanocrystals Bridged by Multichromophoric Polymers. *J. Am. Chem. Soc.* **131**, 7055, (2009).
- 16 Liscio, A. *et al.* Charge transport in graphene-polythiophene blends as studied by Kelvin Probe Force Microscopy and transistor characterization. *J. Mater. Chem.* **21**, 2924, (2011).
- 17 Katz, H. E., Mushrush, M., Facchetti, A., Lefenfeld, M. & Marks, T. J. Easily processable phenylene-thiophene-based organic field-effect transistors and solution-fabricated nonvolatile transistor memory elements. *J. Am. Chem. Soc.* **125**, 9414, (2003).
- 18 Vaidyanathan, S. *et al.* Investigation of solubility-field effect mobility orthogonality in substituted phenylene-thiophene co-oligomers. *Chem. Mater.* **19**, 4676, (2007).
- 19 Bonini, M. *et al.* Competitive Physisorption Among Alkyl-Substituted pi-Conjugated Oligomers at the Solid-Liquid Interface: Towards Prediction of Self-Assembly at Surfaces from a Multicomponent Solution. *Small* **5**, 1521, (2009).
- 20 Smith, J. *et al.* The Influence of Film Morphology in High-Mobility Small-Molecule:Polymer Blend Organic Transistors. *Adv. Funct. Mater.* **20**, 2330, (2010).
- 21 Mushrush, M., Facchetti, A., Lefenfeld, M., Katz, H. E. & Marks, T. J. Easily Processable Phenylene-Thiophene-Based Organic Field-Effect Transistors and Solution-Fabricated Nonvolatile Transistor Memory Elements. *J. Am. Chem. Soc.* **125**, 9414-9423, (2003).
- 22 Mannsfeld, S. C. B., Tang, M. L. & Bao, Z. Thin Film Structure of Triisopropylsilylethynyl-Functionalized Pentacene and Tetraceno[2,3-b]thiophene from Grazing Incidence X-Ray Diffraction. *Adv. Mater.* **23**, 127-131, (2011).

There is nothing too difficult to be accomplished when done carefully with unflinching endeavor.

-Thiruvalluvar, Poet and Philosopher

6 Charge Transport through SAMs

6.1 CHARGE INJECTION AND TRANSPORT THROUGH BIPHENYLTHIOL SAMs

This section describes the molecular structure-electronic function relationship for a series of biphenylthiol derivatives with varying torsional degree of freedom in their molecular backbone when self-assembled on gold electrodes. These biphenyl thiol molecules chemisorbed on Au exhibit different tilt angles with respect to the surface normal and different packing densities. The charge transport through the biphenyl thiol self-assembled monolayers (SAMs) showed a characteristic decay trend with the effective monolayer thickness. Based on parallel pathways model the tunneling decay factor β was estimated to be 0.27 \AA^{-1} . The hole mobility of poly(3-hexylthiophene)-based thin film transistors incorporating a biphenyl thiol SAM coating the Au source and drain electrodes revealed a dependence on the injection barrier with the highest occupied molecular orbital (HOMO) level of the semiconductor. The possible role of the resistivity of the SAMs on transistor electrodes on the threshold voltage shift is discussed. The control over the chemical structure, electronic properties and packing order of the SAMs provides a versatile platform to regulate the charge injection in organic electronic devices.

6.1.1 Introduction

The prediction by Aviram and Ratner that organic molecules could exhibit the property of electrical current rectification¹ triggered remarkable research efforts which have been blooming with the emergence of molecular electronics. The nanoscale electronic properties in molecule based junctions can be controlled through a proper molecular design.²⁻⁴ A particular approach for preparation of molecular junctions is the chemisorption of sulfur exposing molecules on metallic surfaces like Au, Ag and Pt, which provides a facile route to form highly ordered self-assembled monolayers (SAMs).⁵⁻⁷ These junctions can feature distinct functionalities including electrical current rectification,^{4,8} photo responsive current switching,^{3,9-11} wettability and work function modification.^{12,13} These tunable properties, which depend on the choice of the molecule and metal electrode, have been shown to make SAMs ideal component for optimizing the charge

injection at metal-organic interfaces for application in organic thin-film transistors (OTFTs)¹²⁻¹⁵ A deep knowledge on the transport properties through the SAMs can thus be a determinant information for the design and further fabrication of the organic electronic devices incorporating these monolayers. The charge transport through molecules sandwiched between two metallic electrodes has been probed using a variety of different techniques such as conducting-probe atomic force microscopy (CP-AFM),^{3,16,17} Hg droplet based electrodes,^{18,19} mechanically controlled break junctions,²⁰⁻²² scanning tunneling microscopy (STM),^{2,23} nano-pores,²⁴ crossed-wire tunneling junctions,²⁵ junctions formed via surface-diffusion-mediated deposition (SDMD),²⁶ and non-intrusive conformal junctions on the SAM comprising of a liquid metallic gallium indium (GaIn^E) tip as the probe electrode.²⁷ Each of the above mentioned techniques has its own *pros* and *cons* with variable range of set-up complexities, junction areas, geometry of contacts and conditions necessary for experimentation. The GaIn^E based junction is particularly interesting since it exploits the peculiar property of the eutectic alloy of the liquid metallic gallium and indium to behave like a non-Newtonian liquid at room temperature. Importantly, it can be molded into conical tip which retains its shape under ambient conditions. Significantly, GaIn^E features an intrinsic property to form a thin oxide layer (~ 1-2 nm) when exposed to air; importantly, such a self-bounding oxide (Ga₂O₃) sheath enables the bulk of the underlying GaIn^E to hold its shape.²⁷ The ease of forming reliable and reproducible conical shaped GaIn^E tips has been exploited to study the charge transport of delicate μm^2 sized single molecular layer junctions.^{4,27-30}

In contrast, other types of counter-electrodes like those based on Hg-drop needed a protecting alkanethiol layer coating the counter-electrode to improve the yield³¹ by mitigating formation of junction short-circuits when placing the drop in contact with the SAM on the metallic substrate.^{19,32,33} Similarly, thin conducting film of PEDOT:PSS polymer^{11,34} or graphene³⁵ has been employed to protect the SAM prior to deposition of top Au electrodes in large area molecular junctions.

Traditionally *n*-alkanethiols have been widely studied,^{16,19,23,24,30,34,36,37} and successfully employed to change the wettability and work function properties of gold contacts, but their scope as functional components for molecular electronic devices is limited. The better conducting aromatic compounds offer a far more versatile platform to modulate their electronic properties

by altering the chemical structure of the molecule^{28,38-44} or by influence of external stimuli like thermal energy or light.^{3,29,33}

Here we have designed and synthesized a new library of mono-thiolated biphenyl molecules featuring different torsion angles between the two phenyl subunits along the molecular backbone. Although there have been studies on the single molecular conductance of biphenyl units thiolated in both α and ω positions,^{2,45,46} the charge transport through biphenyl mono-thiol SAMs with varying torsion in the molecular long axis have not yet been explored on a macroscopic scale. On the one hand, once chemisorbed on Au(111), we investigated the charge transport through the biphenyl mono-thiol SAMs embedded in a two terminal junction based on a top GaIn^E counter-electrode. On the other hand, we functionalized the source and drain electrodes of OTFTs with biphenyl mono-thiol SAMs exploited them to tune the charge injection at the metal-organic interface of the devices.

The torsion angle between individual aromatic rings in doubly thiolated biphenyl derivatives has been shown, via single molecule break junction based on STM, to govern the electrical conductivity across single molecular scale.^{2,45,46} Both theoretical⁴⁰ and experimental results^{2,45-47} provided evidence for a correlation between the cosine square of the torsions angle and the single molecule conductance. The increasing torsion angle is accompanied by a decrease in the extent of the geometrical overlap of p_z orbitals; as a result the corresponding single molecular conductance decreases since the electron transfer rates scale as a function of the square of p_z orbital overlap. Moreover if the contribution due to tunneling transport through the σ -orbitals is neglected, the theory predicts a linear relationship between the molecular conductance with the square of the cosine of torsion angle.⁴⁸

The different mono-thiolated biphenyl derivatives exploited and characterized in the present study are:

Molecule **1**: 9*H*-fluorene-2-thiol, denoted here as **5m BPT** due to the fluorene group bridging the two individual phenyl rings;

Molecule **2**: 1,2-bis(9,10-dihydrophenanthren-2-yl)disulfane denoted as **6m BPT**;

Molecule **3**: [1,1'-biphenyl]-4-thiol denoted as **BPT**;

Molecule **4**: 2,2'-dimethyl-[1,1'-biphenyl]-4-thiol denoted as **tBPT** (i.e., twisted BPT).

See ref for the complete synthesis details of the biphenylthiol derivatives.

6.1.2 SAM Packing Density and Orientation

6.1.2.1 HRXPS on biphenylthiol SAMs.

The C 1s and S 2p HRXPS spectra of all the SAMs used in this study are shown in **Error! Reference source not found.**. The spectra were gathered at wave energies of 350 eV and 580 eV for the C 1s and at 350 eV for the S 2p emission. In the C 1s spectra a single emission at 284.2-284.3 eV is observed, which is attributed to the aromatic backbone of the SAM constituents.

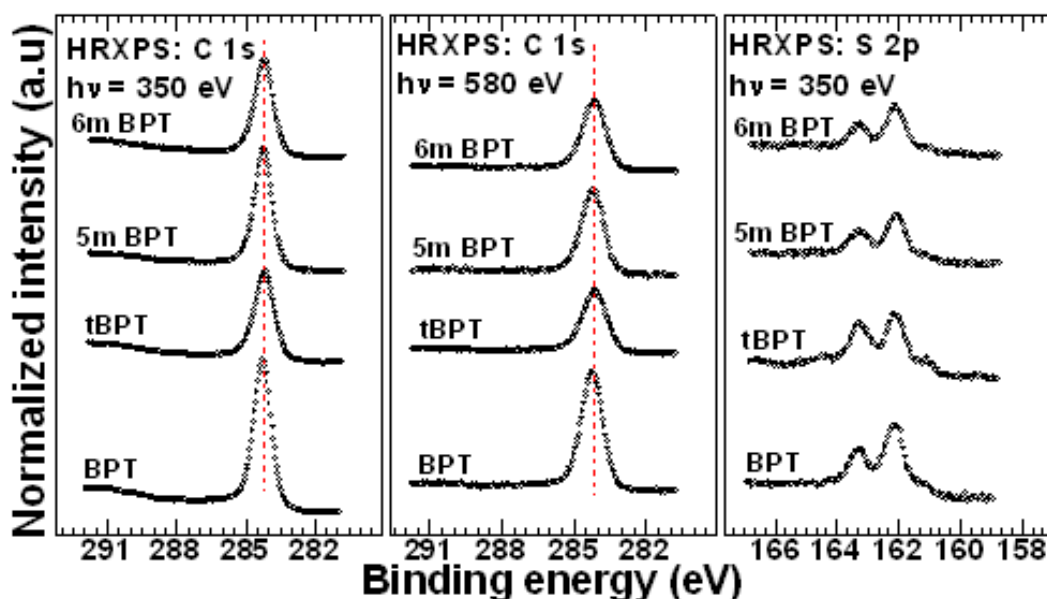


Figure 6.1.1 C 1s (left and middle panels) and S 2p (right panel) HRXPS spectra of the target SAMs acquired at photon energies of 350 eV (left and right panels) and 580 eV (middle panel). The red lines are guide for the eye and are placed at a BE of 284.2eV.

A characteristic emission in a similar binding energy (BE) range of 284.2-284.3 eV has previously been reported for biphenyl-derivative dithiols (BPDTs).⁴⁹ The S 2p spectra of the SAMs are dominated by the S 2p_{3/2,1/2} doublet with at 162.0 eV (S 2p_{3/2}) corresponding to a thiolate-type bonding of the SAM constituents to the substrate.^{49,50} This doublet is the only feature in the spectra of 6m BPT and 5m BPT SAMs but is accompanied by an additional weak doublet at a BE of ~161.0 eV (S 2p_{3/2}) in the spectra of BPT and tBPT monolayers and by a further weak doublet at a BE of 163.4-163.5 eV in the spectrum of tBPT SAMs. The former doublet can be assigned to the differently (but strongly) bound SAM constituents while the latter

to the unbound or weakly bound molecules which are either caught in the hydrocarbon matrix of the SAM or physisorbed at the SAM/ambience interface,⁵¹ the content of all these species is however quite low.

Further, the effective thicknesses of the SAMs were calculated according to standard procedure using the intensity ratios of the C 1s and the Au 4f signals and the standard attenuation lengths for the Au 4f and C 1s emissions at the given kinetic energies.^{50,52} In addition to the above thickness values, the packing density in the target SAMs were estimated on the basis of the S2p/Au4f intensity ratio, using a SAM with a known packing density, viz. dodecanethiol on Au(111) in the given case, as a reference.⁵³ The derived values of the effective thickness and packing density of the target SAMs are displayed in Table 6.1-1. A smaller thickness of the SAM in comparison to the estimate of the length of the BPT molecule (~12 Å) in the gas phase suggests that the SAM constituents have some degree of inclination. The packing density of the target SAMs is of the following trend BPT > 6m BPT > 5m BPT > tBPT.

Table 6.1-1 Effective SAM thickness in Å along with packing density of the molecules in for the different BPT SAMs in comparison to the reference of dodecanethiol SAM.

SAM	Effective thickness (Å)	I(S 2p)/I(Au 4f _{7/2})	Packing density x 10 ¹⁴ mol/cm ²
C12	15		4.63
5m BPT	11.68	0.06867	3.67
6m BPT	9.08	0.068842	3.68
BPT	11.45	0.079533	4.25
tBPT	8.13	0.054446	2.91

6.1.2.2 NEXAFS measurements.

Figure 6.1.2 shows the C K-edge NEXAFS spectra of the target SAMs. The spectra in the panel were acquired at the so called magic X-ray incidence angle (55°), which offers spectra independent of the molecular orientation, representative of the electronic structure of the only unoccupied molecular orbitals.⁵⁴ The curves in the right panel are the differences between the spectra acquired at X-ray incidence angles of 90° and 20°; such curves are representative of the molecular orientation.⁵⁴ The spectra are dominated by the intense π_1^* resonance of the phenyl rings at ~285.1 eV accompanied by the respective π_2^* resonance at 288.8 eV, the R*/C-S*

resonance at ~ 287.8 eV, and several broad σ^* resonances at higher photon energies (the assignments were performed in accordance with literature data).^{49,50,55-57} Note that the pattern of the absorption resonances for the SAMs used in this study is similar to that of benzene as can be expected.^{52,58} In the case of BPT SAM this pattern can be attributed to the localization of the excited molecular orbitals at a particular aromatic ring.⁵⁸ In accordance with the literature data,⁴⁹ the aliphatic bridging group in the 5m and 6m BPT does not change this pattern significantly, which means that the conjugation between the aromatic rings is not affected. Note that this correlates with the spacing between the rings in these compounds which exceeds a critical value of 1.477 \AA .⁵⁹ On the basis of the intensity of the π_1^* resonance, the quality of the target SAMs follows the trend BPT > 5m BPT > 6m BPT > tBPT in agreement with the HRXPS results (see previous Section). In addition, the π_1^* resonance for the tBPT SAMs is somewhat broader than for the other monolayers of the given study, which is a further evidence for the higher degree of heterogeneity in this particular film.

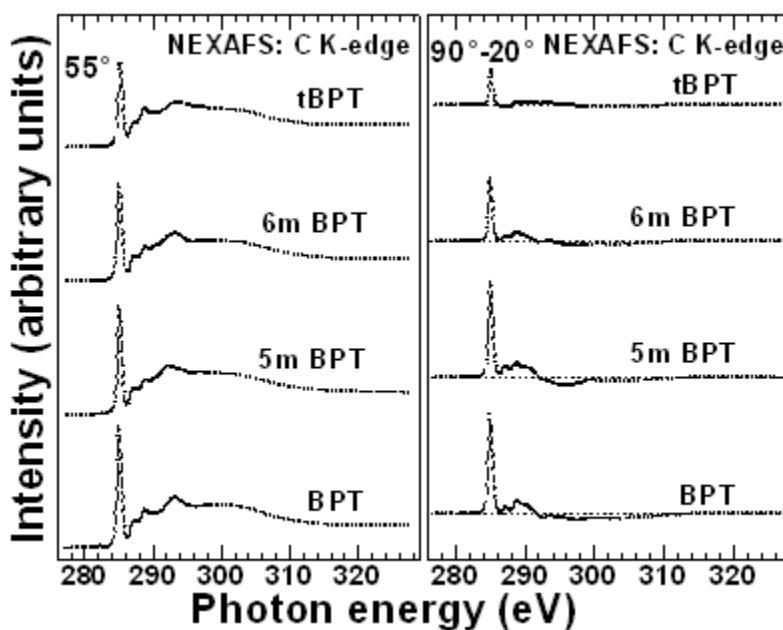


Figure 6.1.2 C K-edge NEXAFS spectra of the target SAMs acquired at an incidence angle of 55° (left panel) and the difference of the spectra acquired at X-ray incidence angles of 90° and 20° (right panel). Horizontal dashed lines in the right panel correspond to zero.

In addition to the above analysis of the 55° spectra, information on the molecular orientation in the target SAMs could be obtained on the basis of the entire set of the NEXAFS data. In particular, the average tilt angle of the aromatic chains in these films can be estimated by a

quantitative analysis of the angular dependence of the NEXAFS resonance intensities⁵⁵. For this analysis, the π_1^* resonance was selected as the most intense and distinct resonance in the absorption spectra. In addition, the intensities of this resonance could be derived directly from the NEXAFS spectra, without a sometimes ambiguous fitting procedure. As soon as these intensities I are known, the average tilt angle α of the π_1^* orbitals with respect to the surface normal can be derived from a standard expression for a vector-type orbital,⁵⁴

$$I(\alpha, \theta) = A \left\{ P \times \frac{1}{3} \left[1 + \frac{1}{2} \cdot (3 \cdot \cos^2 \theta - 1) \cdot (3 \cdot \cos^2 \alpha - 1) \right] + (1 - P) \frac{1}{2} \sin^2 \alpha \right\} \quad (6.1.1)$$

where A is a constant, α is the average tilt angle of the molecular orbital, P is the polarization factor and θ is the incidence angle of the incoming X-rays. The tilt angle α of the π_1^* orbitals is directly related to the tilt angle φ of the molecular axis with respect to the surface normal and to the average twist angle \mathcal{G} of the aromatic rings with respect to the plane spanned by the surface normal and the molecular axis.⁶⁰

$$\cos \alpha = \cos \mathcal{G} \cdot \sin \varphi \quad (6.1.2)$$

This expression allows estimation of the tilt angle of the molecular axis as soon as some assumptions about the value of the twist angle are made. In the case of the SAMs of this study it is reasonable to assume a herringbone arrangement which is typical for aromatic bulk systems and for aromatic SAMs.^{61,62} This means two different spatial orientations of the aromatic moieties occurring with opposite signed (i.e., reverse) twist angles $\mathcal{G}_1 = -\mathcal{G}_2$ and the similar tilt angles $\varphi_1 = \varphi_2$. The different signs of the twist angle are not a problem since $\cos \mathcal{G} \cos \varphi$ is an even function. The most reasonable assumption for the absolute value of the twist angle is 32° which is the value observed in the biphenyl bulk materials⁶¹ and well applicable to aromatic SAMs.^{60,63,64} Table 6.1-2 collects the estimated average tilt angle of π_1^* orbitals (α), tilt angles of molecules (φ) and the assumed twist angle (\mathcal{G}). Note that we assume a coplanar arrangement of individual rings within the biphenyl backbone in the BPT SAMs, which is a reasonable assumption considering that this arrangement is typical for densely aromatic compounds where the dihedral rotation is lifted due to the intermolecular interaction.⁶¹ The backbone of 5m BPT SAMs has the planar conformation,⁶⁵ while the torsion angle for the backbone of the 6m BPT SAM is $\sim 16.8^\circ$ (see Table 6.1-3 and ref.⁶⁶). The torsion angle for the backbone of the tBPT SAM

is close to 80° (see Table 6.1-3 and ref.⁴⁹), so that the assumed twist angle can only be considered as an average value over the both rings. The accuracy of the derived tilt angles is about $\pm 3^\circ$ which is partly related to the uncertainty of the twist angles. The derived tilt angles represent average values over macroscopic area of the SAM and thus can be taken as a fingerprint of the orientational order. Indeed, a totally disordered molecular film exhibits no linear dichroism and can be associated with an average tilt angle of a vector orbital of 54.7° since $I(a,q)$ does not depend on q at $a = 54.7^\circ$ (see eq 1). A deviation from this value, as it occurs for the SAMs of this study, means a certain degree of the orientational order, with a higher degree for a higher deviation.

The highest orientational order is observed for the BPT and 5m BPT SAMs, in accordance with the planar conformation of 5m BPT⁶⁵ and the assumed planar conformation of BPT;^{59,61} such a conformation should favor high orientational order and dense molecular packing. Even slight deviation from the planar conformation, as is the case for 6m BPT⁶⁶ results in a lower packing density (see previous section) and some deterioration of the orientational order (see Table 6.1-2). Finally, a distinct non-planar conformation adopted by tBPT causes even lower packing density (see previous Section) and even worse orientational order (see Table 6.1-2). Thus, the results from the HRXPS and NEXAFS seem to corroborate the fact that the quality and packing density of the SAMs is the highest for the BPT SAM, slightly worse for the 5m BPT SAMs, distinctly worse for the 6m BPT SAMs, and the worst for the tBPT SAMs, in full correlation to the torsion angle in the biphenyl backbone. The slightly better quality of the BPT SAMs as compared to the 5m BPT monolayers is presumably related to the presence of the side bridge in the latter case, which can be associated with additional sterical demands.

Table 6.1-2 Tilt angle and parameters estimated from the NEXAFS data.

SAM	ϑ_t (deg) ^a	α (deg) ^b	ϑ (deg) ^c	φ (deg) ^d
5m BPT	0^{65}	69.0	32.0	25.0
6m BPT	20^{66}	66.9	32.0	27.6
BPT	0^{61}	71.5	32.0	22.0
tBPT	79.7^{49}	62.4	32.0	33.0

^a solid state torsion angle. ^b average tilt angle of π_1^* molecular orbital. ^c assumed twist angle. ^d average tilt angle all in degrees.

6.1.3 Charge Transport through Biphenylthiol SAMs

To gain insight into the charge transport across the target SAMs supported on Au we performed *I-V* measurements in 2-terminal junctions by using a GaIn^E tip as the top counter-electrode. We describe the junctions formed following the naming convention Au–SAM/Ga₂O₃||GaIn^E in which “–” indicates a covalently bonded contact, “/” denotes the physically formed contact between the surface of the SAM and the Ga₂O₃ layer, and “||” denotes the interface between Ga₂O₃ and GaIn^E bulk.

Tunneling is known to be the governing charge transport mechanism through π -conjugated molecules shorter than ~ 3 nm.^{67,68} The current density (J) due to tunneling typically follows an exponential decay with molecular length according to the simplified approximation of Simmons model, $J = J_0 e^{-\beta d}$ where d is the molecular length (in Å) (in this present work d is considered to be the SAM effective thickness) and β (in Å⁻¹) is the tunneling decay constant. To gather adequate amount statistical data for the range of charge tunneling through the target SAMs we formed a minimum of at least 20 junctions for each of these monolayers and analyzed the resulting data without “selecting”, “eliminating”, “excluding” or “discarding” any of the recorded data points to arrive at the actual range of J distribution across each of the SAMs. The oxide skin covering the GaIn^E bulk was reported to have an electrical resistivity of 0.4 MΩcm, corresponding to a J of 5.5 A/cm² at 0.2 V,⁶⁹ which is much lower than the resistivity of any SAM in this study. The above current density is nearly 3 orders of magnitude greater than the analogous value for the tBPT SAM ($J = 2.1 \times 10^{-2}$ A/cm² at 0.2 V) which is the most conductive sample in this study. This would imply that the corresponding resistance of the least resistive tBPT SAM is ~ 3 orders of magnitude greater than the Ga₂O₃ layer. Hence the resistivity contribution of the oxide skin to the overall J measured for the junctions can be reasonably neglected, since the total resistance is the direct sum of the two individual resistive components of the oxide in series with that of the SAM. Figure 6.1.3 shows the variation of the mean of $\log|J|$ with the applied bias across the junctions for all SAMs of this study. The charge transport through these monolayers clearly shows a trend which would be expected in the case of non-resonant tunneling.^{70,71} The distribution of J through the SAM follows a log-normal tendency this is attributed to the exponential dependence of charge tunneling over the distance d .^{19,30,72} In addition the J is more biased to higher values which arises due to junction shorts conversely the

log-mean of J ($\mu_{\log|J|}$) results in a more reasonable estimate of J taking into account the high and low end (i.e., shorts and non-contact $J(V)$ traces respectively) of the distribution of J . The geometric mean of $\log|J|$ is given by,

$$\langle J \rangle_{\log} = 10^{\mu_{\log|J|}} \quad \text{In which } \mu_{\log|J|} = \left(\frac{1}{n_{jn}} \sum_{obs=1}^{n_{jn}} \log_{10}|J_{obs}| \right) \quad (6.1.3)$$

Where n_{jn} is the total number of J observations (J_{obs}) recorded at a particular voltage taken from the J - V traces.

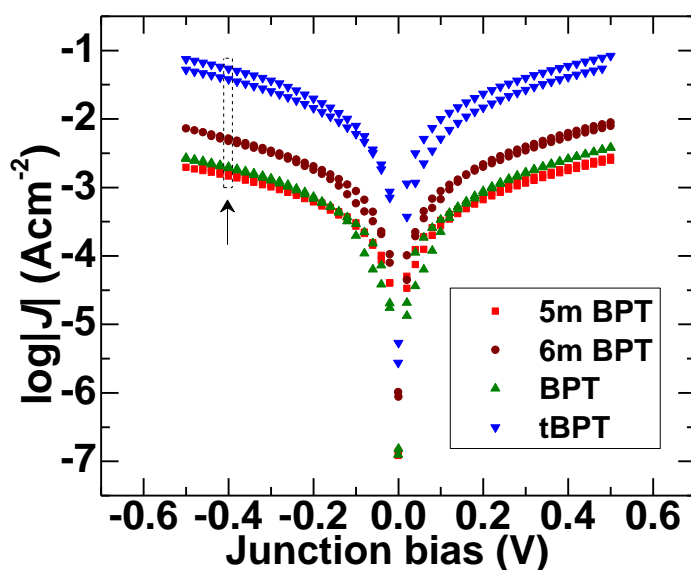


Figure 6.1.3 Characteristics of mean log current density as a function of junction bias for the Au-5m BPT/Ga₂O₃||GaIn^E, Au-6m BPT/Ga₂O₃||GaIn^E, Au-BPT/Ga₂O₃||GaIn^E and Au-tBPT/Ga₂O₃||GaIn^E junctions indicating forward and reverse traces. The arrow indicates the bias value from which the $\log|J|$ values were extracted to populate the histogram.

Figure 6.1.4 exhibits the $\log|J|$ distributions for the 5m BPT, 6m BPT, BPT and tBPT SAMs, respectively. The log-normal histograms for each of the monolayers were populated by taking the $\log|J|$ values at a bias voltage of -0.4 V. From the peak of the Gaussian fitting of the histograms it was possible to estimate the $\mu_{\log|J|}$ value which offers an estimate of highest likelihood occurrence of J for a particular SAM. All histogram plotting and corresponding data analysis were done using the ggplot2⁷³ package of R.⁷⁴ Although in a chemisorbed SAM the molecules are believed to be arranged in well-ordered (i.e., similar to a 2D crystal pattern)

manner, it is likely that there can be structural defects which may arise from several factors, including the presence of physisorbed adlayers, trace impurities on the electrode, defects induced by the substrate surface profile among others. As these features influence the charge transport across the SAMs, it is imperative to acquire a large number data to obtain a meaningful estimate of J for each of the target monolayers. In total more than 20000 J values were collected with at least a minimum of 3206 I - V traces recorded for each of the SAMs on at least 2 samples per SAM.

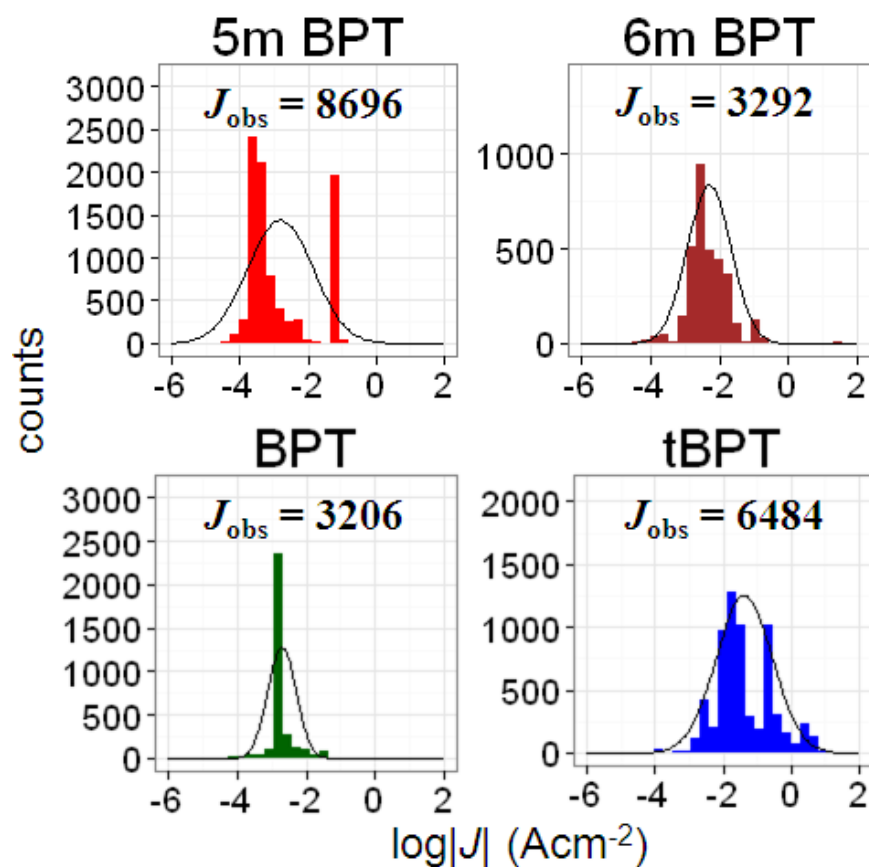


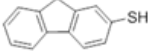
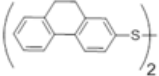
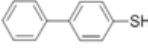
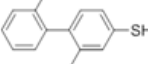
Figure 6.1.4 $\log|J|$ distribution profiles at a bias of -0.4V for the corresponding biphenyl thiol SAMs in the order of 5m BPT, 6m BPT, BPT and tBPT from left to right the total number of recorded J observations (J_{obs}) are indicated in respective histograms.

The higher degree of disorder and lower packing density of the tBPT SAMs influences the J showing clearly several distinct multiple peaks (with broader distribution range) in the $\log|J|$ histogram (see Figure 6.1.4). This is in contrast with the more narrow distribution of the $\log|J|$ in SAMs of BPT and 6m BPT as a result of a better packing density. The corresponding J values

were used to populate the histograms. The statistical data for the recorded J values are collected in Table 6.1-3 along with the molecular chemical structure.

The thickness of the SAMs depends on the tilt angle with respect to the surface normal, i.e. the greater the tilt angle the lower the effective thickness that corresponds to the separation between electrodes. An illustration of how the effective thickness of the SAM changes with increase of the tilt angle is shown in . From the plot of $\log|J|$ vs. d (i.e., effective monolayer thickness) the parameters J_0 and β can be extracted on the basis of the y-intercept and linear slope, respectively. We observed that the SAM with a greater tilt angle, i.e. tBPT-SAM, was more conductive than that with a lower tilt angle, i.e. 5m BPT-SAM, by a factor of ~ 27 in the linear scale (~ 2 in $\log|J|$ magnitude). In oligo-aromatic architectures the charge tunneling contributions are likely due to through-bond tunneling and through-space tunneling.⁷⁵

Table 6.1-3 Molecular structure and charge transport properties of biphenyl thiol SAMs

SAM	Molecular structure ^a	torsion angle (deg) ^b	n_{jn}^c	J_{obs}^d	J_{sc}^e	yield (%) ^f	$\mu_{\log J } \pm \sigma$ (A/cm ²) ^g	$\mu_J \times 10^{-3}$ (A/cm ²) ^h
5m BPT		1.1	24	8696	6	99.93	-2.81 ± 0.62	1.55
6m BPT*		16.8	30	3292	18	99.45	-2.30 ± 0.35	5.01
BPT		36.4	20	3206	3	99.90	-2.71 ± 0.10	1.94
tBPT		79.7	34	6484	6	99.91	-1.38 ± 0.58	41.69

^a Molecular structure of different BPT derivatives used. ^b Torsion angle between the planes of the phenyl rings from x-ray structure adapted from ref 45 and 46. ^c Number of junctions formed. ^d Total number of J observations for each SAM. ^e Number of J - V traces which resulted in a short where I reach 10^{-3} A. ^f yield given as the ratio between the difference between total and shorting $J(V)$ traces to the total J observations. ^g Mean of $\log|J|$ from the log-normal distribution of J . ^h Mean value of J .

Owing to the minimal difference in the molecular length for the biphenyl thiol derivatives it was not possible to resolve unequivocally the influence of tunneling due to through-bond molecular length.

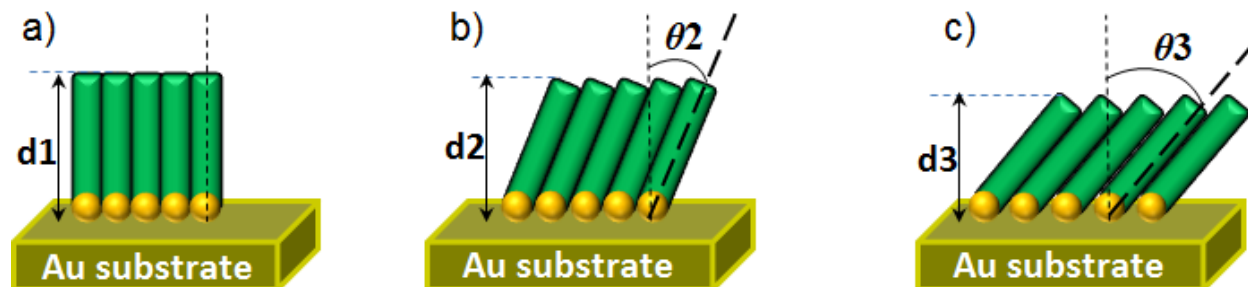


Figure 6.1.5 Schematic illustration of the change in the effective SAM thickness with increase in the tilt angle of the molecules with respect to the surface normal. The dark yellow circles and the green bars represent the sulfur atoms and the molecular backbone respectively. The ratio of the width-to-height sufficiently represents the scaled-up geometry of the biphenylthiol molecules on the gold surface.

To understand if the current density exhibits dependence on the SAM medium we plotted the $\log|J|$ with respect to the effective monolayer thickness (Figure 6.1.6). We observed a β of $0.27 \pm 0.08 \text{ \AA}^{-1}$ from data extracted at a bias of -0.4V (Figure 6.1.6); this is in agreement with the β extracted from a series of phenylene oligomers based SAM measured in a large-area molecular junction.⁷¹

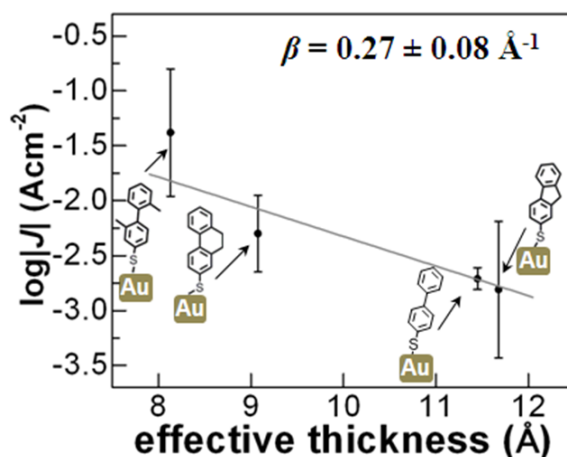


Figure 6.1.6 Plot of $\log|J|$ vs. effective monolayer thickness for BPT SAMs at a bias of -0.4V showing the respective tunneling decay factor estimated from the slope.

On closer inspection of the decay of current density with respect to the effective thickness for the biphenyl thiol monolayers, it is clear that there is characteristic attenuation with increase in the distance of separation. It is interesting to note that the $\log|J|$ dependence with cosine square torsion angle for our biphenyl thiol SAMs exhibits an opposite trend observed in similar molecules on a single molecular scale (see Figure 6.1.7).^{45,46}

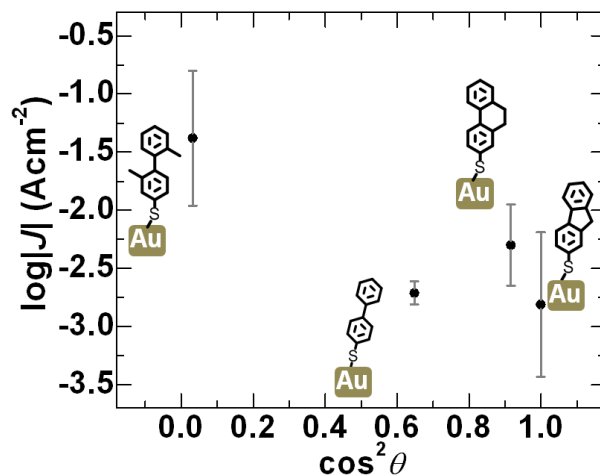


Figure 6.1.7 $\log|J|$ variation with the cosine square of torsion angle recorded at a bias of -0.4V.

We attribute this to the likely weaker cohesive interaction between the SAM and top GaIn^E electrode⁸ which is considered to be of van der Waals nature, being in contrast to the much stronger covalent electronic coupling between the biphenyl dithiol molecules and gold electrodes studied by Vonlanthen et al.^{45,46}

6.1.4 Biphenylthiol SAMs in OTFT electrodes

6.1.4.1 OTFT performance

To bestow information onto the charge injection properties of OTFT electrodes modified with biphenyl-based SAMs we fabricated and characterized transistors in bottom-gate bottom-contact device geometry by using P3HT as active semiconducting layer. The channel length (L) and width (W) for the OTFTs under study amounted to 10 and 10000 μm , respectively. Given that the performance of OTFTs was acutely sensitive enough to detect the subtle differences in charge transport across SAMs chemisorbed on the source and drain electrodes,¹² we sought to determine the influence of the varying torsion angle molecules composing the SAM. Figure 6.1.8 shows the OTFT device configuration along with the chemical structure of the molecules incorporated in the electrodes and the active layer of the transistor.

The route to modify the electrode work function (Φ_M) by means of SAMs and thereby to adjust the energy levels in the system to either inject or extract charge carriers (electrons or holes) more effectively in organic electronic devices have been vastly exploited.^{14,76-80} In particular, the chemisorption of alkanethiols and partially perfluoroalkanethiols has been used to lower or raise the work function of Au electrodes, respectively, to ultimately improve the injection of electron

or holes.⁷⁶ The shift in the work function is generally attributed to the total of effective dipole moment formed between the Au-S bond along with the dipole moment due to monolayer chemical composition of the molecule in the SAM,⁸¹ the tail groups contributing notably to the overall interfacial dipole.^{82,83} Among different possibilities, the work function of the metal can be measured by means of the contact potential difference (CPD) technique of a macroscopic Kelvin probe. We extracted the work function of Au electrodes comprising of biphenyl-based SAMs from the CPD using an Au reference tip ($\Phi \sim 5.1$ eV). Table 6.1-4 collects the respective data along with the work function of a bare Au electrode. The work function for the BPT SAM was measured to be $\sim 4.81 \pm 0.01$ eV, which is in the range of the reported value in literature.¹⁴

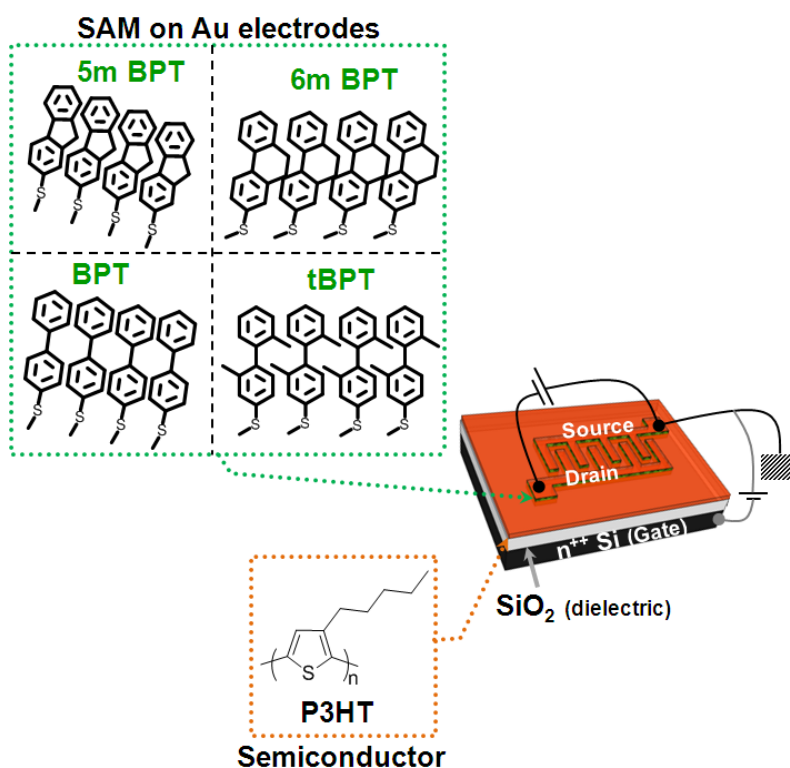


Figure 6.1.8 Schematic of the OTFT with the chemical structure of the molecules used in the SAM and the active layer. The biasing configurations for the respective electrodes are indicated.

The work function difference between the more disordered Au-tBPT SAM with respect to the ordered Au-BPT SAM was ~ 210 meV, note that being the molecules intrinsically quite non-polar the effective shift in the work function due to the variability in packing densities and tilt angle of the assembled monolayer is fairly evident from the recorded values of Φ_M . The surface wetting properties of the Au-SAM were estimated over macroscopic areas from the static water

contact angle (θ_{ca}) measurements giving values spanning between ~ 70 and 79 degrees (see Table 6.1-4), therefore highlighting a higher hydrophobic nature of the coated electrodes respect to the bare gold. The θ_{ca} for Au-BPT SAM ($\sim 78.9^\circ$) was in excellent agreement for the similar type of metal-SAM surface reported by us earlier.¹⁴ Note that these values match closely to the contact angle reported in the literature for non-substituted biphenyl thiol SAMs on Au(111).⁸⁴ The output (drain current (I_D) vs. source-drain voltage (V_{DS})) and transfer (I_D vs. gate voltage (V_{GS})) characteristics were measured for the devices incorporating electrodes modified with the BPT family SAMs and compared with devices with non-functionalized electrodes. The I_D vs. V_{DS} plot obtained for the device with the biphenylthiol SAM (BPT SAM) modified electrodes are portrayed in Figure 6.1.9.

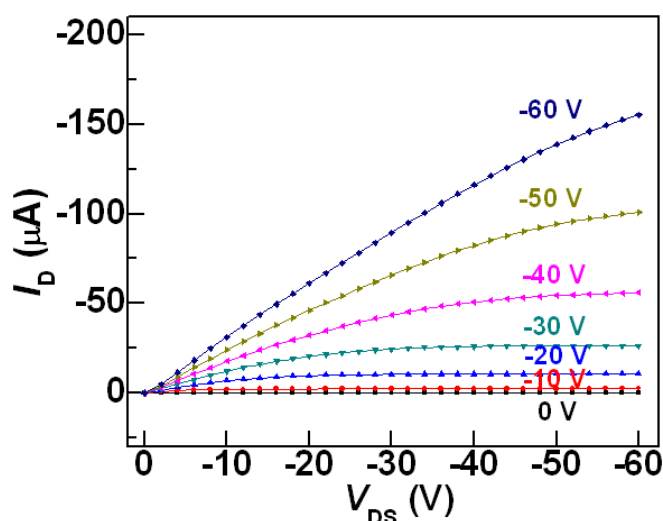


Figure 6.1.9 Output characteristics for TFT based on Au-BPT SAM modified electrodes ($W=10000 \mu\text{m}$ and $L=10\mu\text{m}$) with respective V_{GS} denoted.

The recorded I_D vs. V_{GS} curves for the TFTs with the electrodes modified with the different SAMs are shown in Figure 6.1.10. The other key device performance indicators like turn on voltage (V_{on}) and the threshold voltage (V_T) were estimated from the transfer plots. The V_{on} is the voltage value in which a change in slope sign occurs in the log scale on the transfer curves and was extracted from the I_D - V_{GS} plots in the linear regime. V_T is the intercept with gate voltage axis from the plot of $\sqrt{|I_D|}$ vs. V_{GS} (Figure 6.1.10) and provides the value of gate potential at which most of the traps levels are filled up.

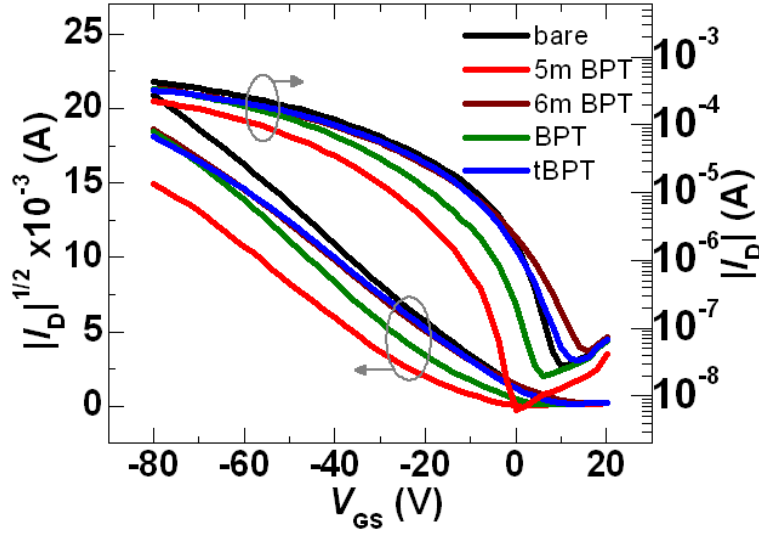


Figure 6.1.10 Transfer curves for the OTFTs based on electrodes with different BPT SAMs showing variation of square root of I_D vs. V_{GS} (left axis) and semilog I_D vs. V_{GS} (right axis) when $V_{DS} = -60$ V with lines indicating 5m BPT (red), 6m BPT (brown), BPT (green), tBPT (blue) and bare Au (black).

The hole injection barrier (Φ_{bh+}) is defined as the energy difference between IE and the WF of the functionalized Au electrode. Note that the IE for the P3HT film used in our devices is $\sim 4.86 \pm 0.02$ eV as measured by ambient photoelectron spectroscopy (see Figure 6.1.14). The evaluated injection barrier can give a good indication of the energetic mismatch at the metal-SAM/semiconductor interface. The field-effect mobility was extracted from the saturation regime by estimating the slope of the $\sqrt{|I_D|}$ vs. V_{GS} and then using the following relation

$$\mu_{sat} = \frac{2L}{WC_i} \left(\left. \frac{\partial \sqrt{|I_D|}}{\partial V_{GS}} \right|_{V_{DS}} \right)^2 \quad (6.1.4)$$

where C_i is the capacitance of the gate dielectric layer (230 nm of SiO_2) and has a value of 15nF/cm^2 . For the P3HT solution, we used toluene which has a high boiling point (110.6°C) since it was reported that higher boiling point solvents tend to promote formation of polymeric micro crystalline domains in the active layer of the channel, which can enhance charge transport.⁸⁵ The devices incorporating the BPT SAM exhibited the highest field-effect mobility with μ_{h+} of $9.0 \times 10^{-3} \text{cm}^2/\text{Vs}$. This result can be attributed to the combination of low energetic injection barrier and better electrode wettability by the non-polar P3HT (P3HT film has a θ_{ca} of $\sim 106^\circ$ on the surface of SiO_2)⁸⁶ over the other, more hydrophobic BPT-based monolayer (see

Table 6.1-4). The interfacial packing of the P3HT is likely to be better in more hydrophobic electrodes. In contrast, the devices with Au-tBPT electrodes exhibited the lowest field-effect mobility (μ_{h+} of $6.4 \times 10^{-3} \text{ cm}^2/\text{Vs}$) in comparison with all other SAMs. This lower mobility for devices comprising of Au-tBPT can be correlated with the relatively larger hole injection barrier of 164 meV which is greater by a factor of ~ 4 than the devices with highest mobility injection barrier for Au-BPT electrodes. The carrier mobility in organic semiconductors has been shown to be influenced by the injection barrier with the charge injecting electrode.⁵³ Hence the lower the injection barrier the higher is the current injection efficiency. It has been shown for OTFTs the contact resistance plays a big role in the lower source-drain bias^{87,88} while at sufficiently high source-drain potentials the resistance offered by the contacts is limited.⁸⁸ Since we estimate the field-effect hole mobility at a V_{DS} of -60 V, the effect of the contact resistance has been reasonably omitted. Note that the standard deviation of mobility was within 15% indicating good consistency for all the tested devices.

Table 6.1-4 Contact angle, work function of electrodes and other key device performance indicators

electrode surface	$\theta_{ca} \pm \sigma$ (deg)	$\Phi_M \pm \sigma$ (eV)	Φ_{bh+} (meV) ^a	$\mu_{h+,sat} \pm \sigma \times 10^{-3}$ (cm^2/Vs) ^b	$V_{on} \pm \sigma$ (V)	$V_T \pm \sigma$ (V)
bare Au	18.56 ± 4.20	4.88 ± 0.06	25	7.8 ± 1.0	8.8 ± 1.1	3.6 ± 0.6
5m BPT	71.63 ± 3.40	4.98 ± 0.01	121	6.7 ± 0.8	3.0 ± 5.4	-9.2 ± 5.5
6m BPT	69.30 ± 0.56	4.93 ± 0.01	72	7.2 ± 0.6	11.5 ± 1.4	0.3 ± 1.3
BPT	78.93 ± 1.88	4.81 ± 0.01	43	9.0 ± 0.6	5.5 ± 0.9	-8.4 ± 1.0
tBPT	67.96 ± 2.19	5.02 ± 0.02	164	6.4 ± 1.0	11.8 ± 1.9	2.2 ± 1.0

^a Hole injection barrier with respect to the *IE* level of P3HT. ^b Average hole mobility calculated in the saturation regime along with the standard deviation for at least 8 devices. The surface of the clean bare Au is hydrophilic,⁸⁹ the θ_{ca} of which was measured within 60 s after performing UV/Ozone treatment.

6.1.4.2 Morphology of Semiconductor

The morphology of the spin coated P3HT films (~ 8 nm thick measured with a profilometer) on the modified Au electrodes of the OTFTs exhibited a fairly isotropic grain like morphology featuring a lower roughness (Figure 6.1.11 a-d). Table 6.1-5 collects the root mean square roughness (R_{RMS}) for the Au-BPT SAMs/P3HT films.

Table 6.1-5 Root mean square roughness (R_{RMS}) for the Au-SAM and Au(111) electrode used in charge transport measurements.

Surface	R_{RMS} (nm)
Au-5m BPT/P3HT	0.5441
Au-6m BPT/P3HT	0.5179
Au-BPT/P3HT	0.5438
Au-tBPT/P3HT	0.5412
Au(111)	1.2365

For the biphenyl SAMs on Au the lateral size is $2.0 \times 2.0 \mu\text{m}^2$ and for the surface of Au(111) $5.0 \times 5.0 \mu\text{m}^2$

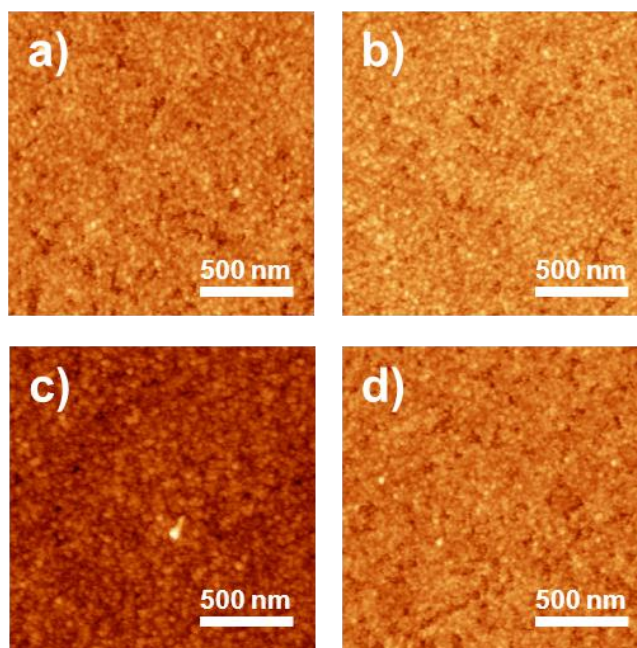


Figure 6.1.11 Surface morphology of P3HT film on top of (a) Au-5m BPT SAM. (b) Au-6m BPT SAM. (c) Au-BPT SAM. (d) Au-tBPT SAMs. Z scales are 7.6 nm

6.1.4.3 Morphology of Electrodes

To gain insight into the morphology of the gold OTFT source-drain electrodes and gold used for charge transport measurements through SAMs we recorded topographic images by means of tapping mode-AFM.

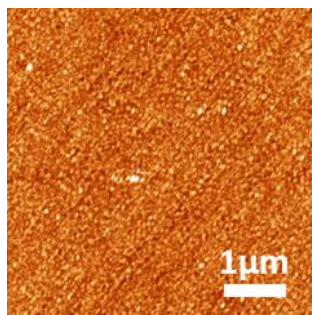


Figure 6.1.12 AFM topographical height image of Au electrode/ITO (adhesion layer)/Si/SiO₂ substrate which served as the source-drain electrodes for the OTFTs having a R_{RMS} of ~ 0.4519 nm estimated from the lateral size of $5.0 \times 5.0 \mu\text{m}^2$. Z-scale is 4 nm.

On close observation of the morphological images of the Au electrodes in the OTFT (Figure 6.1.12) with the monocrystalline gold on mica (Figure 6.1.13) used for the charge transport measurements, it is clear that there is significantly higher number of grains and grain boundaries. Notably the grain size of the polycrystalline gold electrodes in the TFTs had a size of few nanometers compared to the much larger terraces in the gold on mica.

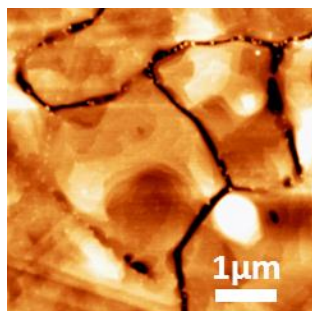


Figure 6.1.13 AFM topographical height image of Au(111) on mica used as supporting platform to form biphenyl thiol SAMs for spectroscopic and charge transport characterization. Z-scale is 6.3 nm.

Since the trenches and step edges of the monocrystalline gold on mica is deeper, the R_{RMS} for this gold surface is higher than the polycrystalline small grain gold in OTFT electrodes.

6.1.4.4 Ionization Energy of Semiconductor

The *IE* level of the P3HT film was then measured by extrapolating the energy point (in eV) where the square root of the photoelectron yield begins to rise upon excitation from the ground state.⁹⁰ Figure 6.1.14 displays the variation of the square root of the photoelectron yield as a function of the incident energy.

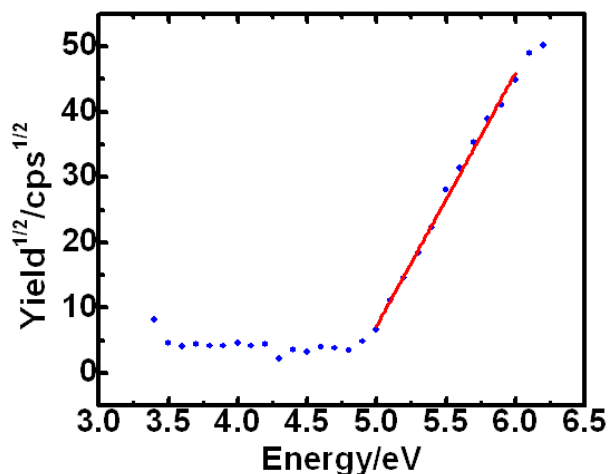


Figure 6.1.14 The ionization energy was estimated to be 4.8 eV from the x-axis intercept of the photoelectron yield.

6.1.5 Discussions

In order to address the charge transport through the SAMs, the molecular structure, monolayer structural defects and packing density are among the pertinent factors that should be considered. The HRXPS data showed that the well-ordered BPT SAM on Au had a packing density ~ 1.5 greater than the tBPT monolayer which features the lowest orientational order. The molecular packing densities are probably heavily influenced by the intramolecular steric hindrance in tBPT SAM which indeed features the highest torsion angle. Closer inspection of the histograms obtained from the charge transport measurements revealed a narrower $\log|J|$ distribution for well-ordered BPT, 6m and 5m BPT SAMs if compared to the wider distribution for disordered tBPT SAM. This suggests that the measured J are sensitive to the structural characteristics of the biphenyl SAMs chemisorbed on Au. We believe that the charge transport through our biphenyl thiol SAMs is due to a combination of pathways tunneling through the molecule along with transport through inter chain hops between adjacent molecules. While the length of the pathway through the molecular chain is the length of the molecule in its long axis, in the case of the parallel pathways model proposed by Slowinski et al.⁷⁵ the pathway due to the through space hops decreases with the effective thickness of the SAM. Least square fitting of the current density with the effective monolayer thickness yielded β of $0.27 \pm 0.08 \text{ \AA}^{-1}$.

The electrical resistivity (ρ) of the biphenyl thiol SAMs can be estimated from the current density (estimated from the charge transport measurements with GaIn^E probe) dependence with the applied electric field (E). As expected the ρ shows a monotonic increase with increasing

effective thickness (Figure 6.1.15). Note that despite the polycrystalline nature of the Au electrodes in the OTFT and the monocrystalline character of the Au used for the measurements with a GaIn^E-based junction (see section 6.1.4.3 for AFM images), a fairly good correlation between the electrical resistivity and the relative threshold voltage shift for the transistor comprising of biphenyl thiol coated electrodes was found.

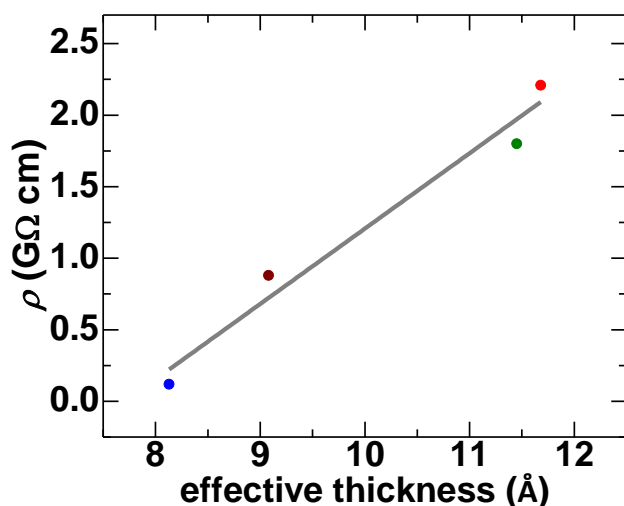


Figure 6.1.15 Electrical resistivity dependence on effective thickness of the biphenyl thiol SAMs estimated for a bias of -0.4V with a linear least squares fitting.

The V_T extracted from the transfer curve in Fig. 6 was under biasing conditions where V_{GS} was swept from +20 V \rightarrow -60 V while holding V_{DS} fixed at -60 V. It was observed that the V_T was \sim +2.2 V for transistors comprising Au-tBPT SAM electrodes and the corresponding electrical resistivity $\rho \sim 0.12$ G Ω cm also being the lowest; on the other hand the devices with Au-5m BPT electrodes had a more negative shift of V_T of -9.2 V and the highest $\rho \sim 2.2$ G Ω cm (see Figure 6.1.15). This difference in the V_T for devices based on Au-5m BPT electrodes of nearly 18 V in the upper bounds when compared Au-tBPT can be attributed directly to the resistivity increase by a similar one to one correlation (i.e., the ρ increases by factor of ~ 18 for electrodes comprising of 5m BPT with respect to tBPT SAMs). For P3HT transistors the majority charge carrier are holes (i.e., increase in I_D tends to predominantly occur when V_{GS} is negative). Note that while the potential sweep for the gate electrode starts from positive voltage and proceeds to the negative (Figure 6.1.10) the TFTs exhibited V_T shifts towards more negative voltages in the order of tBPT, 6m BPT, BPT and 5m BPT, being in good agreement with the concomitant trend of increasing resistivity through the biphenyl thiol SAMs.

The OTFT charge carrier mobility unambiguously reveals, as expected, that the hole injection barrier from the electrodes plays an important role in the transport through the semiconducting film (Figure 6.1.16). It is interesting to note that although the injection barrier for bare Au and Au-BPT electrodes were in the same range, confined within error bars (see Table 6.1-4), for the device with just the bare gold the mobility was $\sim 0.0078 \text{ cm}^2/\text{Vs}$ which in comparison to devices with Au-BPT electrodes were lower by a factor of ~ 1.2 .

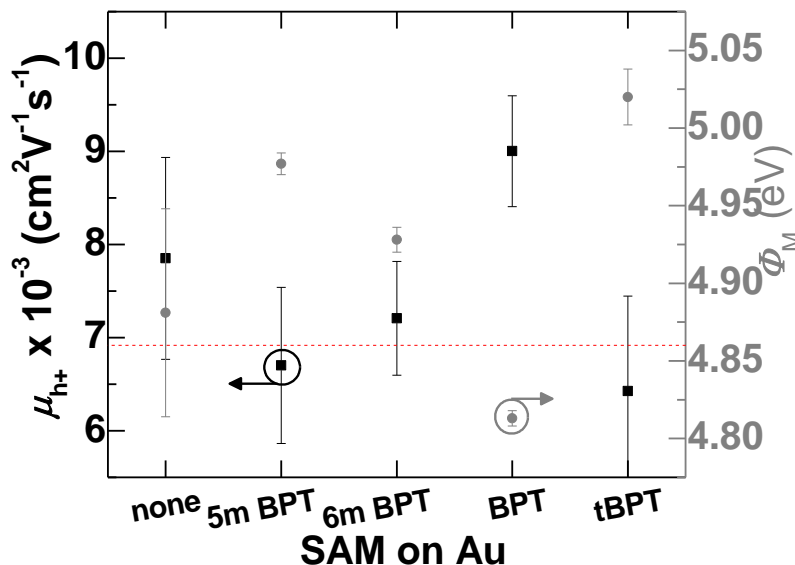


Figure 6.1.16 Hole carrier mobility in saturation mode and respective work function for OTFTs based on electrodes with and without biphenyl thiol SAMs. The dashed red line indicates the ionization energy level of P3HT, which is taken as the reference to estimate the hole injection/extraction barrier to the source-drain electrode.

The top-surface morphology of the P3HT film on the modified electrodes exhibited an isotropic grain-like pattern (see the respective AFM images in Figure 6.1.11) featuring a fairly similar root mean square roughness (R_{RMS}). The increase in mobility for devices with BPT coated electrodes can be attributed to the better arrangement of the semiconductor at the interface with the more hydrophobic surface over hydrophilic bare Au electrode surface which having similar injection barrier has a lower mobility than the Au-BPT which has a more hydrophobic surface. An illustration of the electrode-semiconductor energetic interface is shown in Figure 6.1.17. This suggests that, as in various cases previously reported in literature, the mobility of our TFTs is dictated by (i) the injection barrier of electrode with semiconductor, (ii) electrode surface wettability of the semiconductor film and also (iii) the packing density of the molecules in the SAM. The well-ordered BPT SAM on electrodes exhibited a mobility which was ~ 1.4 greater

than that of the mobility for devices based on more disordered Au-tBPT SAM, indeed reflecting the variable packing density of the molecules adsorbed on the Au electrodes.

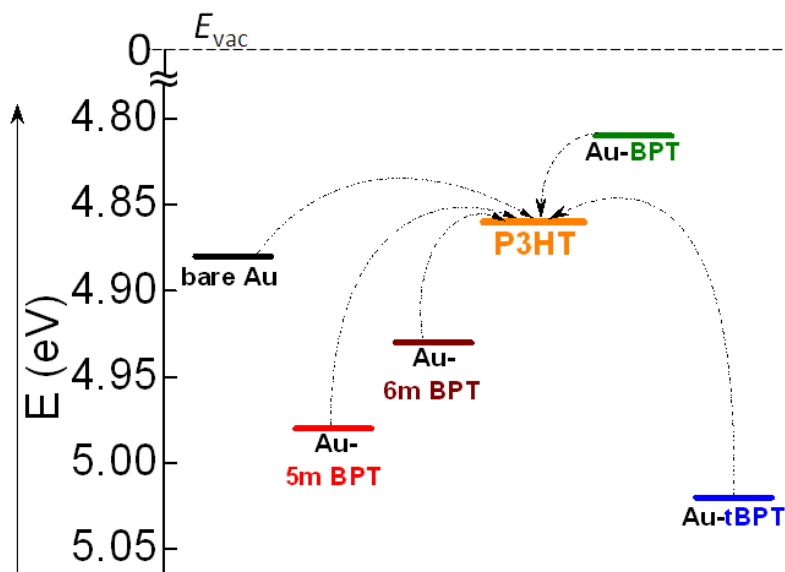


Figure 6.1.17 Schematic of the energetic mismatch between the Fermi level of the electrodes and the ionization energy level of P3HT. The curved dashed lines give an indication of the hole carrier injection barrier from the electrode to the semiconductor.

Overall, the transistor responses show that our devices are an effective means to monitor the energy level adjustment and the corresponding electronic coupling at the interface and the threshold voltage shifts scale with the tunneling resistivity through the biphenyl SAMs on the Au electrodes.

6.1.6 Conclusions

In summary, the charge transport through a family of biphenyl-based SAMs with varying torsion angle chemisorbed on Au surfaces exhibits a good degree of correlation with the packing density and orientational order in the monolayers. The latter parameters were mostly governed by molecular conformation which was specifically adjusted by the site bridging or substitution of/at the individual rings. The efficiency of the charge tunneling through the SAMs shows a characteristic decay with the increasing separation between the metallic contacts (i.e, increase of the effective SAM thickness). The charge transport experiments revealed a through-space β of $0.27 \pm 0.08 \text{ \AA}^{-1}$. For transistors the threshold voltage shifts were influenced by scaling resistivity through biphenyl SAMs on electrodes. A good agreement between the transistor electrode-SAM energetic injection barrier dependence on the field-effect mobility was found. These results show that a proper design of thiolated molecules chemisorbed on Au electrodes is needed for realizing more efficient organic electronic devices via improved control over the electrode-semiconductor interface.

6.1.7 References

- 1 Aviram, A. & Ratner, M. A. Molecular rectifiers. *Chem. Phys. Lett.* **29**, 277-283, (1974).
- 2 Venkataraman, L., Klare, J. E., Nuckolls, C., Hybertsen, M. S. & Steigerwald, M. L. Dependence of single-molecule junction conductance on molecular conformation. *Nature* **442**, 904-907, (2006).
- 3 Mativetsky, J. M. *et al.* Azobenzenes as Light-Controlled Molecular Electronic Switches in Nanoscale Metal–Molecule–Metal Junctions. *J Am Chem Soc* **130**, 9192-9193, (2008).
- 4 Nijhuis, C. A., Reus, W. F., Siegel, A. C. & Whitesides, G. M. A Molecular Half-Wave Rectifier. *J Am Chem Soc* **133**, 15397-15411, (2011).
- 5 Bain, C. D. & Whitesides, G. M. Molecular-level control over surface order in self-assembled monolayer films of thiols on gold. *Science* **240**, 62 (1988).
- 6 Caldwell, W. B. *et al.* A Highly Ordered Self-Assembled Monolayer Film of an Azobenzenealkanethiol on Au(111): Electrochemical Properties and Structural Characterization by Synchrotron in-Plane X-ray Diffraction, Atomic Force Microscopy, and Surface-Enhanced Raman Spectroscopy. *J Am Chem Soc* **117**, 6071-6082, (1995).
- 7 Pace, G. *et al.* Cooperative light-induced molecular movements of highly ordered azobenzene self-assembled monolayers. *P Natl Acad Sci USA* **104**, 9937-9942, (2007).
- 8 Nijhuis, C. A., Reus, W. F. & Whitesides, G. M. Molecular Rectification in Metal-SAM-Metal Oxide-Metal Junctions. *J Am Chem Soc* **131**, 17814-17827, (2009).
- 9 Crivillers, N., Orgiu, E., Reinders, F., Mayor, M. & Samorì, P. Optical Modulation of the Charge Injection in an Organic Field-Effect Transistor Based on Photochromic Self-Assembled-Monolayer-Functionalized Electrodes. *Adv Mater* **23**, 1447-1452, (2011).
- 10 Karpe, S. *et al.* Oligothiophene-derivatized azobenzene as immobilized photoswitchable conjugated systems. *Chem Commun* **46**, 3657-3659, (2010).
- 11 Kronemeijer, A. J. *et al.* Reversible Conductance Switching in Molecular Devices. *Adv Mater* **20**, 1467-1473, (2008).
- 12 Stoliar, P. *et al.* Charge injection across self-assembly monolayers in organic field-effect transistors: Odd-even effects. *J Am Chem Soc* **129**, 6477-6484 (2007).
- 13 Cheng, X. *et al.* Controlling Electron and Hole Charge Injection in Ambipolar Organic Field-Effect Transistors by Self-Assembled Monolayers. *Adv Funct Mater* **19**, 2407-2415 (2009).
- 14 Orgiu, E., Crivillers, N., Rotzler, J., Mayor, M. & Samorì, P. Tuning the charge injection of P3HT-based organic thin-film transistors through electrode functionalization with oligophenylene SAMs. *J. Mater. Chem.* **20**, 10798 (2010).
- 15 Gemayel, M. E. *et al.* Tuning the Photoresponse in Organic Field-Effect Transistors. *J Am Chem Soc* **134**, 2429-2433, (2012).
- 16 Engelkes, V. B., Beebe, J. M. & Frisbie, C. D. Length-Dependent Transport in Molecular Junctions Based on SAMs of Alkanethiols and Alkanedithiols: Effect of Metal Work Function and Applied Bias on Tunneling Efficiency and Contact Resistance. *J Am Chem Soc* **126**, 14287-14296, (2004).
- 17 Engelkes, V. B., Beebe, J. M. & Frisbie, C. D. Analysis of the Causes of Variance in Resistance Measurements on Metal–Molecule–Metal Junctions Formed by Conducting-Probe Atomic Force Microscopy. *J. Phys. Chem. B* **109**, 16801-16810, (2005).
- 18 Selzer, Y., Salomon, A. & Cahen, D. The Importance of Chemical Bonding to the Contact for Tunneling through Alkyl Chains. *J. Phys. Chem. B* **106**, 10432-10439, (2002).
- 19 Weiss, E. A. *et al.* Influence of Defects on the Electrical Characteristics of Mercury-Drop Junctions: Self-Assembled Monolayers of n-Alkanethiolates on Rough and Smooth Silver. *J Am Chem Soc* **129**, 4336-4349, (2007).
- 20 Gonzalez, M. T. *et al.* *Nano Lett* **6**, 2238-2242 (2006).
- 21 Reed, M. A., Zhou, C., Muller, C. J., Burgin, T. P. & Tour, J. M. *Science* **278**, 252-254 (1997).
- 22 Reichert, J. *et al.* *Phys. Rev. Lett.* **88**, 1768041-1768044 (2002).

- 23 Cui, X. D. *et al.* Reproducible Measurement of Single-Molecule Conductivity. *Science* **294**, 571-574, (2001).
- 24 Wang, W., Lee, T. & Reed, M. A. Mechanism of electron conduction in self-assembled alkanethiol monolayer devices. *Phys Rev B* **68**, 035416 (2003).
- 25 Kushmerick, J. G. *et al.* Metal-Molecule Contacts and Charge Transport across Monomolecular Layers: Measurement and Theory. *Phys. Rev. Lett.* **89**, 086802 (2002).
- 26 Bonifas, A. P. & McCreery, R. L. /Soft/Au, Pt and Cu contacts for molecular junctions through surface-diffusion-mediated deposition. *Nature Nanotech.* **5**, 612-617 (2010).
- 27 Chiechi, R. C., Weiss, E. A., Dickey, M. D. & Whitesides, G. M. Eutectic Gallium–Indium (EGaIn): A Moldable Liquid Metal for Electrical Characterization of Self-Assembled Monolayers. *Angew Chem* **120**, 148-150, (2008).
- 28 Fracasso, D., Valkenier, H., Hummelen, J. C., Solomon, G. C. & Chiechi, R. C. Evidence for Quantum Interference in SAMs of Arylethynylene Thiolates in Tunneling Junctions with Eutectic Ga–In (EGaIn) Top-Contacts. *J Am Chem Soc* **133**, 9556-9563, (2011).
- 29 Lilly, G. D. *et al.* Switchable photoconductivity of quantum dot films using cross-linking ligands with light-sensitive structures. *J. Mater. Chem.* **21** (2011).
- 30 Thuo, M. M. *et al.* Odd-Even Effects in Charge Transport across Self-Assembled Monolayers. *J Am Chem Soc* **133**, 2962-2975, (2011).
- 31 Yield is referred to as ratio of the difference between the total number of $J(V)$ traces to the traces that ended up with a short (instrument reached compliance limit) with the total J observations.
- 32 Tran, E. *et al.* Experimental approaches for controlling current flowing through metal–molecule–metal junctions. *Adv Mater* **18**, 1323-1328 (2006).
- 33 Ferri, V. *et al.* Light-powered electrical switch based on cargo-lifting azobenzene monolayers. *Angew Chem Int Edit* **47**, 3407-3409, (2008).
- 34 Akkerman, H. B., Blom, P. W. M., de Leeuw, D. M. & de Boer, B. Towards molecular electronics with large-area molecular junctions. *Nature* **441**, 69-72, (2006).
- 35 Wang, G., Kim, Y., Choe, M., Kim, T.-W. & Lee, T. A New Approach for Molecular Electronic Junctions with a Multilayer Graphene Electrode. *Adv Mater* **23**, 755-760, (2011).
- 36 Love, J. C., Estroff, L. A., Kriebel, J. K., Nuzzo, R. G. & Whitesides, G. M. Self-Assembled Monolayers of Thiolates on Metals as a Form of Nanotechnology. *Chem. Rev.* **105**, 1103-1170, (2005).
- 37 Qi, Y. *et al.* Mechanical and Charge Transport Properties of Alkanethiol Self-Assembled Monolayers on a Au(111) Surface: The Role of Molecular Tilt. *Langmuir* **24**, 2219-2223, (2008).
- 38 Li, D., Swanson, B. I., Robinson, J. M. & Hoffbauer, M. A. Porphyrin based self-assembled monolayer thin films: synthesis and characterization. *J Am Chem Soc* **115**, 6975-6980, (1993).
- 39 Anariba, F., Steach, J. K. & McCreery, R. L. Strong Effects of Molecular Structure on Electron Transport in Carbon/Molecule/Copper Electronic Junctions. *J. Phys. Chem. B* **109**, 11163-11172, (2005).
- 40 Wolfgang, H. *et al.* Variable contact gap single-molecule conductance determination for a series of conjugated molecular bridges. *J. Phys. Condens. Matter* **20**, 374119 (2008).
- 41 Ricks, A. B. *et al.* Controlling Electron Transfer in Donor–Bridge–Acceptor Molecules Using Cross-Conjugated Bridges. *J Am Chem Soc* **132**, 15427-15434, (2010).
- 42 Bruno, G. *et al.* Tailoring Density and Optical and Thermal Behavior of Gold Surfaces and Nanoparticles Exploiting Aromatic Dithiols. *Langmuir* **26**, 8430-8440, (2010).
- 43 Operamolla, A., Omar, O. H., Babudri, F., Farinola, G. M. & Naso, F. Synthesis of S-acetyl oligoarylenedithiols via Suzuki-Miyaura cross-coupling. *J. Org. Chem.* **72**, 10272-10275, (2007).
- 44 Casalini, S. *et al.* Mono/bidentate thiol oligoarylene-based self-assembled monolayers (SAMs) for interface engineering. *J. Mater. Chem.* **22**, 12155-12163, (2012).
- 45 Mishchenko, A. *et al.* Influence of Conformation on Conductance of Biphenyl-Dithiol Single-Molecule Contacts. *Nano Lett* **10**, 156-163, (2009).

- 46 Vonlanthen, D. *et al.* Chemically Controlled Conductivity: Torsion-Angle Dependence in a Single-Molecule Biphenyldithiol Junction. *Angew Chem Int Edit* **48**, 8886-8890, (2009).
- 47 Mishchenko, A. *et al.* *J. Am. Chem. Soc.* **133**, 184-187 (2011).
- 48 Woitellier, S., Launay, J. & Joachim, C. The possibility of molecular switching: Theoretical study of [(NH₃)₃Ru-4, 4'-bipy-Ru(NH₃)₅]⁺. *Chem. Phys.* **131**, 481-488 (1989).
- 49 Shaporenko, A. *et al.* Self-assembled monolayers from biphenyldithiol derivatives: optimization of the deprotection procedure and effect of the molecular conformation. *J. Phys. Chem. B* **110**, 4307-4317 (2006).
- 50 Zharnikov, M. & Grunze, M. Spectroscopic characterization of thiol-derived self-assembling monolayers. *J. Phys. Condens. Matter* **13**, 11333 (2001).
- 51 Zharnikov, M. High-resolution X-ray photoelectron spectroscopy in studies of self-assembled organic monolayers. *J. Electron Spectrosc. Relat. Phenom.* **178**, 380-393, (2010).
- 52 Horsley, J. A. *et al.* Resonances in the K shell excitation spectra of benzene and pyridine: Gas phase, solid, and chemisorbed states. *J. Chem. Phys.* **83**, 6099-6107 (1985).
- 53 Shen, Y., Klein, M. W., Jacobs, D. B., Campbell Scott, J. & Malliaras, G. G. Mobility-dependent charge injection into an organic semiconductor. *Phys. Rev. Lett.* **86**, 3867-3870 (2001).
- 54 Stöhr, J. *NEXAFS spectroscopy*. (Springer-Verlag, 1992).
- 55 Frey, S. *et al.* Structure of Thioaromatic Self-Assembled Monolayers on Gold and Silver. *Langmuir* **17**, 2408-2415, (2001).
- 56 Fuxen, C. *et al.* Structural characterization of organothiolate adlayers on gold: the case of rigid, aromatic backbones. *Langmuir* **17**, 3689-3695 (2001).
- 57 Azzam, W., Wehner, B. I., Fischer, R. A., Terfort, A. & Wöll, C. Bonding and orientation in self-assembled monolayers of oligophenyldithiols on Au substrates. *Langmuir* **18**, 7766-7769 (2002).
- 58 Yokoyama, T., Seki, K., Morisada, I., Edamatsu, K. & Ohta, T. X-ray absorption spectra of poly-p-phenylenes and polyacenes: localization of π orbitals. *Phys. Scr.* **41**, 189 (1990).
- 59 Hargreaves, A. & Rizvi, S. H. The crystal and molecular structure of biphenyl. *Acta Crystallogr.* **15**, 365-373 (1962).
- 60 Ballav, N. *et al.* Direct probing molecular twist and tilt in aromatic self-assembled monolayers. *J. Am. Chem. Soc.* **129**, 15416-15417, (2007).
- 61 Trotter, J. The crystal and molecular structure of biphenyl. *Acta Crystallogr.* **14**, 1135-1140 (1961).
- 62 Bashir, A. *et al.* Selenium as a key element for highly ordered aromatic self-assembled monolayers. *Angew. Chem. Int. Ed.* **47**, 5250-5252, (2008).
- 63 Chang, S. C., Chao, I. & Tao, Y. T. Structure of Self-Assembled Monolayers of Aromatic-Derivatized Thiols on Evaporated Gold and Silver Surfaces: Implication on Packing Mechanism. *J Am Chem Soc* **116**, 6792-6805 (1994).
- 64 Dhirani, A. A., Zehner, R. W., Hsung, R. P., Guyot-Sionnest, P. & Sita, L. R. Self-assembly of conjugated molecular rods: A high-resolution STM study. *J Am Chem Soc* **118**, 3319-3320 (1996).
- 65 Brown, G. & Bortner, M. On the crystal and molecular structure of fluorene. *Acta Crystallogr.* **7**, 139-139 (1954).
- 66 Cosmo, R., Hambley, T. W. & Sternhell, S. Skeletal deformation in 4, 5-disubstituted 9, 10-dihydrophenanthrenes and 4, 5-disubstituted phenanthrenes. *J. Org. Chem.* **52**, 3119-3123 (1987).
- 67 Ho Choi, S., Kim, B. & Frisbie, C. D. Electrical Resistance of Long Conjugated Molecular Wires. *Science* **320**, 1482-1486, (2008).
- 68 Lu, Q. *et al.* From Tunneling to Hopping: A Comprehensive Investigation of Charge Transport Mechanism in Molecular Junctions Based on Oligo(p-phenylene ethynylene)s. *ACS Nano* **3**, 3861-3868, (2009).
- 69 Nijhuis, C. A., Reus, W. F. & Whitesides, G. M. Molecular Rectification in Metal-SAM-Metal Oxide-Metal Junctions. *J Am Chem Soc* **131**, 17814-17827, (2009).

- 70 Ishida, T. *et al.* Electrical conduction of conjugated molecular SAMs studied by conductive atomic force microscopy. *J. Phys. Chem. B* **106**, 5886-5892 (2002).
- 71 Kronemeijer, A. *et al.* Electrical characteristics of conjugated self-assembled monolayers in large-area molecular junctions. *Appl Phys Lett* **97**, 173302 (2010).
- 72 Nijhuis, C. A., Reus, W. F. & Whitesides, G. M. Mechanism of Rectification in Tunneling Junctions Based on Molecules with Asymmetric Potential Drops. *J Am Chem Soc* **132**, 18386–18401 (2010).
- 73 Wickham, H. *ggplot2: elegant graphics for data analysis*. (Springer, 2009).
- 74 R Development Core Team. *R: A language and environment for statistical computing*. (Springer, 2011).
- 75 Slowinski, K., Chamberlain, R. V., Miller, C. J. & Majda, M. Through-bond and chain-to-chain coupling. Two pathways in electron tunneling through liquid alkanethiol monolayers on mercury electrodes. *J Am Chem Soc* **119**, 11910-11919 (1997).
- 76 de Boer, B., Hadipour, A., Mandoc, M. M., van Woudenberg, T. & Blom, P. W. M. Tuning of Metal Work Functions with Self-Assembled Monolayers. *Adv Mater* **17**, 621-625, (2005).
- 77 Heimel, G., Romaner, L., Zojer, E. & Bredas, J. L. The interface energetics of self-assembled monolayers on metals. *Acc. Chem. Res.* **41**, 721-729 (2008).
- 78 DiBenedetto, S. A., Facchetti, A., Ratner, M. A. & Marks, T. J. Molecular Self-Assembled Monolayers and Multilayers for Organic and Unconventional Inorganic Thin-Film Transistor Applications. *Adv Mater* **21**, 1407-1433 (2009).
- 79 Boudinet, D. *et al.* Modification of gold source and drain electrodes by self-assembled monolayer in staggered n-and p-channel organic thin film transistors. *Org Electron* **11**, 227-237 (2010).
- 80 Singh, K. *et al.* Effect of Self-Assembled Monolayers on Charge Injection and Transport in Poly (3-hexylthiophene)-Based Field-Effect Transistors at Different Channel Length Scales. *ACS Appl. Mater. Interfaces* (2011).
- 81 Heimel, G., Romaner, L., Zojer, E. & Brédas, J.-L. Toward Control of the Metal–Organic Interfacial Electronic Structure in Molecular Electronics: A First-Principles Study on Self-Assembled Monolayers of π -Conjugated Molecules on Noble Metals. *Nano Lett* **7**, 932-940, (2007).
- 82 Campbell, I. *et al.* *Phys. Rev. B* **54**, 14321-14324 (1996).
- 83 Venkataraman, N. V. *et al.* *J. Phys. Chem. C* **113**, 5620-5628 (2009).
- 84 Kang, J. F. *et al.* Self-assembled rigid monolayers of 4'-substituted-4-mercaptobiphenyls on gold and silver surfaces. *Langmuir* **17**, 95-106, (2001).
- 85 Chang, J. F. *et al.* Enhanced mobility of poly (3-hexylthiophene) transistors by spin-coating from high-boiling-point solvents. *Chem. Mater.* **16**, 4772-4776 (2004).
- 86 Robinson, L., Isaksson, J., Robinson, N. D. & Berggren, M. Electrochemical control of surface wettability of poly (3-alkylthiophenes). *Surface science* **600**, L148-L152 (2006).
- 87 Horowitz, G., Hajlaoui, R., Bourguiga, R. & Hajlaoui, M. Theory of the organic field-effect transistor. *Synthetic Metals* **101**, 401-404 (1999).
- 88 Podzorov, V., Sysoev, S. E., Loginova, E., Pudalov, V. M. & Gershenson, M. E. Single-crystal organic field effect transistors with the hole mobility $\sim 8 \text{ cm}^2/\text{V s}$. *Appl Phys Lett* **83**, 3504-3506 (2003).
- 89 Worley, C. G. & Linton, R. W. *J. Vac. Sci. Technol. A* **13**, 2281-2284 (1995).
- 90 Ishii, H., Sugiyama, K., Ito, E. & Seki, K. Energy level alignment and interfacial electronic structures at organic/metal and organic/organic interfaces. *Adv Mater* **11**, 605-625 (1999).

6.2 COMPARATIVE STUDY OF WORK FUNCTION MODIFICATION OF Au ELECTRODES BY FLUORINATED AZOBENZENE

In this part of the chapter the work function flat gold electrodes modified by chemisorption of a photoactive self-assembled monolayer (SAM) is reported. The molecules used to form the SAM are based on azobenzene, the structure of which can be modified by excitation at specific wavelength of light. The property of azobenzene to adopt two distinct bistable isomeric forms enabled us to tune the work function of Au-SAM optically. To address this issue we performed a combined theoretical and experimental study encompassing a wide array of techniques from quantum chemical calculations, macroscopic potential difference mapping to photoelectron spectroscopy.

6.2.1 Motivation

Azobenzenes are one class of photochromic compounds which undergoes change in its molecular structural confirmation upon external electromagnetic stimuli. The azobenzene molecule is particularly interesting since it can photoisomerize from its fully extended *trans* state to the bent and bulky *cis* form upon ultraviolet (UV) irradiation and this process can be fully reversed by white light irradiation upon which molecules in the *cis* state re-photoisomerize and adopt the *trans* form.¹⁻⁴ This property of azobenzene have been exploited to achieve functions such as work function modification of electrodes,⁵⁻⁸ variable current switching in mono molecular layers,^{9,10} photo-responsive units in opto-electronic devices³ and charge injection properties in an organic field-effect transistor (OFET).¹¹

In this study we investigate the work function shift induced by a SAM comprising of azobenzene molecules with fluorine atoms crowning the carbon atoms of the terminal phenyl ring (we term this molecule as Fazob) in both its *trans* and *cis* isomeric forms on Au. To address this we performed theoretical simulations to arrive at a quantitative estimate of the work function and the shift in the work function with respect to the vacuum level caused by the molecules adsorbed on Au electrodes.

The chemical structure of Fazob is shown in Figure 6.2.1. The changes in work function induced by the chemisorption of Fazob molecules (in both isomeric forms) on flat Au films was recorded by ultraviolet photoelectron spectroscopy, macroscopic Kelvin probe and kelvin probe force

microscopy. Note that for forming the SAMs in our experiments we use the acetoester group protecting sulfur atom, while for the theoretical study hydrogen was considered bonded to the sulfur to reduce the complexity and computing processing costs.

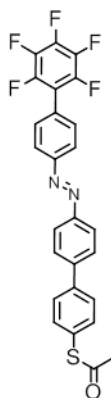


Figure 6.2.1 Structural scheme of the fluorinated azobenzene (Fazob) molecule in its fully extended *trans* form, showing the pentafluoro terminal phenyl and acetoester groups attached to the tail and head positions of the molecule.

6.2.2 Results and discussions

6.2.2.1 Quantum chemical calculations

We designed the initial structure of the Fazob molecules in both isomeric forms in GaussView version 5.0 (Gaussian Inc). The molecular structure in the gas phase was then minimized to its optimal form using SIESTA 3.1 package. The optimized structure of the molecule was then placed on a 5X5 gold face centered cubic (FCC) lattice. For both the Fazob *trans* and *cis* forms two molecules were positioned per unit cell of Au, the distance between the individual molecules was set according to the results of azobenzene molecular packing from STM.¹² For the Fazob *trans* the arrangement of the molecules has a herringbone pattern while for the *cis* form the two molecules were placed to point in opposite directions, again based on STM images for azobenzene on Au.

The naming convention followed here for a SAM on Au is Au-Fazob *trans*, where “-” indicates a covalent bond between the Au and the Fazo *trans* molecule, similar nomenclature is used for Fazo *cis* molecules. Shown in Figure 6.2.2 is the molecular packing order for the Au-Fazob *trans*, with illustration of the top and side views.

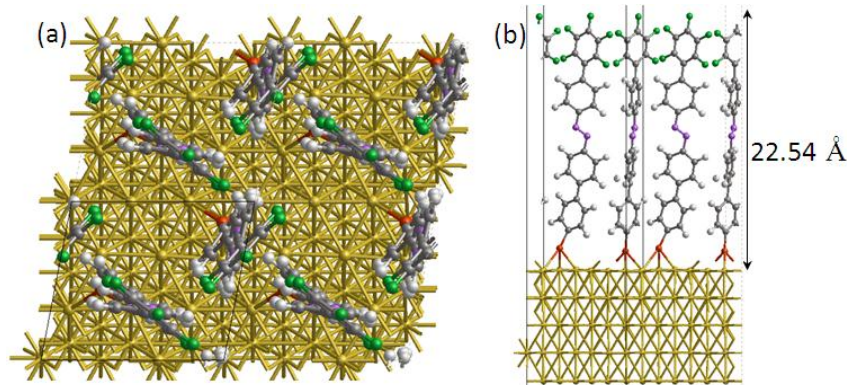


Figure 6.2.2 (a) Top view in left the dotted line represents a single unit cell boundary and, (b) side view in right along with the length of the molecule from the surface of the Au to the terminal fluorine atom for the Au-Fazob *trans*. The colors of the atoms are, carbon (dark gray), fluorine (olive green), hydrogen (light gray), nitrogen (purple), sulfur (red), and gold (golden yellow).

The unit cell parameters for the Au-Fazob *trans* are $a = 6.5 \pm 0.5 \text{ \AA}$; $b = 8.9 \pm 0.5 \text{ \AA}$ and $\alpha = 84^\circ \pm 0.5^\circ$ (Figure 6.2.3). Since there are two Fazob *trans* molecules per unit cell, the surface covering area for one molecule is ca. 28.77 sq\AA . The arrangement of the Fazob *cis* molecules on Au is shown in Figure 6.2.4a. The Au-Fazob *cis* has unit cell parameters of $a = 8.7 \text{ \AA}$; $b = 7.7 \text{ \AA}$ and $\alpha = 79^\circ$ and the corresponding coverage area by per molecule of $\sim 32.88 \text{ sq\AA}$. The dihedral angle for the Fazob *cis* molecule near the C-N=N group in the gas phase was 124° (Figure 6.2.4) and on the Au surface were 129° and 133° for the molecules with their tail oriented right and left respectively.

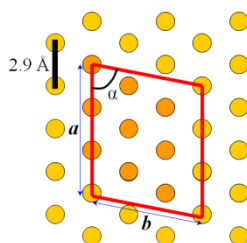


Figure 6.2.3 Unit cell dimensions of Au used for theoretical of packing Fazob molecules on Au slab. The yellow circular dots are gold atoms. Two molecules were arranged per unit cell.

The experimental details from the STM also had previously demonstrated that the position of the anchoring sulfur group is not modified upon photo isomerization from the *trans* to the *cis* state.

The nominal effective length for the Fazob *trans* and *cis* molecules from the surface of the gold; considering gold-sulfur bond distance of 2.42 Å were estimated using SIESTA to 22.54 Å and 19.16 Å respectively.

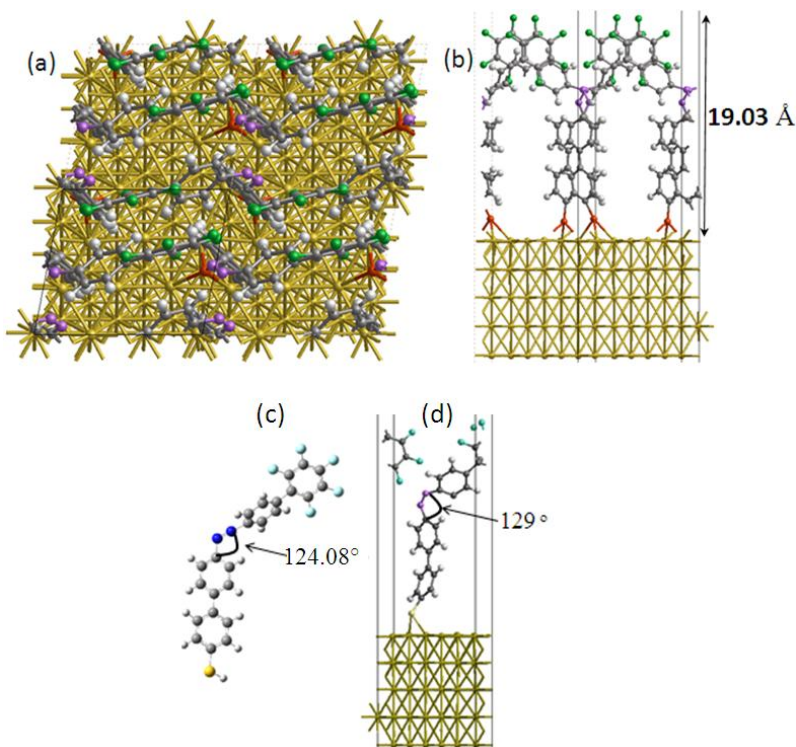


Figure 6.2.4 (a) Top view in left dotted line represents a single unit cell boundary and, (b) side view in right along with the length of the molecule from the surface of the Au to the terminal fluorine atom for the Au-Fazob *cis*. The colors scheme for the atoms are, carbon (dark gray), fluorine (olive green), hydrogen (light gray), nitrogen (purple), sulfur (red), and gold (golden yellow); (c) Dihedral angle at the C-N=N bond for the *cis* isomer in gas phase (left) and (d) for the molecule on Au with tail group oriented right (right).

The difference in the length of the Fazob *cis* molecules and the *trans* is ~ 3.4 Å. The Au unit cell was optimized and the electronic structure is described according to density function theory (DFT) using local density approximation (LDA),¹³ after the molecules adopted the optimal structural relaxation on the Au surface in the SIESTA. Only the first two layers of gold were considered, with the description of the core electrons by Trouillier-Martin nonlocal pseudopotentials and the valence electrons by the LCAO approximation. For the molecule and Au *s* channel a double ρ +polarization basis set were used.

For the Au-Fazo *trans* the molecule has a tilt angle of $\sim 7.2^\circ$ with respect to Au surface normal (Figure 6.2.2b) while for the Au-Fazo *cis* (Figure 6.2.4b) the tilt angle is more than the *trans* isomer with a value of $\sim 16^\circ$, this is likely due to the contribution of the bend near the azo group ($-\text{N}=\text{N}-$) which increases the tilt angle. Note that for the Fazo *cis* the dihedral angle at the $-\text{C}-\text{N}=\text{N}$ unit is lower than for the molecules packed in the Au-Fazo *cis* (Figure 6.2.5) this is possibly due to the intermolecular sterical constraints for between the molecules which prevents further bending of the molecular backbone.

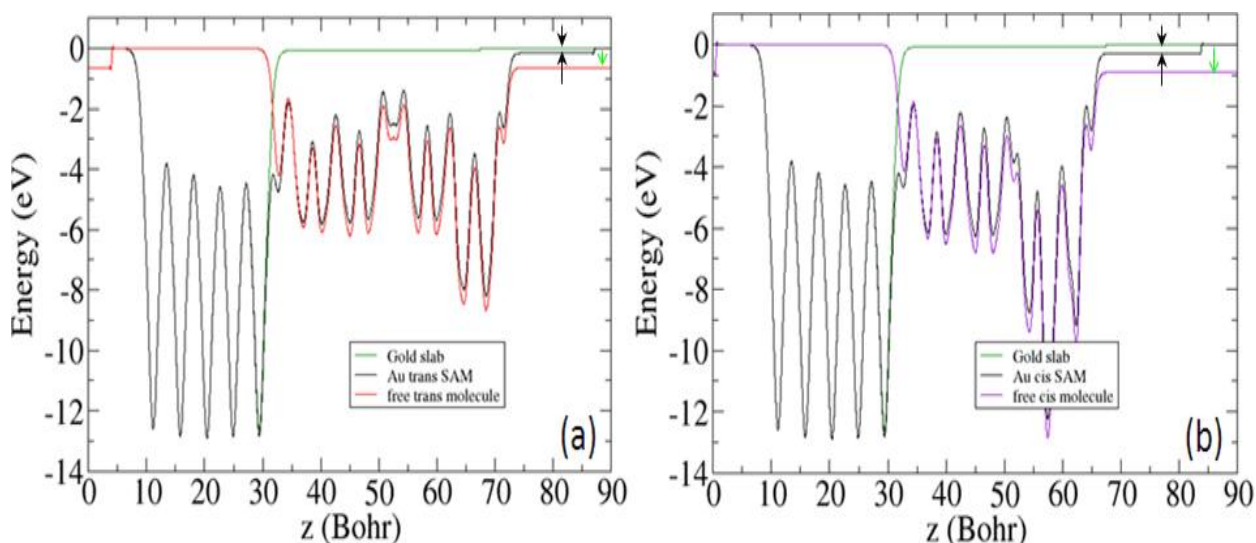


Figure 6.2.5 Plots illustrating the plane averaged potentials for (a) Au-Fazo *trans*, free Fazo *cis* molecular layer along with the potential profile for Au(111) bulk and (b) Au-Fazo *cis*, free Fazo *trans* molecular layer along with its corresponding Au (111) potential. Green arrows indicate the vacuum level shift arising due to the molecules and the inverted black arrows refer to the vacuum level offset for the Au-Fazo SAM and the difference between the two gives the bond dipole. In both the plots the contribution by the five layers of Au can be seen in the distinct profile potential fluctuations and the contribution due to the molecular system for *cis* and *trans* are represented by violet and red lines respectively.

An estimate of the work function shift can be obtained for the Au-SAM full system under equilibrium conditions by plotting the plane-averaged electrostatic potential along the normal axis from the Au surface and superimposing this plot with that of the contribution due to the Au surface and only the free molecules as shown in Figure 6.2.5.

The work function shift is due to the contribution of the bond dipole between gold and sulfur (BD_{Au-S}) and due to the plane average potential difference for the free molecule (ΔV_{mol}) and is expressed by equation 6.2.1.

$$\Delta\Phi = BD_{Au-S} + \Delta V_{mol} \quad (6.2.1)$$

The ΔV_{mol} is the difference between the left and right plane average potential of the optimized molecular layer alone excluding the Au surface. The work function for the Au-Fazob *cis* estimated from Figure 6.2.5 was 4.96 eV. The shift in the work function due to the Fazob *cis* free molecular contribution amounted to -0.28 eV and a bond dipole of 0.66 eV.

The work function shift caused by the Fazob *trans* is shown in Figure 6.2.5. It was estimated that the work function shift for the Au-Fazob *trans* of ~ -0.16 eV arising due to the sum of bond dipole contribution of 0.52 eV and $\Delta V_{Fazob\ trans}$ of -0.68 eV. The work function for the Au-Fazob *trans* was calculated to be 5.10 eV, this value was ~ 20 meV greater than that of the Au-Fazob *cis*. Table 6.2-1 collects the work function, bond dipole and the plane average potential difference for Fazob SAMs in both isomeric forms.

Table 6.2-1 Theoretically computed parameters including work function shift induced by Au-Fazob *trans* and *cis* SAMs

SAM on Au properties	Fazob	
	<i>cis</i>	<i>trans</i>
Φ (eV)	4.96	5.1
$\Delta\Phi$ (eV)	-0.28	-0.16
ΔV (eV)	-0.94	-0.68
Bond dipole (eV)	0.66	0.52
Bond dipole (Debye)	-0.97	-1.21
$\Phi_{trans-cis}$ (meV)	140	
$\Delta\Phi_{trans-cis}$ (meV)	120	

6.2.2.2 Ultraviolet photoelectron spectroscopy

Importantly work function estimated by simulations exhibited a similar trend to the experimentally recorded values by means of ultraviolet photoelectron spectroscopy (UPS) for both the *trans* and *cis* SAMs, wherein the work function of the former was greater than the latter.

The mean work function values measured with UPS were $\sim 5.28 \pm 0.01$ eV and 4.99 ± 0.08 eV for the Au-Fazob *trans* and *cis* respectively. The conditions used for performing the work function measurements were a sample scanning energy range from 4.0 to 6.2 eV with a measurement interval of 0.1 eV and UV spot intensity of 10nW.

To compare the work function shift induced by the chemisorption of the Fazob molecules the work function of pristine Au electrode immersed in chloroform for 24h was recorded and it amounted to 5.08 ± 0.02 eV. The work function of the electrodes was extracted from the minimum threshold energy after which the emission of photo excited electrons occur from the ground energy state (Figure 6.2.6).

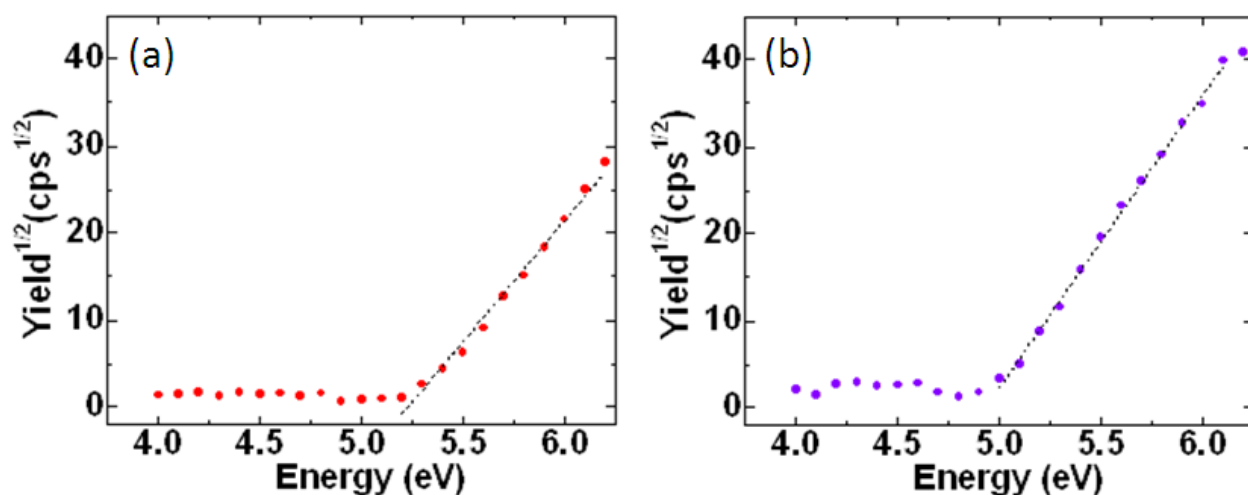


Figure 6.2.6 Square root of photoelectron emission yield as a function of scan energy for Fazob SAMs on Au/mica (a) *trans* and (b) *cis* forms. The dotted lines are the linear fits from which the *x*-axis intercept gives the work function of the Au-SAM.

The work function difference ($\Delta\Phi$) between Fazob *trans* and *cis* of ~ 290 meV has a good agreement with the theoretically simulated estimates, although being a factor of two higher. This modest deviation can be accounted to the inherent defects in the Fazob SAMs of the experimental samples, as opposed to the ideal ordering and packing of the SAMs taken for the theoretical computations.

6.2.2.3 Contact potential difference of Fazob SAMs on Au

By means of macroscopic Kelvin probe the contact potential difference (CPD) for the SAMs of Fazob in *trans* and *cis* forms on gold was monitored over 5 different sets of measurements over a duration of 12h. The duration of each measurement was ~ 20 min and the sequence in which the CPD was recorded was in the order of bare Au, Au-Fazo *cis* and Au-Fazob *trans*. Taking the difference between the contact potential difference for the Au-*trans* ($\Delta\text{CPD}_{\text{trans-Au}}$) or *cis* ($\Delta\text{CPD}_{\text{cis-Au}}$) SAMs to that of the bare Au revealed that there was $\sim +80$ to $+120$ mV shift for Fazob *trans* SAM. The $\Delta\text{CPD}_{\text{cis-Au}}$ was reduced from -100 to -30 mV over 12h (Figure 6.2.7b) suggesting that the gradual thermal recovery of the molecules in the *cis* form back to that thermodynamically stable *trans* form.⁷ The work function changed from 5.15 to 5.26 eV and 5.34 to 5.40 eV for Au-Fazob *cis* and Au-Fazo *trans* SAMs respectively with time.

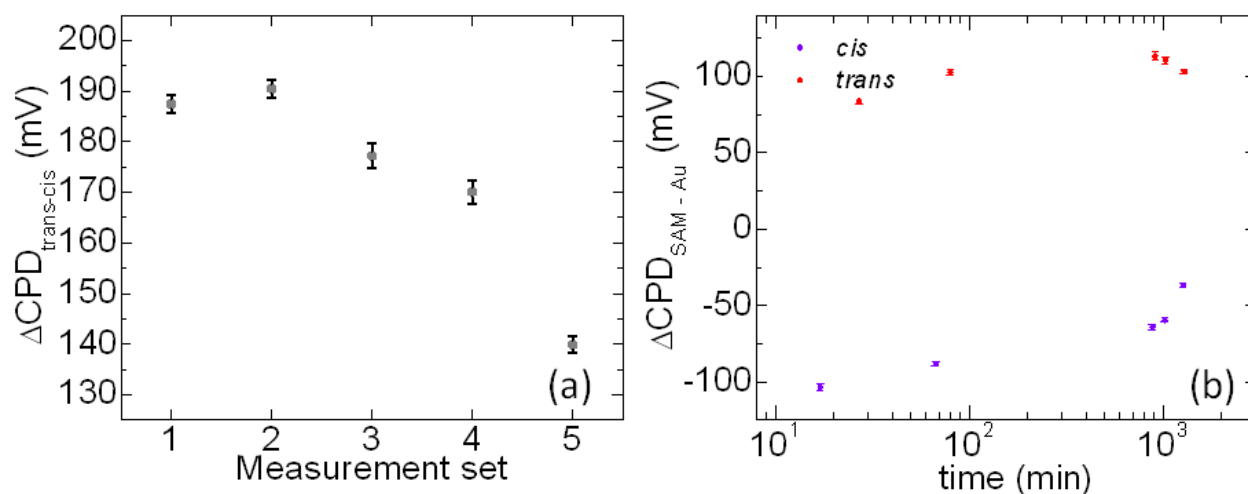


Figure 6.2.7 Contact potential difference between (a) Fazob *trans* and *cis* SAMs on Au, (b) SAMs in both isomeric forms with respect to Au reference sample.

The variation in the ΔCPD with time becomes apparent by taking the difference of the CPD for both the *trans* and *cis* ($\Delta\text{CPD}_{\text{trans-cis}}$) states. The $\Delta\text{CPD}_{\text{trans-cis}}$ spanned from initial value of 190 mV and dropped to 140 mV (Figure 6.2.7a).

6.2.2.4 Comparison of different techniques

The difference in work function between the Au-Fazob *trans* and *cis* SAMs were ~ 290 meV. It must be noted that the simulated values of the work function were best estimates for an ideal packing of the Fazob molecules in both isomeric forms on the Au(111) surface, but in reality due to the inherent structural defects present in the Fazob SAMs causes the deviation in the observed experimental values.

The observed contact potential difference of 190 to 140 mV for the Au-Fazob *trans* and *cis* SAMs again clearly provides a quantitative proof that the work function of the Au electrode modified by the Fazob molecules in the *cis* form is lower than the *trans*. The CPD which was recorded in ambient conditions probes the potential difference induced by the difference in the capacitance formed by the vibrating metallic tip over the sample. This method which is a non-contact technique can thus be employed to monitor the change in CPD over an extended interval a time without causing changes in the chemical composition of the surface. The $\Delta\Phi$ between the Au-Fazob *trans* and *cis* measured by KP revealed a value in range of ~ 190 to 140 meV. Remarkably the lower bounds of the difference in work function of the Au-Fazob *trans* and *cis* SAMs matched closely to the theoretically predicted difference. More crucially the trend in the work function values of gold modified by Fazob recorded experimentally and calculated theoretically showed remarkable consistency, such that the Φ of the *trans* SAM was always greater than the *cis* by at least 140 meV.

6.2.3 Conclusions

The theoretical study work function for a system of fluorinated azobenzene SAMs on Au(111) with *trans* and *cis* forms revealed that the work function shift and the work function of the Au-Fazob *trans* was greater than the Au-Fazob *cis* by ~ 120 and 140 meV respectively. The experimentally measured values for the Fazob SAMs in both isomeric forms showed a difference of nearly 290 meV when the *trans* form was coated to the Au surface than the *cis*. The similar work function trend for the simulated and measured values proves the robustness of the fluorinated azobenzene self-assembled system on flat gold substrates across completely diverse techniques.

Outlooks: Directions for extended work

With the understanding of the work function shift for Fazob SAM on Au, we wanted to investigate the effect of structural modifications theoretically of the starting molecule (Figure 6.2.8a) upon replacement of fluorine atoms with hydrogen atoms in the ortho (Figure 6.2.8b) and meta (Figure 6.2.8c) positions respectively.

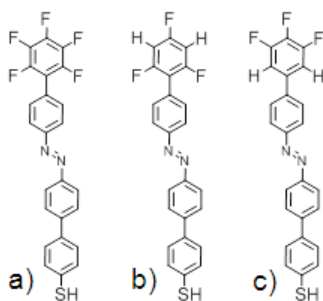


Figure 6.2.8 Scheme of the chemical structure of (a) Fazob *trans*, (b) Fazob without fluorine in ortho position of terminal phenyl ring (FazobnoFO *trans*), and (c) Fazob without fluorine in meta position of terminal phenyl ring (FazobnoFM *trans*).

Theoretical simulations were performed for the both the Fazob without fluorine in ortho position (abbreviated as FazobnoFO *trans*) and in meta position of terminal phenyl ring (abbreviated as FazobnoFM *trans*) with the similar packing on the Au(111) cell as shown in Figure 6.2.2. The work function shifts were estimated for the respective optimized structures and are summarized in Table 6.2-2.

On close observation of the results from the simulations, it is clear that there is a dramatic influence in the work function of the Au-Fazob *trans* when the fluorine atoms are removed and replaced with hydrogen atoms in the ortho positions resulting in a total work function shift of ~ -0.79 eV. The contribution to this huge shift in the work function arises mainly from the potential difference in the FazobnoFO *trans* free molecular layer with a value of ~ -1.41 eV. In contrast to the work function shift to the FazobnoFO the FazobnoFM SAM exhibited the opposite total shift of ~ 0.27 eV.

Table 6.2-2. Summary of parameters extracted from theoretical simulations for the Fazob SAMs on Au with different structural alterations to the starting Fazob molecule. The negative sign in front of work function shift as vacuum level offset.

Au-SAM parameters	Fazob <i>trans</i>	Fazob <i>cis</i>	Fazob noFO <i>trans</i>	Fazob noFM <i>trans</i>
E_{ads} (eV)	-4.42	-4.26	-4.36	-4.35
Φ (eV)	5.10	4.96	4.48	5.54
$\Delta\Phi$ (eV)	-0.16	-0.28	-0.79	0.27
ΔV_{mol} (eV)	-0.68	-0.94	-1.41	-0.35
Bond dipole (D)	-1.21	-0.97	-1.13	-1.13
Bond dipole (eV)	0.52	0.66	0.62	0.62

It is interesting that the bond dipole of the Fazob *trans* molecules with or without the removal of fluorine atoms remains fairly constant with a value of 0.62 eV, this suggests that the effective change in the work function shift mainly arises due to the replacement of fluorine by hydrogen in respective positions of the terminal phenyl ring.

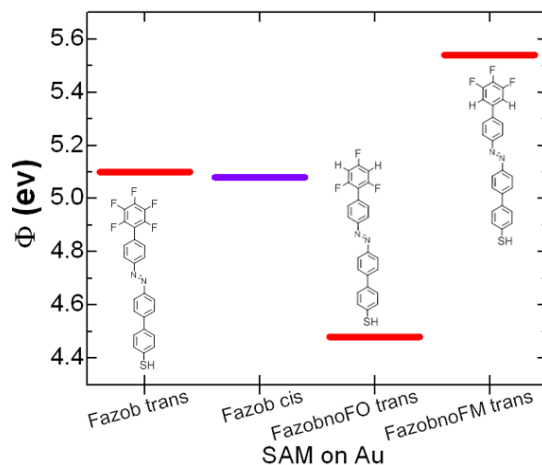


Figure 6.2.9 Work function values of the Fazob SAM on Au(111) based on theoretical simulations. The *trans* form of the molecule is indicated with red and *cis* isomer with violet bars respectively. The corresponding structure of the free molecule is overlaid in the plot for clarity.

These results quite clearly show that simple structural modifications can play a very significant role in fluorine terminated azobenzene SAMs as evidenced by the work function difference of >1

eV for the Au-FazobnoFO *trans* ($\Phi \approx 4.48$ eV) and Au-FazobnoFM *trans* ($\Phi \approx 5.54$ eV). Figure 6.2.9 shows the work function values of all the systems studied thus far, currently simulations are underway to obtain the work function values for the Fazob *cis* with the replacement of fluorine in both ortho and meta positions similar to the *trans* isomeric case.

6.2.4 References

- 1 Griffiths, J. II. Photochemistry of azobenzene and its derivatives. *Chem. Soc. Rev.* **1**, 481-493 (1972).
- 2 Sekkat, Z., Wood, J. & Knoll, W. Reorientation mechanism of azobenzenes within the *trans*-*cis* photoisomerization. *J. Phys. Chem.* **99**, 17226-17234 (1995).
- 3 Ikeda, T. & Tsutsumi, O. Optical Switching and Image Storage by Means of Azobenzene Liquid-Crystal Films. *Science* **268**, 1873-1875, (1995).
- 4 Tamai, N. & Miyasaka, H. Ultrafast Dynamics of Photochromic Systems. *Chem. Rev.* **100**, 1875-1890, (2000).
- 5 Qune, L. F. N. A., Akiyama, H., Nagahiro, T., Tamada, K. & Wee, A. T. S. Reversible work function changes induced by photoisomerization of asymmetric azobenzene dithiol self-assembled monolayers on gold. *Appl. Phys. Lett.* **93**, 083109-083103 (2008).
- 6 Nagahiro, T., Akiyama, H., Hara, M. & Tamada, K. Photoisomerization of azobenzene containing self-assembled monolayers investigated by Kelvin probe work function measurements. *J. Electron. Spectrosc. Relat. Phenom.* **172**, 128-133, (2009).
- 7 Crivillers, N. *et al.* Photoinduced work function changes by isomerization of a densely packed azobenzene-based SAM on Au: a joint experimental and theoretical study. *PCCP* **13**, 14302-14310 (2011).
- 8 Crivillers, N. *et al.* Large Work Function Shift of Gold Induced by a Novel Perfluorinated Azobenzene-Based Self-Assembled Monolayer. *Adv. Mater.* **25**, 432-436 (2013).
- 9 Ferri, V. *et al.* Light-powered electrical switch based on cargo-lifting azobenzene monolayers. *Angew Chem Int Edit* **47**, 3407-3409, (2008).
- 10 Mativetsky, J. M. *et al.* Azobenzenes as Light-Controlled Molecular Electronic Switches in Nanoscale Metal-Molecule-Metal Junctions. *J. Am. Chem. Soc.* **130**, 9192-9193, (2008).
- 11 Crivillers, N., Orgiu, E., Reinders, F., Mayor, M. & Samorì, P. Optical Modulation of the Charge Injection in an Organic Field-Effect Transistor Based on Photochromic Self-Assembled-Monolayer-Functionalized Electrodes. *Adv. Mater.* **23**, 1447-1452, (2011).
- 12 Pace, G. *et al.* Cooperative light-induced molecular movements of highly ordered azobenzene self-assembled monolayers. *Proceedings of the National Academy of Sciences* **104**, 9937-9942, (2007).
- 13 Rusu, P. C. & Brocks, G. Work functions of self-assembled monolayers on metal surfaces by first-principles calculations. *Phys. Rev. B* **74**, 073414 (2006).

6.3 CHARGE TRANSPORT THROUGH SELF-ASSEMBLED MONOLAYERS OF FLUORINATED AZOBENZENE ON AU ELECTRODES

In the part of the chapter the charge transport through self-assembled monolayers (SAMs) on gold of two different fluorinated azobenzene derivatives is reported. The difference in tunneling rates when the azobenzene molecule undergoes photo isomerization is investigated by means of measurements in a two terminal setup comprising of liquid metallic gallium-indium as the top probe electrode. Based on the switching pattern of the azobenzene molecules in solution between two photo-stationary states the samples were prepared separately via ex-situ preparation in both *trans* and *cis* isomeric forms and characterized as prepared.

6.3.1 Motivation

The assembly of thiol based molecules on noble metal such as gold surfaces by auto organization provides a viable route to realize densely packed, ordered single molecular thick (or thin in the realistic sense) 2D crystalline films. This self-assembly is driven by the affinity of the thiol molecules to form a strong covalent type of bond with the Au surface and occurs by the process termed as chemisorption (i.e., chemical adsorption).^{1,2} Making use of self-assembly selective molecules with appropriate anchoring atoms can be adsorbed onto the surface of noble metals to change its work function, wettability properties and charge injection in a device. In other words a specified pre-programmed function based on the intrinsic structure and property of the molecule can deliver a customized function once assembled onto metallic electrodes such as gold. The use of photochromic molecules such as azobenzene in SAMs on Au adds in electronic bi-functionality to entire system owing to the property of azobenzene to undergo photo induced reversible isomerization. In essence it behaves as a bistable switch, wherein one state can act as an ON (lower resistive component with respect to the other state) and the other state performing the opposite OFF (higher resistive component) operation due to change in the tunneling resistances induced by the molecule in the two different isomeric forms. This property of azobenzene SAMs has been exploited to demonstrate electrical current switching on Au electrodes^{3,4} and also work function modification of electrodes in devices.⁵⁻⁹ Here we study the

charge transport through novel fluorinated azobenzene derivatives assembled onto gold electrodes in both its isomeric forms.

6.3.2 Results and discussions

6.3.2.1 Optical properties of fluorinated azobenzene solution

The chemical structures of the two different azobenzene derivatives used in this study are depicted in the inset of Figure 6.3.1. The fluorinated azobenzene molecule is abbreviated as Fazo (Figure 6.3.1 inset) and the azobenzene with two phenyl rings is either end of the azo (-N=N-) group is termed as Fazob (see inset of Figure 6.3.1).

To understand time necessary to induced complete isomerization from the *trans* to *cis* forms in solution for both Fazo and Fazob we performed standard UV-vis absorption spectroscopy. The absorption spectrum of 10 μ M Fazo and Fazob solution in CHCl₃ was obtained from wavelength range of 300 to 600 nm by either UV or white light in the long lateral face of the cuvette containing the solution.

For the Fazo solution the absorption spectrum was recorded in intervals of 10, 10, 10, 30, 60, 120 s respectively while irradiating with UV light (8 W power intensity at a fixed distance) at λ of 365 nm between successive measurements. After 120 s from the initial time the spectrum saturated reaching its photo-stationary state, irradiation of another 120 s with UV did not change the resulting spectrum thus confirming that 120 s was sufficient to convert the molecules to the *cis* isomeric form. The reverse switching back to the initial *trans* state of the Fazo molecule was obtained by irradiation with white light at intervals of 10, 10, 30, 60 s respectively. After 110 s of white light irradiation the molecules adopted the *trans* state, which was observed by the recovery of the initial absorption characteristics of the Fazo solution. The photo isomerization duration for *cis* \rightarrow *trans* was as expected greater than *trans* \rightarrow *cis* since the *trans* isomer is the more thermodynamically favorable among the two species. Two distinct isosbestic points were observed at λ of 321.1 and 430.4 nm respectively.

For the Fazob solution the absorption spectrum was recorded in intervals of 10, 10, 40, 60 s respectively while irradiating with UV light at λ of 365 nm between each measurement. The spectrum saturated reaching its photo-stationary state after 80 s, further irradiation of another 60

s with UV resulted in no noticeable change in the spectrum thus confirming that a minimum duration of 80 s UV irradiation was sufficient to convert the molecules to the *cis* isomeric form. Further UV irradiation after 140 s yielded no change in the spectrum.

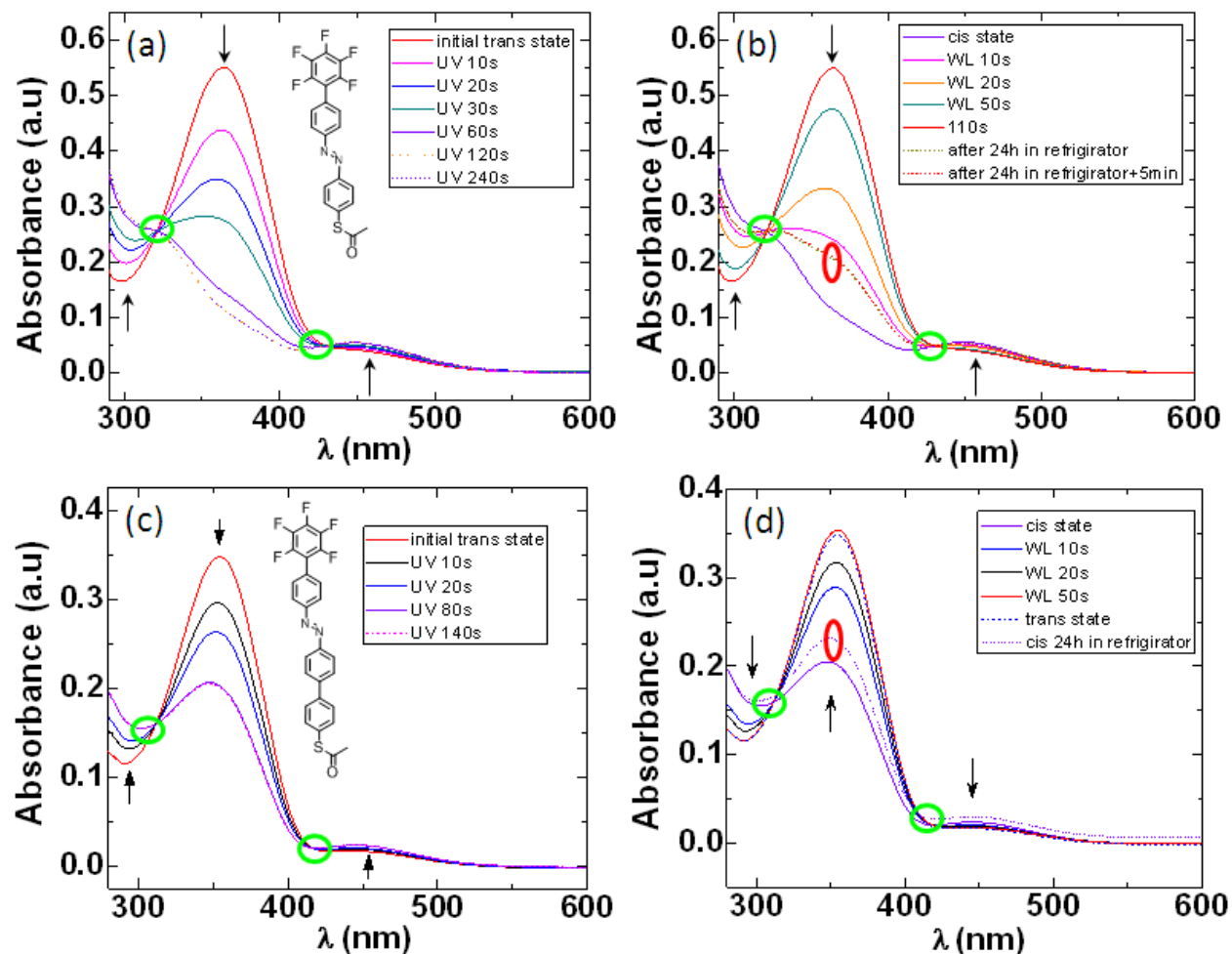


Figure 6.3.1 UV-vis spectrum of Fazo solution from (a) *trans* to *cis*, and (b) *cis* to *trans* and of Fazob solution (c) *trans* to *cis*, and (b) *cis* to *trans*. The chemical structure the molecules are represented as the inset of (a) Fazo and (c) Fazob. The isosbestic points are indicated with green circles and the red oval shows the spectrum after 24h cooling in a refrigerator.

To switch the molecules back to its *trans* isomeric form irradiation with white light at intervals of 10, 10, 30 s respectively. It was observed that after 50 s of white light irradiation the molecules adopted the *trans* state, this was evident upon overlaying the initial spectrum with the photo converted *trans* spectrum.

Again for the Fazob solution similar to Fazo, the photo isomerization duration for *cis* → *trans* was as expected greater than *trans* → *cis* since the *trans* isomer is the more thermodynamically favorable among the two species. There were two distinct isosbestic points at λ of 311.2 and 417.1 nm respectively.

The major difference along the differences in the isosbestic points between the Fazo and Fazob solution were, (1) the absorption peak in the initial *trans* isomeric form of Fazob was 354.1 nm which was nearly 10 nm blue shifted in comparison to Fazo with peak of 364.1 nm, (2) the transition offset wavelength window between the isosbestic points for Fazo of 109.3 nm was moderately larger than Fazob 105.9 nm and (3) the profile of the absorption minima of Fazo within the isosbestic points was much flatter and suppressed with the disappearance of the peak than for Fazob which showed the presence of a clear peak. These major differences between Fazo and Fazob in solution are due to the relative dipole moments induced by the molecule and its interaction with the surrounding solvent environment.

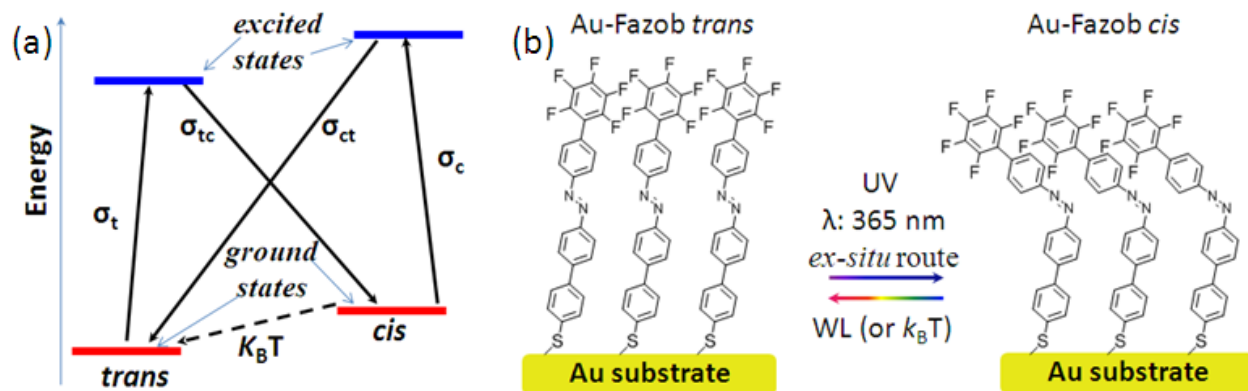


Figure 6.3.2 (a) Illustration of a simplified model of azobenzene photo isomerization process, the possible mechanism of transition from *trans* to *cis* and the reverse process is shown. (b) Scheme showing the change in the molecular confirmation of Fazob in *trans* isomeric form to *cis* confirmation upon *ex-situ* UV irradiation of Fazo solution and subsequent chemisorption of Fazob *cis* species directly to form Au-Fazob *cis* SAM. The Fazob *cis* molecules adsorbed onto gold does not retain a large bend in the azo group due to the steric repulsion between fluorine atoms of adjacent molecules at the tail of the SAM.

The simplified transition mechanism from *trans* to *cis* occurs by the absorption of photon (Figure 6.3.2) from the energy of the UV light after which the azobenzene molecule gets excited to the intermediate excited state and after which it relaxes to the ground state in the *cis* isomeric form.¹⁰

The cross section of absorption of one photon for *trans*, *cis*, *trans-cis* and *cis-trans* intermediate states are σ_t , σ_c , σ_{tc} , σ_{ct} respectively. The molecules in the *cis* form apart from being excited by photons of white light can also undergo thermal relaxation to the *trans* ground state since the corresponding energy of the *cis* isomer is higher than the *trans* (Figure 6.3.2).

For preparing the SAMs in the *trans* form clean gold substrates were incubated in 10 μ M Fazo and Fazob solutions for 24h. The preparation of the SAMs in *cis* isomeric form involved first irradiation of the respective Fazo and Fazob solutions with UV light for duration of 240 or 140 s respectively to fully photo isomerize the molecules to *cis* form after which the gold substrates was immersed in this solution and the sample along with the solution was kept inside a refrigerator at 4°C in dark for 24h. This Fazo or Fazob solution still predominantly contained molecules in the *cis* form in solution after 24h according to the UV-vis spectrums (Figure 6.3.1). Thus this method of preparation of the SAM in the *cis* form is termed as *ex-situ*. After removal from the respective solutions after 24h the substrates were rinsed thoroughly with CHCl₃ solvent.

6.3.2.2 Electrical characterization of Fazo and Fazob SAMs

We employed the eutectic alloy of gallium-indium (GaIn^E) which due to intrinsic nature to behave like a non-Newtonian liquid could be employed as a soft probe over the layer of SAM to record the charge transport properties. In other words the GaIn^E can conform to the profile of the surface of the SAM without altering the underlying structure. The GaIn^E bulk can be molded into a conical shaped tip which could be employed as the non-intrusive top contact on the SAM.

Nomenclature of junctions: We denote the junctions formed with the following naming convention, Au-SAM/Ga₂O₃||GaIn^E where “-” denotes a covalently bound contact, “/” the physical contact between the gallium oxide with the SAM and “||” the interface between the gallium oxide (Ga₂O₃) layer and the GaIn^E bulk. Figure 6.3.3 shows the schematic of a junction of Fazob *trans* SAM sandwiched between Au and GaIn^E electrodes along with the biasing conditions.

A single channel source measure unit (SMU) served as the potential source (Keithley 2635) interfaced with the two terminal junctions by means of a triaxial cable to minimize leakage losses. For all junctions the applied DC potential sweep was from -0.5V \rightarrow +0.5V (unidirectional

I - V trace) and for the bidirectional bias sweep the potential direction followed $-0.5\text{V} \rightarrow +0.5\text{V} \rightarrow -0.5\text{V}$. The entire setup was housed in a custom built Faraday cage to reduce the electrostatic discharge (ESD).

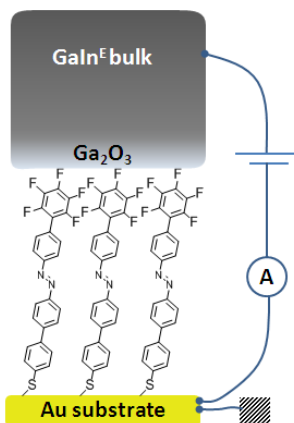


Figure 6.3.3 Schematic illustration of an Au-Fazob *trans*/Ga₂O₃||GaIn^E junction along with the biasing configuration. The Au substrate is held at electrical ground, while the potential is applied to the GaIn^E electrode.

The charge transport across the SAMs are quantified by means of the current density (J) obtained for the each of the formed junctions. The outcome for a single measurement is a current vs. voltage (I - V) trace which is further processed to obtain the actual J which is a function of the junction bias. Then normalization of I recorded for each measurement over the corresponding area of the junction yields J . Much number of measurements were performed in different junctions and at varied regions of the sample and multiple samples to arrive at a reasonable consensus of the range of distribution of the current density through a particular SAM. The J generally tends to have a log-normal type of distribution this is attributed to the exponential relationship with distance of charge tunneling.

The charge transport measurement results for the Fazob *trans* SAM plotted as $\log|J|$ histogram is shown in Figure 6.3.4. In total histogram for Fazob *trans* SAM the histogram comprises of **78 $\log|J|$ recorded** values taken at a bias of -0.4V . The histogram is fitted with a gaussian fit where the peak of the gaussian curve indicating the mean $\log|J|$, which gives the most probable occurrence for $\log|J|$ over the entire distribution this value, was estimated to be -1.8 ± 0.5 in $\log|J|$ magnitude ($J = 15.7 \text{ mA/cm}^2$).

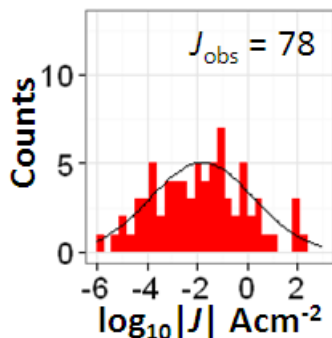


Figure 6.3.4 Histogram indicating the frequency of occurrence of $\log|J|$ recorded for Fazob *trans* form SAM on Au extracted at a bias of -0.4V. The number of occurrences of $\log|J|$ (J_{obs}) in this histogram is indicated.

Shown in Figure 6.3.5 is the $\log|J|$ distribution for the Fazob *cis* SAM constituting **121 $\log|J|$ observations** (J_{obs}) in total. The mean in $\log|J|$ magnitude was estimated to be -1.6 ± 0.4 which corresponds to a mean J value of 26.7 mA/cm^2 .

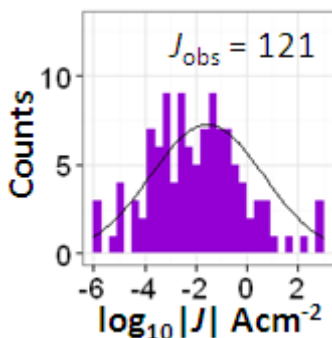


Figure 6.3.5 $\log|J|$ distribution for Au-Fazob *cis* SAM at a bias of -0.4V fitted with a Gaussian curve.

The mean $\log|J|$ vs. V profile for the Fazob SAMs on both isomeric forms on Au is shown in Figure 6.3.6. The mean $\log|J|$ for the shorter *cis* is greater than that of the *trans* isomer, this is due to the lower amount of tunneling resistance induced by the shorter *cis* SAM than the longer *trans*.⁴

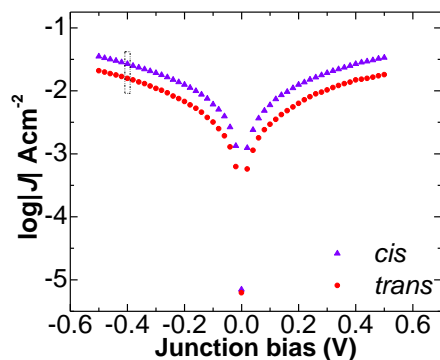


Figure 6.3.6 The current density vs. junction bias profile for the Fazob SAMs on Au in both trans and cis forms. The mean value of J is depicted for clarity. The dotted line at -0.4 V represent the potential value from which the $\log|J|$ histograms were populated.

The charge transport measurements through the Fazo SAMs on gold were carried out similar to the procedure outlined above for the Fazob SAMs. The $\log|J|$ distribution at a bias value of -0.4 V for Fazo *trans* and *cis* SAMs is illustrated in and the corresponding mean $\log|J|$ vs. V profile is shown in Figure 6.3.7.

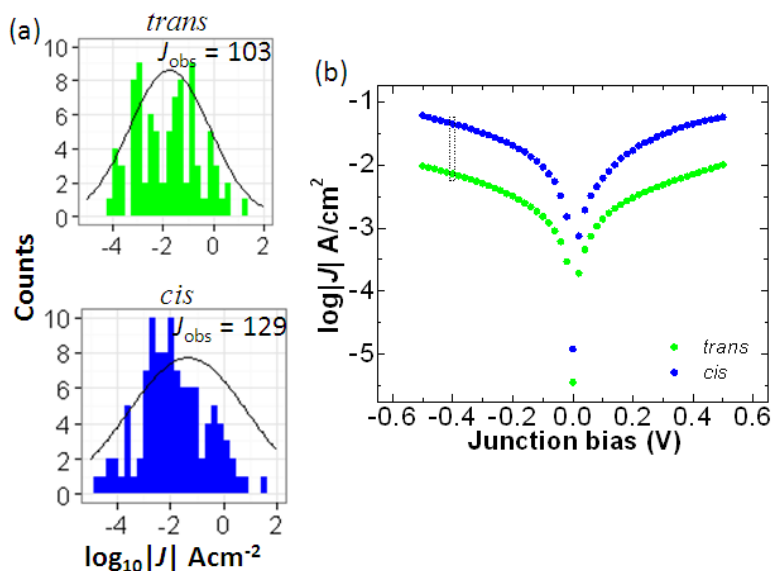


Figure 6.3.7 (a) $\log|J|$ distribution at -0.4 V for junctions of **Au-Fazo *trans*/Ga₂O₃||GaIn^E** (top) and **Au-Fazo *cis*/Ga₂O₃||GaIn^E** (top), the total number of observations in the histograms are represented appropriately. (b) Variation of mean $\log|J|$ with junction bias for the Fazo SAMs on gold, the dotted lines at -0.4 V illustrates the point in the J - V profile from which the values of the $\log|J|$ histograms are populated from.

For the Fazo SAM in the *trans* form the mean of $\log|J|$ magnitude from a total of 103 J_{obs} amounted to -1.7 ± 0.3 which equates to a mean J of 18.3 mA/cm^2 . While for the Fazo *cis* SAM the observed mean $\log|J|$ at a junction bias of -0.4 V was -1.4 ± 0.4 from 129 J_{obs} and its equivalent mean current density was 44.5 mA/cm^2 .

6.3.2.3 Discussions

The charge transport across SAMs based on conjugated molecules follows a relationship described as Simmons model which gives the relationship between the charge density, the tunneling decay and the distance. The Simmons model in the simplified form is given by $J = J_0 e^{-\beta d}$ where β gives the exponential decay due to increase in the charge tunneling length d and J_0 is the current density which might be expected in a hypothetical case when the tunneling distance is 0.^{3,11-13}

Since the charge transport in the molecular monolayer is governed by the molecular length, we estimated the individual length of the Fazob molecule both in the *trans* and *cis* isomeric forms (Figure 6.3.8) to be 22.5 \AA and 19.11 \AA respectively, this is taking into account the Au-S bond linkage distance of 2.36 \AA . In the case of Fazob *trans* the length is estimated from the Au to the terminal fluorine atom when the molecule is in its full extended form (Figure 6.3.8), while for Fazob *cis* the length is considered to be from the Au to the fluorine atom in the ortho position of the terminal phenyl ring (Figure 6.3.8). So in principle in considering that the charge tunneling through the Fazob *trans* and *cis* SAMs is dominated by the distance dependence of tunneling, the J for the Fazob *trans* should be lower than the shorter length SAM based on Fazo *cis*. The extracted value of J for Fazob *trans* SAMs after the statistical data analysis yielded a values in the range of $5.4 \times 10^{-3} - 45.9 \times 10^{-3} \text{ A/cm}^2$ and $10.6 - 67.6 \text{ mA/cm}^2$ for the Fazo *cis* SAM which results in a factor of ~ 2 to 1.5 higher J in the lower and upper bound limits respectively for the shorter *cis*. The lower and upper bounds of the $\log|J|$ reported here are taken from one standard deviation width of the log-normal distribution. The statistical analysis and the plotting of histogram was performed using ggplot2 package¹⁴ in R.¹⁵

It is expected that in the case of conjugated molecules through Fazo and Fazob SAMs on gold the charge transport is through bond non-resonant tunneling.^{4,16} The charge tunneling decay

through the Fazo SAM can be estimated by plotting the mean of the $\log|J|$ vs. the distance of tunneling. The β estimated from the slope of the plot shown in amounted to 0.16\AA^{-1} .

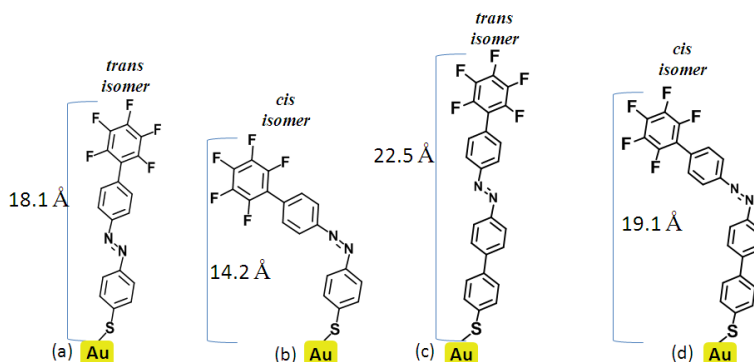


Figure 6.3.8 Illustration of length of Fazo molecule adsorbed on gold in (a) *trans* and (b) *cis* isomeric form. Similar representation of the Fazo molecules chemisorbed on gold in (c) *trans* and (d) *cis*. In the case of *cis* isomers for both Fazo and FazoB the length was estimated from the Au surface to the fluorine atom pointing upwards in the terminal phenyl ring in the ortho position.

The lengths of the Fazo SAMs chemisorbed on gold surface similar to the FazoB SAMs were estimated from theoretical simulations after optimization of the molecules packed onto the surface of gold. The optimization algorithm considers the highest probable tilt angle based of repeated iterations and the length thus estimated reflects the true value which might be the case for the ideal ordered packing of the molecules.

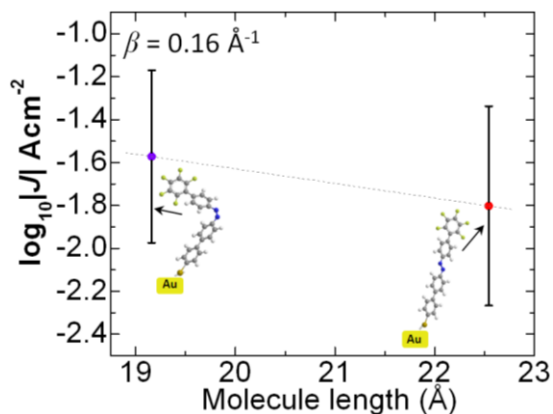


Figure 6.3.9 $\log|J|$ vs. distance plots showing the tunneling decay observed for FazoB SAMs on Au. The dashed line is the linear least square fit.

The Fazo SAM length for *trans* and *cis* isomeric forms were 18.1 Å and 14.2 Å respectively. The current density values at lower and upper bound of single standard deviation for Fazo *trans* SAMs were in the range of 8.9 – 37.6 mA/cm² and 18.1 – 109.5 mA/cm² for the Fazo *cis* SAM. The lower and upper limits within 68% confidence interval of the log|*J*| distribution of Fazo *cis* was two to three fold greater than the *trans* SAM. The tunneling decay between the two isomers of Fazo SAM was then extracted from the slope of the log|*J*| vs. *d* plot (Figure 6.3.10) was 0.23 Å⁻¹ and is the range reported in the literature for systems of π-conjugated molecular based SAMs.^{12,16}

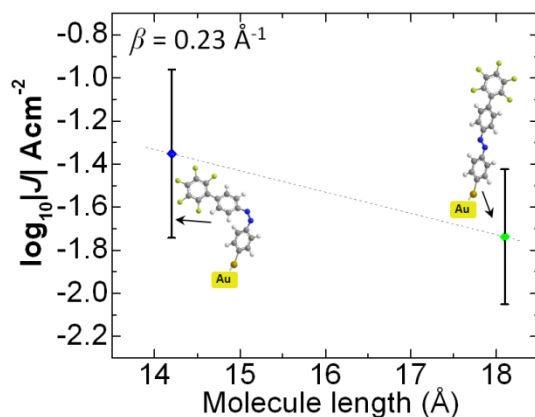


Figure 6.3.10 Variation of the log|*J*| with distance for Fazo SAMs on Au. The corresponding *trans* and *cis* SAMs are depicted adjacent to its mean log|*J*| values. The error bar represents denote one standard deviation interval and dashed line is the linear fit.

Influence of defects in the monolayer: SAMs on Au adopting both *trans* and *cis* confirmation of either Fazo or Fazob can have defects in the monolayer due to inherent defects such as grain boundaries, step edges on the Au supporting substrate along with defects caused by adventitious materials adsorbed to either the Au or GaIn^E electrodes and also due to steric repulsive effects of between adjacent molecules during SAM formation (Figure 6.3.11). The deviation from the ideal dense uniform ordering of the molecules in the SAM is also one of the major reasons for the larger span of log|*J*| distributions.

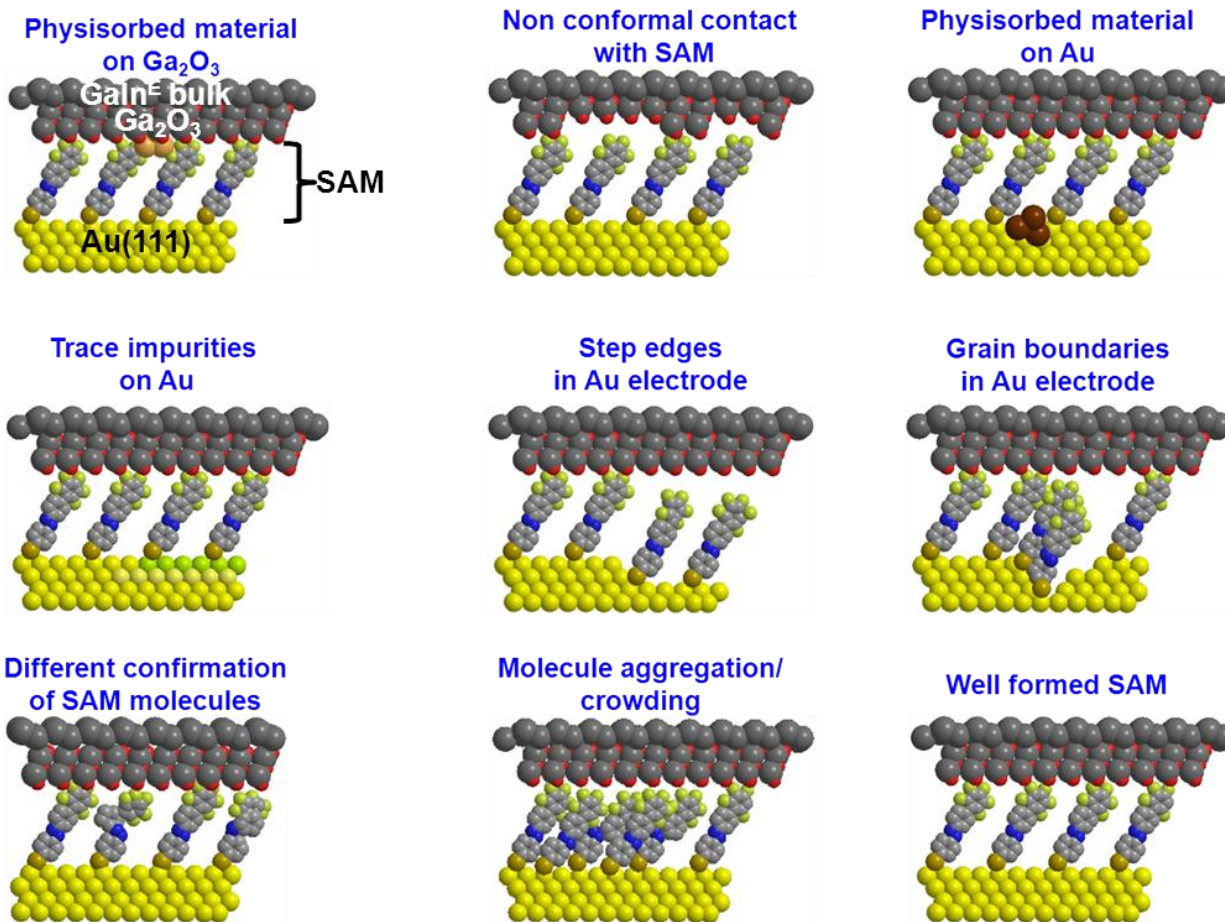


Figure 6.3.11 Cartoon showing the possible arrangements or defects in Au-Fazo *trans*/Ga₂O₃||GaIn^E junctions. The defects can significantly influence the overall outcome of the charge transport measurements in SAMs.

6.3.3 References

- 1 Nuzzo, R. G. & Allara, D. L. Adsorption of bifunctional organic disulfides on gold surfaces. *J. Am. Chem. Soc.* **105**, 4481-4483 (1983).
- 2 Ulman, A. Formation and structure of self-assembled monolayers. *Chem. Rev.* **96**, 1533 (1996).
- 3 Ferri, V. *et al.* Light-powered electrical switch based on cargo-lifting azobenzene monolayers. *Angew Chem Int Edit* **47**, 3407-3409, (2008).
- 4 Mativetsky, J. M. *et al.* Azobenzenes as Light-Controlled Molecular Electronic Switches in Nanoscale Metal–Molecule–Metal Junctions. *J. Am. Chem. Soc.* **130**, 9192-9193, (2008).
- 5 Qune, L. F. N. A., Akiyama, H., Nagahiro, T., Tamada, K. & Wee, A. T. S. Reversible work function changes induced by photoisomerization of asymmetric azobenzene dithiol self-assembled monolayers on gold. *Appl. Phys. Lett.* **93**, 083109-083103 (2008).
- 6 Nagahiro, T., Akiyama, H., Hara, M. & Tamada, K. Photoisomerization of azobenzene containing self-assembled monolayers investigated by Kelvin probe work function measurements. *J. Electron. Spectrosc. Relat. Phenom.* **172**, 128-133, (2009).
- 7 Crivillers, N. *et al.* Photoinduced work function changes by isomerization of a densely packed azobenzene-based SAM on Au: a joint experimental and theoretical study. *PCCP* **13**, 14302-14310 (2011).
- 8 Crivillers, N., Orgiu, E., Reinders, F., Mayor, M. & Samorì, P. Optical Modulation of the Charge Injection in an Organic Field-Effect Transistor Based on Photochromic Self-Assembled-Monolayer-Functionalized Electrodes. *Adv. Mater.* **23**, 1447-1452, (2011).
- 9 Lazzarini, G. M. *et al.* Increased efficiency of light-emitting diodes incorporating anodes functionalized with fluorinated azobenzene monolayers and a green-emitting polyfluorene derivative. *Appl. Phys. Lett.* **101**, 153306-153305 (2012).
- 10 Sekkat, Z., Wood, J. & Knoll, W. Reorientation mechanism of azobenzenes within the trans-fwdarw. cis photoisomerization. *J. Phys. Chem.* **99**, 17226-17234 (1995).
- 11 Ho Choi, S., Kim, B. & Frisbie, C. D. Electrical Resistance of Long Conjugated Molecular Wires. *Science* **320**, 1482-1486, (2008).
- 12 Masillamani, A. M. *et al.* Multiscale Charge Injection and Transport Properties in Self-Assembled Monolayers of Biphenyl Thiols with Varying Torsion Angles. *Chem. Eur. J.* **18**, 10335-10347, (2012).
- 13 Reus, W. F. *et al.* Statistical Tools for Analyzing Measurements of Charge Transport. *J. Phys. Chem. C* **116**, 6714-6733, (2012).
- 14 Wickham, H. *ggplot2: elegant graphics for data analysis.* (Springer, 2009).
- 15 R Development Core Team. *R: A language and environment for statistical computing.* (Springer, 2011).
- 16 Kronemeijer, A. *et al.* Electrical characteristics of conjugated self-assembled monolayers in large-area molecular junctions. *Appl. Phys. Lett.* **97**, 173302 (2010).

6.4 TRANSMISSION STUDIES THROUGH SINGLE MOLECULE AZOBENZENE DERIVATIVES LINKING GOLD ELECTRODES

Aim

To study the electronic transport through an azobenzene based molecular wires attached to gold leads. The transmission through the molecule changes with the strength of the linker group with the electrode and if there is physisorption or the presence of a small gap is introduced at one side of the junction, the transmission through the junction is expected to drop significantly due to the weak electronic coupling. In the project we aim to investigate how the transmission varies through different structural and geometrical configurations of single azobenzene molecules linking gold electrodes.

6.4.1 Motivation

The azobenzene molecule undergoes reversible photoisomerization from thermodynamically stable fully extended *trans* form to *cis* upon selective excitation with appropriate electromagnetic wavelength. The same azobenzene molecule also exhibits distinct conductive state between the two isomers. Here we investigate the transmission through the azobenzene molecule covalently linked to gold electrodes (Figure 6.4.1).

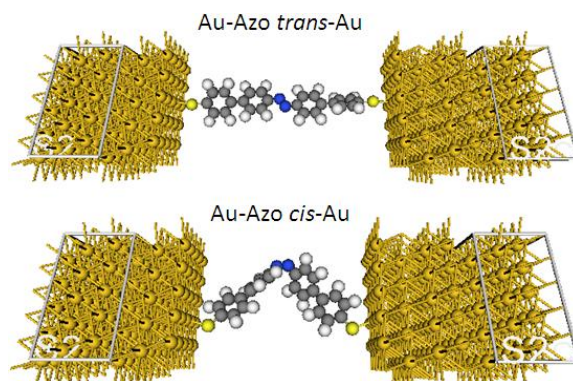


Figure 6.4.1 Schematic illustration of azobenzene molecule between periodic Au(111) surface in *trans* and *cis* isomeric states.

6.4.2 Provisional results

The system under investigation comprises of a left electrode (L), azobenzene (azo) as a molecular wire and right electrode (R). Sulfur was the linker to both the electrode. We consider

equilibrium conditions wherein the charge screening is neutral for the entire system of the Au electrodes along with the azobenzene. The Fermi level is constant at equilibrium and the conductance through the molecule can be estimated from Landauer formula given by,

$$\sigma = 2e^2 T(E_F) / h \quad (6.4.1)$$

Where $T(E_F)$ is the transmission coefficient through the molecule as a function of the Fermi energy (E_F). Using DFT the effective potentials were estimated. The transmission coefficients through the azo in *trans* along with the eigenstates of the molecular self-projected Hamiltonian (MPSH) is shown in Figure 6.4.2. The transmission at E_F for Au-azo *trans*-Au was 0.06 while for Au-azo *cis*-Au was 0.013. The transmission coefficients through the azo in *cis* along with the eigenstates of MPSH levels is shown in Figure 6.4.3.

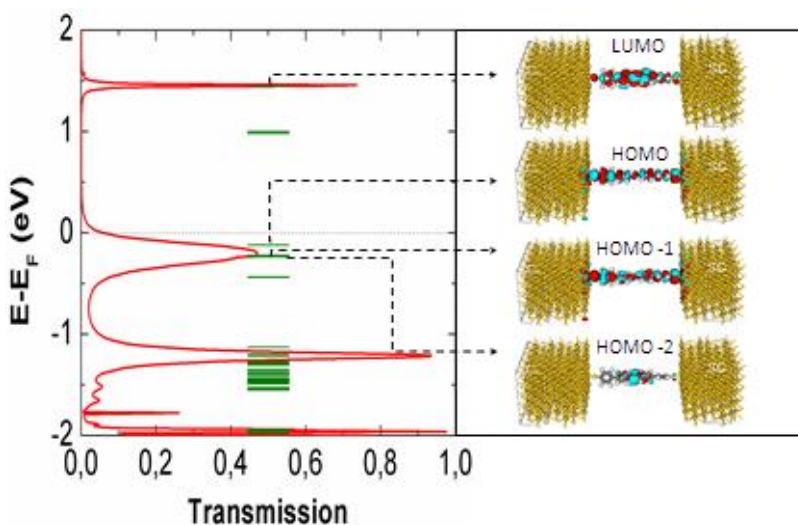


Figure 6.4.2. Transmission coefficients through the Au-azo *trans*-Au along with the molecular self-projected Hamiltonian levels depicted with green bars (left panel). Charge density localization along the Au-azo *trans*-Au system, the corresponding MPSH levels are labeled and indicated with respective arrows. The red and the turquoise lobes are the orbital projections.

The broad transmission close to the E_F for both the *trans* and *cis* azo suggests the transport through the Au-azo-Au with molecules in both isomeric states are due to resonant tunneling mechanism. The ratio of the transmission from *trans* to *cis* is ca. 4.6 which suggests that at the Fermi energy the *trans* state is more conductive than the *cis*.

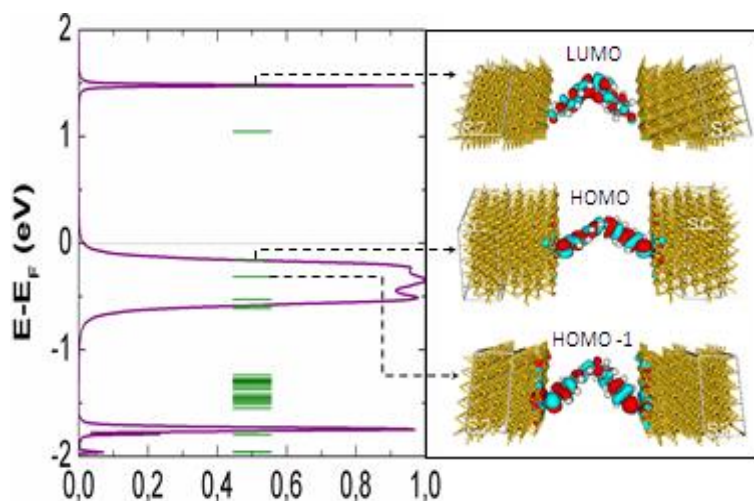


Figure 6.4.3 Transmission coefficients through the Au-azo *cis*-Au along with respective MPSH levels as green bars (left panel). Charge density localization along the Au-azo *cis*-Au system, the corresponding MPSH levels are labeled and indicated with respective arrows. In the right panel the orbital projections are portrayed in the red and turquoise colors.

The highest occupied molecular orbital (HOMO) and lowest unoccupied molecular orbital charge localization of the azo molecules in the gas phase is represented in Figure 6.4.4.

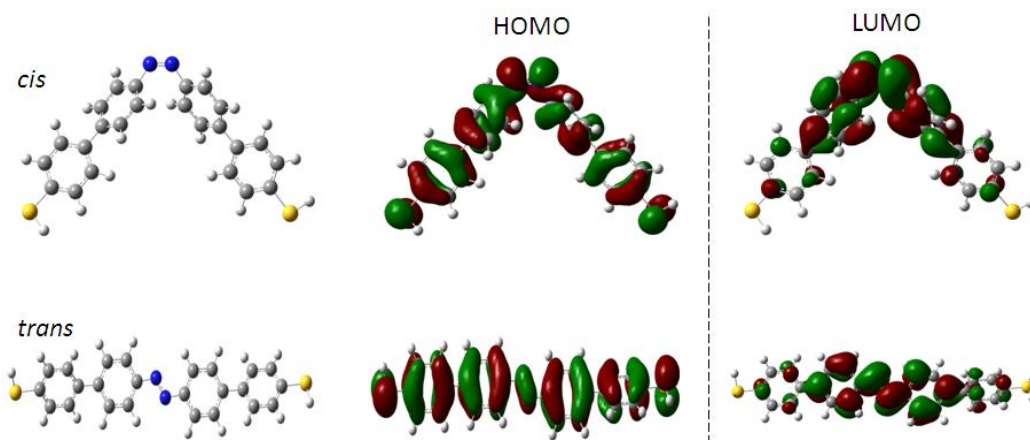


Figure 6.4.4 Optimized molecular structure of the azo in the gas phase in *cis* and *trans* states (left), corresponding HOMO and LUMO orbital charge localization lobes are displayed in the middle and right respectively.

On closer inspection of the transmission spectrum and on comparison of the MPSH levels with the HOMO and LUMO levels of the molecule in the gas phase we can note that there is a Fermi level pinning effect induced when the azo molecule is linked to the gold electrodes. Figure 6.4.5

shows the comparative plot of the HOMO-LUMO levels in the gas phase and Au-azo-Au. The HOMO LUMO gap for the free azo molecule upon covalent linkage to the Au electrode is lower indicating a Fermi level pinning of gold-azo which vanishes in the gas phase of the molecules.

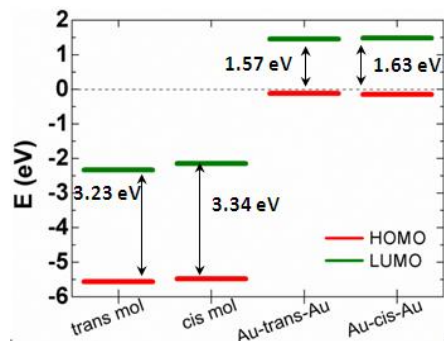


Figure 6.4.5 Comparison the HOMO and LUMO levels of the azo molecules in gas phase and between Au electrodes, illustrating the pinning effect upon attachment with gold. The dashed line represents the Fermi level of gold-azo.

The study of transmission through the azobenzene was extended to other derivatives such as fluorinated azobenzene monothiol (Fazo2, see Figure 6.4.6a), and biphenyl variant dithiol (Fazo3, see Figure 6.4.6) and monothiol (Fazo3|Au, see Figure 6.4.6c).

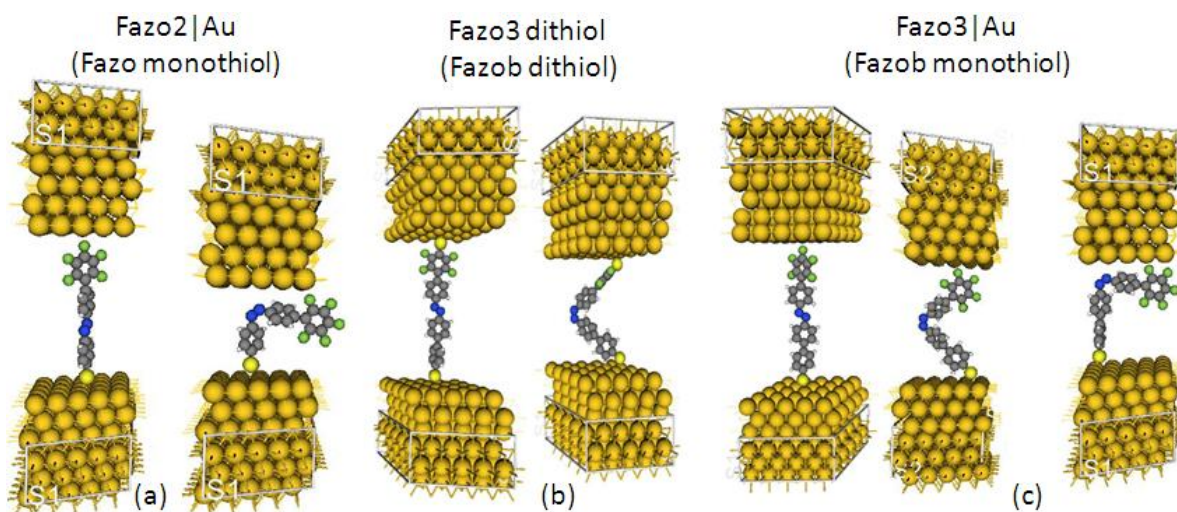


Figure 6.4.6 Different configuration of azobenzene between gold electrodes (a) Monothiol linked only to bottom electrode, (b) biphenyl variant linked to both electrodes, (c) monothiol linked to bottom electrode. All azobenzene derivatives are depicted in their *trans* and *cis* isomeric forms.

The summary of the transmission coefficient spectrum from simulations is illustrated in Figure 6.4.7. All these transmission was calculated considering no bias (0 V) between the electrodes.

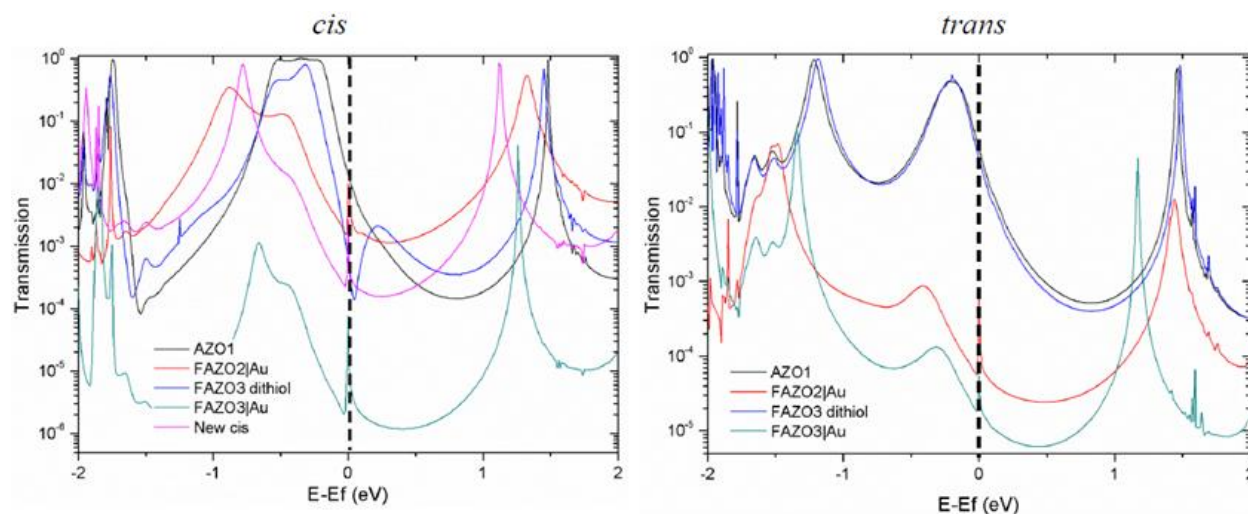


Figure 6.4.7 Change in transmission through the different azobenzene molecule linked to gold electrodes.

The magnitude of the transmission when there is monothiol is around 3 orders of magnitude lower at the Fermi level in the *trans*, this is due to the weak orbital overlap into the gold electrode near the gap.

Currently simulations are underway to estimate transmission through all these junctions considering bias applied to the electrodes.

Reason's last step is the recognition that there are an infinite number of things which are beyond it.

-Blaise Pascal (1623-1662), Polymath

7 Epilogue

7.1 CONCLUSIONS AND OUTLOOKS

In this thesis the complete aspects of charge transport in organic π -conjugated molecular based systems were studied. The immediate impacts of this field of research are manifold, wherein the techniques employed to study the charge transport in prototypical OFETs would pave the way forward in the development of more efficient organic devices by greater control over/ improving understanding of:

- (1) The device channel by the incorporation of solution processed polymer gate dielectrics of a specific molecular weight which enhances carrier mobility by better matching the surface properties at the semiconductor/dielectric interface.
- (2) The switching stability over extended periods of operation by employing dielectrics with a good breakdown strength and low leakage losses combined with lower amount of dipolar surface defects.
- (3) The understanding of the rate of charge carrier trapping provides a deep insight into the mechanism governing this phenomenon from which vital clues and design considerations can be deduced, for the development of transistors with high reliability.
- (4) Charge injection from electrodes by chemisorption of molecules with different geometries and functional groups. The molecules used to form monolayers on electrodes can be tailored to maximize the carrier injection efficiency by minimizing the hole/electron injection barrier to the transport HOMO/LUMO levels. This aspect has profound implications in a wide array of devices from organic light emitting diodes, organic photovoltaic along with transistors. Moreover each of the electrodes can be functionalized with different molecules thereby creating asymmetry between the charge injecting and collecting electrodes which would facilitate the realization of complementary logic circuits over large areas with a single semiconductor active layer.

5) The tuning of the intrinsic properties of charge transport in single component¹ organic semiconductor integrated as the active layer in a device by customized pre deposition and post processing methods.

(6) Charge transport modulation of the conductivity of a pristine semiconductor upon addition of extrinsic dopant type of photo-tunable small molecules. The entire paradigm governing intrinsic charge transport properties of the starting semiconductor compound can be dramatically altered by controlled blending with photochromic molecules. This creates a viable platform to envisage completely new functionalities for the bicomponent systems such as optical sensing, optoelectronic switching and photo induced memory effects.

(7) Mixing two or more components can be done solely to enhance the efficiency of one component at the expense of sacrificing performance of others. In other words blending can be **constructively competitive** for a single preferential component while detrimental to the remaining compounds. The other approach could involve **cooperative effect** wherein all the isolated compounds when combined together either enhance the function of one component or allow the emergence of multiple yet distinct functionalities in a single material or a device. The properties of molecular orientation, arrangement and rearrangement upon blending, phase separation, inter component physical-mechanical-electronic-chemical interactions, selective response to distinct external stimuli, affinity between the entire ensemble of compounds with the substrate and electrodes are some of the issues which should be considered for designing multi-responsive devices.

(8) The incorporation of photo responsive self-assembled monolayers (SAMs) as one of the building blocks in organic electronic devices makes it tractable to modulate certain functions within the device without affecting the performance of another part. For instance, the optical stimuli can be precisely localized to a specific region of a larger area panel with varied combination of devices to control the electrical output state of one device, which might be supplied as the input signal to completely different electronic device in the same panel.

¹ This can comprise of any single one of the following compounds such as long chain polymers (and copolymers), shorter oligomers or small molecules possessing semiconductive properties.

(9) How structural modifications of thiol based molecules chemisorbed on gold to form SAMs influence the electronic function such as charge transport rates and conductivities. The premise that practically infinitely diverse molecular geometries can be used to alter the electronic function based on the structure opens up countless opportunities to tune the work function of electrodes, charge injection properties and electrical current switching states.

7.2 GENERAL LONG-TERM PERSPECTIVES AND DIRECTIVES

Controlled blending to achieve optimal intermixing and minimal inter component interfacial defects can be taken a step further by combining more than two different components comprised of energetically favorable properties of transport levels in donor/acceptor, though this might increase the complexity of the underlying charge transport. If this can be fully mastered, this could potentially play a major role in improving efficiency in the organic solar cells by greater charge separation and collection with lower recombination losses.

Embedding photo responsive SAMs in distinct regions of large scale electronic circuits can be supplemented by employing multiple stimulations simultaneously or with a controlled time lag at different wavelengths² of excitation directly over appropriate molecules spatially isolated. The output signals of which can be modulated by the external photo induced stimuli the logical states of the output can be then either combined or multiplexed to perform customized digital logic functions. The main advantage of using photochromic molecules in SAMs thus can be fully put to use in extremely low weight and ultra-low power consuming sensors, nanoscale motion detectors, molecular motors and machines.

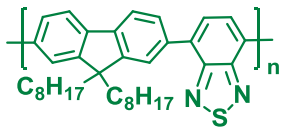
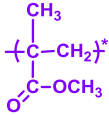
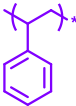
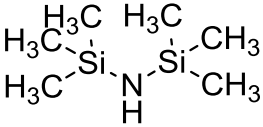

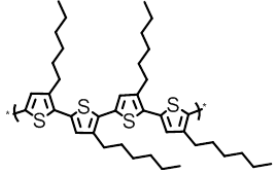
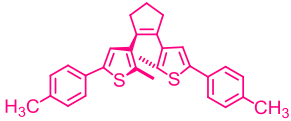
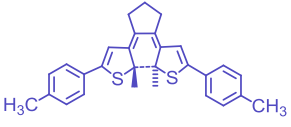
The dielectric constant of the polymeric dielectrics film could be increased significantly by addition of nanoparticles at different ratios. The incorporation of high permittivity dielectrics makes it plausible to conceive organic transistors with very low operating power.

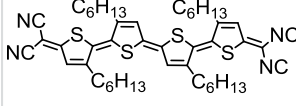
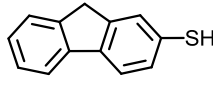
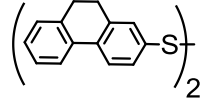
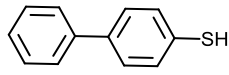
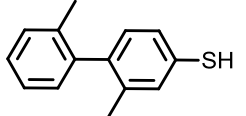
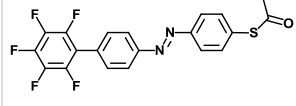
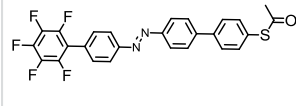
Looking at the wider picture the molecular electronics can diversify into the fields of nanobiotechnology. Here individual molecules or a set of molecules grouped in a nanodevice which can be used to attach to a malignant tumor for example in a biological specimen and this device could be controlled by a wireless signal to scavenge cell samples or to destroy locally the

² This is referred to target molecule(s) oriented excitation wavelength, which would be distinct to each of the different molecular structures depending of the optical spectral signature.

cancerous cells. The rates of charge tunneling in healthy cells and cancerous cells could also be studied to potentially find solutions for preventive and alternative treatments.

List of Molecules used in this thesis

Entry	Molecule structure	Full extended name	Abbreviated name	Property/Function	Source ^a	Referred in chapter(s)
1		Poly[(9,9-di- <i>n</i> -octylfluorenyl-2,7-diyl)- <i>alt</i> -(benzo[2,1,3]thiadiazol-4,8-diyl)]	F8BT	Polymer Semiconductor	C	5.1
2		Poly(methyl methacrylate)	PMMA	Polymer Dielectric	C	5.1
3		Polystyrene	PS	Polymer Dielectric	C	5.1
4		Hexamethyldisilazane	HMDS	Surface passivator	C	5.1
5		1-Undecanethiol	C11	Electrode surface modifier	C	5.1
6		Poly(3-hexylthiophene-2,5-diyl)	P3HT	Polymer Semiconductor	C	5.2, 5.4 and 6.1
7		1,2-bis(2-methyl-5-(<i>p</i> -tolyl)thiophen-3-yl)cyclopent-1-ene	DAE _{open}	Semiconductor /small molecule	S	5.2
8		(9aR)-9a,9b-dimethyl-2,8-di- <i>p</i> -tolyl-5,6,9a,9b-tetrahydro-4H-indeno[5,4-b:6,7-b']dithiophene	DAE _{closed}	Semiconductor /small molecule	S	5.2

Entry	Molecule structure	Full extended name	Abbreviated name	Property/Function	Source ^a	Referred in chapter(s)
9		2-((2E,2''E,2'''E)-5'''-(diisocyanomethylene)-3,3',3''',4''-tetrahexyl-5H,5'''H-[2,2':5',2'':5'',2'''-quaterthiophen]-5-ylidene)malononitrile	QQT(CN)4	Semiconductor oligomer	S	5.3
10		9H-fluorene-2-thiol	5mBPT	small molecule/electrode surface modifier	S	6.1
11		9,10-dihydrophenanthrene-2-thiol	6mBPT	small molecule/electrode surface modifier	S	6.1
12		[1,1'-biphenyl]-4-thiol	BPT	small molecule/electrode surface modifier	S	6.1
13		2,2'-dimethyl-[1,1'-biphenyl]-4-thiol	tBPT	small molecule/electrode surface modifier	S	6.1
14		(E)-S-(4-((2',3',4',5',6'-pentafluoro-[1,1'-biphenyl]-4-yl)diazenyl)phenyl)ethanethioate	Fazo	small molecule/electrode surface modifier	S	6.2
15		(E)-S-(4'-((2',3',4',5',6'-pentafluoro-[1,1'-biphenyl]-4-yl)diazenyl)-[1,1'-biphenyl]-4-yl)ethanethioate	Fazob	small molecule/electrode surface modifier	S	6.2 and 6.3

^a This denotes how the compound was acquired either from commercial (C) or synthesized (S) sources.

Logical flow of commands to remotely measure $I-V$ trace

I developed the software code to remotely control the electrometer which performs the application of the bias and records the current values by means of user-defined functions.

Figure 1 shows the time taken for the electrometer to source the bias for the forward and reverse $I-V$ traces for metal-SAM-metal two terminal junctions.

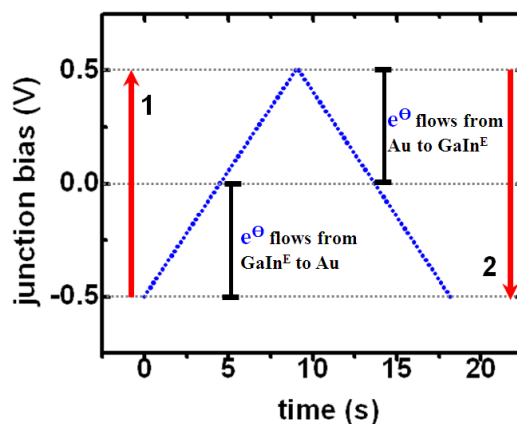


Figure 1 Time (in seconds) taken by the electrometer to source the bias, with black lines indicating the direction of electron flow during the potential sweep and red arrows indicates (1) Forward and (2) reverse trace.

Portrayed in Figure 2 is the sequence of the flow of commands followed in the software code to control the electrometer to perform a bidirectional potential sweep and record the corresponding current flowing through the junction respectively.

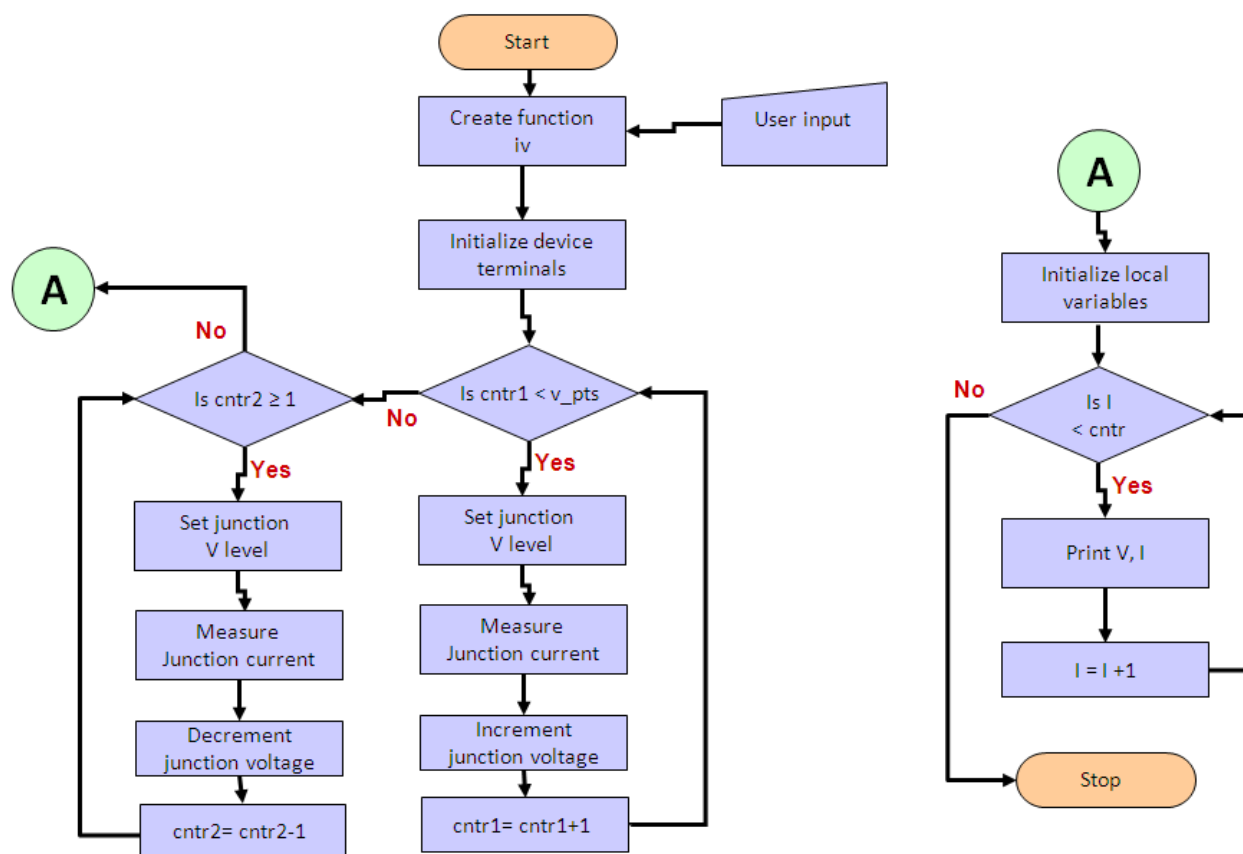


Figure 2 Logical flow of commands of the software code used to remotely control the electrometer for the application of forward and reverse potential sweeps and for measuring the respective currents.

LIST OF PUBLICATIONS

(1) *Multiscale Charge Injection and Transport Properties in Self-Assembled Monolayers of Biphenyl Thiols with Varying Torsion Angles.*

Masillamani Appan Merari, Núria Crivillers, Emanuele Orgiu, Jürgen Rotzler, David Bossert, Ramakrishnappa Thippeswamy, Michael Zharnikov, Marcel Mayor, and Paolo Samorì.

[Chemistry-A European Journal 18, no. 33 \(2012\): 10335-10347.](#)

(2) *Enhanced mobility in P3HT-based OTFTs upon blending with a phenylene–thiophene–thiophene–phenylene small molecule.*

Orgiu, Emanuele, Appan Merari Masillamani, Jörn-Oliver Vogel, Emanuele Treossi, Adam Kiersnowski, Marcel Kastler, Wojciech Pisula, Florian Dötz, Vincenzo Palermo, and Paolo Samorì.

[Chemical Communications 48, no. 10 \(2012\): 1562-1564.](#)

(3) *Increased efficiency of light-emitting diodes incorporating anodes functionalized with fluorinated azobenzene monolayers and a green-emitting polyfluorene derivative.*

Lazzerini, G. M., S. Mian, F. Di Stasio, A. Merari Masillamani, N. Crivillers, F. Reinders, M. Mayor, P. Samorì, and F. Cacialli.

[Applied Physics Letters 101, no. 15 \(2012\): 153306-153306.](#)

(4) *Molecular weights of polymeric gate dielectrics: role on the stability, reliability and performance of F8BT based ambipolar OTFTs.*

Masillamani Appan Merari, Emanuele Orgiu, Paolo Samorì. (to be submitted soon)

(5) *Study of work function of a novel fluorinated azobenzene derivative on Au electrodes.*

Masillamani Appan Merari, Osella Silvio, Liscio Andrea, Reinders Federica, Mayor Marcel, Cornil Jérôme, Paolo Samorì. (Manuscript in preparation)

(6) *Intrinsic carrier mobility of dual mode polymeric semiconductor-photochromic molecular blend based field effect transistors.*

Emanuele Orgiu, Masillamani Appan Merari, Musser Andrew, Friend Richard, Paolo Samorì.
(Manuscript in preparation)

(7) *Activation energy of hole carriers in organic field-effect transistors based on Quinoidal Oligothiophene derivative.*

Masillamani Appan Merari, Ribierre Jean-Charles, Emanuele Orgiu, Paolo Samorì. (Manuscript in preparation)

(8) *Charge transport through fluorinated azobenzene self-assembled monolayers on gold electrode.*

Masillamani Appan Merari, Osella Silvio, Reinders Federica, Mayor Marcel, Cornil Jérôme, Paolo Samorì. (Manuscript in preparation)

(9) *Studies of single molecule charge transport through photochromic azobenzene derivatives linking gold electrodes.*

Osella Silvio, Masillamani Appan Merari, Cornil Jérôme, Paolo Samorì. (Manuscript in preparation)

Acknowledgements

It gives me great pleasure to thank Prof. Paolo Samorì who gave me the opportunity and support to work in his group. He provided me with thought provoking and challenging projects to bring out the creative best in me which made me a better researcher.

Big credit goes to Prof. Franco Cacialli who instilled in me initial enthusiasm for pursuing research.

It has been a memorable three years working in this group during which I learnt a lot from fellow colleagues. Huge credit goes to Dr. Markus Döbbelin for interesting suggestions about science, life and beyond. Dr. Núria Crivillers has been instrumental in helping me characterize molecular monolayers, it was really great to work with her. I give credit to Drs. Jeffrey Mativetsky and Jörn-Oliver Vogel for teaching me the working principles of an Atomic force microscope.

Many projects were successful by the strong support from our collaborators who provided us with the compounds. To this end I convey my deep gratitude to Drs. Jürgen Rotzler, Federica Reinders, Mr. David Bossert and Prof. Marcel Mayor from University of Basel, Switzerland who provided us with the biphenyl thiol and azobenzene compounds. Prof. Jean-Charles Ribierre and Dr. Florian Dötz provided the quinoidal oligomer and PTPP compounds respectively. My gratitude goes to Dr. Ramakrishnappa Thippeswamy and Prof. Michael Zharnikov for the characterization of the biphenyl monolayer on gold.

A special thanks to Mr. Silvio Osella and Dr. Jérôme Cornil for helping me during my secondment in University of Mons and giving me good advices on how to perform theoretical computer simulations of molecules on gold surfaces.

It was enriching to work, share and learn from all the members of the team past and present Drs. Pasquale D'Angelo, Oliver Fenwick, Carlos-Andres Palma, Corinna Raimondo, Andrea Cadeddu, Matthias Treier, Rebecca Savage, Emanuele Orgiu, Artur Ciesielski along with fellow doctorate candidates Chiara Musumeci, Maria Del Rosso, Mirella El Gemayel, Tim Leydecker, Thomas Mosciatti, and Sébastien Haar.

On a personal note there are many who I should thank for making me the person who I am today. I am very grateful to my father and mother who educated me and gave me the values that I stand for, I would not be here if it was not for your faith in me. Big thanks to my grandmother Mrs. Selvam Masillamani who keeps me in her well wishes and earnest prayers. I also express my heartfelt thanks to my good friend Linda, you have been my pillar of support. My sincere thanks go to my brother, cousins and friends Gaius, Farah, Sneha, Topaz, Ajay, Matthieu, Rohini and Kutty athai.

Last but not the least I like to acknowledge the Marie Curie fellowship from the European Commission RTN Threadmill (MRTN-CT-2006-036040) and ITN Superior (PTN-CT-2009-238177) which enabled me to carry out this research.